EFFECTS OF TRACE SO_2 AND NA_2SO_4 DEPOSIT ON THE REACTION BEHAVIOR OF AL_2O_3-SCALE FORMING ALLOYS

by

Xu Liu

Bachelor of Science, Northeastern University, 2005

Master of Science, Chinese Academy of Science, 2008

Submitted to the Graduate Faculty of

the Swanson School of Engineering in partial fulfillment

of the requirements for the degree of

Doctor of Philosophy

University of Pittsburgh

2014

UNIVERSITY OF PITTSBURGH

SWANSON SCHOOL OF ENGINEERING

This dissertation was presented

by

Xu Liu

It was defended on

January 13, 2014

and approved by

Gerald H. Meier, Ph.D., Professor, Department of Mechanical Engineering and Materials Science

Badie I. Morsi, Ph.D., Professor, Department of Chemical and Petroleum Engineering

Guofeng Wang, Ph.D., Assistant Professor, Department of Mechanical Engineering and Materials Science

Dissertation Director: Brian M. Gleeson, Ph.D., Professor, Department of Mechanical Engineering and Materials Science

EFFECTS OF TRACE SO_2 AND NA_2SO_4 DEPOSIT ON THE REACTION BEHAVIOR OF AL_2O_3-SCALE FORMING ALLOYS

Xu Liu, PhD

University of Pittsburgh 2014

This study focused on the effects of minor alloying elements (Si, Pt), trace SO_2, and Na_2SO_4 deposit on oxidation and 900°C sulfate-deposit-induced hot corrosion behavior of Al_2O_3-scale forming alloys.

In the first part of this study, the effects of Si, Pt and Si+Pt on the oxidation and hot corrosion behavior of γ′-Ni_3Al-based alloys were studied. This was done by conducting exposure tests at 900°C in air, and in air with an Na_2SO_4 deposit (hot corrosion). All alloys showed similar behavior during oxidation in air, while an improved hot corrosion resistance was achieved with the addition of Si and Pt. The tracking of alloy performance during different stages of hot corrosion showed that: 1) Formation of a continuous and tenacious oxide scale of Al_2O_3 or $(Al,Cr)_2O_3$ is necessary for hot-corrosion protection; 2) Maintenance of a protective alumina scale or sub-scale depends on the scale adhesion and the re-healing capability of the alloy subsurface; and 3) Onset of breakaway corresponds to the alloy's inability to maintain protective alumina scale formation. It was further found that the presence of Na_2SO_4 deposit favored α-Al_2O_3 establishment. The inferred reasons for this are presented.

The next focus of this study was on the effects of SO_2 and Na_2SO_4 deposit on the oxidation and corrosion behavior of alumina-scale forming alloys. In one set of experiments, low Cr model and commercial alloys were oxidized in atmospheres with and without 0.1% SO_2 or 1%SO_2 at 900 or 1000˚C. It was found that a small amount of SO_2 can be beneficial by promoting the transition

from internal to external Al_2O_3-scale formation and favoring the early kinetic establishment of the thermodynamically stable α-Al_2O_3. In another set of experiments, Na_2SO_4-deposited PWA1484 were exposed at 900˚C in air and O_2-SO_2 gases for containing up to 0.1% SO_2. With an increase in SO_2 content, the extent of attack increased, particularly the extent of internal sulfidation. Thus, with a deposit, SO_2 can be detrimental. This was due to SO_2 introducing internal sulfidation as a mode of degradation beyond that found with 900°C hot corrosion.

TABLE OF CONTENTS

LIST OF TABLES

LIST OF FIGURES

ACKNOWLEGEMENTS

First of all, to my supervisor Prof. Brian Gleeson, I cannot find a word to describe my appreciation for the time, energy, patience and sacrifice he has invested in training me to be a better researcher and better person. Without his supervision and encouragement, the thesis could never have been accomplished at this level. It is such an inspiring, lucky and enjoyable experience to work with him.

I'd like to thank Prof. Gerald Meier, Prof. Badie Morsi, Prof. Guofeng Wang for their helpful advices during the course of completing this work.

To my colleagues, Wei Zhao, Zhihong Tang, Juan Manuel Alvarado Orozco, Mike Task, Keeyoung Jun, and Nan Mu, I have benefited from research discussions and technique help. Thanks are due to David Hovis and Maryam Zahiri at Case Western Reserve University for conducting advanced characterization. Thanks are also due to Cecile Bonifacio at Lawrence Berkeley National Laboratory for chemieSTEM characterization.

To my parents, my brother and my fiancé Fei Long, thank you for your unconditional love and support. Without your understanding, I would not accomplish this. To my friends, thanks for your accompany.

Finally, thanks are due to the Office of Naval Research for providing the funding for this research.

I'd like to dedicate this thesis to my heavenly Father

1.0 INTRODUCTION

Driven by the need for higher thermal efficiency in conjunction with increasing atmosphere pollution and the necessity of using low grade fuel, gas turbines used in marine shipping, power plant and aircraft are increasingly susceptible to experiencing corrosion by one or more species, including O_2, Na_2SO_4, SO_2, H_2O, or some combination of these. This poses significant challenges for materials used at high temperature, which include weakening in mechanical strength, high temperature corrosion and thermal instability of structure. The desired mechanical strength is provided by the structural materials—superalloys; while the resistance to environmental degradation is provided by high-temperature coatings through the formation of a protective oxide layer when exposed to high temperature and highly corrosive environments. The establishment and maintenance of a complete, intact protective layer is critical for materials being resistant to severe degradation. This oxide layer is often alumina for high-temperature gas turbine applications.

Under certain conditions, sulfate-rich salt can deposit on the surface of gas-turbine hardware, with the prototypical salt deposit being Na_2SO_4. It is commonly asserted that the Na_2SO_4 forms by the reaction between salt in the atmosphere, such as NaCl, and SO_2/SO_3, stemming from sulfur impurity in the fuel [1]. When turbine engines operate in near coastal regions, there is significant risk for Na_2SO_4 formation. When the temperature is below the dew point of Na_2SO_4, salt deposits on the surface of components and this can lead to a highly accelerated form of

attack and causes failure of very costly turbine components. This salt-induced materials degradation is referred to as hot corrosion.

Hot corrosion generally follows a two-stage process: an initiation stage during which the rate of corrosion is slow and similar to that which occurs in the absence of the deposit; and a propagation stage during which rapid, sometimes catastrophic corrosion occurs. The incubation stage is a consequence of oxidation, and, more importantly, maintaining the formation of a protective oxide scale. The initiation of the propagation stage is associated with disruption of the protective oxide scale.

Many of the previous investigations on hot corrosion were focused on the mechanisms active during the propagation stage. From a practical point of view, the extension of lifetime is most important and that is determined by the duration of the incubation stage. However, oxide-scale formation during the incubation stage has only been recently studied [2, 3] and that investigation was done on the β-NiAl system. A reasonable understanding of the processes involved is still limited, especially for other alloy systems such as those containing predominantly γ′-Ni_3Al—the primary phase of many Ni-based superalloys and γ+γ′ coating materials. Knowledge about identifying the nature of oxide-scale formation beneath a salt deposit and the ability of an alloy to influence the duration of the incubation stage is important for developing tractable engineering solutions for extending the service lives of high-temperature components exposed to hot corrosion conditions.

Section 5.1 in this thesis will mainly investigate the hot corrosion of Si and/or Pt modified γ′-Ni_3Al-based alloys. Through studying the oxidation and hot corrosion behavior of these alloys at different stages, the critical properties of oxide scale and alloy capability that dictate the duration

of the incubation stage will be assessed. The role of minor alloying element Pt and Si on the oxidation and hot corrosion of alumina scale forming alloy will be investigated.

To better understand oxide-scale growth during the incubation stage of hot corrosion, it is necessary to investigate the role of environmental effects on oxide scale formation. A limited amount of literature has reported in this aspect[2]. Except for the presence of Na_2SO_4 deposit, an important and commonly present species in the service environment is a trace amount of SO_2. The sources of SO_2 include the combustion of low-grade fuel and the atmospheric pollution. Regarding the latter being important, this is significantly dependent on geographic region of the world. Specifically, the growing global air pollution adds another source to the susceptibility of turbines to hot corrosion.

Given that alloys and coatings used in the environments described often rely on alumina–scale formation for protection, it is important to understand this formation process in the presence of Na_2SO_4 and SO_2. Very little work has been done on the effects of trace SO_2 and Na_2SO_4 deposit on the reaction behavior of Al_2O_3-scale forming alloys, particularly during the early-stages of reaction. However, the knowledge related to this not only directly contributes to the scientific understanding of the alumina-scale growth and its interaction with the environmental species related to hot corrosion, it may also help to elucidate the key factors governing the hot-corrosion resistance.

Alumina has a number of polymorphic structures and the scale establishment also requires a critical aluminum concentration below which forming external alumina scale is impossible. This critical aluminum concentration is an important factor because it provides guidance to alloy design. Section 5.2 in this thesis will study the effects of environmental sulfur on the structural stability of alumina scales. It will focus on interesting sulfur-induced phenomena that were

observed and the underlying mechanisms will be explored. Section 5.3 in this thesis will then study the effects of environmental sulfur on the establishment of alumina scale. Another interesting observation on scale establishment will be shown and the rationale underlying this non-widely reported phenomenon will be presented.

The last section of this thesis investigates the effect of SO_2 on type I hot corrosion. Of particular interest is the contribution of SO_2 to the overall degradation process. The results obtained represent a previously unreported modified mode of type I hot corrosion that is dependent on the alloy or coating system. Specifically, for those systems that are borderline protective against hot corrosion, the SO_2 provide a source for internal sulfidation. The mechanisms associated with this mode of degradation are discussed.

2.0 TECHNICAL BACKGROUND

2.1 HIGH TEMPERATURE APPLICATIONS AND MATERIALS

2.1.1 Commercial applications

Driven by increasing societal needs for more and cleaner energy, faster transportation and rapid information exchange, advanced materials must operate in progressively higher temperature environments. In energy–conversion systems such as, gas turbines used in marine shipping, power plants, a higher operating temperature means a higher thermal efficiency. Materials used in these environments currently operate above about 600°C and perhaps even for periods at temperature exceeding 1000°C. There is a thermal efficiency gain to pushing operating temperature to higher values.

This continued need for increasing temperature poses significant challenges for materials used as gas turbine components. These challenges include weakening in mechanical strength, thermal instabilities of structure, and high temperature corrosion [4]. All these challenges add limitations for selecting materials for high-temperature application.

Figure 2.1 shows stress-rupture creep strength as a function of temperature for different alloy materials. It is seen that there is a significant decrease in mechanical strength as the temperature increases, especially when it reaches a certain value. Among the different kinds of

structural materials, such as carbon steels, austenitic steels and Fe-Cr-Ni alloys, Ni and Co-based alloys are the strongest at temperatures higher than 1000K. As a result, for high temperature application, Ni and Co-based alloys, such alloys are generally referred to as superalloys, which connote strength at high temperatures. Over the past 60 years, materials for use at high temperatures, particularly superalloys and associated protective coatings have been the focus of significant research and development [4-6].

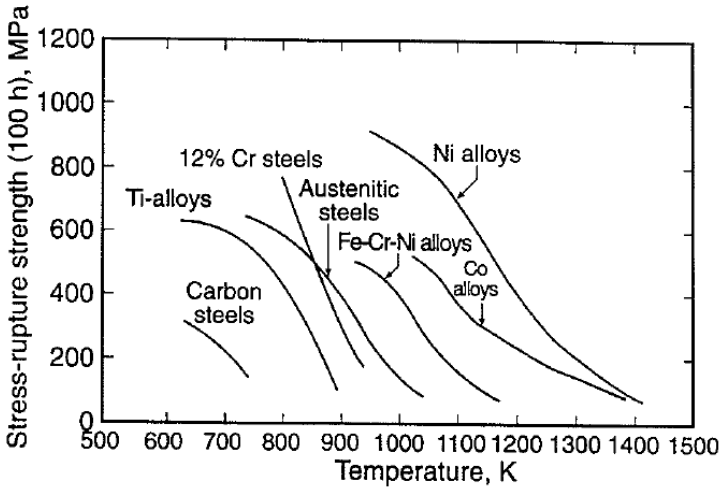

Figure 2.1 Stress required to produce creep rupture in 100 hours for various alloys (after Weronski and Hejwowski, 1991) [4]

2.1.2 Superalloys

A superalloy is an alloy developed for elevated temperature service, usually based on group VIIIA elements, where relatively severe mechanical stressing is encountered, and where high surface stability is frequently required [7].

Superalloys are divided into three classes: nickel-based; cobalt-based; and iron-based. Nickel and cobalt are favored base metals as they tend to be strongest and have greatest thermal stability. Nickel-based alloys are more widely used and will be the focus of this discussion.

Superalloys are defined in the physical sense by their chemical composition, phase constitution and microstructure. These three are discussed next in sequence.

2.1.2.1 Chemical composition

Superalloys can have complex chemical compositions. For instance, a number of commercial alloys contain more than ten elements. Figure 2.2 summarizes the major elements that may be present in a given nickel-based alloy, with the height of element blocks indicating the amount that may be present. The role of elements is also indicated in Figure 2.2. It can be seen that most elements are added to improve strength such as through precipitate strengthening, solid-solution strengthening, and grain-boundary strengthening. Two elements—Al and Cr—confer surface protection. When being exposed to high temperature, superalloys with sufficient Al or Cr concentration form a continuous Al_2O_3 or Cr_2O_3 layer. These oxide layers are solid, highly stable, and slowly growing, thus efficiently acting as barriers that protect the underlying alloy from corrosive species existing in the operating environments.

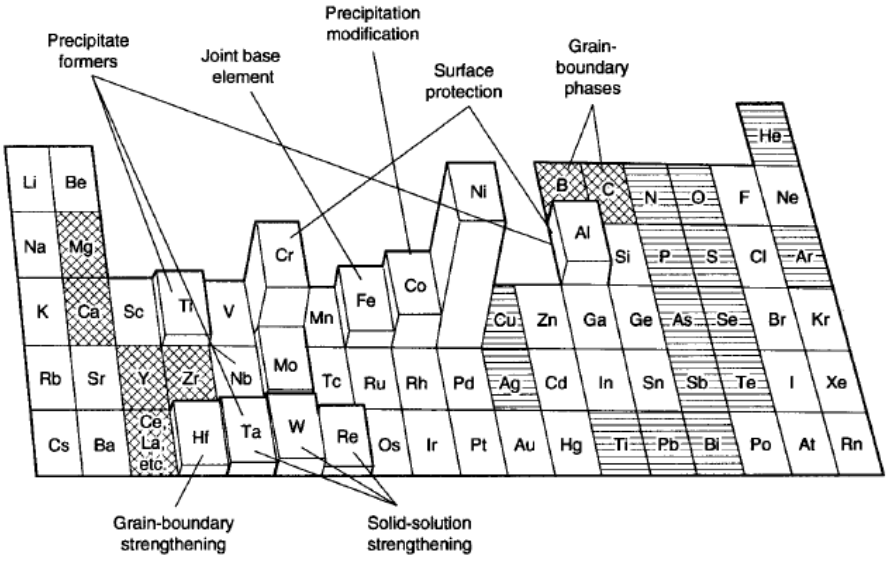

Figure 2.2 Alloy elements used in nickel-based superalloys. Beneficial minor elements are cross-hatched, while detrimental tramp elements are marked with horizontal lines [8].

The developing trend in superalloy chemical composition has been to increase strength by adding more strengthening elements. To maintain alloy stability, this trend has resulted in a significant decrease in Cr content. Details of this will be given later in this chapter.

2.1.2.2 Phase constitution

Common phases in a superalloy include gamma (γ-Ni), gamma prime (γ′-Ni_3Al), gamma double prime (γ′′-Ni_3Nb), carbides ($M_{23}C_6$, M_6C) and perhaps undesirable compounds such as μ, σ, and Laves. The superalloy matrix is γ-Ni, which is a close-packed FCC phase with many alloying elements such as Co, Cr, Mo, W, Re, Ta in solid solution. Gamma prime (γ′-Ni_3Al) is rich in Al, Ti, and Ta and it forms as precipitate, which is partially coherent with the γ-matrix. In Nb-rich Ni-Fe superalloy, γ′′-Ni_3Nb, another body-centered-tetragonal precipitate phase is apt to be present. Both γ′ and γ′′ precipitates distributed in the γ-matrix serve as obstacles to

dislocation movement and therefore confer strengthening [9].Carbides ($M_{23}C_6$, M_6C) are important phases, at least for polycrystalline superalloys, because they strengthen the grain boundaries[10]. Laves, μ, and σ are phases which are detrimental to mechanical properties and they tend to form when an alloy contains a high content of refractory elements (e.g., Mo, W, Cr, Nb and Re).

As chemical composition influences the phases present, the phases in turn create the microstructure. Figure 2.3 shows the dramatic evolution of superalloy microstructure from the 1930s through to the 1980s. In the 1930s-1940s, when superalloys were initially developed, there were hardly any precipitates in the microstructure. In the 1950s, there came a much improved understanding of the direct relationship between precipitate phases and mechanical properties. As a result, the alloys developed contained more "structure", which made them increasingly stronger. The major "structure" addition was γ′ precipitates. In the 1950s, very complex grain boundaries containing Cr-rich $M_{23}C_6$ carbides were created. Until the 1960s, the alloy matrix was mainly filled with both spherical and cuboidal γ′. To further pack up more γ′ into a given volume, only cuboidal γ′ was kept. In the middle of the 1970s, an ordered arrangement of cuboidal γ′ in the γ matrix was observed. Later, it was found that random grain boundaries can be a source of weakness at higher temperature service. In the 1980s, the development of directional solidification processing created aligned grain structures with consequential directional properties. Most important, high-temperature strength was relatively high in the direction-aligned with the grains. Soon after the establishment of directionally-satisfied (DS) superalloys, single-crystal superalloys were developed. With the elimination of grain boundaries, single crystal superalloys made it possible to further increase service temperature by about

~100°C[11, 12].The upper limit of superalloy service temperature is 90% of its melting point [13].

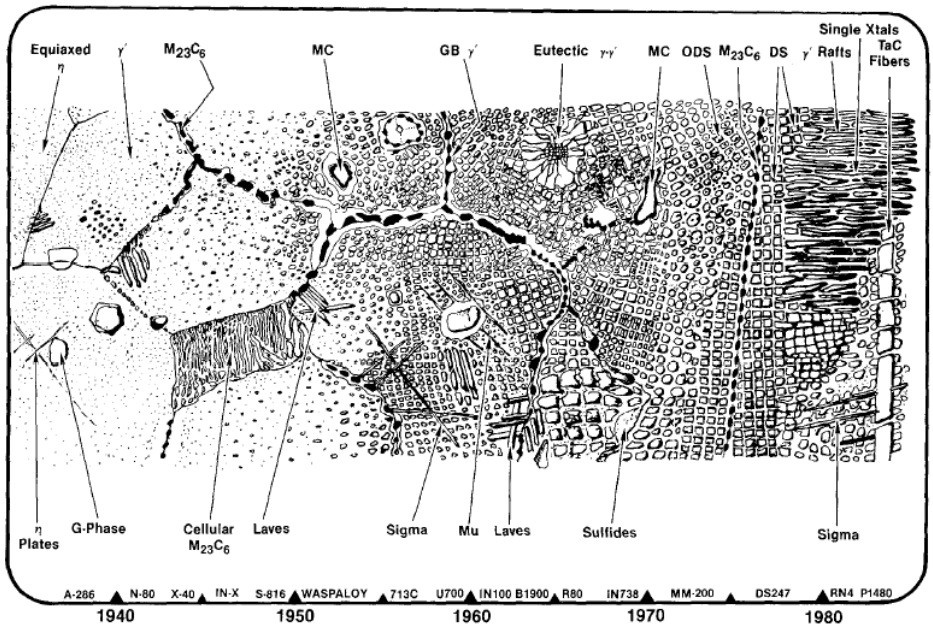

Figure 2.3 Panorama of the development of nickel Superalloy microstructure, showing both useful and deleterious phases[14]

As can be seen from the evolution of microstructure, the major driver for superalloy development was to achieve improved mechanical properties at elevated temperatures, i.e., high yield strength, high fracture toughness, long creep lifetime, and high fatigue life time. This development trend is shown in Figure 2.4. Based on the most typical alloys for each period, this figure shows the temperature capabilities of superalloys, as represented by creep strength, have steadily increased over the years. This improvement is due to advances in manufacturing processes, chemical composition adjustment and microstructure optimization.

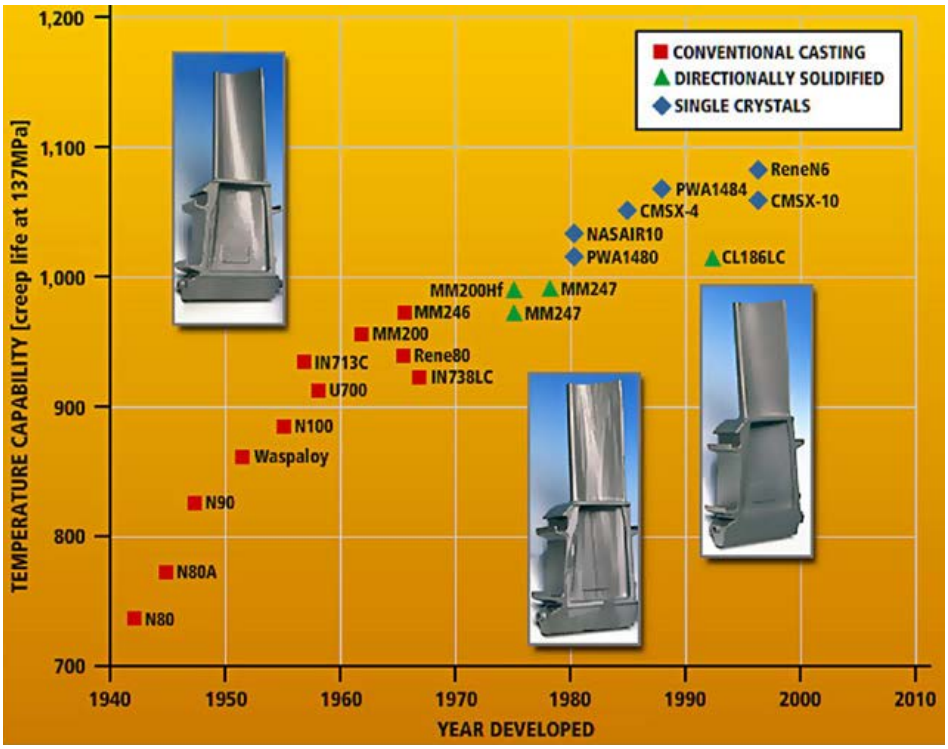

Figure 2.4 Progress of the temperature capability of the superalloys over the past 60 years (Y-axis temperatures are in °C)[15]

Single-crystal superalloys have been intensively developed for last 20-30 years[5]. Strategic elements like Re and Ru have been added to recent superalloys—so called 2nd to 5th generation superalloys—to increase strength and improve thermal ability. As a consequence, however, other elements such as Cr have had to be reduced in the alloys. This is indicated in Figure 2.5. Chromium is critical for environmental resistance; the less the Cr content in the alloy, the less resistant will that alloy be to environmental degradation.

As expected, from turbine airfoil alloy advances (Figure 2.6), the creep and fatigue strength of superalloys greatly increased. Along the way during that development, oxidation also improved owing to the increases in the aluminum content. However the corrosion resistance was decreasing due to a corresponding decrease in the chromium content. Then finally for the newly

developed alloys, even greater strength was reached, but that was with a debit in oxidation resistance. Because of insufficient Al and/or Cr contents, recently developed superalloys oxidize at unacceptably rapid rates at operating temperatures and they are vulnerable to environmental degradation. The engineering solution to this has been to use separate materials to perform separate functions. Specifically, the strong superalloy components are protected by oxidation-resistant metallic coatings. This has led to the development of high-temperature coatings.

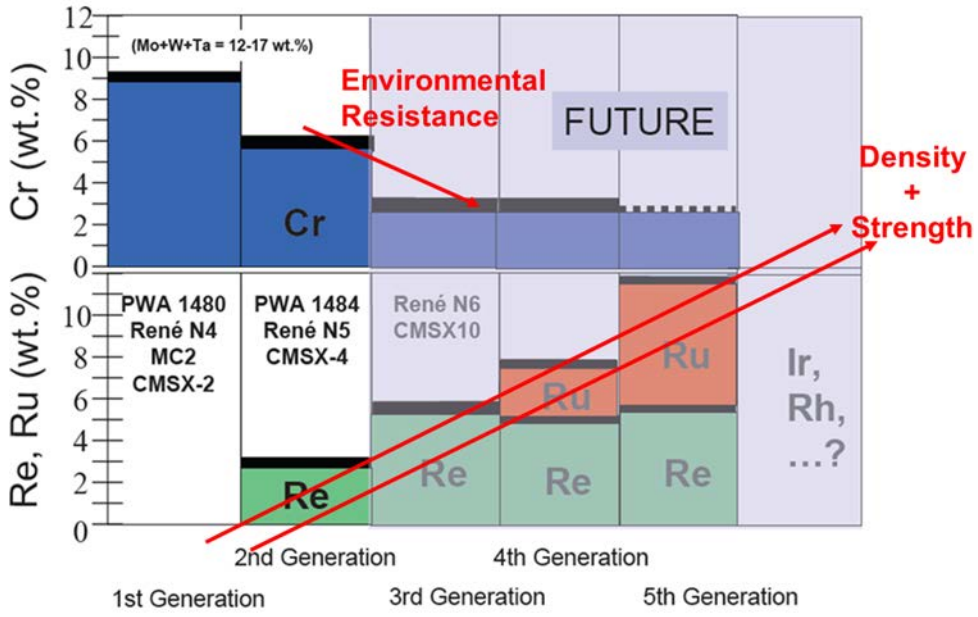

Figure 2.5 Single crystal superalloy development trends[16]

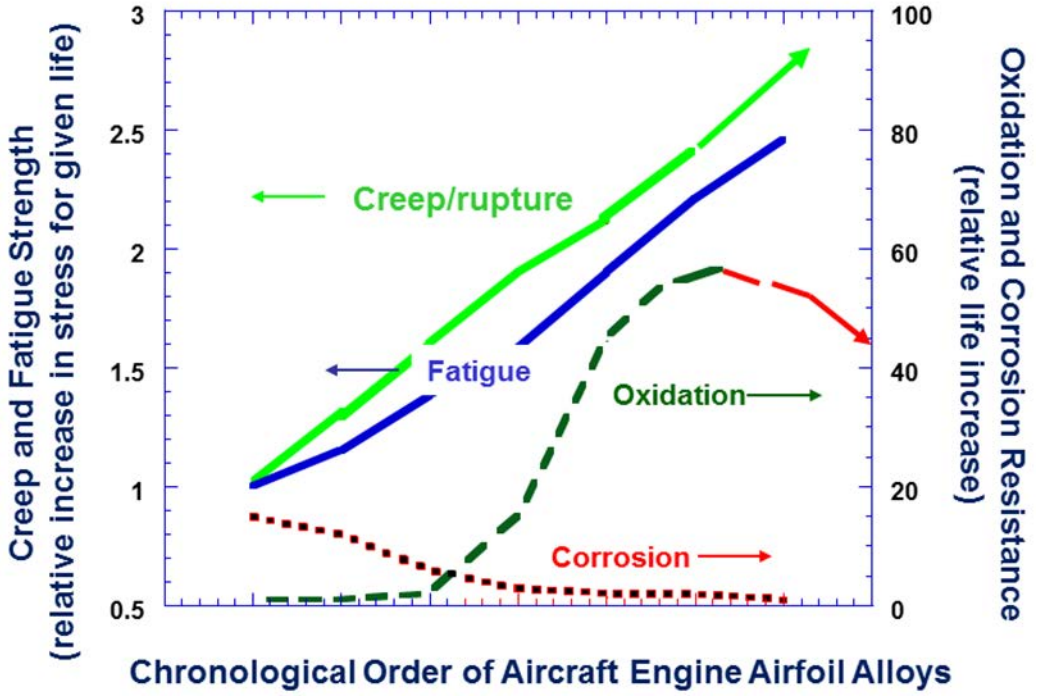

Figure 2.6 Turbine airfoil alloy advances[16]

2.1.3 High-temperature coatings

High-temperature metallic coatings are specially designed to combat environmental degradation. When exposed to high temperatures, a protective oxide scale forms on the coating surface, which provides protection against harsh environments. Except for forming a protective scale, high-temperature coatings must be chemically and mechanically compatible with the superalloy substrate, stable during service, and easy to apply.

The evolution of high-temperature coatings tracks to the need to address different forms of corrosion attack found in the field. Three main forms of high-temperature corrosion are high temperature oxidation; type I hot corrosion; and type II hot corrosion. The earliest coatings applied on turbine blades and vanes were aluminide coatings, which were deposited by a slurry

or vapor process including pack cementation. For Ni-based alloys, the aluminide or β-NiAl with sufficient Al content provides long-term oxidation resistance via Al_2O_3-scale formation. Because these coatings were produced through diffusion processes, they are generally referred as diffusion coatings [17]. In the late 1960s, with the increasing evidence of high temperature (type I) sulfate deposit induced hot corrosion formed in the service. Pt was added into β-NiAl coatings by electroplating a several micrometer Pt layer on to the superalloy before diffusion aluminizing. Pt-aluminide coatings were developed to provide greater resistance to this mode of corrosion and to oxidation during thermal-cycling conditions. In the middle 70s, low temperature form of hot corrosion (type II) became common and requires increased chromium to confer resistance [18]. Since β-NiAl diffusion coatings have limited solubility for Cr addition, it became necessary to develop MCrAlY-type overlay coatings, where M is Ni, Co or a combination of the two. Overlay coatings were deposited by electron beam vapor deposition (EB-PVD) or thermal spray. The coatings compositions are very close to the source composition, thus allowing for greater control. The phase constitutions of MCrAlY coatings are usually β-NiAl and γ-Ni at temperatures above about 1000°C [19]. CoCrAlY coatings generally out-perform NiCrAlY and NiCoCrAlY coatings in type I hot corrosion resistance [20, 21]. The beneficial effect of Co to type I hot corrosion was thought to be [22]: 1) Co destabilizes γ'-Ni_3Al phases and γ'-Ni_3Al was considered as not good for hot corrosion as it has limited Cr content; 2) Co increase Cr content in β-NiAl phases. NiCrAlY coatings have better oxidation resistance. NiCoCrAlY coatings are generally found to be a compromise between oxidation and hot corrosion resistance[4]. Recently, γ+γ′ coatings, a new type of diffusion coating has been developed [23]. One of the unique advantages of such coatings is their compatibility with the superalloy substrate, which has the same γ+γ′ phase constitution. To improve the resistance of these coatings to environmental degradation, Hf, Y, Pt, Si, Cr are

added to γ+γ' coatings. Through composition adjustment, their high-temperature oxidation behavior can outperform the best Pt-modified β-NiAl coatings [24] and the performance in hot corrosion environments is also reasonable [25]. These coatings can potentially provide protection to superalloys against various modes of high-temperature degradation.

2.2 HIGH TEMPERATURE OXIDATION

Above >1000°C, a major mode of component degradation is high temperature oxidation. The high-temperature oxidation process is controlled by both thermodynamics and kinetics. The oxidation products are dependent on the alloy or coating system, temperature, and environment. A basic knowledge of metal oxidation is needed to understand alloy oxidation.

2.2.1 Metal oxidation

2.2.1.1 Thermodynamics of metal oxidation

When a metal is exposed to high temperatures, it tends to react with the oxidizing gas (taken here to be O_2) to form oxide scale (Figure 2.7). Once a continuous and intact oxide scale is established, the reactants are separated and further reaction requires transport through the scale, thus slowing further base metal degradation. To be protective, an oxide scale should be stable, compact, slow-growing, adherent, continuous and homogeneous [26].

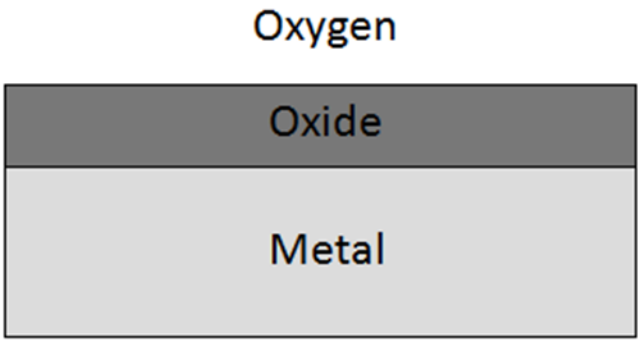

Figure 2.7 Schematic representation of metal oxidation

The stabilities of different oxides can be compared on an Ellingham diagram shown in Figure 2.8. The standard Gibbs free energy of formation (ΔG°) of different oxides is plotted as a function of temperature. The values of ΔG^{o} are expressed as per mole O_2, so the stabilities of various oxides may be compared directly. The lower the position of a given line on the diagram, the more stable is the oxide. It is seen that MgO and CaO are the most stable oxides. However, their molar volumes are smaller than that of the metal (Mg or Ca) which means that the formation of these oxides is not sufficient to cover the entire metal. As a consequence, protection cannot be provided by either oxide. Alumina, chromia and silica are stable oxides based on their low positions in the Ellingham diagram. They are able to form continuous scales as their molar volumes are larger than those of metals.

The partial pressure of oxygen at which the metal and oxide coexist, i.e., the dissociation pressure of the oxide ($P_{O_2}^{M/MO}$) can be obtained directly from the Ellingham diagram. The approach is drawing a straight line from the original marked O through free-energy line at the temperature of interest and reading the value of $P_{O_2}^{M/MO}$ at the intersection of the line and the

P_{O_2} scale on the right. Using this approach, it can be found that $P_{O_2}^{Al/Al_2O_3} < P_{O_2}^{Cr/Cr_2O_3} < P_{O_2}^{Ni/NiO}$.

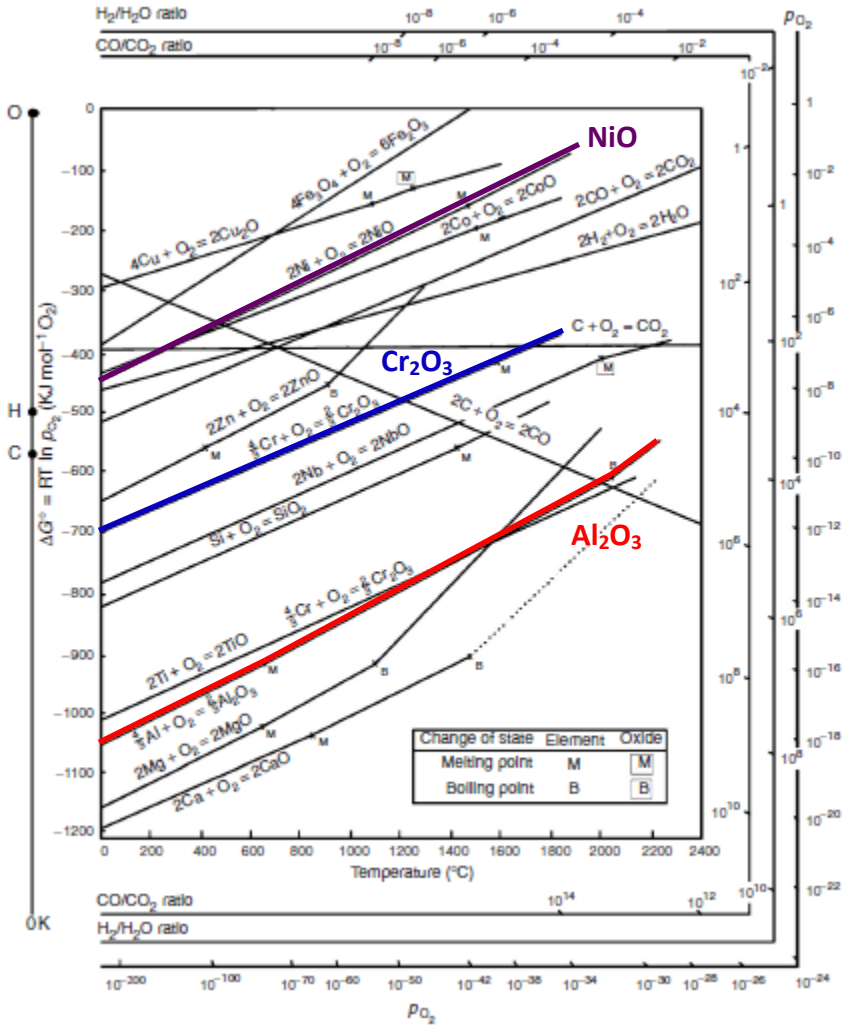

Figure 2.8 Ellingham diagram of oxide stability at different temperature and oxygen pressure

2.2.1.2 Kinetics

In addition to thermodynamics, oxidation kinetics are very important. The formation of oxide scale can be either controlled by an interfacial reaction or by solid-state diffusion through

the scale. If it is diffusion controlled, the rate of oxidation decreases as diffusion distance increases, i.e.,

$$\frac{dx}{dt} = \frac{k_p'}{x} \tag{2. 1}$$

where x is scale thickness, t is time and k_p' is a proportionality constant. Integration of the above equation gives

$$x^2 = k_p t + D \tag{2. 2}$$

Here k_p is the parabolic constant ($k_p = 2k_p'$) with typical units of cm^2/s. Thus, the diffusion-controlled growth rate of a continuous and intact scale follows parabolic kinetics.

Figure 2.9 shows the temperature dependence of the growth rate of the oxides of Fe, Co, Ni, Cr, Al and Si. The k_p values of different oxides are seen to vary by several orders of magnitude. The k_p values for Cr_2O_3, Al_2O_3 and SiO_2 are considerably lower than these of the common base metal oxides of Fe, Co, and Ni. With the advantage of being kinetically slow, thermodynamically stable, and continuous as a scale, Al_2O_3, Cr_2O_3 and SiO_2 are protective oxides. Accordingly, high-temperature materials rely on forming an Al_2O_3, Cr_2O_3, or SiO_2 scale for surface-degradation resistance under high-temperature oxidizing conditions. A Cr_2O_3 scale is generally considered to be not suitable above 950°C for long-term resistance, especially in high-velocity gases, due to the formation of volatile CrO_3 oxide [27-29]. The presence of water vapor further limits the resistance provided by Cr_2O_3 due to the formation of volatile $Cr(OH)_3$ [29, 30].

SiO_2 is generally not suitable for coatings used on superalloys because the large amount of silicon in the coating needed to form a SiO_2 scale will diffuse rapidly into the substrate, decreasing the melting point of superalloys [31]. SiO_2 may also reduce to the volatile SiO at elevated temperatures [29, 30]. Besides, SiO_2 has moisture sensitivity due to the reaction with

H_2O forming $Si(OH)_4$ at high temperature[29, 32]. Silica can react with H_2O to form (SiOH). Lastly, due to a CTE mis-match between SiO_2 and its forming substrate [33]; cracks can easily form in the oxide scale during temperature variation. Due to the limitation of SiO_2 and Cr_2O_3 scale, most high-temperature coatings rely on forming Al_2O_3 scale for environmental protection.

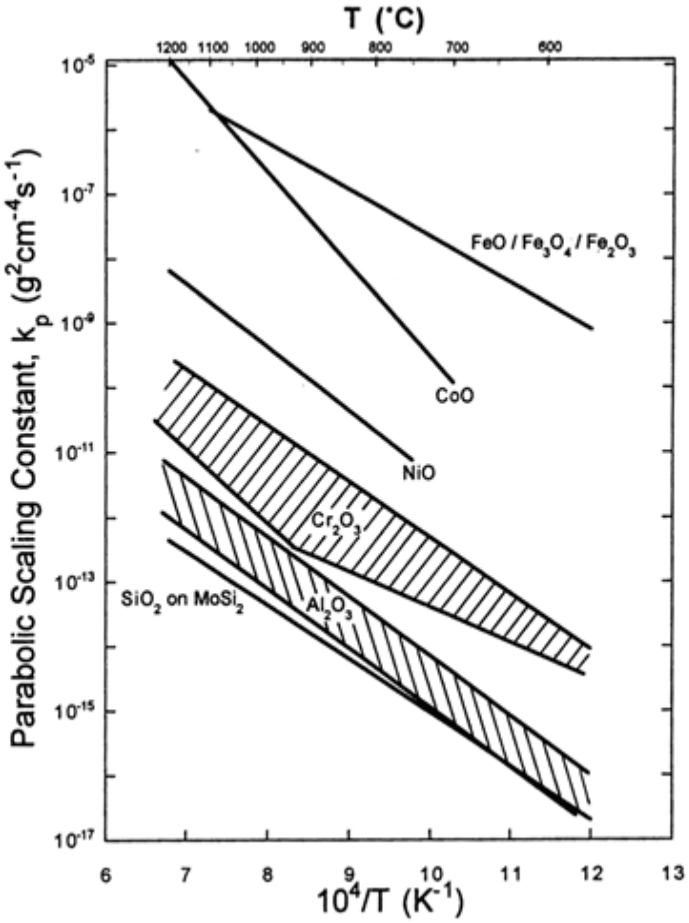

Figure 2.9 Arrhenius plot of parabolic oxidation rate constant, k_p , for the growth of various oxide scales as a function of temperature

2.2.2 Alloy oxidation

2.2.2.1 Simplified situations for binary alloy oxidation

Alloy oxidation is generally much more complex than pure metal oxidation. Two limiting situations for binary alloy AB oxidation are shown in Figure 2.10. A and B can form stable oxides AO and BO, assuming BO is more stable than AO. Depending on the relative fluxes of B and O, there can be internal oxidation (Figure 2.10(a)) or external oxidation (Figure 2.10(b)) of B.

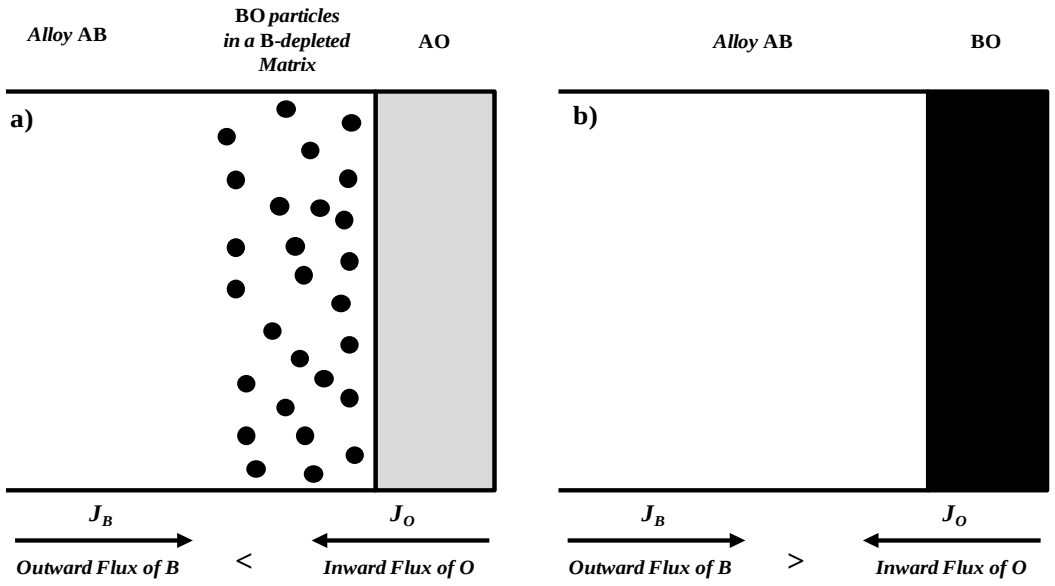

Figure 2.10 Schematic representation of **(a)** an internal BO particles formation beneath an AO scale and **(b)** the formation of an external protective BO scale. Adapted from [34].

Figure 2.11 shows typical cross-sectional morphologies of alloys forming alumina internally and externally. In Figure 2.11(a), a dilute Ni-1%Al alloy was oxidized in dry air at 1000ºC for 24h. The alumina reacts with oxygen in the alloy to form discrete internal oxides which includes internal alumina and primarily $NiAl_2O_4$ [35]. The internal oxides penetrate as deep as 100 microns into the alloy. The thick external layer is NiO. In Figure 2.11 (b), the Ni-Cr-

Al alloy with higher Al (6%) and Cr (8%) addition was oxidized in 1100°C for 1h. Alumina forms externally, separating the reactant gas from the alloy substrate and serving as a barrier against accelerated oxidation.

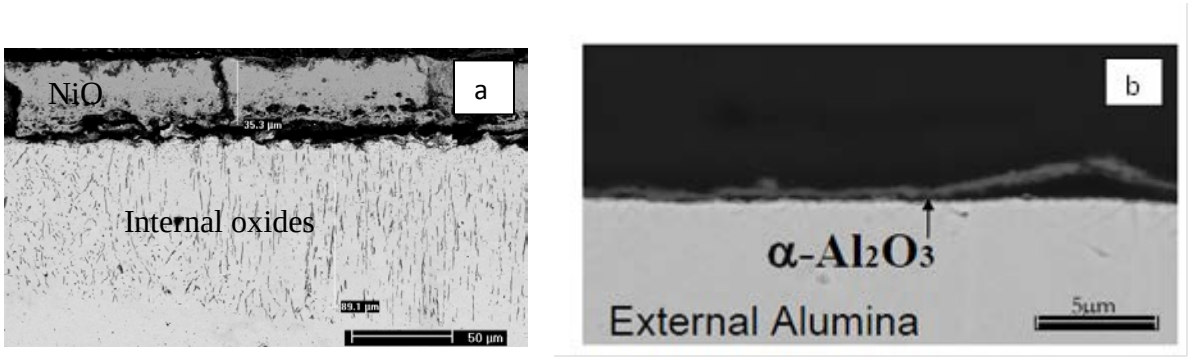

Figure 2.11 Examples of (a) internal alumina formation on Ni-1wt% Al after oxidized in dry air at 1000ºC for 24h and (b) external alumina formation on Ni-8Cr-6Al alloys oxidized at 1100°C for 1h [36]

2.2.3 Internal oxidation

For internal oxidation, one key parameter is the penetration rate of internal oxidation. To show that, consider a simple case where there is no external oxide formation. It is assumed that 1) the concentration profiles for O and B are linear; 2) at the oxidation frontier, the concentration of O and B is zero; and 3) all the supplying oxygen flux is consumed by forming BO_v at the internal oxidation front [37]. These assumptions are indicated in Figure 2.12. Through balancing the amount of oxygen consumed to form internal BO_v oxide and the oxygen supplied through diffusion, the penetration depth of the internal oxidation zone is calculated to be

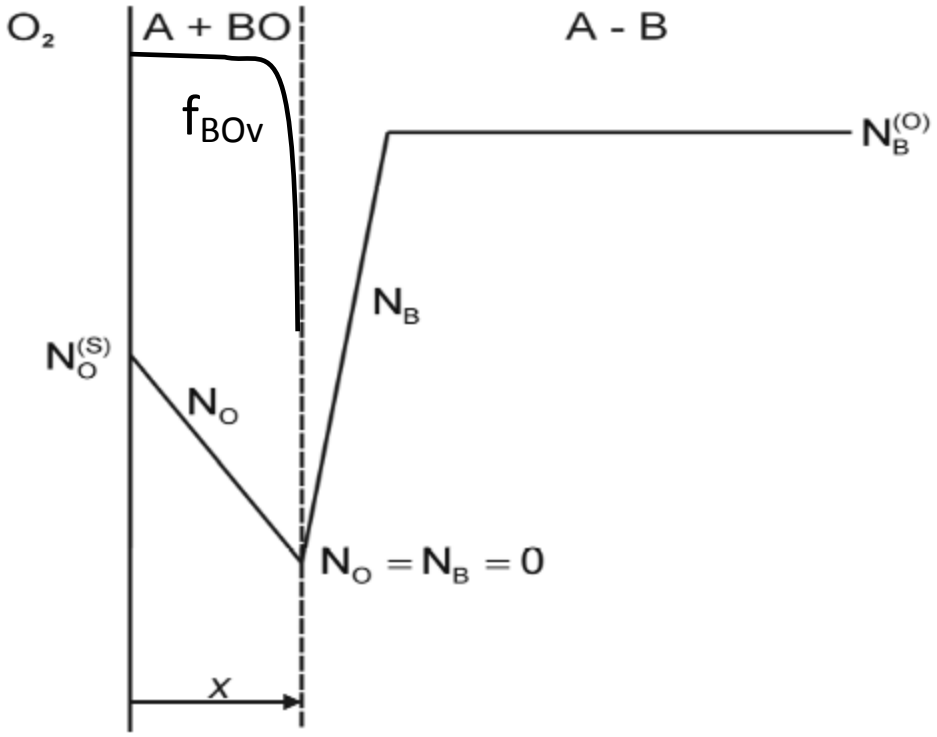

Figure 2.12 Simplified concentration profiles for the internal oxidation of A-B

$$X = \left[\frac{2N_O^{(s)}D_O}{\nu N_B^{(o)}}t\right]^{1/2} \quad (2.\ 3)$$

where $N_O^{(S)}$ is the oxygen solubility in A (atom fraction) at the surface, ν is stoichiometric factor, and D_O is the diffusivity of oxygen in A (cm^2/s), $N_B^{(o)}$ is the initial concentration of B in the alloy. The equation shows that the penetration depth has a parabolic time dependence. Moreover, it also shows the penetration depth is proportional to the square root of oxygen permeability $N_O^{(S)}D_O$.

What is shown in Figure 2.12 is a simplified case, because in a real system concentration is not linear; B and O concentrations at oxidation frontier are not zero; oxide has solubility in the alloy; and an external AOv scale usually forms. More rigious treatment is done by Wagner[38]

considering the corresponding concentration gradient. Bohm and Kahlweit modified Wagner's analysis[38] and include a finite solubility product of the oxide in the alloy matrix[39]. Maak[40] modified the Wagner's model [38] to take into account the effect by the growth of an external AO_v scale

2.2.3.1 Limiting case of transition to external scale formation

To achieve protective oxide-scale formation, a critical concentration of solute element must be exceeded, above which the outward diffusion of the solute will be fast enough to form a blocking layer of BO_v which mitigates internal oxidation and the growth of solvent oxide AO. This critical solute concentration, $N_B^{*(1)}$, determines at which composition the alloy will transition from internal to external oxidation. Wagner quantitatively determined the critical concentration of solute element [38]. For a limiting case where oxygen permeability is significantly less than the corresponding product of B, the critical concentration for transition from internal to external scale can be expressed as [41]:

$$N_B^{*(1)} > \left[\frac{\pi g^*}{2\nu} N_O^{(s)} \frac{D_O V_m}{D_B V_{ox}}\right]^{1/2} \quad (2.4)$$

where D_B is the diffusion coefficient of solute in the alloy, V_m is the molar volume of the solvent metal, V_{ox} is the molar volume of oxide, and g^* is the critical volume fraction of BO_v. Based on Wagner's definition [38], g^* is the volume fraction of internal oxide at which oxide growth (i.e., lateral growth, in particular) is favored over new oxide formation.

To study the Ni-Al alloy oxidation, the critical aluminum concentration for transition from internal to external oxidation, in other words, for establishing external alumina scale $N_{Al}^{*(1)}$ can be estimated by equation 2.4. The temperature dependence of $N_{Al}^{*(1)}$ can also be estimated as

followings based on the expression in equation 2.4. Not considering the temperature induced effect on $N_O^{(s)}$, it appears that the critical aluminum concentration is

$$N_{Al}^{*(1)} \propto \left[\frac{D_O}{D_{Al}}\right]^{\frac{1}{2}} \quad (2.5)$$

The critical solute concentration is determined by the relative diffusion rates of solute and oxygen in the alloy. For alumina formation on high temperature coatings or alloys, the diffusion coefficient of aluminum in the alloy (D_{Al}) has been reported as [42, 43]

$$D_{Al} = 1.0 exp\left(\frac{-260\text{kJ/mol}}{RT}\right) cm^2/\sec \quad (2.6)$$

Park and Altstetter[44] measured the oxygen diffusion coefficient in solid γ-Ni by a solid-state electrochemical method and reported the diffusivity of oxygen in nickel is

$$D_O = 4.9 \times 10^{-2} \exp\left(-\frac{164kJ/mole}{RT}\right) cm^2/\sec \ (850°C \ to \ 1400°C) \quad (2.7)$$

With an increase in temperature, both D_{Al} and D_O increase. However, due to the activation energy for aluminum diffusion (260kJ/mole) being larger than that of oxygen (164kJ/mole), D_{Al} increases much faster than D_O. Thus, $N_{Al}^{*(1)}$ decreases with increasing temperature. This is demonstrated by the left boundary (transition region I) in the binary oxidation map (Figure 9), which was determined by Pettit[45] in 1967 by a systematic study of the oxidation behavior of Ni-Al alloys. Binary Ni-Al containing 7 wt.% of Al is not sufficient to form an external Al_2O_3 scale at 900°C, but can be enough at 1100°C, especially during the initial stage of oxidation.

2.2.3.2 Maintaining the growth of an external scale

However, for long time oxidation, more aluminum concentration is needed (~ 17 wt.% at 900-1200°C) in the alloy to maintain a stable external Al_2O_3 scale. This is shown by the boundary on the right (transition region II). According to Meier [46], this boundary represents the criterion for sustaining exclusive growth of a protective scale (supply criterion). The rationale of this criterion is that assuming an external alumina scale is established, in order for this alumina be able to maintain itself, the Al supply from the substrate must be at least equal to the Al consumption by scale growth. Through mass balance, the limiting critical aluminum concentration determined by this criterion is expressed as [47]

$$N_{Al}^{*(2)} \geq \frac{V_m}{32v}\left(\frac{\pi k_p}{D_{Al}}\right)^{1/2} \quad (2.\ 8)$$

where $N_{Al}^{*(2)}$ is the critical aluminum concentration for sustaining the growth of an external alumina scale. k_p is the alumina growth-rate constant. This critical aluminum concentration is therefore set by a supply criterion determined by the diffusivity of aluminum in the alloy (Al supply) and the growth rate of oxide (Al consumption). The boundary on the right (transition region II) in Figure 2.13 is based on this supply criterion. Between 900-1200°C, due to relatively fast scale growth metastable alumina which tends to form at low temperatures, and a relatively low D_{Al}, aluminum supply is an issue. At 1200°C, slowly growing α-Al_2O_3 forms which requires less aluminum consumption compared to a metastable alumina, while the diffusion rate of aluminum is higher such that the Al supply is not an issue. So the supply criterion is applicable at temperature below 1200°C.

In Figure 2.13, it seems the critical aluminum concentration determined by the supply criterion is independent of temperature. Theoretically, that is probably not the case as there

appears some distinction in the activation energies for k_p and D_{Al} at the lower temperatures. Specifically, the activation energy for aluminum diffusion in pure Ni is reported as 260kJ/mole [42, 43]; the activation energy for θ-Al_2O_3 growth is 215 kJ/mole [48]. In the end, the apparent independence has to be a consequence of the merging of different activation energies.

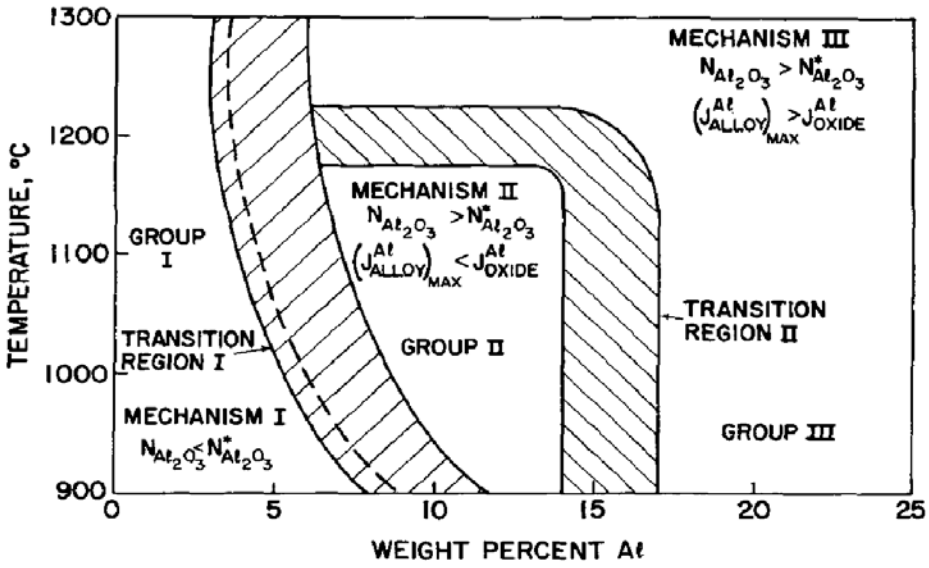

Figure 2.13 Compositional effects on the oxidation of binary Ni–Al alloys[49]

As summarized in Figure 2.13, when binary Ni-Al is oxidized in air, depending on aluminum concentration and exposure temperature, it shows three trends or groups of oxidation behavior: group I (0-7 wt.%Al) where the alloys form external NiO and internal Al_2O_3 (+$NiAl_2O_4$) scales; group II (7-16 wt.% Al) where aluminum concentration is large enough to form Al_2O_3 externally, but smaller than the amount necessary for a steady-state external Al_2O_3 scale growth; and group III where steady-state Al_2O_3-scale formation is achievable by a sufficient supply of Al. In group II, the alloys form external Al_2O_3 initially but are soon overtaken by rapid growing NiO and $NiAl_2O_4$. The cross-hatched boundaries may show the

transition between different groups which is thought be affected by surface condition and surface composition.

It is seen that ~15 wt.% of Al is needed for the sustained formation of an alumina scale for environmental protection. However, due to mechanical fabrication constraints such as limited welding capability and reduced strength of Al-rich alloys, the use of such a high amount of Al is not practicable. To reduce the Al content, it is well established that Cr addition has a highly beneficial "third element effect" [50-52].

2.2.3.3 Third element effect of Cr and the Ni-Cr-Al oxide map

Third element effect was initially observed on the Cu-Zn-Al system by Wagner [50]. It was noted that ternary alloys form protective alumina scales at lower aluminum concentration than were required for Cu-Al binary alloys. Wagner suggested that the explanation lay in that Zn (the third element) forms an oxide of stability intermediate to those of the other two metals, lower the oxygen activity at the scale-alloy interface. This concept is often referred as the "gettering" effect. A similar effect was observed for Ag-Zn-Al alloys by Pickering[53]. For Ni-Cr-Al system, the third element effect refers to the addition of Cr into Ni-Al alloy decreases the critical Al concentration for forming an external Al_2O_3 scale. This is demonstrated in the Ni-Cr-Al ternary oxide compositional map which was constructed by Giggins and Pettit [54] in 1971 by superimposing oxidation data on Ni-Cr-Al ternary composition triangle. Figure 2.14 is an example of an oxidation map for Ni-Cr-Al alloys at 1000ºC in air. The three regions on the map correspond to (I) NiO forming with internal oxidation, (II) Cr_2O_3 forming and (III) Al_2O_3 forming. The boundary between the NiO- and Al_2O_3-forming regions is very important as it indicates the minimum Al concentration, N_{Al}^{*}, that is required for an alloy to be an Al_2O_3 former.

The boundary is curved showing that the addition of Cr significantly decreases the critical Al concentration owing, it is generally claimed, to be the third element effect [50-52].

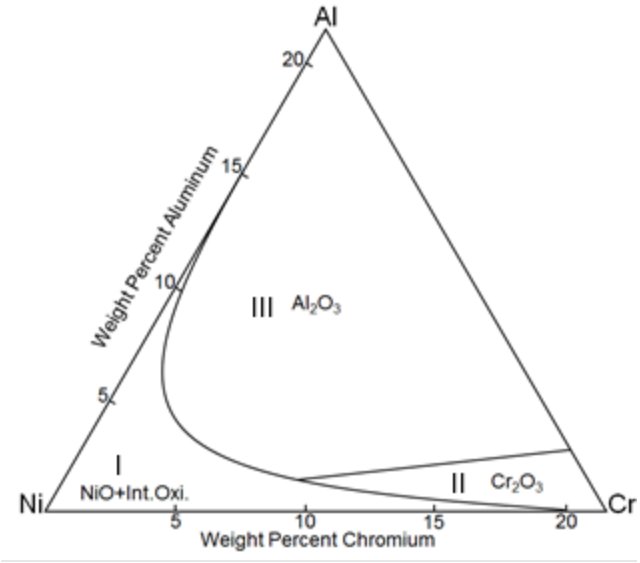

Figure 2.14 Oxidation map for Ni-Cr-Al oxidized in Ar+10% oxygen at 1000ºC for 20 hours (Replot from Giggins and Pettit's work[54])

The critical aluminum concentration boundary is a kinetic boundary as it could be affected by a number of factors such as surface roughness, environmental impurities, gas atmosphere, and so on [55]. Its position has been well established in air which can be seen when comparing Ni-Cr-Al oxide maps reported by Giggins and Pettit [54], Wallwork and Hed [30] and Nicholls et al [56]. A recent study by Zhao and Gleeson [57] on Ni-Cr-Al model alloy oxidation in an atmosphere with and without 30% steam showed that the presence of steam can push the critical aluminum concentration boundary towards higher Al/Cr values, indicating that the critical concentration of Al increases when the environment is wet air. In application, a number of other species such as SO_2, CO_2, or the combination of these with H_2O could exist. It is not known whether these species will affect the position of this kinetic boundary.

In general, these oxide maps establish the primary oxidation processes for any given ternary system. In application, the oxidation maps are very useful because they allow for a first-order assessment of the oxidation behavior of alloys simply based on three compositional components and the service environment. When designing superalloys, the oxide maps provide guidance on the minimum amounts of Al and Cr that should be present in the alloy to form an external Al_2O_3 or Cr_2O_3 scale.

2.2.3.4 Transient oxidation of Ni-based alloy

During the formation of an alumina scale, two short-term oxidation behaviors play a large role on the quality of the final scale: 1) transient oxidation; 2) transition alumina formation.

Transient oxidation refers to the formation of other oxides such as NiO, Cr_2O_3, and spinel during the initial stage before a continuous alumina inner layer is established. Giggins and Pettit [54] proposed a Ni-Cr-Al transient oxidation model to explain the formation sequence of different oxides and its final scale structure as shown in Figure 2.15. At the beginning of oxidation, the rapid uptake of oxygen will convert elements at the surface of alloys into oxides. As little diffusion occurs during a short time, the formed oxide layer is $Ni(Cr,Al)_2O_4$ and NiO, which is illustrated in Figure 2.15 (a). As the oxidation continues, oxygen diffuses into the alloys. The oxygen activities required to form Cr_2O_3 and Al_2O_3 are smaller than that to form NiO. Thus, the diffused oxygen will continue to oxidize Cr and Al with internal Cr_2O_3 and Al_2O_3 precipitates forming as shown in Figure 2.15 (b). If the combined volume of Cr_2O_3 and Al_2O_3 precipitates are sufficient to inhibit the diffusion of oxygen into the alloy, additional Cr_2O_3 and Al_2O_3 will precipitate and form a layer of mixed Cr_2O_3 and Al_2O_3, as Cr and Al diffuse from the inner alloy (Figure 2.15 (c)). The oxygen activity required to oxidize Al is smaller than that

needed to oxidize Cr. If the flux of oxygen after passing through the mixed layer is still large enough to oxidize Al but not enough to oxidize Cr, and if the volume of Al_2O_3 is sufficient to form a continuous layer beneath the mix scale (Figure 2.15 (d)), then the controlling step is transport through the Al_2O_3 scale.

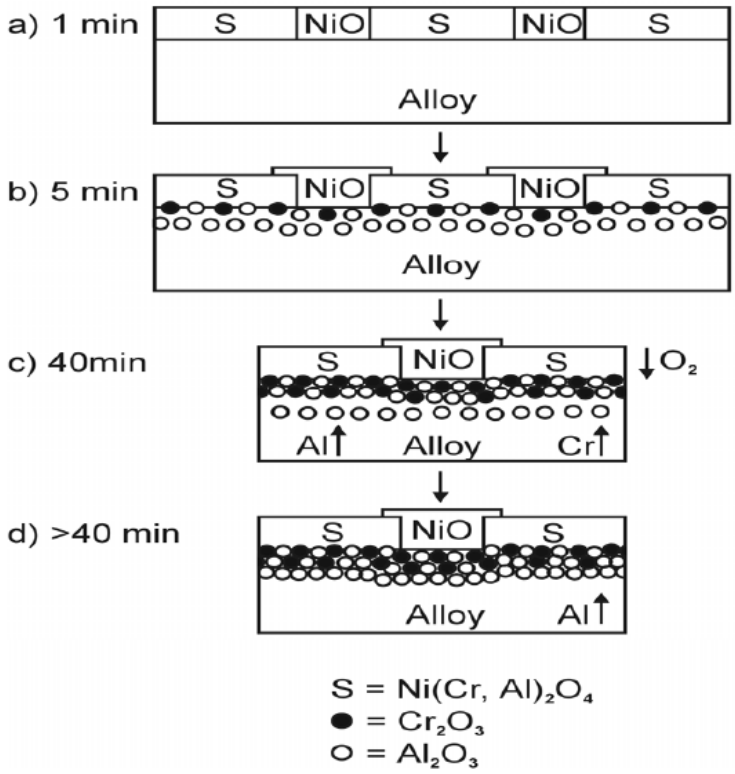

Figure 2.15 Schematic stages in the growth of a protective α-Al_2O_3 scale on a Ni-15Cr-6Al (wt.%) alloy [51]

2.2.3.5 Transition aluminas

The growth of an alumina scale is complicated because alumina exists in a number of crystalline forms, namely γ-, δ-, η-, Θ-, and α-alumina [58]. Ideally a continuous and adherent scale comprised of α-Al_2O_3 is preferred because this oxide is thermodynamically the most stable

and kinetically the slowest growing [59]. However, during the initial stages of oxidation, particularly at temperatures below almost 1050°C, faster-growing metastable Al_2O_3 structures (γ- and/or Θ-Al_2O_3) usually form first. Being a relatively open structure, metastable Al_2O_3 structures grow very rapidly and they usually transform to α-Al_2O_3 with increase in exposure time. Along with this transformation is a two orders of magnitude [48] oxidation rate decrease (as shown in Figure 2.16) and around 8-10% volume reduction[59]. The latter can lead to cracking within the scale [60].

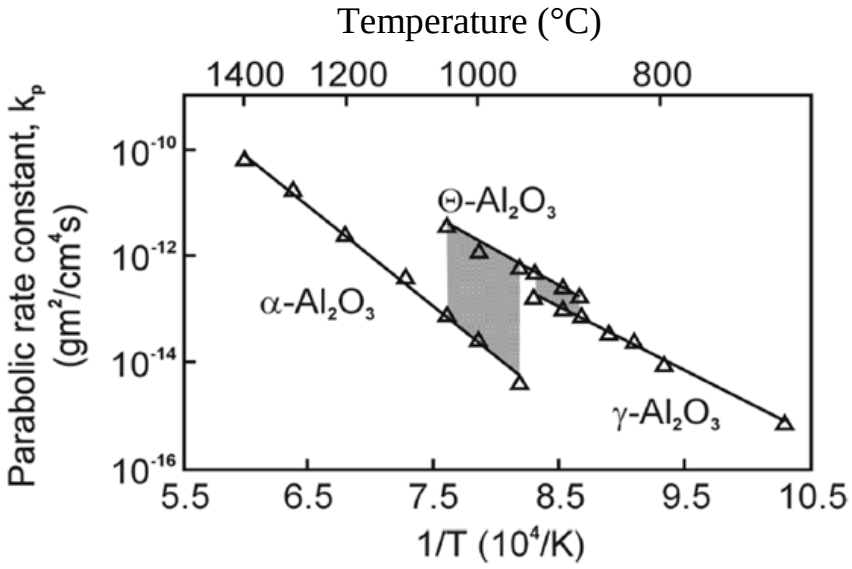

Figure 2.16 Arrhenius plot of k_p for the oxidation of NiAl[61]

The formation of different alumina structures can be sequential. Veal et al. [62] studied the oxidation of β-NiAl(Zr) at 1100°C in air and the oxide scale thickness was tracked with exposure time. Their results (as shown in Figure 2.17) verified that the sequence of scale establishment is predominated initially by theta growth and then, after some time, alpha starts to form. The alpha forms at the expense of theta because the total thickness is relatively constant; finally, a complete continuous alpha scale is formed. During the scale establishment, there is a

kinetic competition between metastable and stable phases. This competition is time dependent; it is initially dominated by metastable alumina but eventually, thermodynamics dictates the final structure.

Since it was first reported [48] in the context of scaling, alumina phase transformation in thermally grow scales has been the subject of extensive investigation[48, 61, 63, 64]. Alloy elements such as Cr [61], Ti [64], Fe [65] have been found to promote the Θ→α transformation; whereas, Zr [48], La, Hf[66], Si [67], Pt[68, 69], Y[70-73] have been reported to delay the transformation. Most investigations have focused on the effects of alloying elements on the transformation in air or pure O_2. Only a few investigations have dealt with the environmental effects and they are usually limited to water vapor [74-77] and the results are still not conclusive. Chevalier et al. [75] compared the growth kinetics of scaling in dry and humid air and indicated an accelerated transformation of transient alumina to α-Al_2O_3 when the Fe_3Al intermetallic was oxidized in humid air. Zhou et al. [74] used photo-stimulated luminescence spectroscopy to identify the phases of alumina formed on NiAl at 950°C and reported that the presence of water vapor promoted the Θ→α transformation. By contrast, Liu et al. [76, 77] studied the oxidation of commercial FeCrAl alloys in O_2+ H_2O and found that water vapor slows γ–Al_2O_3 to α-Al_2O_3 transformation and concluded that water vapor can stabilize the metastable γ-Al_2O_3 by hydroxylation of its surface

For resistance to attack by hot corrosion, it may by necessity that the alloy or coating form an alumina scale beneath a sulfur-containing salt or in an SO_2-containing environment. Moreover, in the temperature range of Type I hot corrosion (~900-1000°C), metastable and stable alumina may co-exist. However, limited research [2, 78] has reported the effects of the environmental sulfur and salt deposit on the stabilities of alumina scale formation during hot

corrosion and a mechanistic understanding of these sulfur or salt on alumina phase transformation is still lacking.

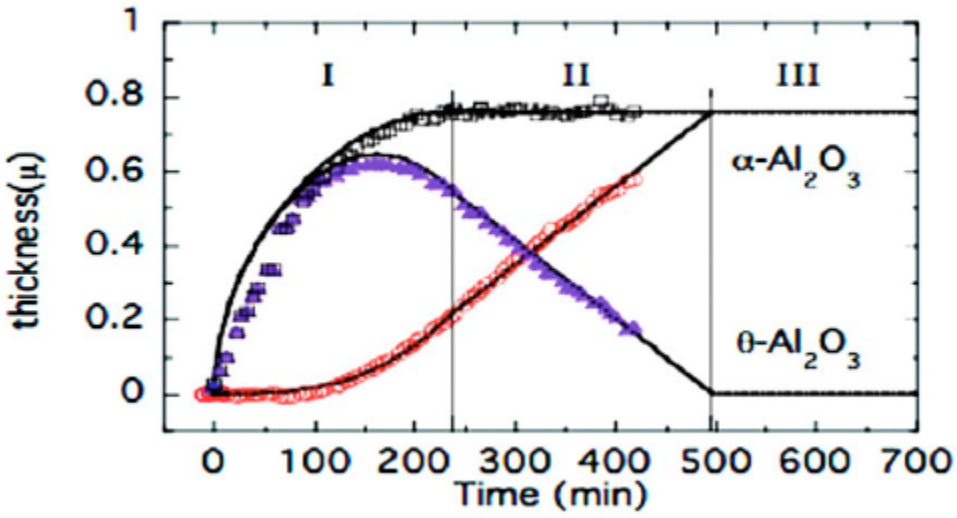

Figure 2.17 Thickness of θ-Al_2O_3 and α-Al_2O_3, grown on diamond polished (001) face of β-NiAl(Zr), as the oxides evolve at 1100 °C[62].

2.3 HOT CORROSION

Hot corrosion is deposit-induced accelerated oxidation. The condition of hot corrosion is schematically represented in Figure 2.18. It occurs in the presence of salt deposit (either molten or solid) and usually with corrosive species (SO_2, SO_3) existing in the gas atmosphere. Hot corrosion is a very rapid mode of degradation and commonly occurs in gas turbines, attacking metallic coatings and/or Ni- or Co-based superalloys. Two field examples of hot corrosion attack are shown in Figure 2.19 and Figure 2.20. The cross-sections were prepared from a β-NiAl(Pt)-coated turbine blade after 5000 hours service. It is seen that the degradation is so severe that not

only the protective coating was lost, but also the underlying substrate alloy was extensively corroded. Hot corrosion clearly caused the failure of very costly turbine components and it is therefore important to understand its mechanism. The severity of attack to such variables as environment and alloy composition is essential to know for aiding in alloy/coating selection and development.

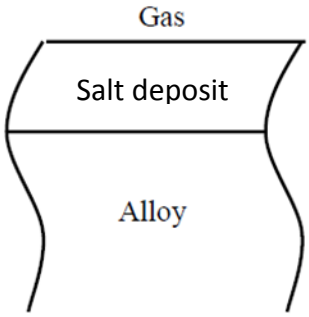

Figure 2.18 the schematic representation of hot corrosion

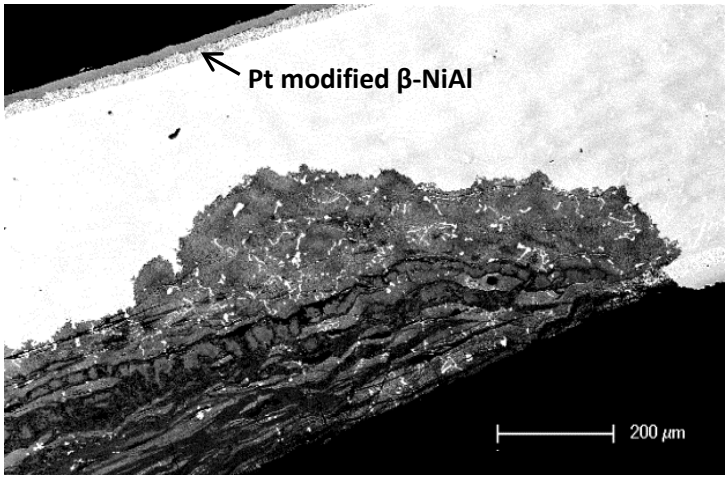

Figure 2.19 Severe hot corrosion attack on the leading edge pressure side of first stage turbine blades

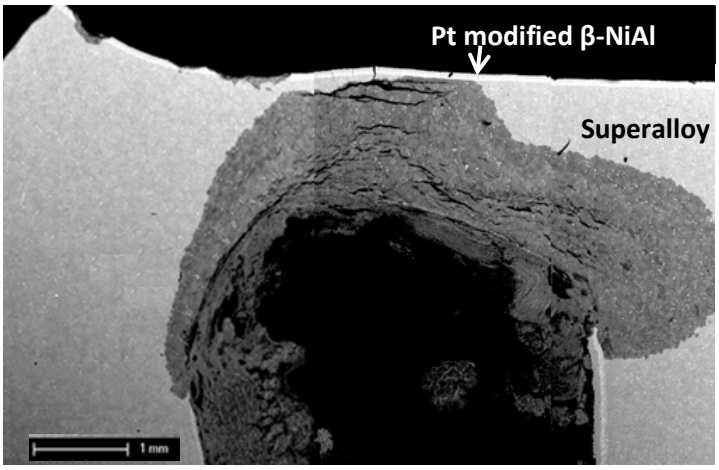

Figure 2.20 The frontier of hot corrosion attack almost crossed the whole under platform of the first-stage turbine blade

2.3.1 Types of salt deposits and the sources of SO_2

A typical salt deposit that induces hot corrosion is Na_2SO_4, which melts at 884°C[79]. Na_2SO_4 can be generated in gas turbines [80]. The engine air intake contains sea salt. Sea salt is comprised primarily of NaCl (84.15%), $MgCl_2$ (10.30%), Na_2SO_4 (3.2%), K_2SO_4 (0.15%), and $CaSO_4$ (2.2%)[1]. For the sake of clarity, it can be taken to be NaCl which can react with SO_2/SO_3, oxygen and/or steam to form additional Na_2SO_4 in the following[81] manners:

$$2NaCl + SO_3{:}SO_2 + O_2{:}1/2O_2 \rightarrow Na_2SO_4 + Cl_2 \quad (2.\ 9)$$

$$2NaCl + SO_3 + H_2O \rightarrow Na_2SO_4 + 2HCl \quad (2.\ 10)$$

$$2NaCl + SO_2 + H_2O + 1/2\ O_2 \rightarrow Na_2SO_4 + 2HCl \quad (2.\ 11)$$

Gas turbines components in aircraft experience exacerbated salt effects when flying at lower altitudes in proximity to coastal regions[1]. The intake air itself could also be a source of sulfate deposit due to the evaporation of sea water.

The environmental sources of SO_2 include the combustion of low grade fuel and the atmospheric pollution, with the latter being particularly unwanted since sulfur in the fuel can be removed, but the removal of sulfur from the atmosphere is not practical. Modern gas turbines use air for the cooling of high-temperature components. The growing global air pollution adds another source to the susceptibility of turbines to hot corrosion. Quite a variation in SO_2 content in the air can be detected around the world [82], as shown in Figure 2.21. It is seen that SO_2 concentration in developing countries can be very high, with certain regions having up to 0.06 ppm SO_2[83] The SO_2 concentrations indicated in Figure 2.21 are based on ground-level measurements.

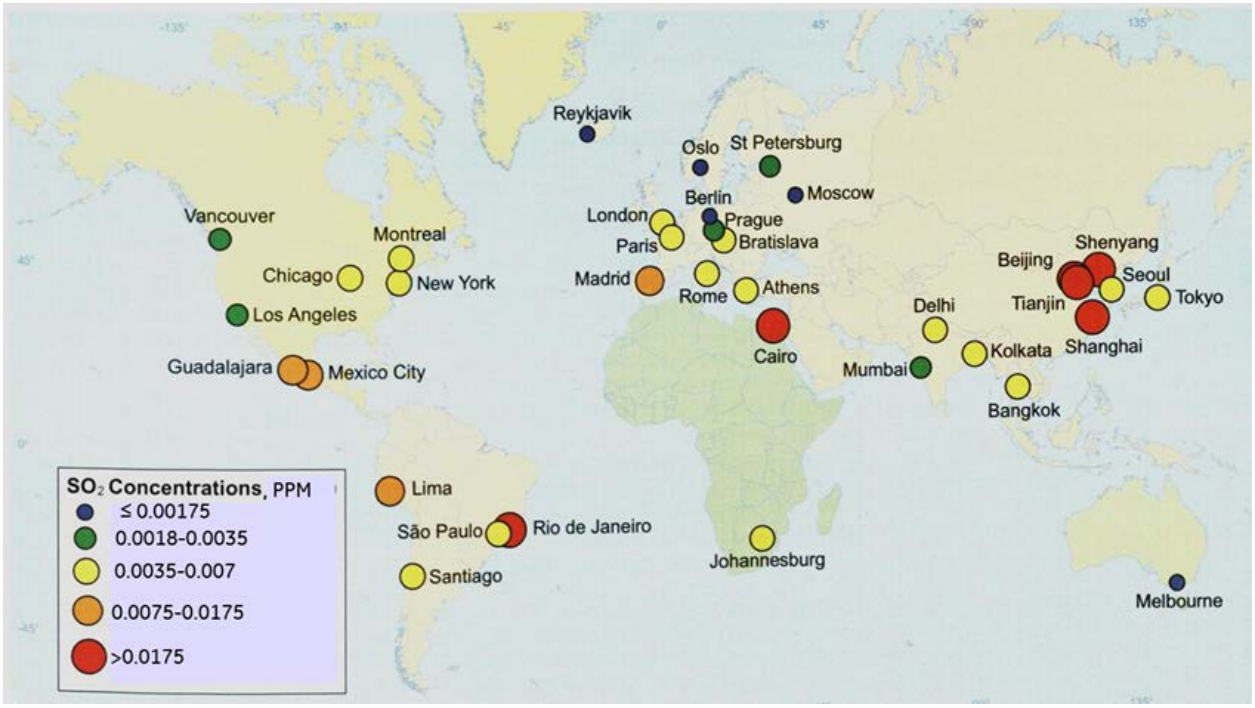

Figure 2.21 Annual concentration of SO_2 in major cities [82]

2.3.2 Types of hot corrosion

2.3.2.1 Temperature difference

Hot corrosion is distinguished as being type I or type II, based on the melting point of the salt, as shown in Figure 2.22. Type I occurs at high temperature. Usually it has little attack below 800°C, maximum attack at 900-950°C and is absent above 1000°C due to the salt evaporating from the components above this temperature[84]. Type II occurs at a low temperature that is below the salt melting point. It is usually absent below 649°C and above 760°C, while being maximum at 706-732°C[84]. The detection of Type II hot corrosion was done in the mid-1970s as a result of operating gas turbines in marine environments at temperature low enough to avoid Type I hot corrosion[85]. It should be noted that both upper and lower threshold temperatures depend on alloy composition and on the testing procedure. Usually, the temperature of occurrence of type I and II hot corrosion, T_{II}/T_I , is found to be : T_{II}/T_I for Fe-based superalloys < T_{II}/T_I for Co-based superalloys< T_{II}/T_I for Ni-based superalloys.

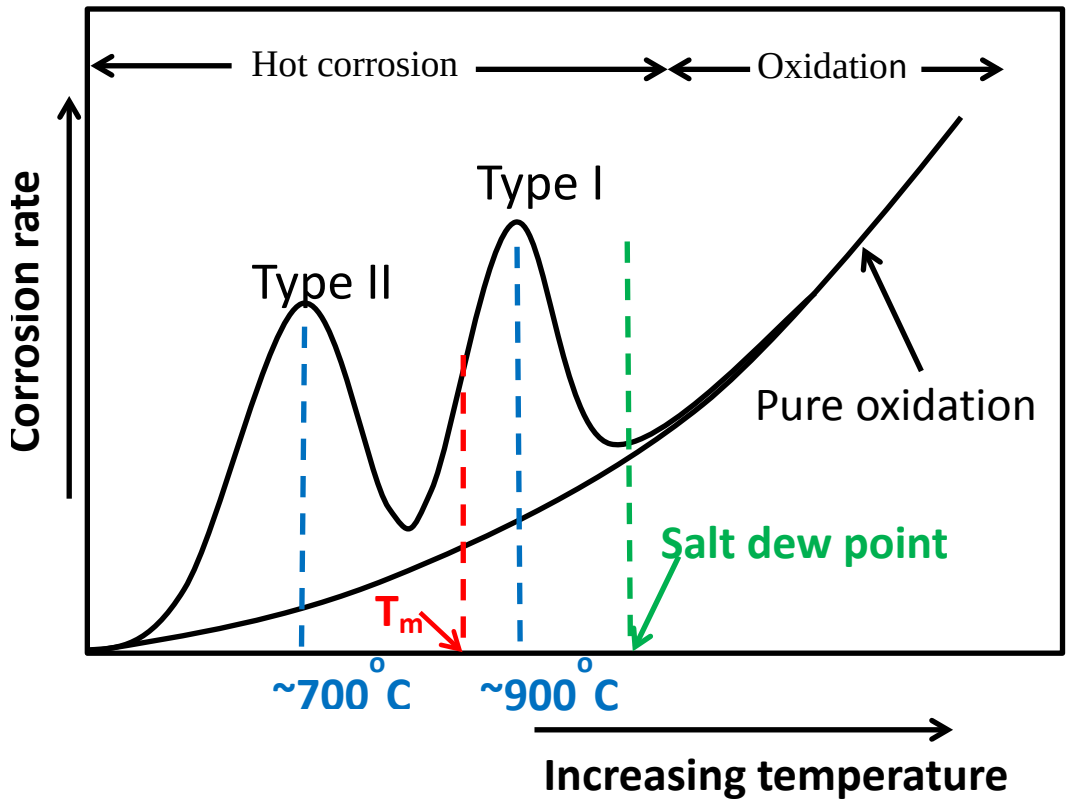

Figure 2.22 the schematic mode of high temperature degradation

2.3.2.2 Liquid formation

Liquid is formed in both types of hot corrosion but it is formed because of different mechanisms. In Type I hot corrosion, liquid forms because the temperature is higher than the melting point of Na_2SO_4. In Type II hot corrosion, traditional thinking considers liquid formation was related to transient base-metal oxides, i.e. NiO, CoO or Co_3O_4. At high SO_3 partial pressure, these oxides react with SO_3 in the atmosphere and form $NiSO_4$ or $CoSO_4$ through the following reactions[86]:

$$\boldsymbol{NiO(s) + SO_3(g) = NiSO_4(s,l)} \quad (2.\ 12)$$

$$CoO(s) + SO_3(g) = CoSO_4(s,l) \quad (2.\ 13)$$

$$^1/_3\, Co_3O_4(s) + SO_3(g) = CoSO_4(s,l) + {}^1/_6\, O_2(g) \quad (2.14)$$

According to the Na_2SO_4-$CoSO_4$ and Na_2SO_4-$NiSO_4$ phase diagrams as shown in Figure 2.23, a considerable amount of $NiSO_4$ and/or $CoSO_4$ can dissolve into solid Na_2SO_4 [87]. Once the composition of salt enters the two phase region of β+liquid, liquid forms and the liquid can be a mixture of Na_2SO_4 and $NiSO_4$ and/or $CoSO_4$. Other than that, liquid can also form from the eutectic reactions in which Na_2SO_4-$NiSO_4$ eutectic melts at 671°C, $CoSO_4$-$NaSO_4$ eutectic melts at 565°C [86, 88]. Recently, Tang and Gleeson [22] found that the liquid formation during type II hot corrosion does not necessarily require the formation of $CoSO_4$ or $NiSO_4$. They studied the stabilities of CoO, Co_3O_4 and NiO in SO_2 containing environment with and without Na_2SO_4 deposit and detected that Co and Ni are present in Na_2SO_4. During that condition, $CoSO_4$ and $NiSO_4$ were not able to form and concludes Co and Ni were dissolved into the Na_2SO_4 deposit. The dissolution of Ni and Co can shift the salt composition to β+liquid regions and forms liquid. Once the liquid was formed, corrosive ion species transport very fast through liquid and causes severe materials degradation

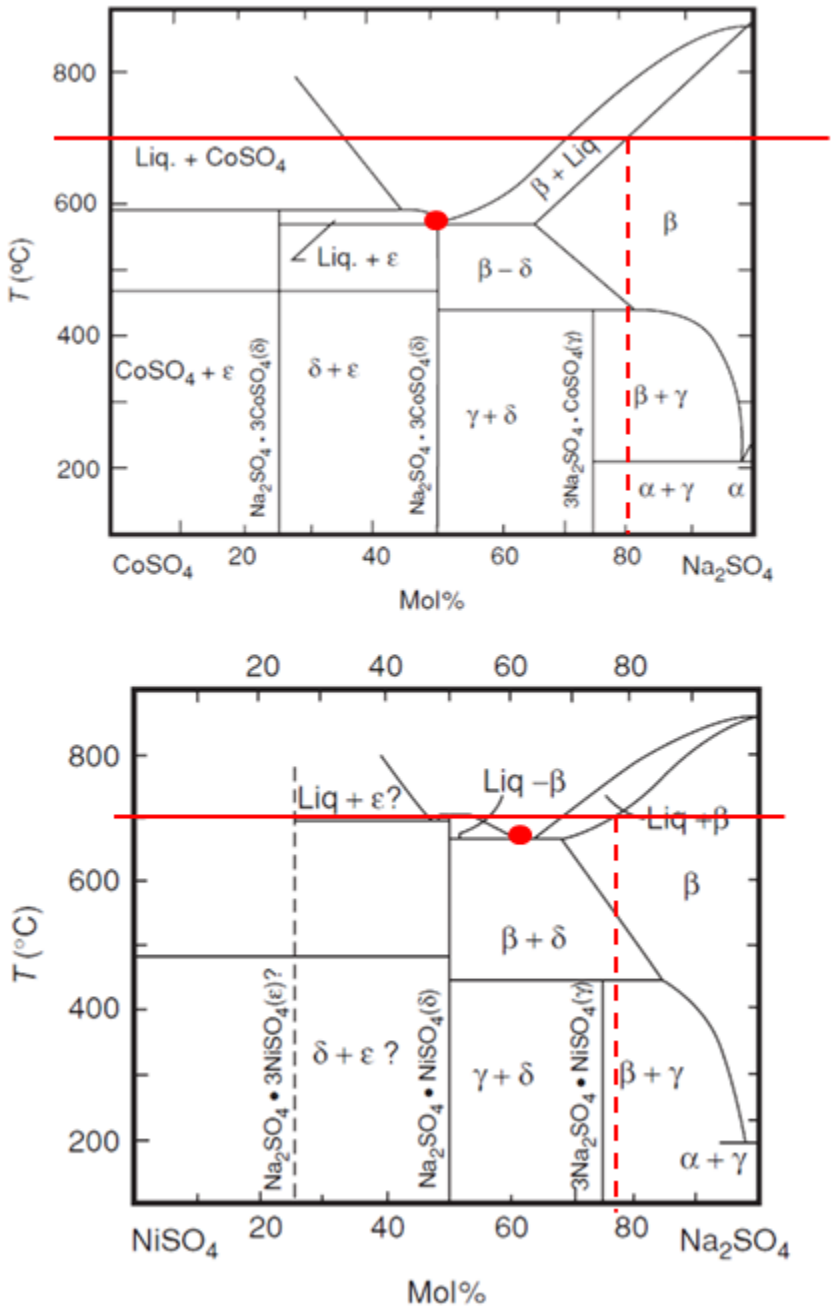

Figure 2.23 Na_2SO_4-$CoSO_4$ and Na_2SO_4-$NiSO_4$ phase diagrams

2.3.2.3 Environmental dependence on SO_2/SO_3 content

Figure 2.24 show the current state of understanding of the environmental dependence on SO_2/SO_3 content. It has been well established that for type II hot corrosion, the presence of SO_2 and SO_3 is very important because it stabilizes the sulfate phases. Studies on Na_2SO_4-induced attack of a CoCrAlY coatings showed that between 650°C and 750°C type II attack is only observed when a certain SO_3 gas pressure is established in the gas mixture [89]. More than that, with an increase in the partial pressure of SO_2 or SO_3 (P_{SO_2} or P_{SO_3}), the extent of attack caused by type II hot corrosion increases. It is difficult to separate the effect of SO_2 or SO_3 because during testing, usually certain amount of SO_2 was converted to SO_3. When a Pt catalyst was positioned upstream above the specimen as shown in Figure 4.1, it will convert SO_2 into SO_3 efficiently. Even if Pt catalyst is not present, the oxide of cobalt or nickel can act as an effective catalyst for the conversion of SO_2 into SO_3 [90, 91]. In general, Type II hot corrosion is dependent on P_{SO_2} or P_{SO_3}.

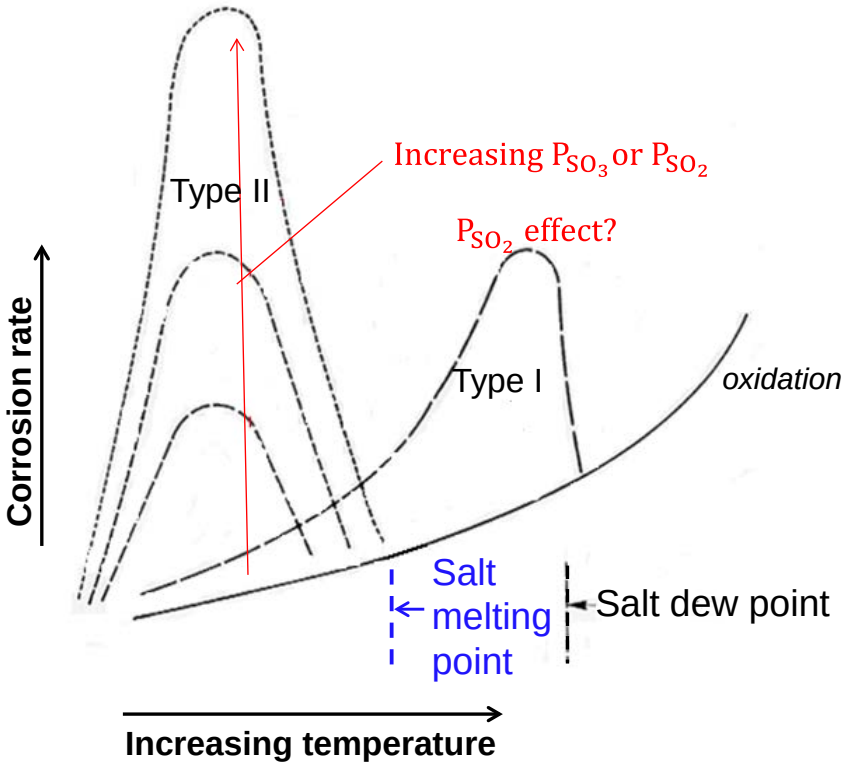

Figure 2.24 the dependence of sulfur on type II hot corrosion

However, for type I hot corrosion, the effect of SO_2 is not clear. The literature reports variable results. Studies on Na_2SO_4-induced attack on Ni-36at.%Al alloy showed that after 100 hours, severe attack occurred in air and catalyzed gas with SO_3 [92] as shown in Figure 2.25, thus indicating that there is no obvious effect of attack on gas composition for this system during long-term exposure. But it is not clear whether SO_3 has an effect on the short-term behavior before severe degradation occurs. No effect of SO_2:O_2 ratio on hot corrosion rate was also reported for Ni-20Cr-X (X stands for 0, 3Al, 5V) ternary alloys [93]. The tested gases were Pt catalyzed mixtures of SO_2 and O_2 in the ratios 2:1 and 1:4. To estimate how important SO_3 on type I hot corrosion, Otuska and Rapp [94] measured the Na_2O activity and P_{O_2} as a function of time on pre-oxidized nickel with a Na_2SO_4 deposit in catalyzed O_2-SO_2 gas mixture. It was found

that P_{O_2} drops significantly and the activities of Na_2O increases due to the removal of oxygen and sulfur from the Na_2SO_4. It seems the effects due to the reaction of Na_2SO_4 with Ni override any influence of the gas environment; consequently the attack is not dependent on the composition of the gas for Ni. Some studies of high purity nickel with a Na_2SO_4 deposit at 900°C showed a larger extent of attack was observed in catalzyed O_2+4.2%SO_2 than in air, but the reason was due to a substantial number of sulfides formed by sulfidation-oxidation being the predominant mode of degradation [95-97]. In general, the presence of SO_3 or SO_2 is considered as not important for type I hot corrosion. As a result, many of the experiments for type I hot corrosion were performed in air or pure O_2. But an important question remains: how important is the presence of sulfur containing gas species SO_2, SO_3 in the gas for type I hot corrosion for systems other than pure Ni? For the poor hot-corrosion resistant β-NiAl system, there was no obvious difference after long-term exposures, but is there any difference during short term? What about alloy system that is more resistant to type I hot corrosion attack? Does the extent of attack caused by type I hot corrosion depend on the content of SO_2? These aspects are worthy of more experimental investigations.

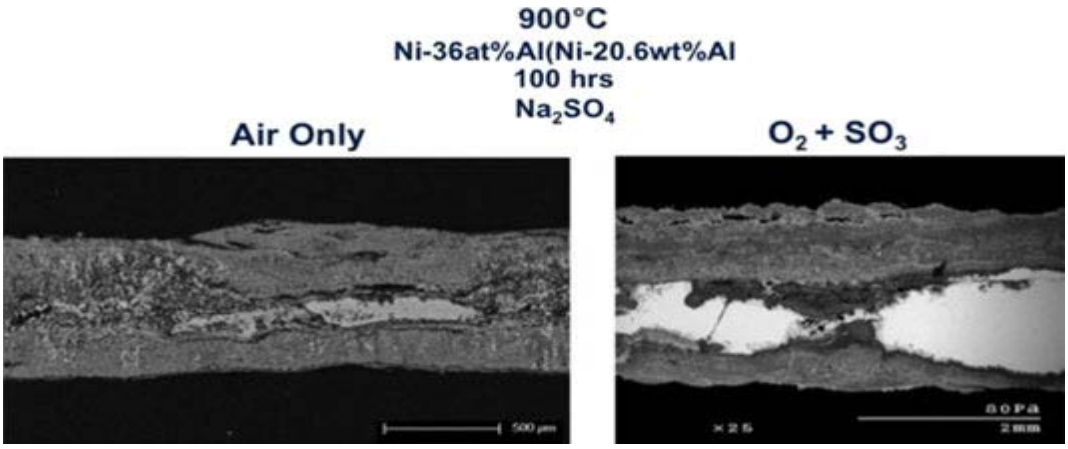

Figure 2.25 Comparison of the degradation occurring for the Na_2SO_4 induced attack of an alloy in air and in oxygen with SO_3. Severe attack occurred in air as well as in a gas with SO_3[89]

2.3.3 Degradation sequence of hot corrosion

The hot corrosion of virtually all susceptible alloys is observed to occur in two stages: an initiation stage during which the rate of corrosion is slow and similar to that which occurs in the absence of the deposit, and a propagation stage in which rapid, sometimes catastrophic, corrosion occurs. Figure 2.26 is a schematic representation of hot corrosion kinetics. The low corrosion rate during initiation is due to the formation and maintenance of a protective oxide scale which prevents the salt deposit from penetrating through and causing severe alloy degradation. During the incubation stage, the deposit, the scale, and the alloy are being altered. This alteration may be due to: oxide scale being dissolved into the salt; deposit compositions being shifted towards more corrosive conditions; cracks or channels developing in the scale; elements for forming the protective scale becoming depleted, etc. All these alterations make the oxide scale less protective and the alloy susceptible to rapid attack. The length of the initiation stage varies from seconds to thousands of hours and a large number of variables could affect this, including alloy

composition, alloy microstructure, gas composition, deposit composition, deposit thickness, temperature and extent of thermal cycling [37].

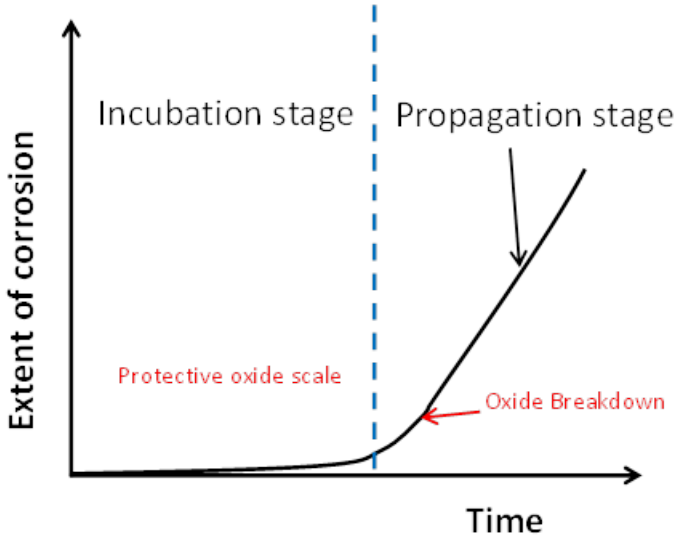

Figure 2.26 Schematic representation of hot corrosion rate as a function of time

The initiation of the propagation stage is associated with the destruction of the protective oxide layer. Several mechanisms have been reported including the fluxing of scale [98-100], the mechanical fracture of the scale [101]. Scale fluxing was very popular in early studies of hot corrosion and it is still invoked in current studies. It has been a major achievement of hot corrosion study and it helps to explain many aspects of rapid degradation caused by a sulfate deposit salt. Scale fluxing is a salt-induced scale damage. It involves oxide scale dissolution into salt as ions, ion transport from oxide/salt interface to salt/gas interface, oxide precipitation as non-protective scale and the penetration of sulfur into alloy.

2.3.4 Scale fluxing

2.3.4.1 Oxide solubility in deposit

To understand scale fluxing, it is necessary to know oxide solubility in a salt. This can be described by starting with the equilibrium reaction for Na_2SO_4, i.e.

$$Na_2SO_4 = SO_3 + Na_2O \quad (2.15)$$

SO_3 is the acidic component, and Na_2O is the basic component. Depending on oxygen partial pressure, and the activity of Na_2O or the SO_3 partial pressure, Na_2SO_4 can be either acidic or basic. Gupta and Rapp [102] measured the solubility of Al_2O_3 in Na_2SO_4 as a function of $loga_{Na_2O}$ (or $logP_{SO_3}$) and their results are shown in

Figure 2.27. The solubility of Al_2O_3 has a minimum at $loga_{Na_2O}$ = -15.4 and it increases with the increase in $loga_{Na_2O}$ (i.e. the decrease in $logP_{SO_3}$) according to the reaction,

$$Al_2O_3 + Na_2O = 2NaAlO_2 \quad (2.16)$$

The above reaction corresponds to the basic dissolution of Al_2O_3 in Na_2SO_4. The solubility of Al_2O_3 also increases below the minimum with decrease in $loga_{Na_2O}$ (i.e. increase in $logP_{SO_3}$) according to the reaction,

$$Al_2O_3 + 3Na_2SO_4 = Al_2(SO_4)_3 + 3Na_2O \quad (2.17)$$

This corresponds to the acidic dissolution of Al_2O_3, suggesting that at higher values of $loga_{Na_2O}$, Al_2O_3 dissolves as AlO_2^- and at lower values as Al^{3+}.

Assuming unit Al_2O_3 activity, the equilibrium constant for the basic dissolution of Al_2O_3 can be expressed as

$$K = \frac{a_{NaAlO_2}^2}{a_{Na_2O}} \quad (2.18)$$

Taking the logarithm of both sides, solving for a_{NaAlO_2}, and differentiating with respect to $-loga_{Na_2O}$, one finds

$$\left[\frac{\partial loga_{NaNiO_2}}{\partial(-loga_{Na_2O})}\right] = -\frac{1}{2}$$

This is the slope of the left portion of the Al_2O_3 dissolution curve in Figure 2.27. Using a similar method for the acidic dissolution reaction

$$K = a_{Al_2(SO_4)_3} \cdot a^3_{Na_2O} \tag{2. 19}$$

$$\left[\frac{\partial loga_{Al_2(SO_4)_3}}{\partial(-loga_{Na_2O})}\right] = \frac{1}{3}$$

This is the slope for the right portion of the Al_2O_3 dissolution curve in Figure 2.27

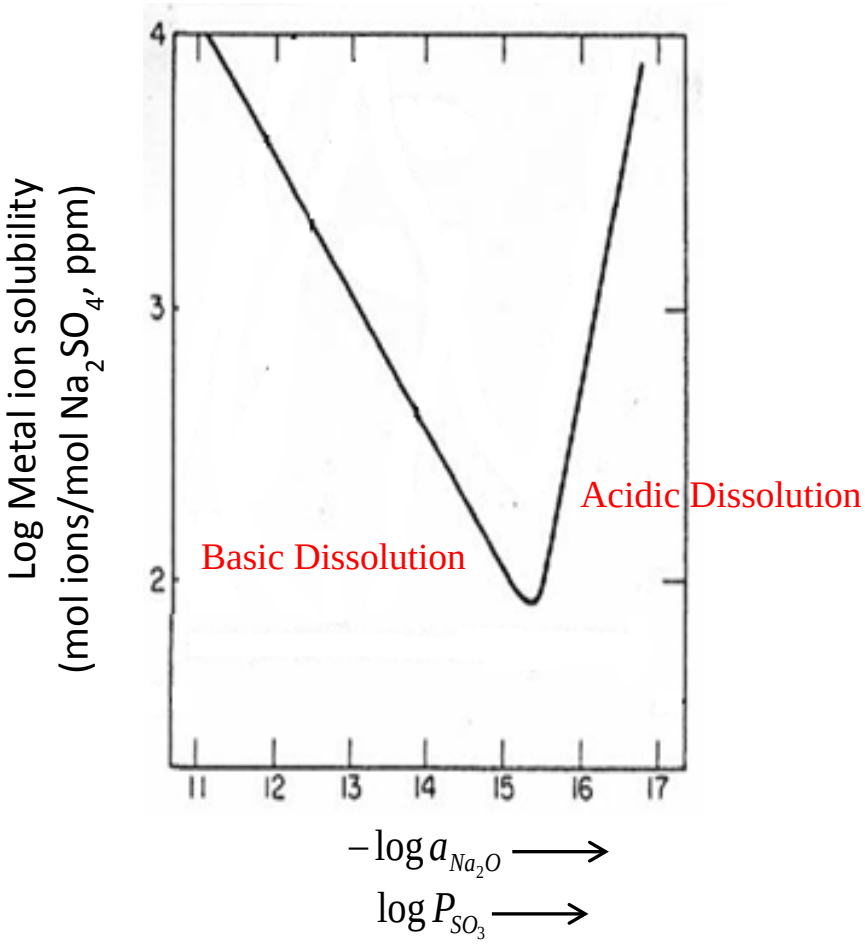

Figure 2.27 Solubility of Al_2O_3 in Na_2SO_4 as a function of melt basicity at P_{O_2}= 1atm and T = 1200°K

2.3.4.2 Basic fluxing-Type I hot corrosion

Rapp and Goto [102] proposed that a negative solubility gradient was necessary in order for a continuous oxide dissolution in the molten deposit. This negative gradient means the solubility of an oxide as a function of distance from the oxide/salt interface is decreasing. This is mathematically shown by the inequality in 2.20

$$\left[\frac{d[Solubility\ of\ oxide]}{dx}\right]_{x=0} < 0 \qquad (2.\ 20)$$

where: x is the thickness of the deposit: at the oxide/salt interface, x=0; and at the salt/gas interface, x>0.

Figure 2.28 shows at the oxide/salt interface, x=0, oxide solubility is large and the oxide therefore dissolves into salt at this interface. Following the solubility gradient, the dissolved oxide ion transfers through fused salt film to the salt/gas interface (x > 0). At that interface, oxide solubility is smaller; thus the dissolved oxide precipitates in the salt as discontinuous particles. These newly precipitated oxides are porous and are not protective. The salt released after oxide precipitation will continue to dissolve oxides at the oxide/salt interface, then new oxides will precipitate at the salt/gas interface. Back and forth, it forms a cycle through which a protective oxide scale was removed. As long as the negative oxide solubility is maintained through the salt film, the dissolution and precipitation is sustainable until the whole protective oxide scale is broken down. This process is called scale fluxing.

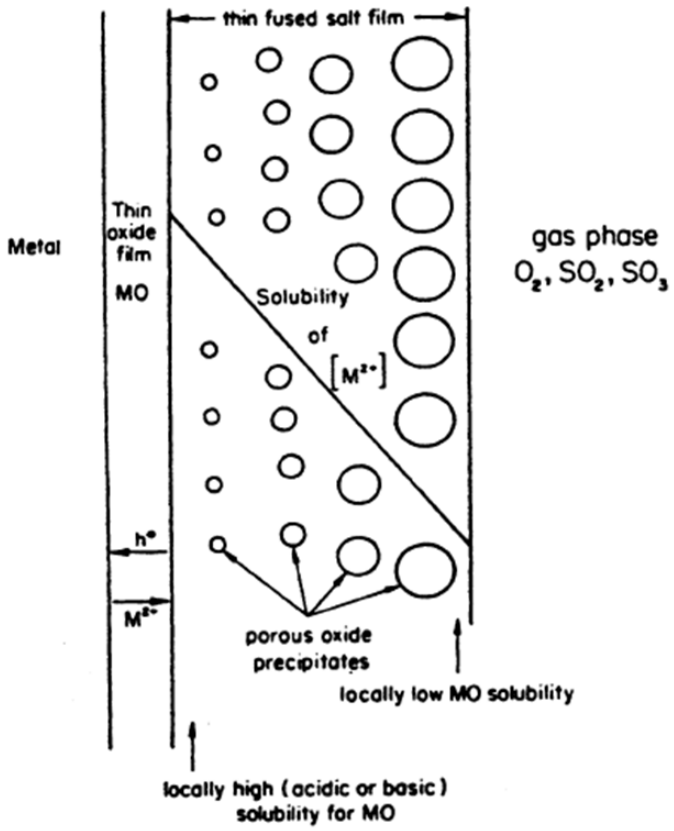

Figure 2.28 schematic representation of negative oxide solubility gradient and the breakdown of oxide scale through fluxing [98]

As mentioned previously, the oxide solubility is a function of the salt basicity. Thus, at a constant Po_2, a gradient of basicity must develop in the salt to the point where the oxide solubility gradient is negative at the scale/salt interface. Figure 2.29 schematically shows how the gradient of basicity in salt could be developed. Three situations (case A, case B, case C) are shown in which basicity gradient or acidity gradient are established. In each case, dashed vertical lines labelled as I represent the oxide/salt interface, and the lines labelled as II represent the salt/gas interface. It is clear that whether the case is acidic or basic or mixed with both, as long as the oxide solubility at interface I is higher than that at interface II, continued oxide dissolution

can occur and hot corrosion is sustainable. In case B, the two interfaces lie on either side of the solubility minimum for the oxide.

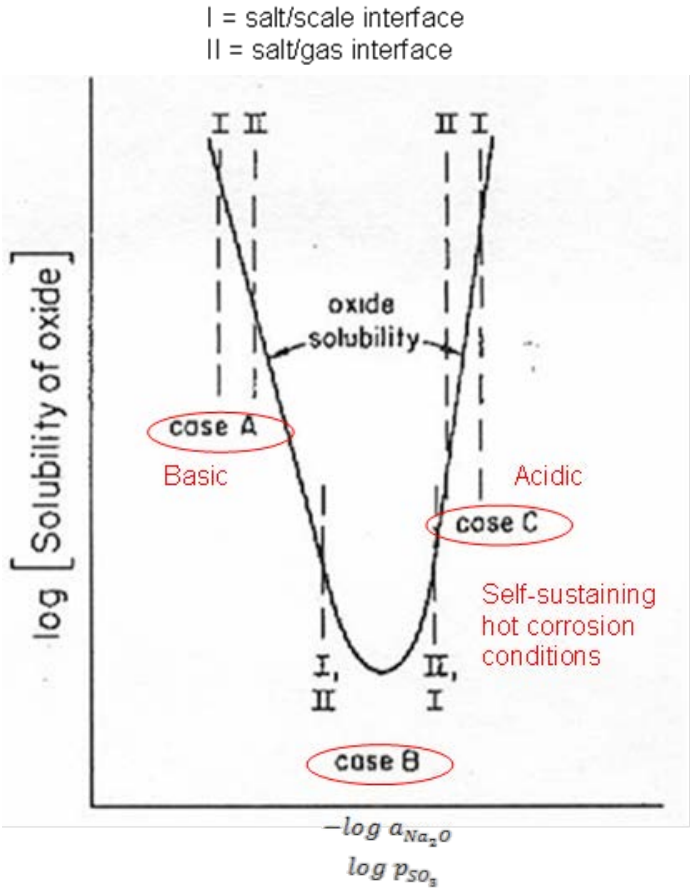

Figure 2.29 Schematic demonstration of Rapp-Goto criterion[99]

Goebel and Pettit [103] presented a model to explain the NiO scale fluxing during type I hot corrosion of pure Ni. It was proposed that a liquid Na_2SO_4 layer was established between the nickel and the gas atmosphere. The formation of NiO decreases the oxygen activities of the Na_2SO_4 deposit. Sulfur is diffused into the alloy. The removal of oxygen and sulfur from the Na_2SO_4 leads to the increase of Na_2O activity in the Na_2SO_4 near the Ni/Na_2SO_4 interface due to the following reaction [92],

Na_2SO_4=Na_2O (in Na_2SO_4) +3/2O_2 (used to form NiO) +1/2S_2 (used to form sulfide)

When the Na_2O activity near the Ni/Na_2SO_4 interface is increased to high enough, a decreasing Na_2O activity levels can be set within the Na_2SO_4, therefore NiO can be fluxed from the alloy surface and precipitated out in the Na_2SO_4 as discontinuous particles. This process is schematically shown in Figure 2.30

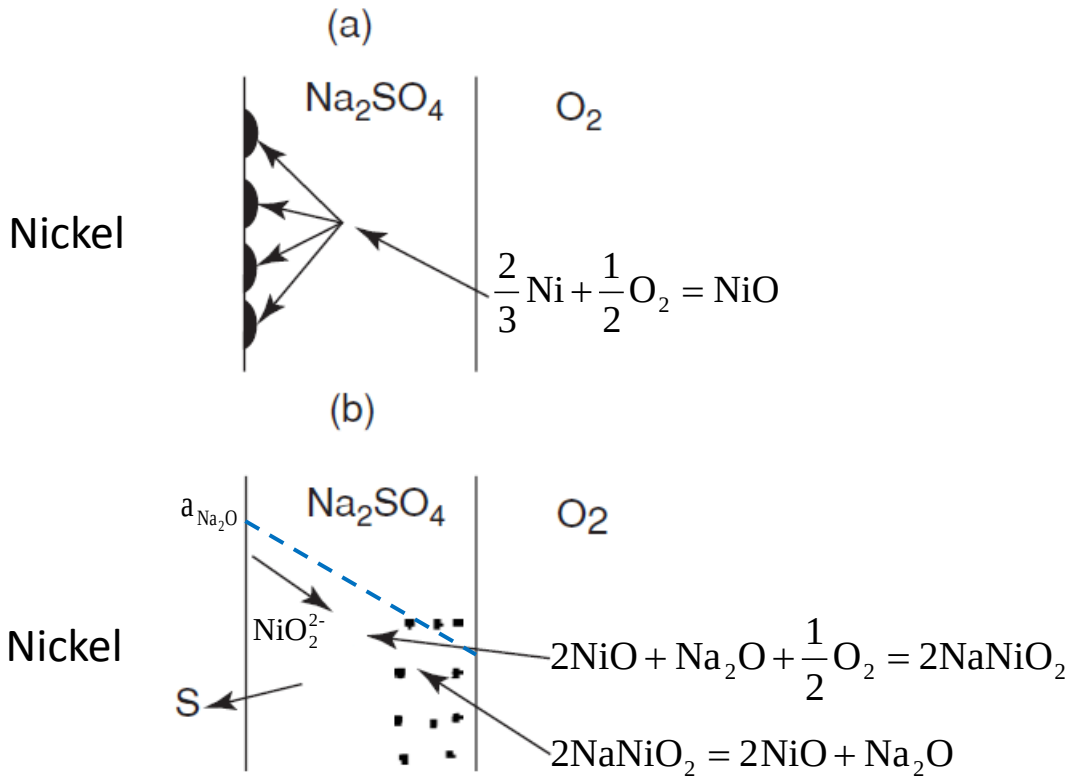

Figure 2.30 Model for Na_2SO_4-induced accelerated oxidation of NiO forming alloy[103]

The scale fluxing theory is helpful to understanding how a protective oxide scale can be destroyed by the presence of a salt deposit. But the understanding to hot corrosion is not complete, as aspects such as alloy chemistry and microstructure are not considered. Task has reported that microstructure can largely affect the Type II hot corrosion resistance of MCrAlY alloys [2, 104]. In his study, NiCrAlY alloys were prepared in bulk form by drop casting (DC) and injection casting (IC), and as a coating by low-pressure plasma spraying (LPPS), it was found that DC and LPPS NiCrAlY displayed very good resistance to type II hot corrosion;

however, IC NiCrAlY developed a rapid Type II attack [104]. Therefore, the type II hot corrosion attack is affected by the microstructure.

For explaining alloying effects, the fluxing mechanism is useful only when the alloying elements were dissolved into salt deposits. For example, Rapp reported that the beneficial role of Cr as an alloy addition to Ni-, Fe- or Co- based alloy in abating type I hot corrosion was partly because the formation of chromite or chromate ions can act as a buffer to restrict an increase in melt basicity as the oxides of Ni, Fe, or Co form acidic solutes [105] . However, not all alloying elements in the alloy play a role through dissolving into the salt. As shown in Figure 2.31, the addition of Pt, Cr, Co+Pt has varied degree of benefit in improving the type I hot corrosion resistance of β-NiAl alloy; however, protective alumina scales formed on these Pt, Cr, Co+Pt modified alloys and platinum and chromium were not detected within or on the alumina scale [2, 106]. In this case, it is difficult to identify that these beneficial elements are in direct contact with a Na_2SO_4 deposit when a protective alumina scale was formed. Therefore, relying on the scale fluxing mechanism to explain the beneficial effects of these alloy elements would be insufficient.

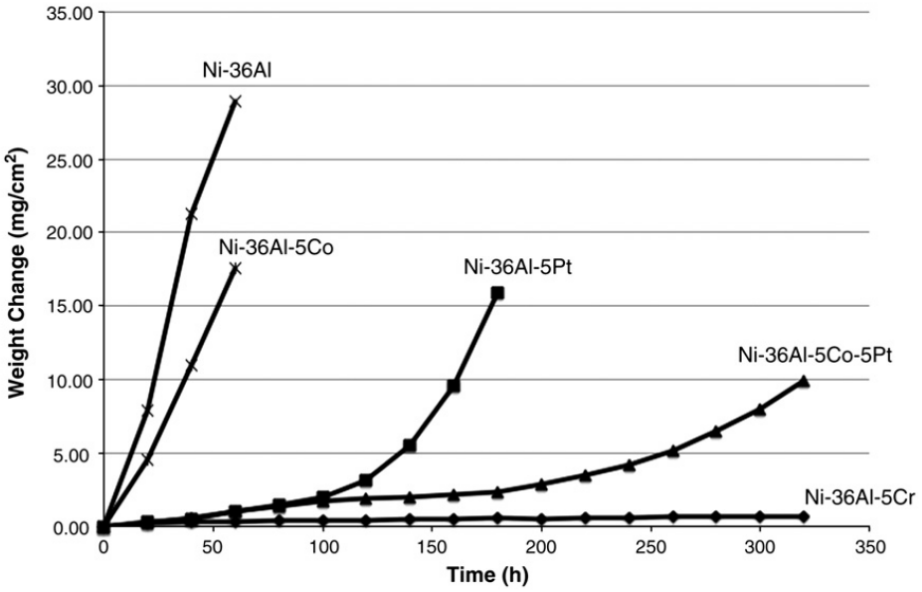

Figure 2.31 Plots of weight change per unit area vs. time for the Type I hot corrosion exposures [2, 3]

From a metallurgical point of view, one would interest in alloy/coating selection and development. However, scale fluxing mechanism can only provide limited information for the alloy design. An investigation of alloy element effect on oxide scale growth and its subsequence performance in air, and type I hot corrosion condition would give better guidance on alloy design, and would also help to identify key factors of alloy abilities and the formed oxides scale for extending component lifetime in hot corrosion conditions.

As mentioned in section 2.3.3, the initiation of the propagation stage is associated with the destruction of the protective oxide layer, scale fluxing is just one mechanism that can cause the failure of a protective oxides. The protective oxides can also be compromised by mechanical mechanism through the cracking and spallation of scale during thermal cycling. If in certain way, the protective oxide layer was lost, the alloy would have to re-heal a new protective oxide scale to maintain resistance to hot corrosion. Because if the molten salt is able to make contact with a

greatly depleted alloy that is unable to reform a protective scale, catastrophic attack will ensue. Therefore, in this situation, the extent of subsurface degradation and the re-healing capabilities of alloy are important. The correlation between the duration of the incubation stage and the alloy's re-healing capabilities has only recently been studied. The investigation was done on β-NiAl system[2, 3]. No research about this was done on other system alloys such as γ′-Ni_3Al—the primary phase of superalloy and γ+γ′ coating materials. For developing better γ+γ′ coatings with excellent hot corrosion resistance, it would be meaningful to investigate the re-healing abilities of alloying modified γ′-Ni_3Al system in hot corrosion conditions and study their effects on the duration of the incubation stage during hot corrosion

Except that alloys' abilities to re-heal a protective scale is important for the duration of incubation stage during hot corrosion, the quality of protective oxide layer itself in terms of homogeneity, phase constitution would also be another aspect for consideration. For the latter, if more resistance to hot corrosion was achieved by the formation of alumina scale rather than NiO or spinel on high temperature coatings, during type I hot corrosion, the alumina has to be formed at a temperature where metastable and stable phases co-exists. The next question is: Do the phase stabilities of alumina affect the alloy's performance in hot corrosion conditions? An investigation on this aspect is still lacking.

3.0 OBJECTIVES

3.1 DEFICIENCIES IN THE CURRENT BODY OF KNOWLEDGE

Past mechanistic research on hot corrosion has focused on the propagation stage, considering issues such as oxide solubilities and scale fluxing. From an engineering standpoint, these studies explain why hot corrosion can be so aggressive. However, for the benefit of lifetime extension, an important variable is the incubation stage of hot corrosion. If this stage can be increased it follows that the hot-corrosion resistance of the coating or alloy will be increased. Thus, an investigation of the factors affecting the duration of the incubation stage is of critical practical and fundamental importance. The incubation stage is a consequence of oxidation, and, more importantly, maintaining the intact presence of the protective oxide scale formed. The initiation of the propagation stage is associated with the disruption of the protective oxide scale. Oxide-scale formation during the incubation stage has only been recently studied [2, 3] and that investigation was done on the β-NiAl system. A reasonable understanding of the processes involved is still limited, especially for other alloy systems such as these containing mainly γ′-Ni_3Al—the primary phase of Ni-based superalloys and γ+γ′ coatings.

It is conjectured that if a protective and tenacious scale is maintained on the alloy surface, the alloy will be highly resistant to hot corrosion. The protective scale is usually alumina for high-temperature systems. Few studies have estimated a γ′-Ni_3Al-based alloy's ability to

establish, maintain and reform/ heal an alumina scale in SO_2-containing environments with or without a salt deposit. Indeed, the main factors governing the lifetime of alloys on coatings in type I hot corrosion conditions are still not clear.

For a systematic study, the environmental effects on alumina scale growth and establishment should also be considered; these effects include the presence of salt deposit and a low SO_2 content in the atmosphere. For alumina-scale formation and subsequent growth, a critical aluminum concentration is needed in the alloy. The critical aluminum concentration can be sensitive to environmental factors, but few studies have investigated whether the presence of SO_2 affects the internal-to-external transition of alumina formation.

At temperatures at which type I hot corrosion typically occur, there is apt to be a metastable→stable alumina phase transformation within the oxide scale. Limited research [2, 78] has reported on the effects of environmental sulfur and salt deposit on alumina-scale structures which form during hot corrosion. Moreover, a mechanistic understanding is still lacking.

An important question remains: How important is the presence of SO_2 in the gas atmosphere to type I hot corrosion? For pure Ni, the extent of attack caused by type I hot corrosion seems independent of the SO_2 partial pressure in the atmosphere [94]. However, investigation is still lacking on commercial alloys.

3.2 AIMS OF CURRENT STUDY

The primary aims of this study are to:

- Investigate the ability of γ′-based alloys to establish, maintain and reform and/or heal an alumina scale under salt deposit and identify the key factors of oxide scale properties and alloy ability for extending the incubation stage in Type I hot corrosion.
- Identify the role of minor alloying elements, Si and Pt, on the oxidation and Type I hot corrosion behavior of γ′-based alloys
- Study the effect of environmental sulfur and salt on the structural stabilities of thermally-grown alumina scales at temperatures relevant to hot corrosion.
- Study the effect of environmental sulfur on the establishment of alumina scale at temperatures relevant to hot corrosion.
- Study the effect of environmental sulfur and salt on the Type I hot corrosion of alumina-scale forming alloys

For the investigation of environmental effects, a systematic approach will be used to fully assess the above aspects. All tests will be done at relatively low temperature (i.e. 900°C). First, oxidation will be done in air, then alloys will be exposed in SO_2-containing environments, and then, finally, tests will be done in the presence of Na_2SO_4 deposit in air and O_2+SO_2 atmospheres, which represent hot corrosion testing.

The experimental approach is represented in Figure 3.1

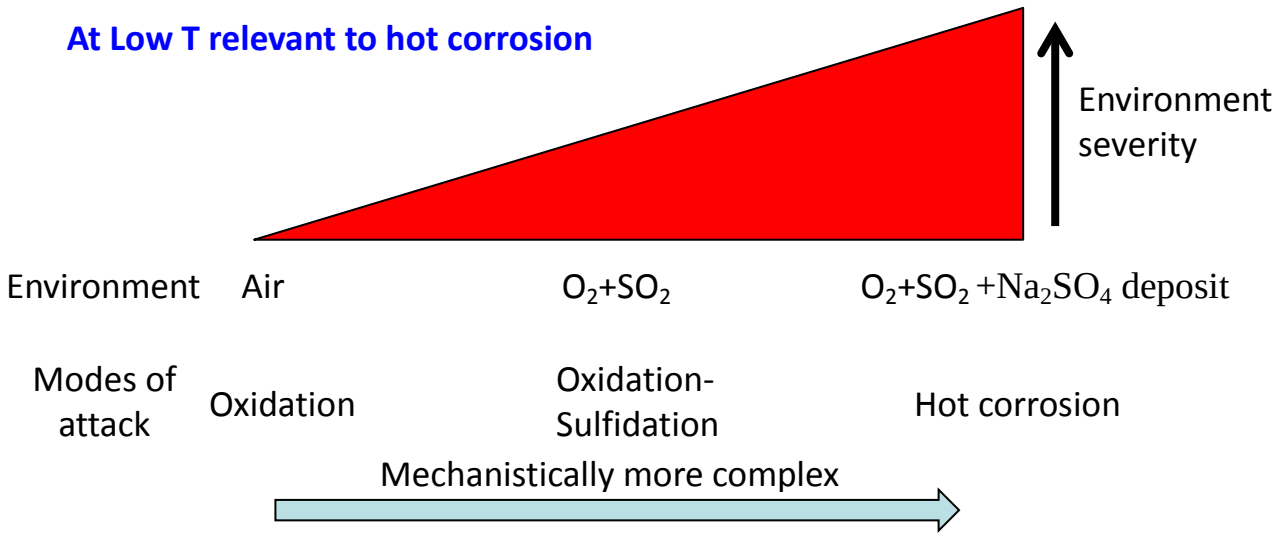

Figure 3.1 Experimental Approach

4.0 EXPERIMENTAL PROCEDURES

4.1 MATERIALS STUDIED

4.1.1 Ni-20Al-(5, 7.5) Cr-(0, 3) Si-(0, 3) Pt-(0.05, 0.1) Hf-0.05Y model alloys

To determine the alloy's ability to establish, maintain and reform and/or heal an alumina scale under salt deposit and identify the key alloying and scaling factors for extending the incubation stage in Types I hot corrosion, six Ni-20Al based model alloys were prepared. These alloys were also used to investigate the environmental sulfur and salt on alumina scale phase stabilities. The nominal compositions of the alloys prepared are presented in Table 4.1. 40 g alloy ingots were processed at the Ames Laboratory's MPC[107] by first Ar-arc melting and then drop-casting to form 10-mm diameter rods. The as-cast rods were then homogenized in vacuum at 1200˚C for 48 h. The heat-treated rods were then cut into 1-mm thick disks. Before testing, the sample disks were polished to a 1200-grit finish and then ultrasonically cleaned in acetone.

Table 4.1 Nominal compositions of the Ni-20Al based model alloys.

Alloy	Element (at.%)						
	Ni	Al	Cr	Pt	Si	Hf	Y
1	Bal.	20	5	-	-	0.1	0.05
2	Bal.	20	5	-	3.0	0.1	0.05
3	Bal.	20	5	3.0	-	0.1	0.05
4	Bal.	20	5	3.0	3.0	0.1	0.05
5	Bal.	20	5	-	-	0.05	0.05
6	Bal.	20	7.5	3.0	3.0	0.1	-

4.1.2 Low Cr Ni-Cr-Al model alloys

To determine the oxide map in sulfur-containing conditions, four model alloys of nominal compositions given in Table 4.2 were prepared. All the model alloys are in the single γ-Ni (Cr, Al) phase region on the phase diagram [108]. All alloy ingots were prepared at the MPC[107] by argon arc-melting followed by drop-casting to form 25mm diameter rods. The alloys were then cut into 5-mm thick disks and then preliminarily heat-treated in vacuum at 1200°C for 48h. Each disk was then cold rolled to about 1mm thickness and then heat treated again in vacuum at 1000°C for 48h to stabilize the microstructure. Samples were cut from the disks and then polished to a 600-grit finish starting from a 240-grit abrasive. This sample preparation procedure was the same as that conducted by Giggins and Pettit [4] in their study to determine a Ni-Cr-Al oxide map.

Table 4.2 Nominal compositions of the low Cr Ni-Cr-Al model alloy

Alloy	Element (wt.%)		
	Ni	Al	Cr
7	Bal.	2.4	4.6
8	Bal.	3	5
9	Bal.	3.1	3.2
10	Bal.	3.9	3.3

4.1.3 Commercial alloys

Three commercial alloys were also tested in this study. The nominal compositions of these alloys are presented in Table 4.3. Single-crystal bars of PWA 1484 and PWA1487 were provided by Pratt & Whitney. During testing, the bar was sliced into 1-mm thick disks and 1cm x1cm square samples were prepared from each disk. Microstructures of single crystal PWA 1484 and PWA1487 alloy are provided in Figure 4.1 A polycrystalline alloy with the same composition as PWA1484 alloy was fabricated by Howmet Corporation, with sulfur concentration less than 1ppm. A single-crystal round disk of Rene N5 alloy was provided by General Electric. Disks were cut and polished to a 1200-grit finish.

Table 4.3 Nominal composition of the alloys studied

Alloy	Commercial alloys (wt.%)										
	Ni	Al	Cr	Co	Mo	W	Ta	Ti	Hf	Re	Y
PWA 1487	Bal.	5.6	5	10	2	6	8.7	-	0.1	3	0.01
PWA 1484	Bal.	5.6	5	10	2	6	8.7	-	0.1	3	-
Rene N5	Bal.	6.2	7	8	2	5	6	-	0.2	3	-

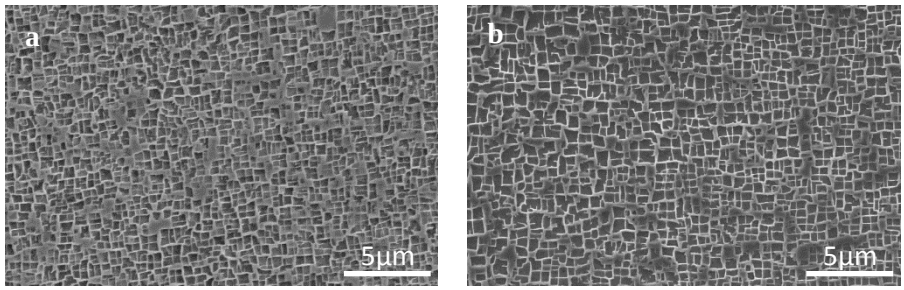

Figure 4.1 The microstructure of (a) PWA1484 and (b) PWA1487, a 2nd generation single-crystal superalloy. The γ′(dark phase) has a very high volume fraction

4.2 HIGH TEMPERATURE EXPOSURE

4.2.1 Oxidation in air

Oxidation tests in air were conducted using either a horizontal resistance-heated tube furnace or a TAG 24 thermobalance (SETARAM instrumentation) with a mass resolution of 0.01mg. Prior to any testing, calibration of the furnace temperature was done. For an oxidation experiment in air

in the horizontal resistance-heated tube furnace, the furnace was initially heated to the target test temperature and held for about 2 hours. The sample was placed horizontally in a ceramic boat and slowly pushed into the hot zone using a steel push-rod to start a test. The pushing took about 3 minutes. The sample weight was measured before and after exposure using an analytical balance with a mass resolution of 0.01mg. During oxidation in the TAG thermobalance, the thermogravimetric data were recorded automatically. The samples were hung on a sapphire hook in the furnace and were heated in dry air from room temperature to the target temperature at a rate of about 100°C/min. After each test, the weight change during the heating stage was excluded by setting the zero time and zero weight gain point at where the sample had reached reaction temperature. Dry air was used during TGA measurements.

4.2.2 Oxidation in SO_2-containing atmospheres

Oxidation tests in O_2-SO_2 atmospheres were carried out in a horizontal resistance-heated tube furnace. Figure 4.2 shows the schematics of sulfidation apparatus setup. Before testing, the samples were kept near the end of the furnace tube while the hot-zone was heated to the desired test temperature of 900°C or 1000°C. The maximum temperature of the samples during this heating period was measured by a thermocouple to be ~170ºC. The furnace tube was first flushed with pure Ar for 2 hours and then flushed overnight with the O_2 + 0.1%SO_2 or O_2 + 1%SO_2 reactant gas mix. In some cases, the reactant gas was passed through a platinized catalyst prior to reaching the hot zone. This was done to equilibrate the gas mixture. The calculated equilibrium gas compositions are shown in Table 4.4. After following this procedure to establish the reacting atmosphere, the samples were pushed into the hot zone of the furnace and

continuously exposed for a fixed amount of time. During oxidation, the flow rate of the reactant gas was 12.5 cm^3/min, which corresponds to a linear velocity of 0.62 cm/min.

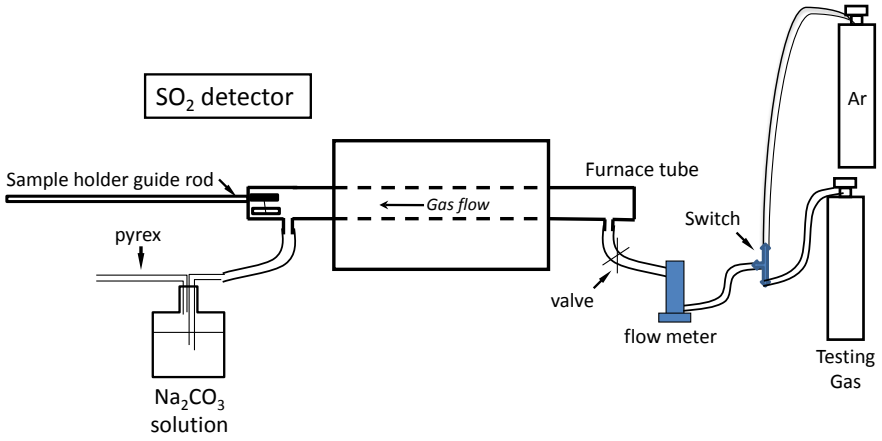

Figure 4.2 Sulfidation apparatus setup

Table 4.4 Equilibrium gas compositions in the furnace

Flowing gas	Catalyzed	Temperature	Equilibrium gas composition*
O_2+1000ppm SO_2	Yes	900˚C	$P_{S_2} = 3.7 \times 10^{-16}$atm; $P_{O_2} = 0.999$atm; $Pso_3 = 2.5 \times 10^{-4}$atm; $Pso_2 = 7.5 \times 10^{-4}$atm
O_2+1000ppm SO_2	No	900˚C	$P_{S_2} = 2.4 \times 10^{-31}$atm; $P_{O_2} = 0.990$atm; $Pso_2 = 9.9 \times 10^{-3}$atm
O_2+1000ppm SO_2	Yes	1000˚C	$P_{S_2} = 7.8 \times 10^{-15}$atm; $P_{O_2} = 0.987$atm; $Pso_2 = 1.28 \times 10^{-4}$atm

*Equilibrium calculations for catalyzed gases allow for SO_3 formation; while SO_3 formation is suspended in the uncatalyzed gas.

4.2.3 Type I hot corrosion

Type I hot-corrosion tests were conducted in three different atmospheres: air, and catalyzed and uncatalyzed O_2+SO_2 mixtures. Air exposures were done in a box furnace, while exposures to O_2+SO_2 atmospheres were done using the same experimental procedure and equipment as discussed above in section 4.2.2. A different furnace tube was used in the hot corrosion test to prevent salt contamination when doing the no-salt tests (such as exposures to an SO_2-containing atmosphere). The samples were pre-deposited with about 2 mg/cm^2 Na_2SO_4 and then exposed at 900˚C for 20 hours. Salt deposition was done by heating the samples on a hot plate to around 150˚C and then spraying a saturated solution of Na_2SO_4 onto one side of each sample. The water evaporated leaving a uniform Na_2SO_4 layer on the sample surface. After 20 hours exposure, the samples were cooled to room temperature, and weight change was measured using an analytical balance with a mass resolution of 0.01mg. The samples were then deposited with another 2-3 mg/cm^2 of Na_2SO_4 prior to another 20 hours of hot-time exposure. The salt-deposition process and 20 hours heating cycle was repeated until the alloys exhibited breakaway from the incubation stage. This repeated process is shown in Figure 4.3.

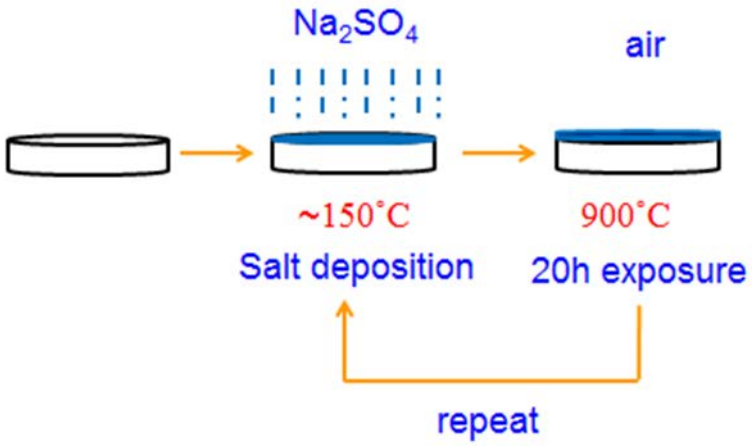

Figure 4.3 Schematic representation of type I hot corrosion experimental procedure

4.3 CHARACTERIZATION TECHNIQUES

The exposed samples were characterized using a number of techniques, including scanning electron microscopy (SEM). The SEM was used for both surface and cross-sectional analyses. The SEM used was a Philips XL-30 field emission gun microscope equipped with secondary electron (SE), and backscatter electron (BSE) imaging capabilities, and detectors for energy dispersive spectroscopy (EDS) analysis.

A Philips X'Pert diffractometer with Cu Kα radiation (λ=0.15418nm) capable of grazing incidence X-ray diffraction (GIXRD) analysis was used to identify the corrosion product phases. The incident angle was fixed at 5° for the GIXRD. To measure the compositional depth profile within the corrosion product and its subscale, an Auger electron spectrometer (AES) equipped with ion beam sputtering was used. During AES measurement, the samples were sputtered at a rate of ~7nm per cycle, and a spectrum was taken after each sputter cycle.

To distinguish θ-Al_2O_3 from α-Al_2O_3 in thinner oxide scales, photo-stimulated luminescence spectroscopy (PSLS) was done with a LabRam™ Confocal Raman Microscope (Jobin-Yvon/Horiba, Edison, NJ0) [109]. Alpha alumina will strongly fluoresce in response to visible laser illumination if trace quantities of chromium are present, giving a peak doublet (R1-R2) at around 693 nm. The θ-Al_2O_3 peak doublet (T1-T2) is blue-shifted from that of α by approximately 10 nm[110]. The origin of the above-mentioned luminescence in alumina is due to the photostimulation and subsequent radiative decay of excited d^3 electrons in substitutional Cr^{3+} ions located on octahedral sites of both θ and α [111, 112]. The luminescence of θ-Al_2O_3 can be 10-12 times weaker than that of α-Al_2O_3 luminescence [60]. The relative amount of α-Al_2O_3 and θ-Al_2O_3 was semi-quantitatively estimated by comparing the R1-R2 and T1-T2 doublet intensities. A correction factor of ϕ=12 was used considering the weaker luminescence signal from θ-Al_2O_3. The α-Al_2O_3 fraction was determined based on the following equation [113]:

$$f_\alpha = \frac{A_{R1}+A_{R2}}{A_{R1}+A_{R2}+\phi(A_{T1}+A_{T2})} \quad (3.\ 1)$$

where A is the integral intensity of characteristic doublet. Fitting of the spectra was performed using Renishaw's WiRE v3.2 software to determine the contributing intensity and the position of the R1-R2 and T1-T2 peaks.

To obtain surface-state information of the sample, X-ray photoelectron spectroscopy (XPS) was used. In certain cases, focused ion beam (FIB) and transmission electron microscope (TEM) were used to characterize very thin films. ChemieSTEM was used to characterize element distribution on TEM samples.

The AES, XPS, PSLS, FIB and TEM analysis were done at the Swagelok Center for Surface Analysis of Materials at Case Western Reserve University. The ChemieSTEM analysis was done at Lawrence Berkeley National Laboratory.

5.0 RESULTS AND DISCUSSION

5.1 GENERAL INVESTIGATION OF THE 900°C OXIDATION AND HOT CORROSION OF γ'-NI_3AL-BASED ALLOYS

5.1.1 Materials design

Four Ni5Cr20Al-based alloys with no, single, and co-addition of Si and/or Pt, were designed and tested. Their position on the 900°C ternary phase diagram is shown in Figure 5.1 and their nominal compositions are presented in Table 5.1.

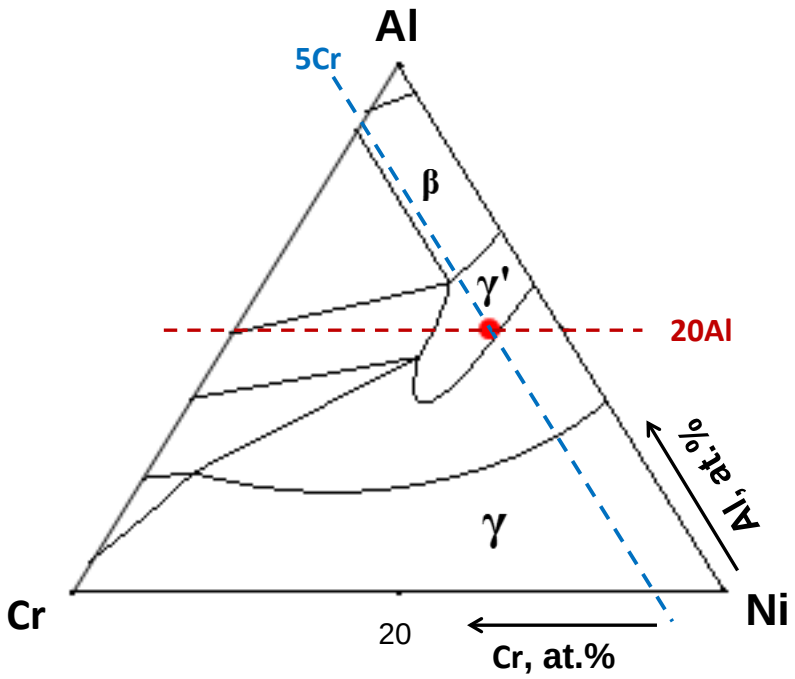

Figure 5.1 Mapping the designed alloy composition on 900°C Ni-Cr-Al phase diagram

Table 5.1 Nominal composition of the alloys studied. All alloys are single-phase γ'-Ni_3Al

Alloy	Element (at.%)						
	Ni	Al	Cr	Pt	Si	Hf	Y
Base	Bal.	20	5	-	-	0.1	0.05
+3Si	Bal.	20	5	-	3.0	0.1	0.05
+3Pt	Bal.	20	5	3.0	-	0.1	0.05
+3Si+3Pt	Bal.	20	5	3.0	3.0	0.1	0.05

5.1.2 Results

5.1.2.1 Alloy microstructure and phase stability

Figure 5.2 shows the microstructure of the base-3Pt alloy in the as-prepared and after-tested states. Alloy preparation was completed with a 1200°C heat treatment for 48 hours. The final structure was comprised of a single phase γ′-Ni_3Al. A few Y-rich white particles were dispersed in the γ′-Ni_3Al matrix. In Figure 5.2(b), the alloy was exposed at 900°C for 100 hours and is seen to have maintained to be a single phase γ′-Ni_3Al structure. Base, Base+3Si, Base+3Pt+3Si alloys showed a similar single-phase γ′-Ni_3Al microstructure, as shown in Figure 5.3. Thus, the addition of 3Pt and/or 3Si did not affect the phase constitution of the alloys. With a single-phase microstructure, any multi-phase effects could be avoided for the investigation of alloy elements effects on hot-corrosion resistance.

Before testing the alloys in hot corrosion conditions, the nature of oxide scale formation in air was first investigated. This will be shown in the next section.

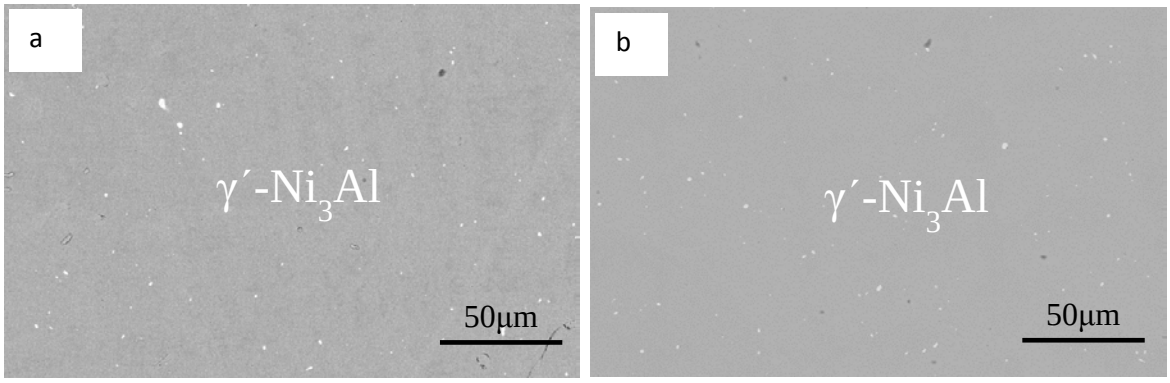

Figure 5.2 Phase stability of Base+3Pt alloy (a) alloy vacuum annealed at 1200°C for 48 hours and (b) un-attacked area of alloy after oxidation at 900°C for 100 hours

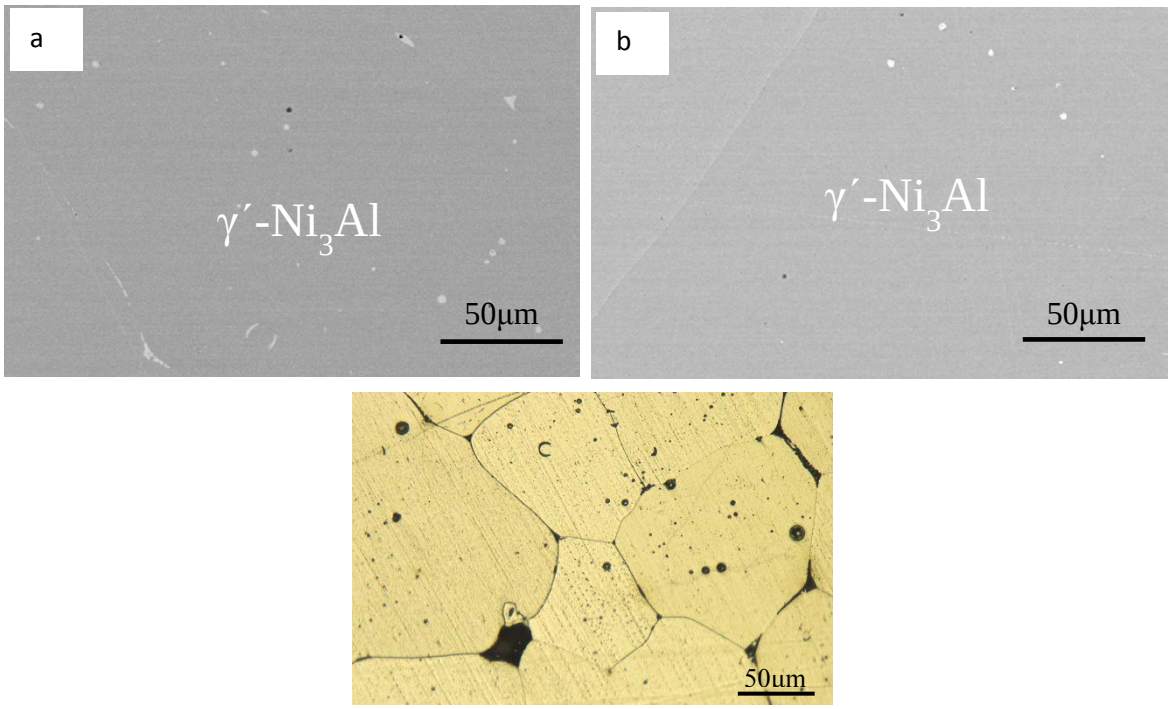

Figure 5.3 Microstructure of (a,c) Base+3Si and (b) Base+3Pt+3Si alloy after vacuum heat treatment at 900°C for 100 hours followed by water quenched to maintain high temperature structure.

5.1.2.2 900°C isothermal oxidation in air

Figure 5.4 show the oxidation kinetics of the model alloys at 900°C in air for 100 hours. It is seen that the four alloys showed similar and very low weight gain (<0.4mg/cm^2) after 100 hours exposure. All additions decreased the weight-gain kinetics of the Base alloy. The addition of Si+Pt only slightly decreased the growth rate of oxide scale and there is not much difference between single addition of Si or Pt and co-addition of both.

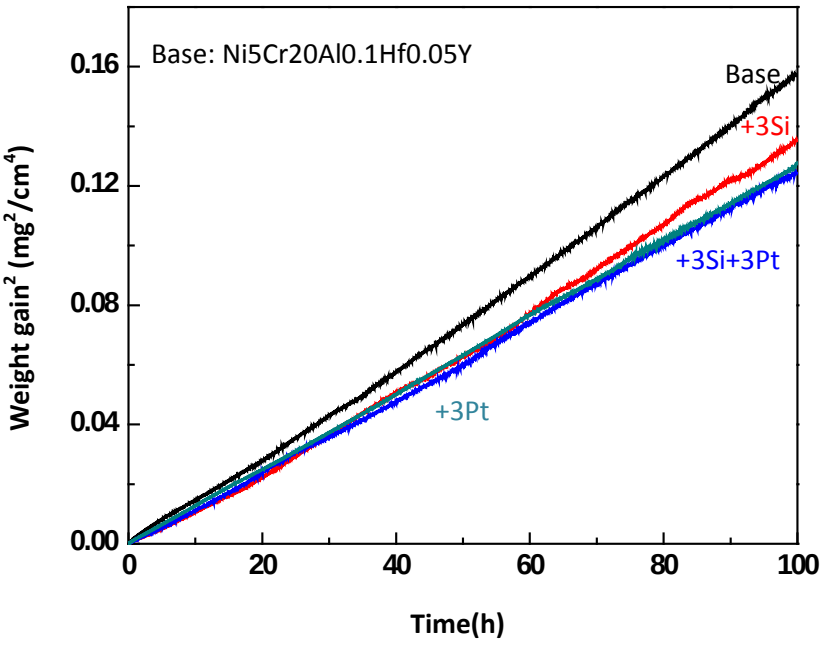

Figure 5.4 The model alloy 900˚C isothermal oxidation in air for 100 hours

A fitting model [57, 114] was used to determine the parabolic growth rate constant for each alloy. Using the Base+3Pt alloy as an example, Figure 5.5 shows the steps in the kinetics analysis. The sample weight gain as a function of time is shown in Figure 5.5(a). Using these measured kinetics, the instantaneous time exponent was determined using the following equation:

$$\boldsymbol{n} = \frac{\boldsymbol{\partial}(\boldsymbol{log}\Delta \boldsymbol{m})}{\boldsymbol{\partial}(\log \boldsymbol{t})} \quad (5.\ 1)$$

When the oxide-scale growth rate is parabolic, n=0.5. The calculated instantaneous n-values are plotted as a function of time in Figure 5.5(b), where it is seen that n maintained a value of 0.5 after a certain initial transient. Due to noise effects associated with the weight-change measurements, fluctuations around n=0.5 were observed, but these fluctuations were not significant, i.e., n=0.5±0.03. From the time at which the instantaneous n is 0.5, the growth rate is

considered to be steady state and parabolic[57]. Accordingly, the instantaneous parabolic rate constants, k_p, were calculated based on the following basic expression:

$$\Delta m = (k_p t)^{0.5} \quad (5.2)$$

Figure 5.5(c) plots the instantaneous value k_p as a function of the square root of time. The average value was determined based on the instantaneous value k_p during the steady state. The average k_p value and associated standard deviation for each model alloy are shown in Table 5.2.These values compare well with reported data on θ-Al_2O_3 scale growth in the literature[61]. As shown in Figure 5.6, the measured rate constants coincide with θ-Al_2O_3 growth. Not only that, the measured k_p values are very close to the extent that Si and Pt do not have much of an effect on the alumina scale growth rate within the time and temperature studied.

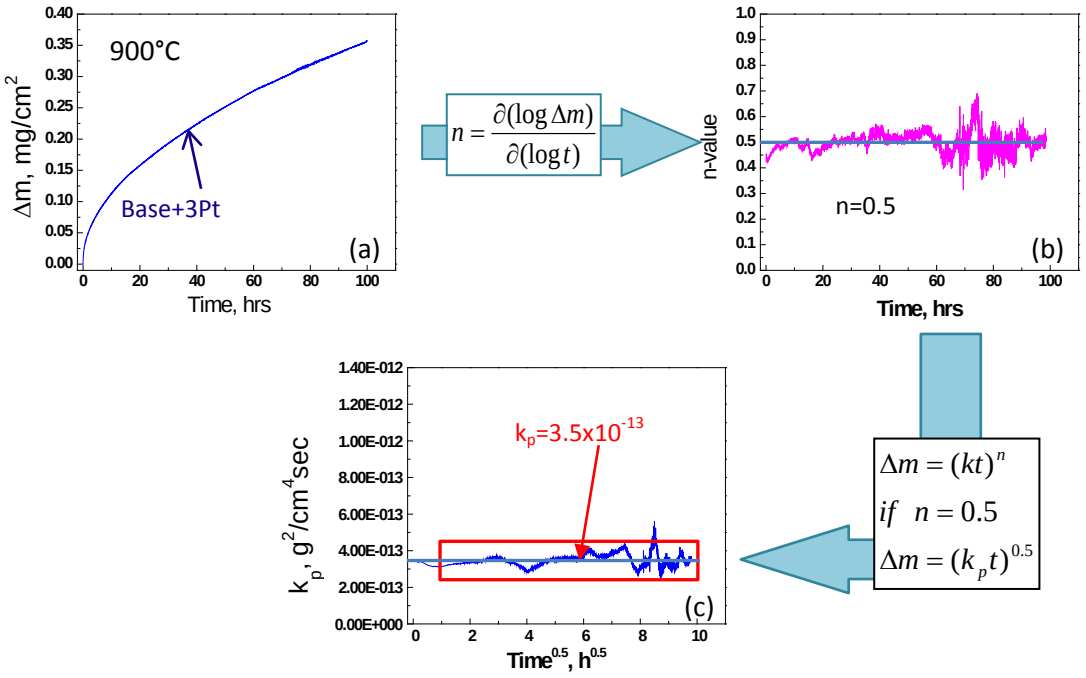

Figure 5.5 Kinetics analyses for the determination of k_p

Table 5.2 The Parabolic constants kp for model alloys

Alloy	$k_p(g^2/cm^4s)$	Standard deviation
Base	$4.9x10^{-13}$	$0.7x10^{-13}$
+3Si	$4.3x10^{-13}$	$1.1x10^{-13}$
+3Pt	$3.5x10^{-13}$	$0.4x10^{-13}$
+3Si+3Pt	$3.6x10^{-13}$	$0.7x10^{-13}$

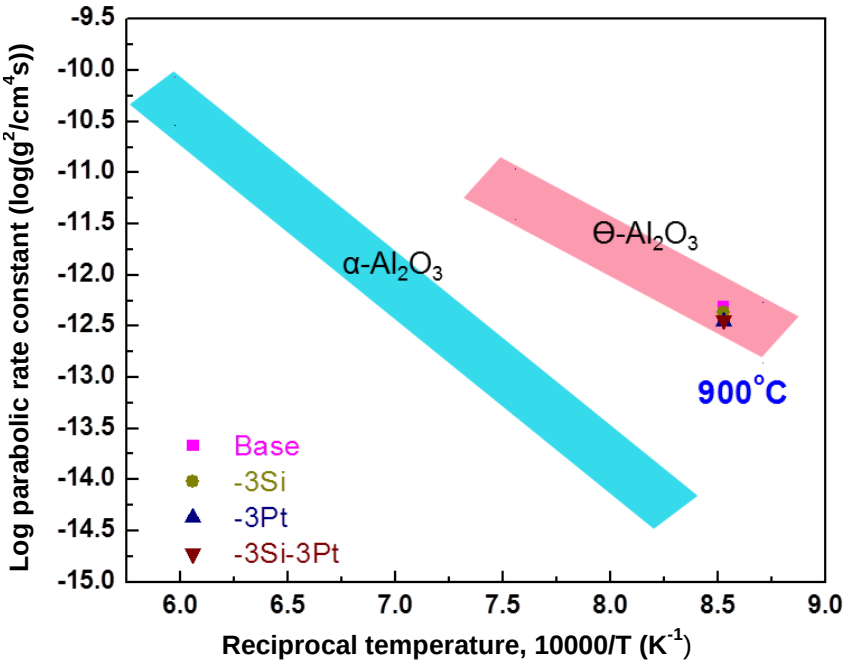

Figure 5.6 Comparison with reported kinetics [48, 61]

The scale phases formed on each oxidized alloy were confirmed using GIXRD. The diffraction patterns obtained on samples after 20 hours of oxidation are shown in Figure 5. 8. X-ray analysis identified the scale to be Al_2O_3, as indicated in Figure 5.7 which shows diffraction peaks from γ'-Ni_3Al (underlying substrate) and Al_2O_3 (scale). Some α-Al_2O_3 peaks can be seen, but the predominant peaks are from Θ-Al_2O_3, which is in agreement with the inference from the measured kinetics that the scale is primarily Θ-Al_2O_3. Figure 5.8 shows the surface morphology of samples after 20 hours oxidation. The whisker and needle-like morphology on the outer surface of the alumina scales are indicative of Θ-Al_2O_3, which has been reported to have a needle-like or blade-like surface morphology [48, 61]. In short, it was concluded that scale formed in air is primarily Θ-Al_2O_3.

In Figure 5.8, it is also observed that some NiO nodules were observed on the base alloy, and less NiO nodules formed on the Base+3Pt alloy and almost no NiO formed on the Si containing alloys. The presence of Si may inhibit NiO formation and this will be discussed in detail in Section 5.1.3.2. A larger amount of NiO nodule would contribute to a slightly larger weight gain, therefore, the Base alloy showed slightly higher weight-gain kinetics as shown in Figure 5.4.

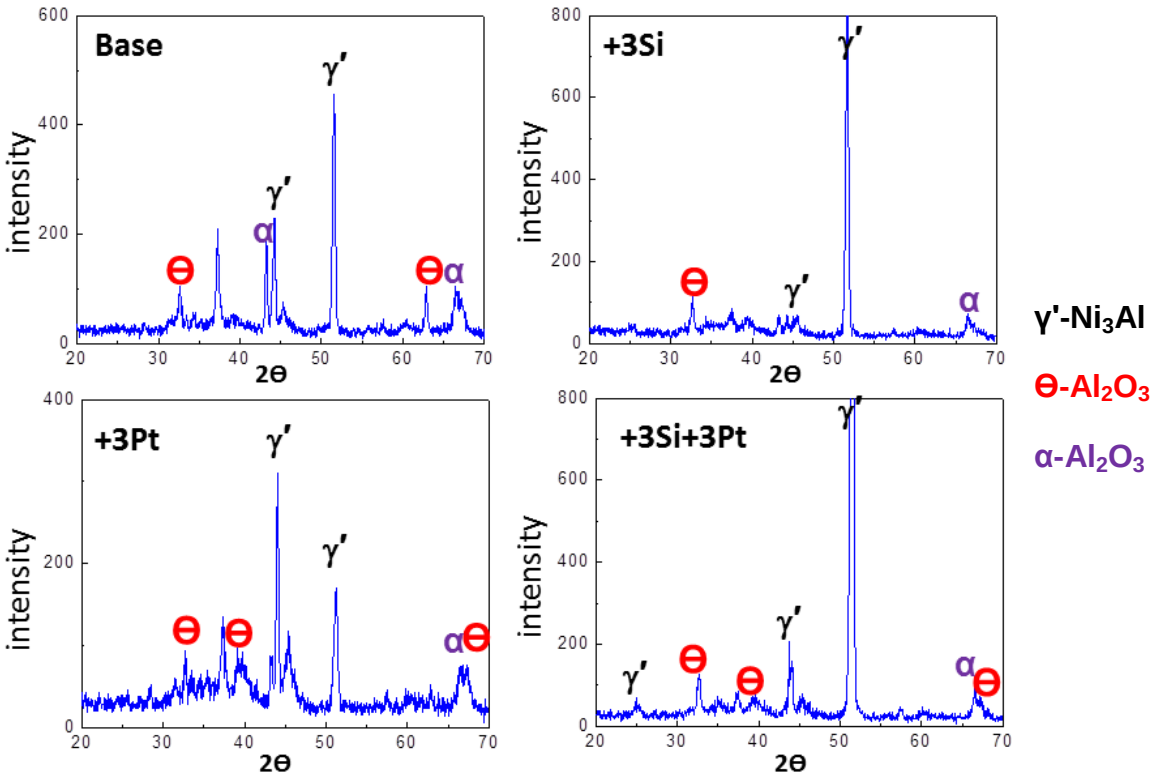

Figure 5.7 Glancing angle X-ray analyses of Ni-20Al-5Cr-(0,3)Pt-(0,3)Si-0.1Hf-0.05Y Alloys after 20 hours of oxidation at 900°C in air

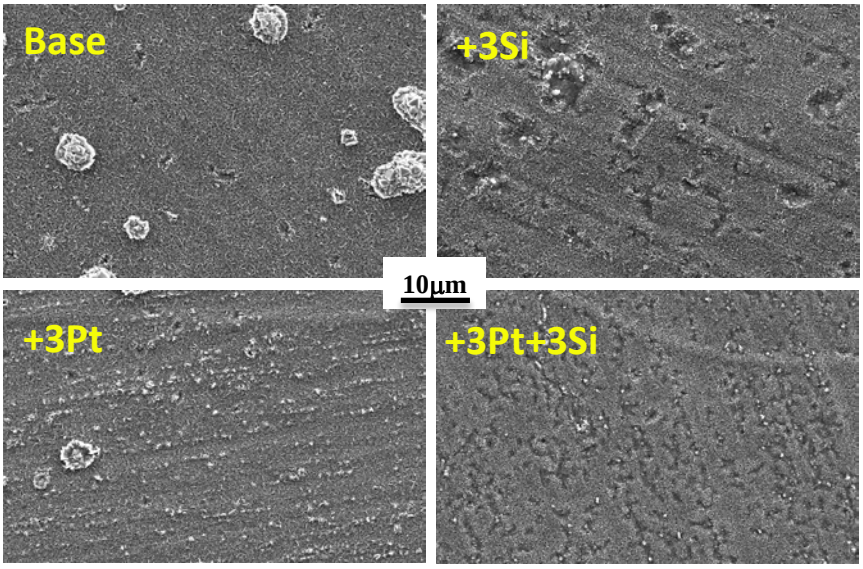

Figure 5.8 The surface morphology of Ni5Cr20Al0.1Hf0.05Y-xSi-xPt after 20 hours oxidation in air

Figure 5.9 shows cross-sectional images of samples after 20 hours of oxidation in air. It is seen that the thickness of oxide scale formed on the different alloys are similar, which is consistent with what was indicated by the weight change. Non-planar oxide/mounting material interfaces were observed, in agreement with theta alumina formation, which is typically needle-like [48, 73]. Underneath the oxide scale, a depletion zone was observed and EDS identified this zone to be γ-Ni. This depletion zone was formed due to the consumption of Al to form external alumina. It was noticed that the Si modified alloys formed thinner subsurface γ zone than in the Si-free alloys. A quantitative analysis of this will be given in section 5.1.3.2. The γ-Ni/γ′-Ni_3Al boundaries were flat, except in the Pt-containing alloys and a relative discussion with this is also included in section 5.1.3.2.

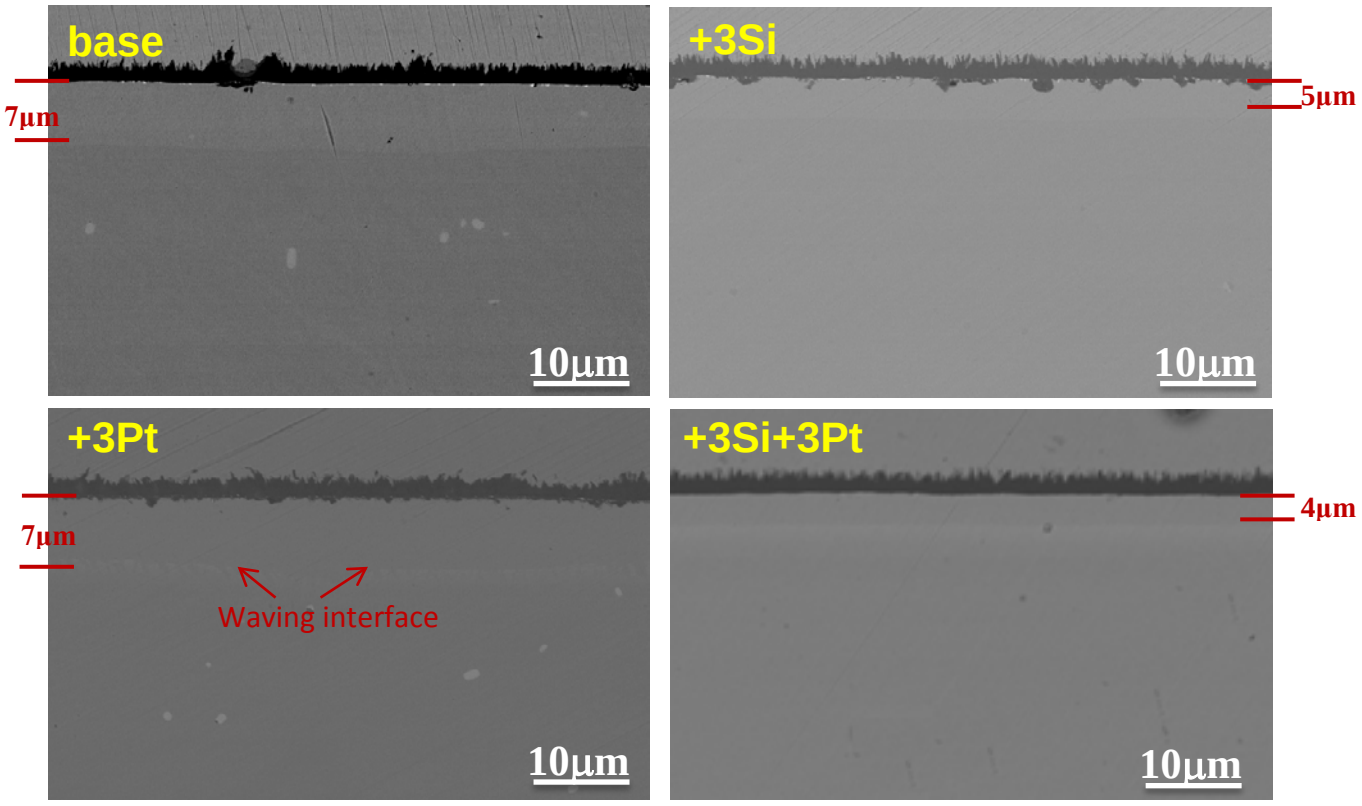

Figure 5.9 The cross-section image of Ni5Cr20Al0.1Hf0.05Y-xSi-xPt after 100 hours oxidation in air

5.1.2.3 900°C hot corrosion in air

Figure 5.10 shows the weight gain as a function of time during type I hot corrosion at 900°C. It is seen that the base alloy showed a linear and very rapid mass-gain increase. There is no indication of an incubation stage. Base+3Si and Base+3Si+3Pt alloys showed high weight gain (~4.5mg/cm^2) after 20 hours of exposure, but the weight gain was maintained to be at a similar level for a very long time until the Base+3Si alloy showed a jump in weight gain after 660 hours of exposure. A significant weight gain increase was not observed for the Base+3Si+3Pt alloy after 1220 hours of testing. The slight weight gain decrease of the Base+3Si+3Pt alloy at around 620 hours and 1200 hours in Figure 5.10 was due to oxide

spallation. Si modified alloys show an improved resistance to type I hot corrosion and the co-addition of Pt and Si extended the incubation time to more than 1200 hours under testing conditions. The addition of Si is obviously beneficial to type I hot corrosion.

The Base+3Pt alloy seems to be most resistant to Type I hot corrosion as it is observed in Figure 5.10 that the Base+3Pt alloy underwent the lowest weight gain (<2mg/cm^2) at the beginning and the mass gain increased very slowly after 1200 hours of exposure and was still in the incubation stage after 1260 hours of testing. However, the performance of this alloy was not stable. As shown in Figure 5.11， six samples of Base+3Pt alloy were tested and the incubation stage for these samples can last as short as 40 hours or longer than 1260 hours. This huge variation in sample performance will be discussed in section 5.1.3.3.

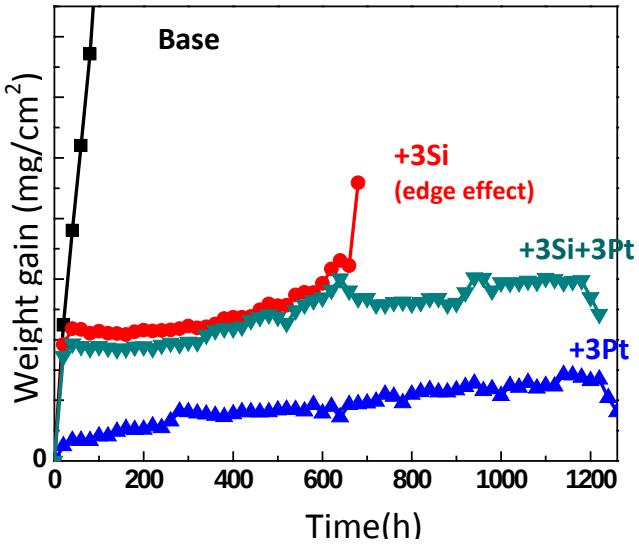

Figure 5.10 Type I hot corrosion of Ni5Cr20Al0.1Hf0.05Y-xSi-xPt alloys at 900°C in air

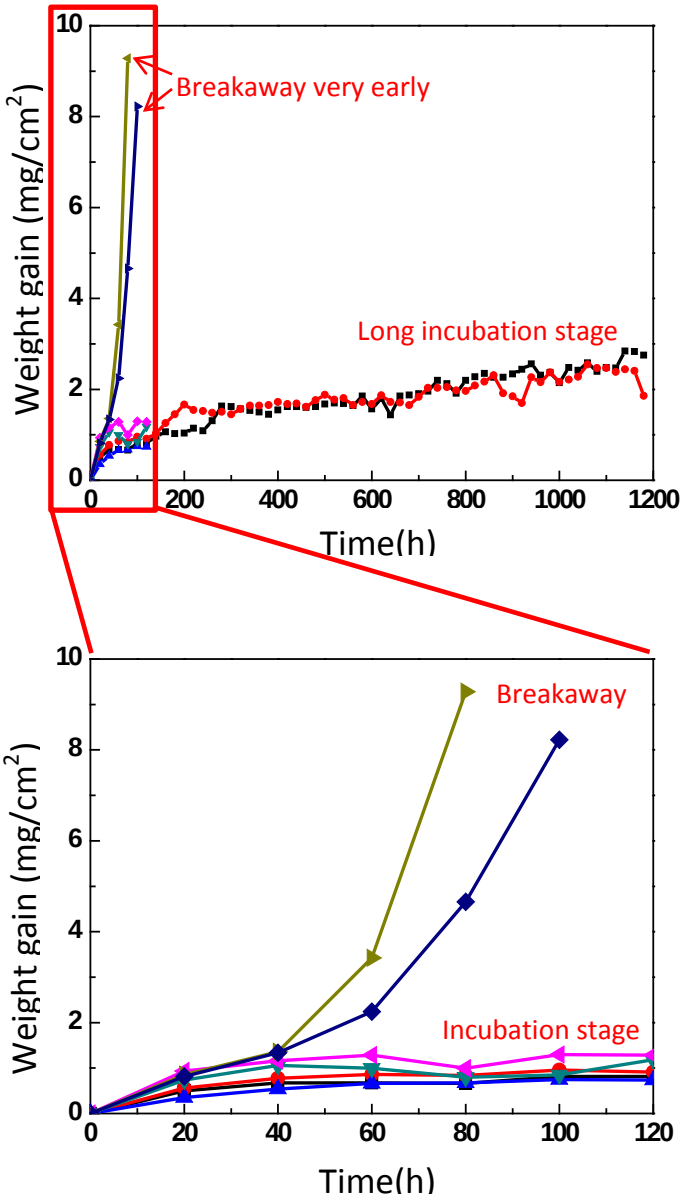

Figure 5.11 Type I hot corrosion of Base-3Pt alloys at 900°C

Characterization of hot corrosion behavior

To further understand the effects of Pt, Si or Pt+Si on type I hot corrosion resistance, characterizations were conducted at the early, later, and breakaway stages of hot corrosion. Each of the stages revealed a difference in the scales formed on each alloy: information on the early

stage illustrates oxide-scale establishment; while cross-sections at the later stage provide insights on the maintenance of the oxide scale. The breakaway stage provides insight on re-healing capabilities of the oxide scale.

(a) Early-stage incubation: *oxide establishment*

Figure 5.12 shows the surface morphologies of the oxide scale formed on the four model alloys after 20 hours exposure under a Na_2SO_4 deposit in air. Four alloys formed different surface oxides, EDS identified that $NiAl_2O_4$ formed on the Base and Base+3Si alloys, faceted NiO formed on the Base+3Si+3Pt and Al_2O_3 formed on Base+3Pt alloy.

Figure 5.13 shows a cross-sectional image of the base alloy after 20 hours of exposure in air with an Na_2SO_4 deposit. The corrosion attack is not uniform and up to ~90μm of corrosion product formed with the majority of the product being $NiAl_2O_4$, as determined by EDS analysis. Cracks were formed within the product. A 20-50μm depletion zone with internal precipitates was formed present beneath the thick external product of oxides. Based on EDS analysis, the internal precipitates are Cr_3S_4. The Al and Cr depletion in this zone was such that Al_2O_3-scale formation was not kinetically possible. Specifically, the Al content was 7at. % and no Cr was detected, which on an oxide map corresponds to NiO forming region [45].

Figure 5.14 shows a cross-sectional image of the base+3Si alloy after 20 hours of exposure in air with an Na_2SO_4 deposit. Around 35μm of the corrosion product formed, with porous Al_2O_3 and NiO on the surface, $NiAl_2O_4$ or mixture of NiO and Al_2O_3 in the middle, and a continuous Al_2O_3 scale underneath. Deeper in, internal Cr_3S_4 precipitates formed in a 10μm thick subsurface zone.

Figure 5.15 shows a cross-sectional image of the base+3Si+3Pt alloy after 20 hours of exposure in air with an Na_2SO_4 deposit. A non-uniform corrosion product formed. Figure 5.15 shows a region of maximum attack. Nickel oxide is present the surface, Ni (Al, $Cr)_2O_4$ in the middle, and an apparently continuous $(Al,Cr)_2O_3$ layer is underneath. Internal Cr_3S_4 precipitates are present in the subsurface zone. It is worthwhile to mention that the inner $(Al,Cr)_2O_3$ layer is continuous and considered protective.

Different from the above alloys, the base+3Pt alloy formed a continuous and protective alumina scale under the same test conditions. As shown in Figure 5.16, the scale was dense and thin and the outer surface is relatively smooth. No internal sulfide was observed.

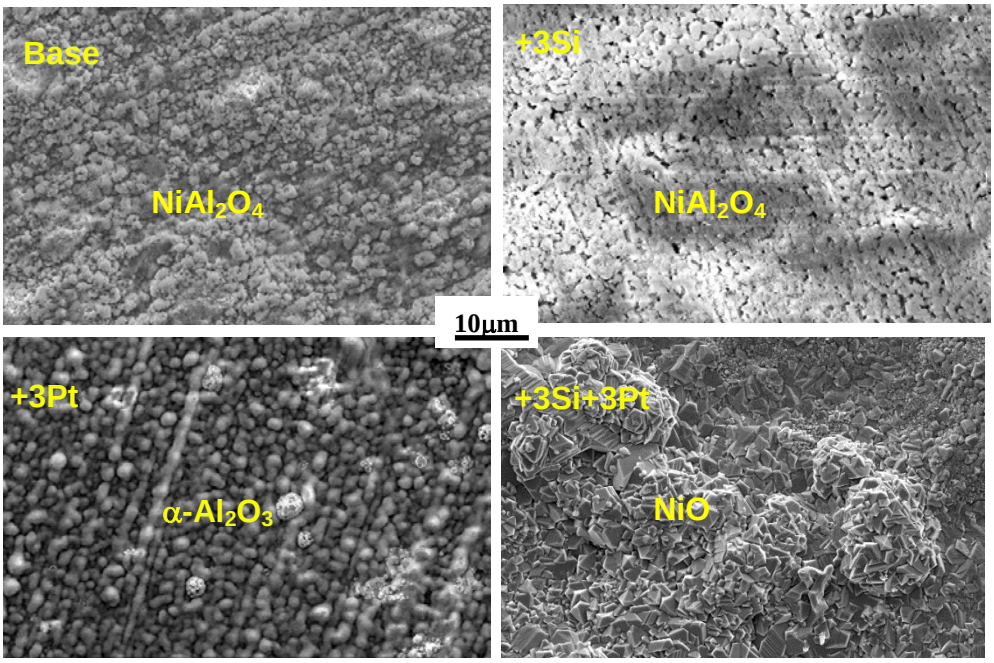

Figure 5.12 Surface morphologies of 20 hours of Type I (900°C) hot corrosion of Ni5Cr20Al0.1Hf0.05Y-xSi-xPt alloys in air

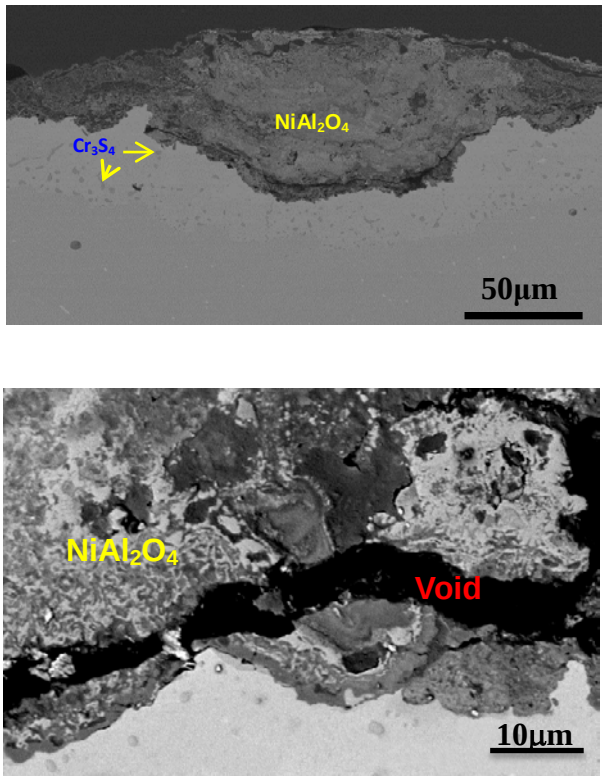

Figure 5.13 Cross-sectional images of 20 hours of Type I (900°C) hot corrosion of Base alloy in air

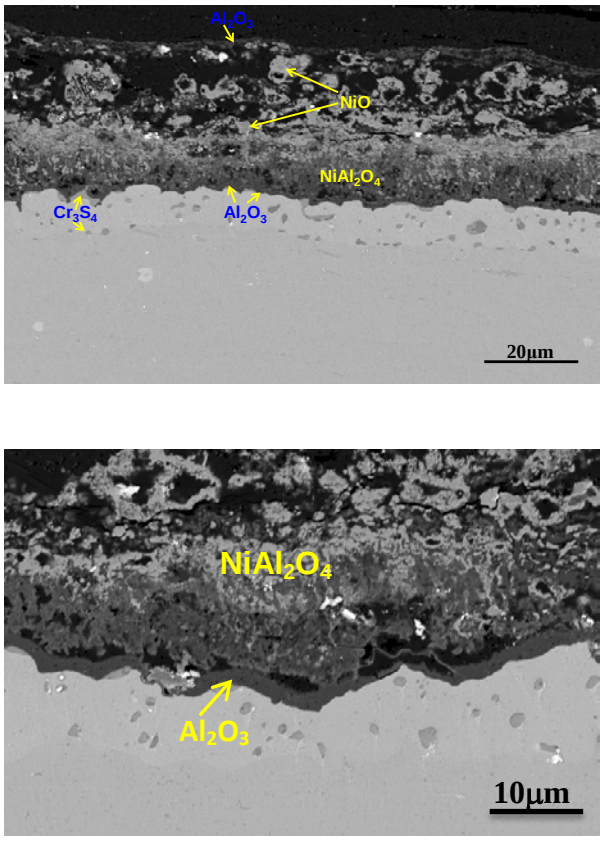

Figure 5.14 Cross-sectional images of 20 hours of Type I (900°C) hot corrosion of Base+3Si alloy in air

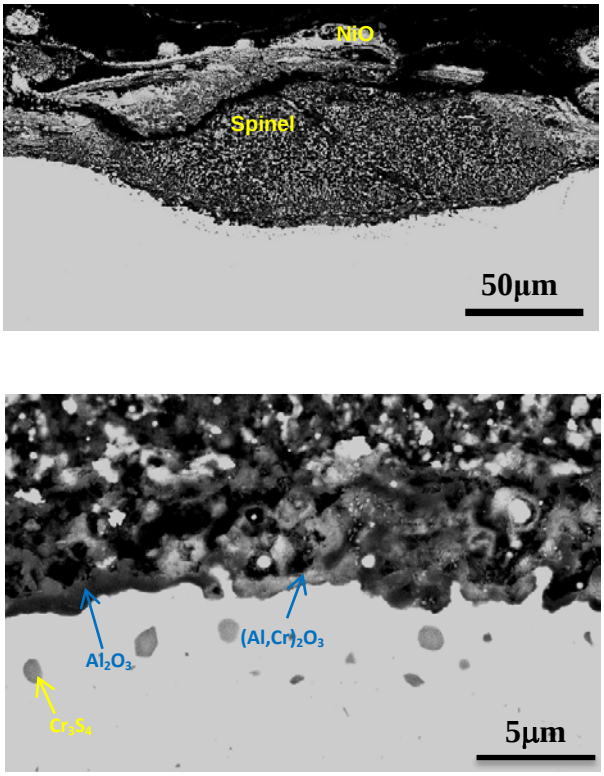

Figure 5.15 Cross-sectional images of 20 hours of Type I (900°C) hot corrosion of Base+3Pt+3Si alloy in air

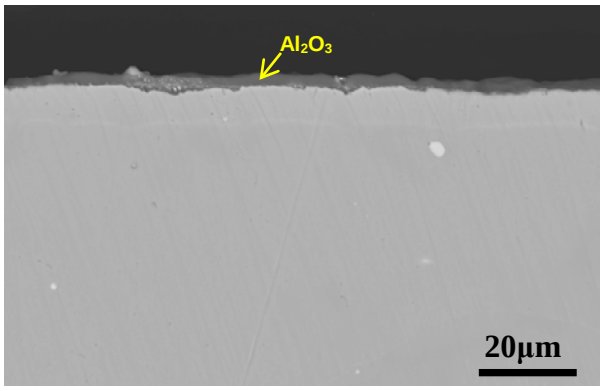

Figure 5.16 Cross-sectional images of 20 hours of Type I (900°C) hot corrosion of Base+3Pt alloy in air

The phase constitution of the alumina scale formed on the Base+3Pt alloy was determined by XRD and the X-ray diffraction pattern obtained is shown in Figure 5.17. The scale was identified to be α-Al_2O_3, as indicated in Figure 5.17, which shows diffraction peaks from γ'-Ni_3Al (underlying substrate) and α-Al_2O_3 (scale). This result was unexpected as the same alloy when oxidized in air without a Na_2SO_4 deposit, forms a continuous primarily θ-Al_2O_3 as determined by both GIXRD identification (Figure 5.7) and kinetic assessment (Figure 5.6). This dramatic differences in Al_2O_3 structure formed indicates that salt can affect the phase stabilities of alumina scale.

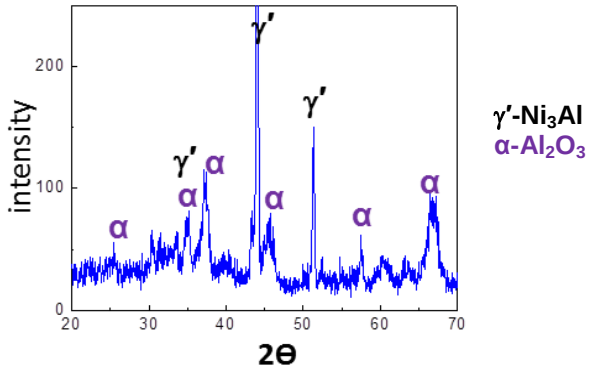

Figure 5.17 The X-ray analyses of base+3Pt alloy after 20 hours of oxidation at 900°C in air with the presence of a Na_2SO_4 deposit

The same result was found with the Ni-7.5Cr-20Al-3Si-3Pt-0.1Y-0.05Hf (at.%) alloy. This will be shown in the next two pages. Figure 5.18 shows the alloy's microstructure before testing. The phase constitution contains β-NiAl and γ′-Ni_3Al. The white precipitates in this alloy were found by EDS to be rich in Y.

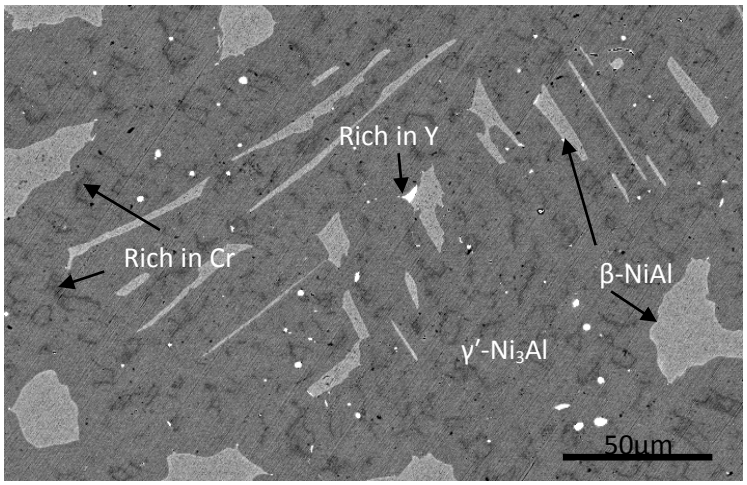

Figure 5.18 The microstructure of Ni-7.5Cr-20Al-3Si-3Pt-0.1Y-0.05Hf before testing

The evidence of salt affecting the phase stabilities of alumina scale on the Ni-7.5Cr-20Al-3Si-3Pt-0.1Y-0.05Hf alloy is provided here. This alloy was isothermally oxidized at 900°C for 20 hours and 100 hours in air. The weight gains as a function of exposure time are plotted in Figure 5.19. The weight gain obtained during the 20 hour test fits very well with the mass-gain results during the 100 hour test, indicating very good reproducibility. Using these measured kinetics, a fitting model [57, 114] was used to determine the growth rate constant for this alloy. The calculated instantaneous n-values and k_p values are plotted as function of time in Figure 5.20(a) and (b), respectively. It is seen that k_p began to be stable after a short period of time, indicate a rapid approach to a steady state. The k_p value stabilized at $3.7x10^{-13}g^2/cm^4s$ which is in good agreement with what has been reported for Θ-Al_2O_3-scale growth(i.e.,$2.2x10^{-13}g^2/cm^4s$[61]).

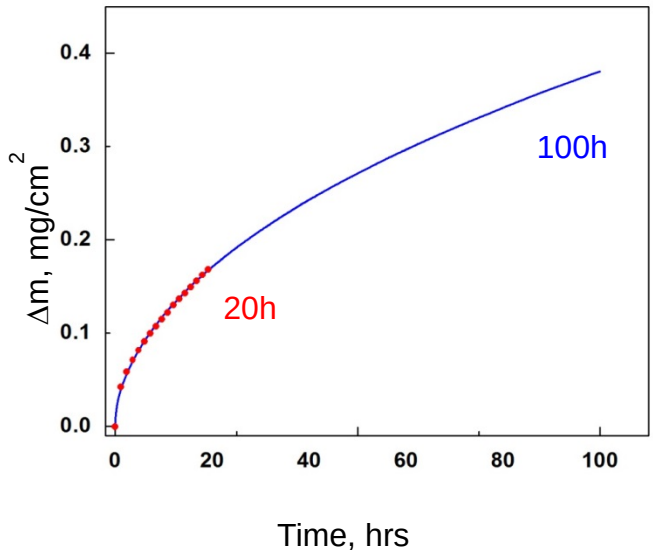

Figure 5.19 Ni-7.5Cr-20Al-3Si-3Pt-0.1Y-0.05Hf (at.%) isothermal oxidation at 900˚C in air for 100 hours and 20 hours

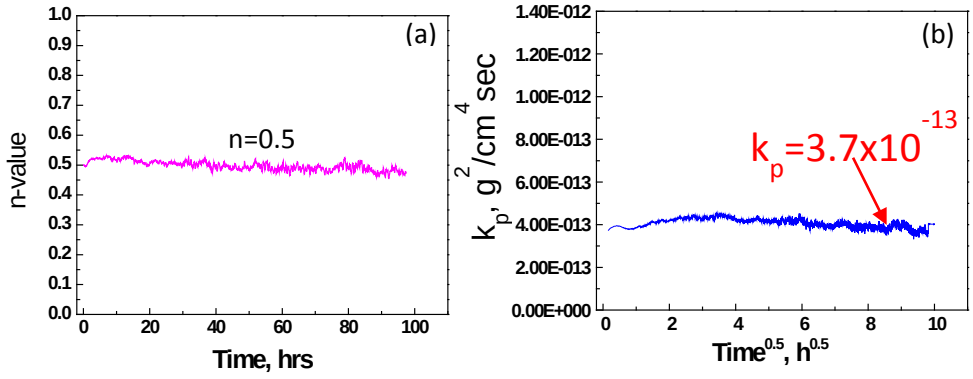

Figure 5.20 Kinetics analysis for the determination of k_p

X-ray diffraction was done on the sample after 100 hours of oxidation in air. The resulting spectrum is shown in Figure 5.21(a). Except for several peaks from the substrate (γ'-Ni_3Al), the rest of the peaks are from Θ-Al_2O_3. Thus, in agreement with the measured kinetics, the scale formed during air oxidation is inferred to be Θ-Al_2O_3.

When the same alloy was oxidized at 900°C for 20 hours under an Na_2SO_4 deposit, the oxide scale formed was α-Al_2O_3 as can be seen in Figure 5.21(b). Therefore, compared to the finding of Θ-Al_2O_3-dominant growth during oxidation in air without a salt deposit, the Na_2SO_4 deposit apparently promotes the α-Al_2O_3 establishment.

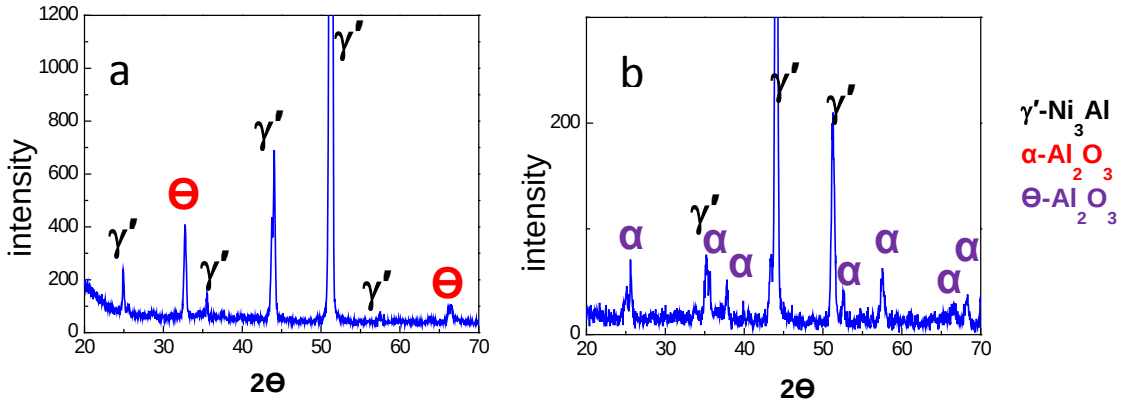

Figure 5.21 The X-ray analyses of Ni-7.5Cr-20Al-3Si-3Pt-0.1Y-0.05Hf (at.%) alloy after (a) 100 hour oxidation at 900°C in air and (b)200 hour oxidation at 900°C with the presence of Na_2SO_4 deposit

(b) Later-stage incubation: oxide maintenance

Figure 5.22 shows the surface morphology and a representative cross-sectional image of the Base+3Si alloy after 60 hours of exposure in air with an Na_2SO_4 deposit. The structure of the corrosion product is not much different from the 20 hour exposure of this alloy (Figure 5.14). It is comprised of porous Al_2O_3 and spinel in the outer layer (Figure 5.22c) and an apparently continuous Al_2O_3 inner layer (Figure 5.22b). Even though there is evidence of scale-fluxing, as can be seen by the existence of top porous oxides, the inner Al_2O_3 layer served to prevent rapid degradation of the alloy. For Base+3Si alloy, as shown in Figure 5.10, its mas-gain curve during hot corrosion remains almost flat between 20 and 500 hours. During experiments, limited oxide

scale spallation was observed. This suggests that the inner Al_2O_3 layer was maintained during this period and was protective.

The surface morphology and cross-sectional images of the Base+3Pt after 60 hours of exposure in air with an Na_2SO_4 deposit are shown in Figure 5.23. In certain regions, alloy substrate was exposed, indicating oxide spallation. During testing, spallation occurred when the Base+3Pt sample was taken out of the furnace for salt re-deposition. Based on the hot corrosion kinetics shown in Figure 5.10, this alloy can maintain a relative constant weight change for up to 1200 hours. Thus in this case, though scale spallation occurred, the alloy was able to sustain Al_2O_3-scale formation and hence maintain resistance to hot corrosion.

The surface morphology and cross-sectional images of the Base+3Pt+3Si alloy after 60 hours of exposure in air and with an Na_2SO_4 deposit are shown in Figure 5.24. EDS identified the corrosion products as an external NiO/spinel with internal Al_2O_3 scale.

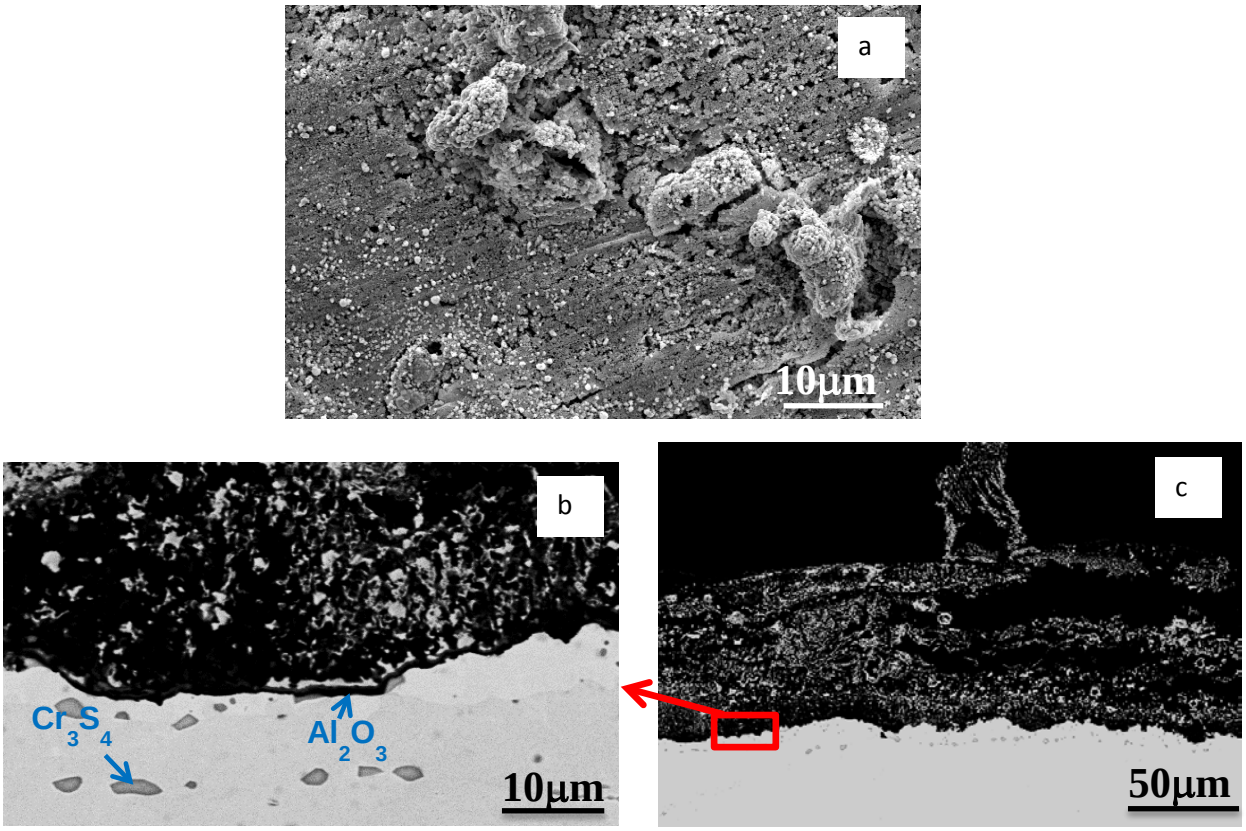

Figure 5.22 The surface morphology (a) and cross-sectional image (b, c) of Base+3Si alloy after 60 hours hot corrosion in air.

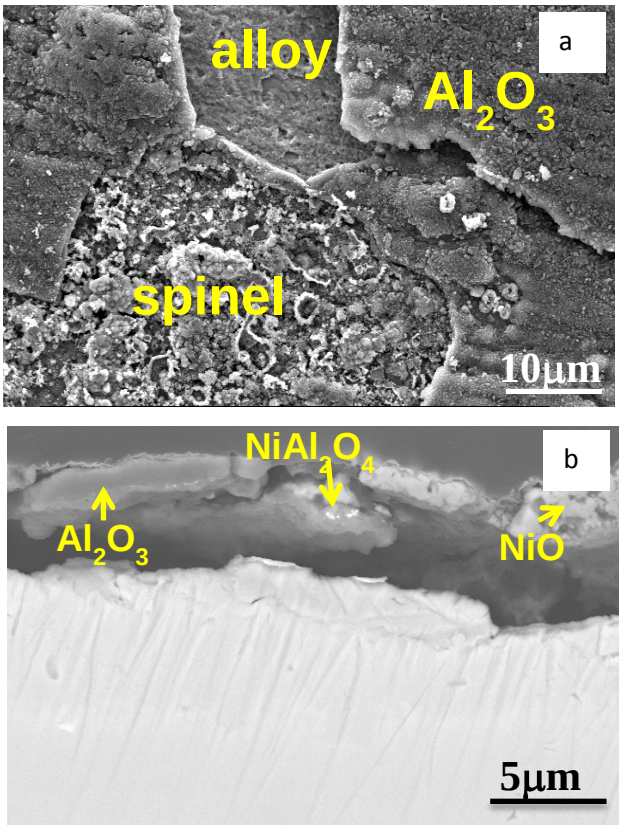

Figure 5.23 The surface morphology (a) and cross-section images (b) of the Base+3Pt alloy after 60 hour hot corrosion.

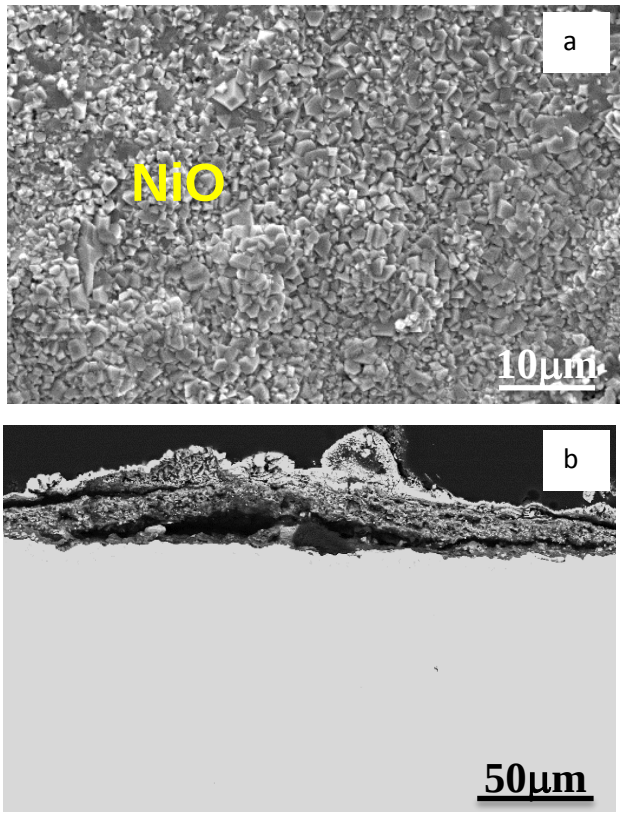

Figure 5.24 The surface morphology (a) and cross-section images (b) of the Base+3Pt+3Si alloy after 60 hour hot corrosion.

As shown in Figure 5.10, Base+3Pt and Base+3Pt+3Si were exposed under a Na_2SO_4 deposit in air for 1260 hours and 1220 hours, respectively and both alloys remained in the incubation stage of degradation. The resulting cross-sectional images of the samples after testing are shown in Figure 5.25. Both alloys formed thick oxide scales with a layered structure containing a mixture of Al_2O_3 and spinel. The layered structure is probably due to the oxide/metal separation induced by the temperature change when the sample was taken out of the furnace for salt re-deposition. A protective Al_2O_3 inner scale was maintained even after very long time exposure.

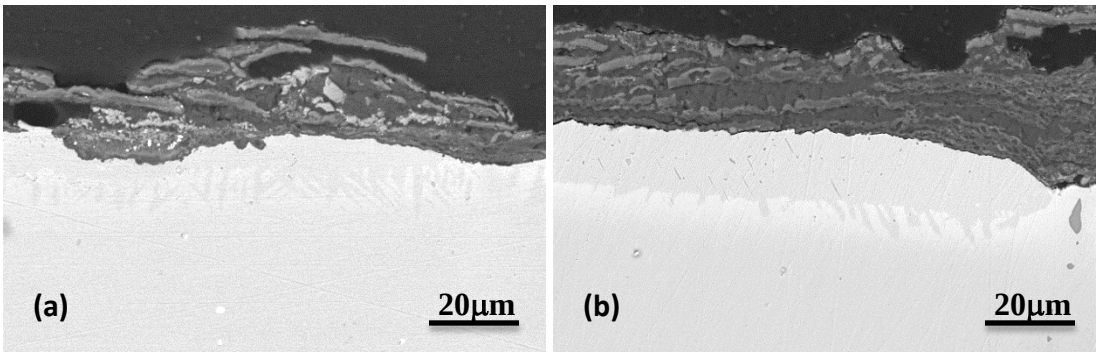

Figure 5.25 The cross-section images of (a) Base+3Pt 1260 hour and (b) Base+3Pt+3Si 1220 hour exposure to hot corrosion in air

(a) Breakaway: *oxide failure*

Figure 5.26 shows the surface morphology and cross-section images of Base+3Si alloy after 680 hours of hot corrosion in air. From the corrosion kinetics (Figure 5.10), it is seen that this alloy just started to break away from the incubation stage. The breakaway was started from the edge as shown in Figure 5.26(a). A cross-sectional image from the edge where local breakaway occurred showed oxide-scale delamination and a protective alumina scale was not present. Based on EDS analysis, the internal precipitates are Cr_3S_4 and Ni_xS_y. The Al and Cr depletion in this zone was such that Al_2O_3-scale formation was not kinetically possible. Specifically, Cr was not detected and the Al was at 6% which on an oxide map corresponds to NiO forming region [49, 54]. In regions where break away did not occur, it is seen that a continuous inner alumina is maintained.

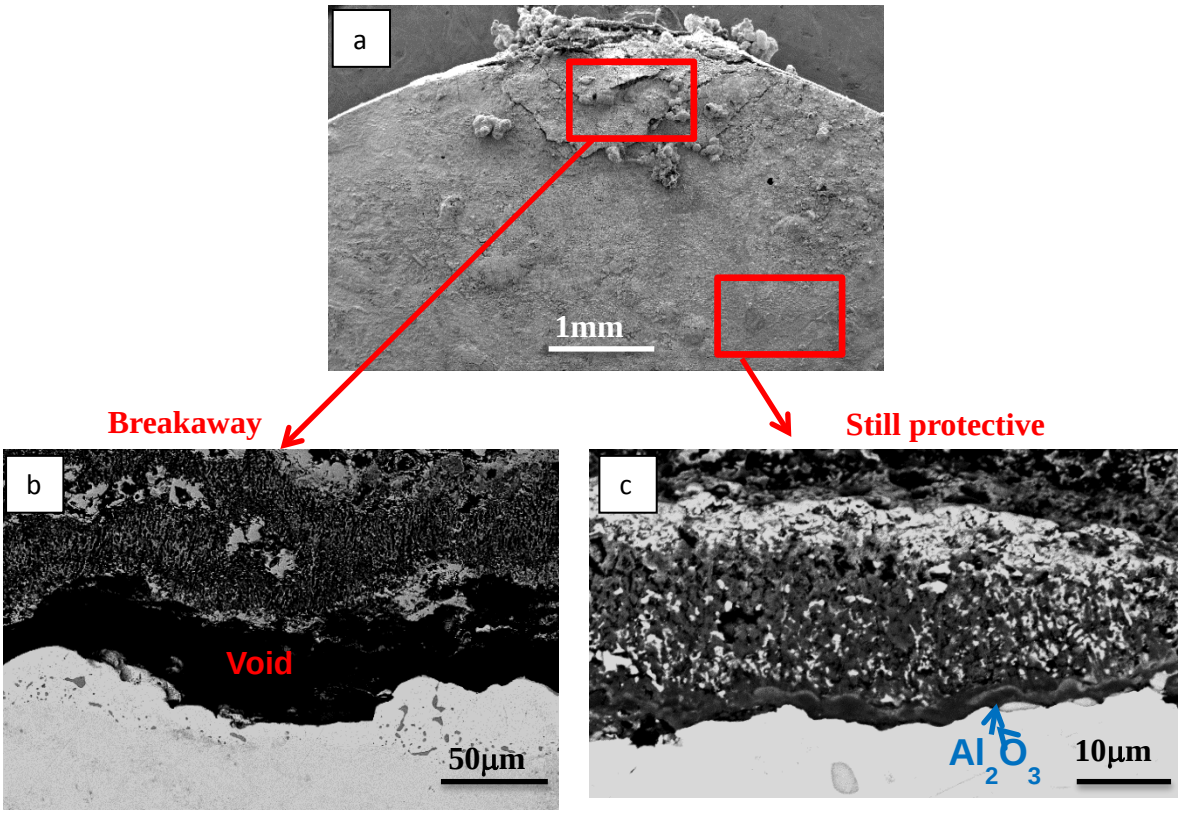

Figure 5.26 The Base+ 3Si alloy after 680 hours hot corrosion in air (at the breakaway stage)

Figure 5.26 shows a cross-sectional image of the Base+3Pt alloy after 80 hours of hot corrosion in air. The kinetic behavior of this sample (shown by the olive green curve in Figure 5.11) was such that breakaway occurred at around 60 hours. The breakaway of this sample initiated very locally, based on surface observation during experiments. After that, the alloy entered the propagation stage. The sample was prepared for SEM cross-section observation after 80 hours of testing, so as to assess the alloy performation during the breakaway stage. It is seen in Figure 5.27 that the alloy developed a deep (up to 200µm) internal oxidation zone, below which a band of Cr_2S_3 precipitates had formed. The internal oxides formed as a network and the appearance of the corrosion product indicates that the degradation mechanism is sulfidation-

oxidation[115, 116] with salt being the source of sulfur. A more detailed discussion about sulfidation-oxidation degradation will be provided in section 5.4

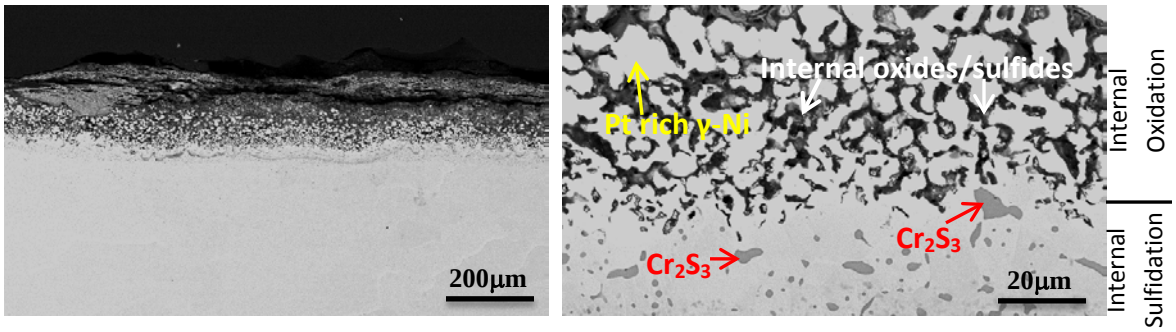

Figure 5.27 Base+3Pt alloy after 80 hours of hot corrosion in air and the alloy was at the breakaway stage.

In this section, hot corrosion kinetics and the microstructure of corrosion product at the early, later, and breakaway stages of hot corrosion were presented. Several key observations have been made: (1) different features of the corrosion products were formed during different stages of hot corrosion; (2) Si and Pt are beneficial for type I hot corrosion, with the role of Si being more obvious based on the hot corrosion kinetics shown in Figure 5.10 and Figure 5.11; (3) Na_2SO_4 deposit can affect phase stabilities of alumina scale as shown by the oxidation of Base+3Pt and Ni-7.5Cr-20Al-3Si-3Pt-0.1Y-0.05Hf in air and O_2+1%SO_2; These results will be discussed sequentially in section 5.1.3.3, 5.1.3.4 and 5.1.3.5.

5.1.2.4 900°C hot corrosion of Pre-oxidized Ni-30Al-20Pt in air

Both Θ-Al_2O_3 and α-Al_2O_3 can form at 900°C, therefore, it would be meaningful to test the effect of initial crystal structure of alumina on the type I hot corrosion. For alloys to resist degradation caused by hot corrosion, a protective and tenacious oxide scale is requisite. The alumina structure affecting hot corrosion performance has not been reported in the literature. In

this study, pre-oxidation and hot corrosion experiments were designed. An Ni-30Al-20Pt (at.%) alloy was selected, because this forms an exclusive alumina scale. Coupons of this alloy were pre-oxidized to form exclusive Θ- or α-Al_2O_3 scales of similar thickness (~0.5 μm). The Θ-Al_2O_3 scale was formed by pre-oxidizing at 900^{o}C for 20 hours, while the α-Al_2O_3 scales was formed by pre-oxidizing at 1150^{o}C for 3 hours. The surface morphology of the different pre-oxidized samples is shown in Figure 5.28, Typical Θ-Al_2O_3[48, 73] and α-Al_2O_3[48] morphologies were obtained. Phases were identified by X-ray diffraction.

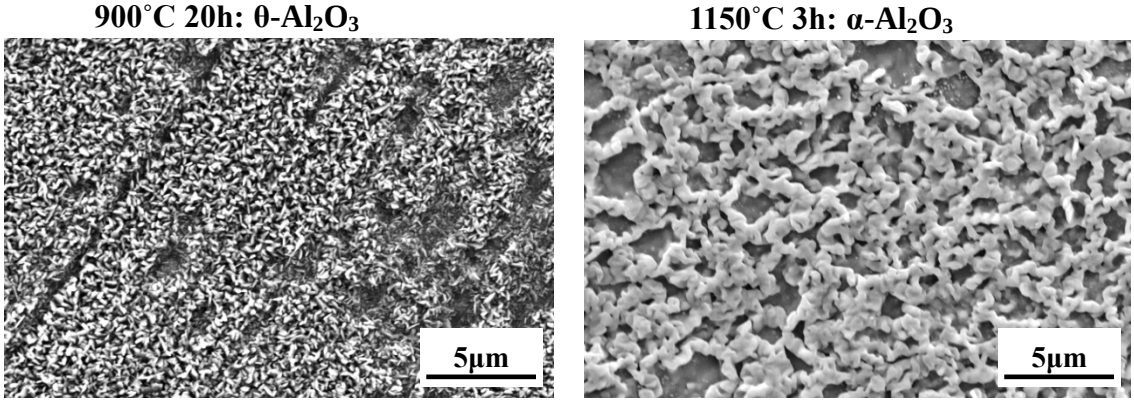

Figure 5.28 Surface morphology of Ni-30Al-20Pt Alloy after (a) 20 hours of oxidation at 900ºC (b) 3 hours of oxidation at 1150°C in air

900^{o}C type I hot corrosion was conducted for the above pre-oxidized samples. For these hot-corrosion tests, 2mg/cm^2 Na_2SO_4 was deposited initially and then every 20 hours. The weight change was measured every 20 hours and the results are shown in Figure 5.29. Except for minor differences at around 20 h, the two samples showed similar weight gain kinetics. Thus, crystal structure of alumina has minimal or no influence on the alloy's overall resistance to type I (900°C) hot corrosion

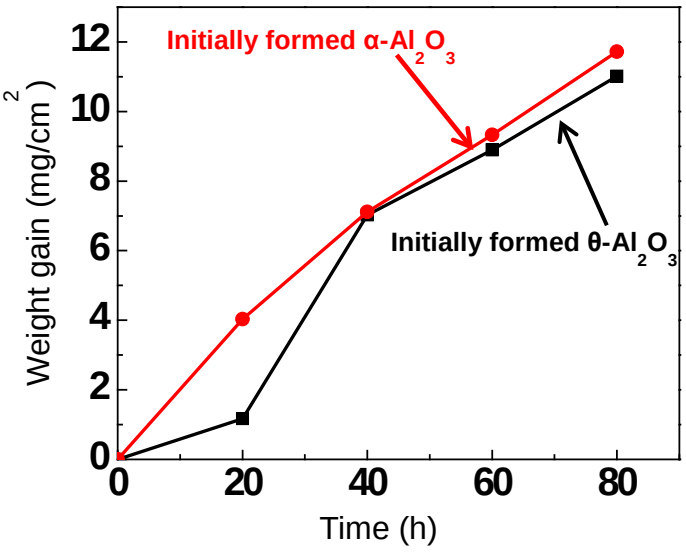

Figure 5.29 the weight gain of pre-oxidized Ni30Al20Pt during Type I (900°C) hot corrosion

5.1.3 Discussion

5.1.3.1 The reproducibility of the Base+3Pt alloy

To understand the unstable performance of the Base+3Pt alloy during hot corrosion as shown in Figure 5.11, tests of a similar base alloy (Ni-20Al-5Cr-0.1Hf, at.%) with different concentrations of Pt were done at 900°C in air with a Na_2SO_4 deposit[83]. The measured kinetics is shown in Figure 5.30. It is seen that the Base and Base+2.5Pt alloy underwent break-away right at the beginning, while the Base+5Pt and Base+10Pt remained protective after 500 hours of exposure.

Thus, 3at.% of Pt in this alloy is apparently too low a content for a reliable performance of this base system. Tang[83] reported that Pt, Al and Cr are all beneficial to type I hot corrosion. In the composition range for Ni-(18-22)Al-(5-10)Cr-(0-10)Pt at.%, the role of Pt is most significant, but Pt content must be larger than or equal to (3-5) at.% for reliable beneficial effects. This is shown in Figure 5.31, which plots of the length of the incubation stage for Ni-20Al-0.1Hf based alloys with different Cr and Pt additions. It is seen that a minor modification in Cr and Pt

contents on certain borderline alloy composition can lead to a huge change in the alloy's performance during hot corrosion. As marked by the red arrow, 3at.% Pt addition lays between alloys with extremely short incubation stage and alloys with very long incubation stages.

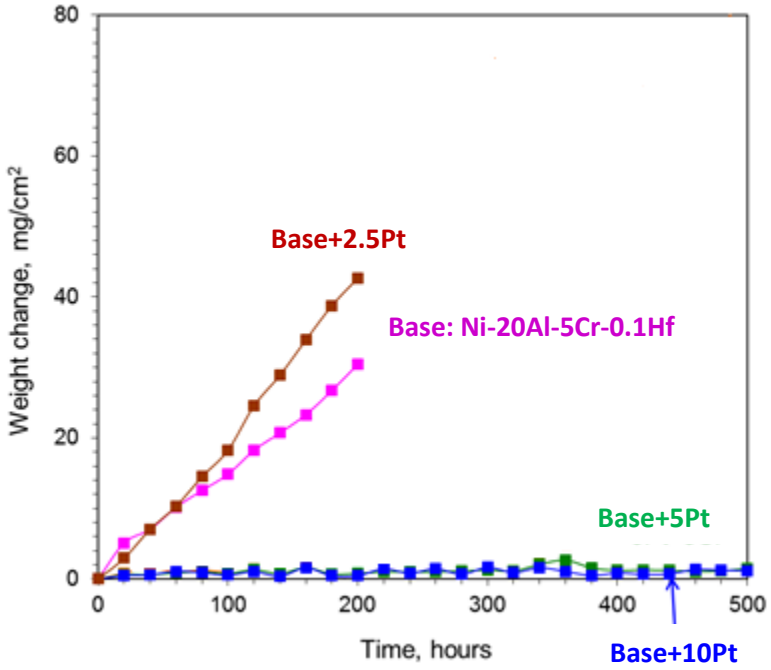

Figure 5.30 Type I hot corrosion kinetics of several γ-Ni +γ′-Ni_3Al alloy with different Pt concentration[83]

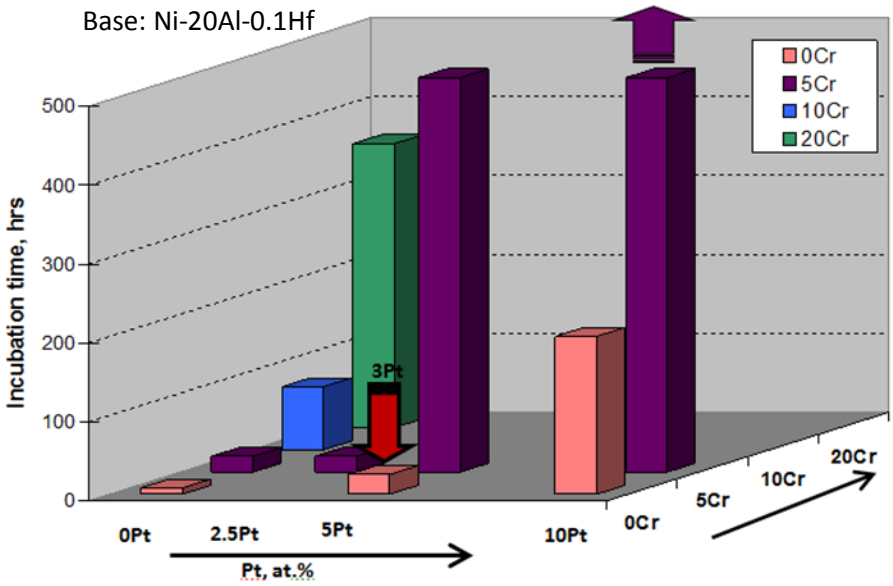

Figure 5.31 The effects of Pt and Cr addition on the duration of incubation stage during type I hot corrosion at 900^{o}C in air [83]

For type I hot corrosion, the initiation of the propagation stage can start locally for some alloy compositions, particularly for those that are borderline. Two local breakaway examples are presented in Figure 5.32 and Figure 5.33. Severe materials degradation occurred in certain regions, while in other regions, not much attack was observed. This result indicates a local susceptibility to corrosion attack can cause severe and rapid degradation of the whole sample.

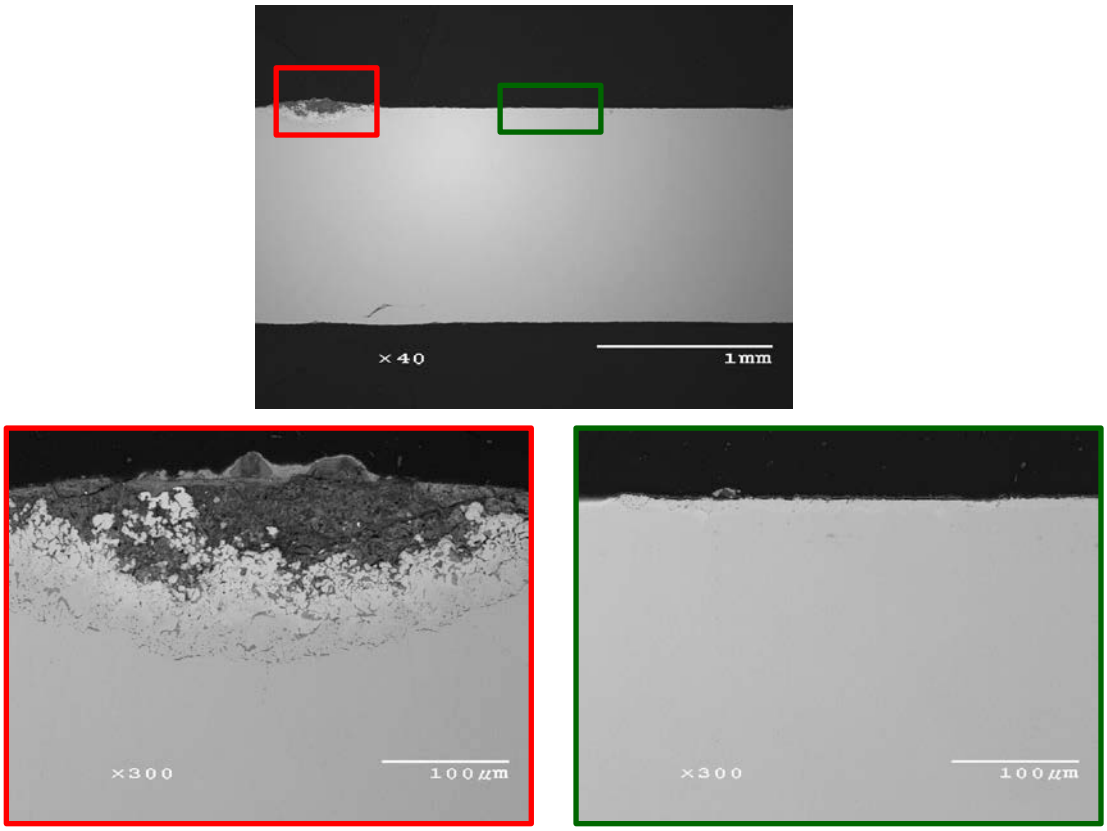

Figure 5.32 Ni-20Al-5Cr-2.5Pt-0.1Hf (at.%) after 20 hours of hot corrosion test at 900°C and severe attack initiated very locally [83]

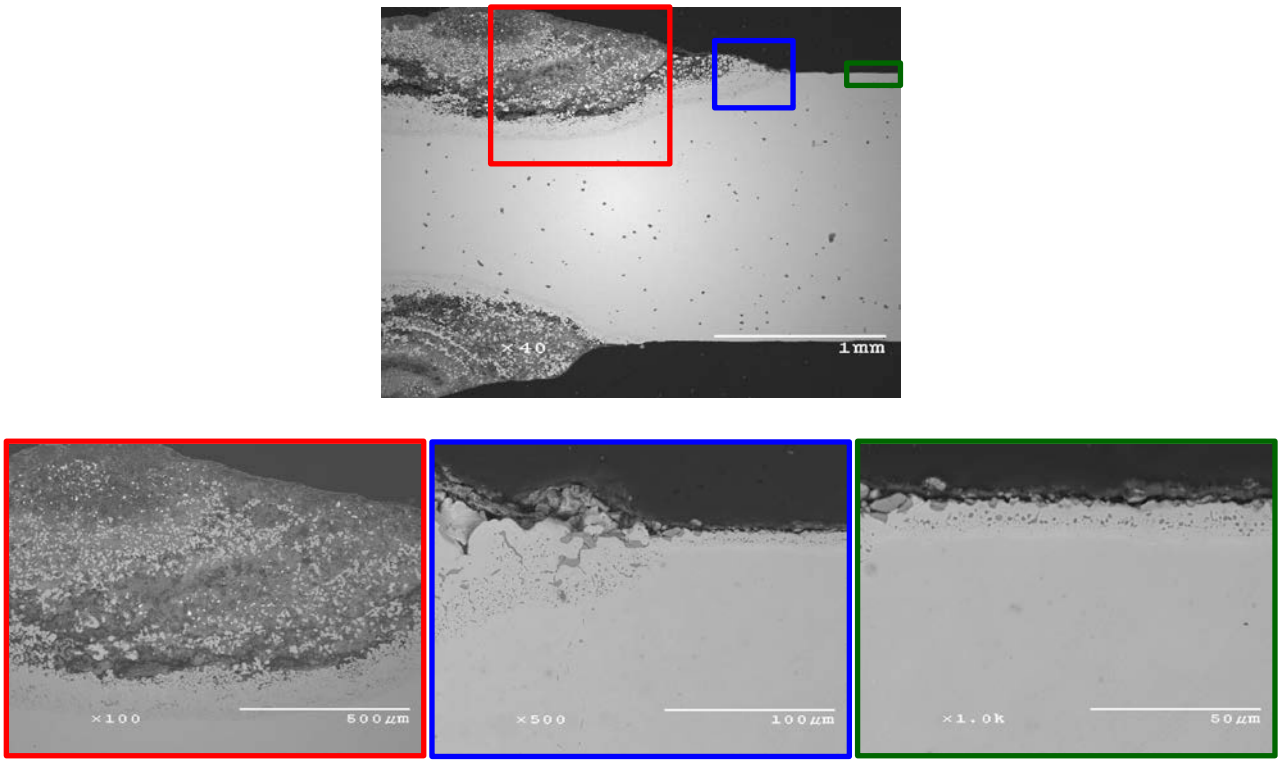

Figure 5.33 Localized hot corrosion attack on Ni-18Al-10Cr-3Pt-0.1Hf. This alloy showed accelerated attack after 200h, while the images shown below were taken after 300 hours[83]. The hot corrosion test was done at 900°C in air

5.1.3.2 The role of Si and Pt during air oxidation

During oxidation in air without a Na_2SO_4 deposit, NiO formation is less favored when Si was added to the γ′-Ni_3Al based alloys. As shown in Figure 5.8, the Base alloy formed a certain amount of NiO nodules while the oxide formed on the Base+3Si alloy is almost free of NiO. A similar phenomenon was observed when oxidizing these two alloys at 700°C for 100 hours. As shown in Figure 5.34, a large number of NiO nodules were formed on the Base alloy whereas no NiO was detected on the Base+3Si alloy. This appears to be reflected by the oxidation kinetics of these two alloys measured in air without a deposit at 900°C. As shown in Figure 5.35, the Base alloy is observed to undergo a period of accelerated oxidation during the first ~2.5 hours of

exposure. This likely correlates with the formation of transient Ni-rich oxides, prior to the establishment of a complete alumina layer. The plot is initially curved, which is indicative of transient oxidation, and then, later turns into a straight line once a complete Al_2O_3 scale is established. For the Base+3Si alloy, almost no transient oxidation is observed; the plot becomes linear at the onset of exposure, indicative of a rapid establishment of Al_2O_3 scale. Therefore, Si appears to hinder the transient oxidation and to facilitate the establishment of an exclusive alumina scale.

The observation of silicon hindering the transient oxidation of nickel may be due to silicon affecting the native oxide layer which is present on the alloy surface at room temperature. This possible effect of Si on the native oxide layer is supported indirectly by an investigation of the early-stage oxidation of a commercially available Ni-20Cr-1.29Si-0.2Al alloy[117]. The oxide layer present on this alloy at room temperature and also what develops during exposure in air at 950ºC for 1-5 minutes were characterized by TEM[117]. At room temperature, the native oxide is comprised of several nanometers of aluminum and silicon oxide. Silicon was identified to be enriched at the oxide/alloy interface. It continues to be enriched at the oxide/alloy interface at 950ºC during the short time of exposures. These results indicate the active nature of silicon and its tendency to enrich in the native oxide layer, which is that starting point for the scale evolution. Started differently, the native oxide layer is able to affect the corrosion product formed at high temperature. By altering the chemistry of the native oxide layer, through the addition of Si to the alloy, it is quite possible for the scale evolution during heating to also be altered in such a way that the extent of the transient oxidation of Ni is significantly reduced.

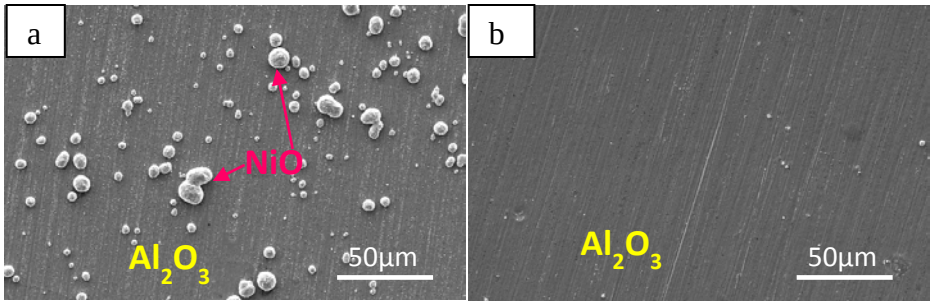

Figure 5.34 Base (a) and Base+3Si (b) alloys after 100 hours of oxidation at 700°C

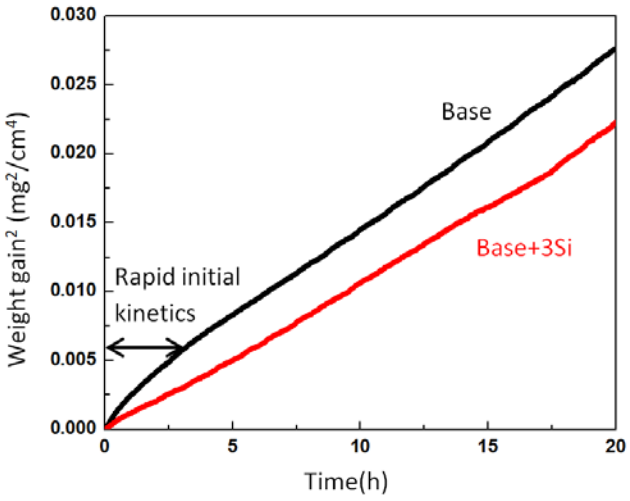

Figure 5.35 The weight gain squared as a function of time during oxidation at 900°C

The presence of Si does appear to have an effect on aluminum diffusion within the substrate, and it does appear to affect phase composition in local equilibrium. As was shown in Figure 5.9, Si-modified alloys exhibited thinner depletion zone thicknesses (smaller X_d) even though the Al consumption, J_{Al}, is similar when comparing to the Si-free alloys based on the similar oxidation kinetics. This is inferred to be related to the Al concentration within the depletion being different. Elemental line scans through depletion zones (γ-Ni) and substrates (γ′-Ni_3Al) were conducted on the Base and Base+3Si alloys using EDS. The results are shown in Figure 5.35. It is observed that the Al concentration within the γ-Ni and γ′-Ni_3Al is flat for both

alloys. The average Al concentration in the γ-Ni depletion zone in the Base+3Si alloy was ~3 at.% lower than that of the Base alloy, with similar Al consumption as indicated by similar alumina scale thicknesses. Therefore, mass balance dictates that a thinner depletion zone formed in the Base+3Si alloy.

As stated above, the results in Figure 5.36 show a flat Al diffusion profile in the γ-Ni and γ′-Ni_3Al zones. A schematic illustration of the flux of Al through a flat diffusion profile is shown in Figure 5.37. The two alloys were very close to the border of γ′-Ni_3Al phase field, as shown in Figure 5.1. Therefore, for simplification, the aluminum concentration within γ′-Ni_3Al phase is considered to be bulk alloy composition. The aluminum concentration within γ′-Ni_3Al phase is the EDS measured Al concentration. Using the measured Ni_{Al}^{γ} values, the depletion zone thickness (Xd) can be estimated in the following manner.

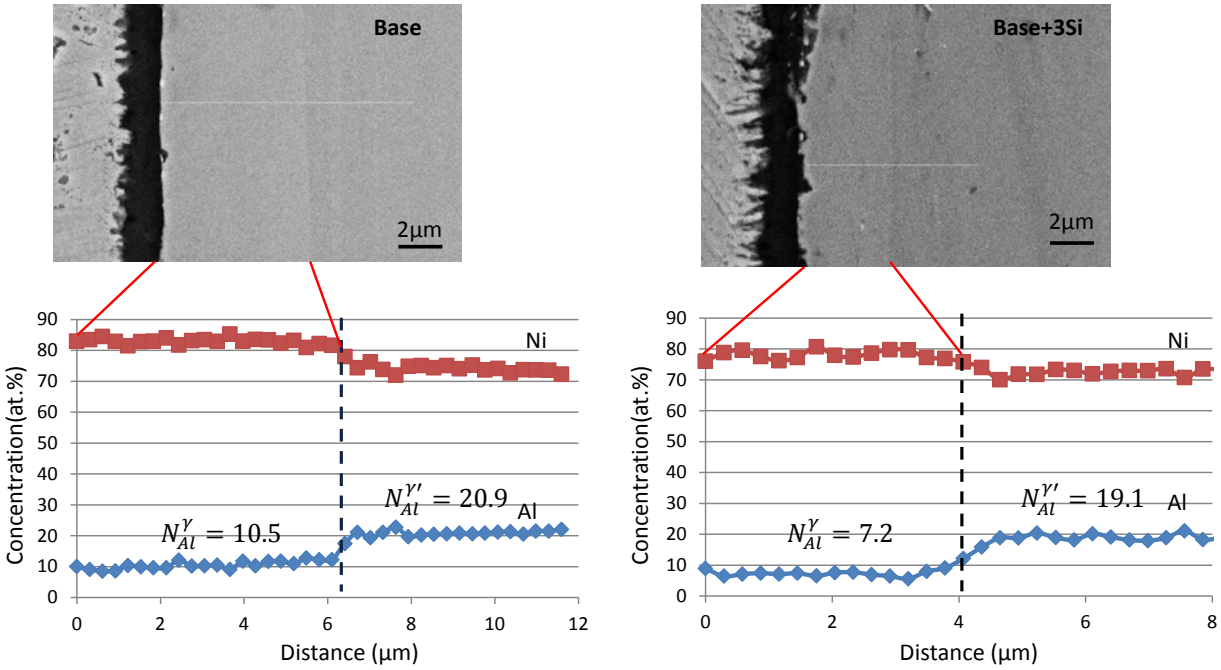

Figure 5.36 EDS line profile for the Base and Base+Si after 900°C for 20 hours

An Al flux in the alloy is given by

$$J_{Al} = \frac{(N_{Al}^{O} - N_{Al}^{\gamma})}{V_{all}} \frac{dX_d}{dt} \quad (5.3)$$

where: N_{Al}^{O} is the bulk composition, N_{Al}^{γ} is the γ-matrix composition in local equilibrium with γ′, V_{all} is the molar volume of the alloy, in $\frac{cm^3}{mol.alloy}$, and X_d is the depletion zone thickness. Under steady-state condition, the flux of Al to the surface is equal to the Al being consumed to form an Al_2O_3 scale, i.e.

$$J_{Al}^{ox} = J_{Al}^{all} \quad (5.4)$$

where

$$J_{Al}^{ox} = \frac{1}{V_{ox}} \left(\frac{k_p}{t}\right)^{1/2} \quad (5.5)$$

V_{ox} is the equivalent molar volume of the oxide, $\frac{cm^3}{mol.AlO_{1.5}}$, k_p is the parabolic constant based on weight gain ($\frac{g^2}{cm^4 \cdot s}$), which is related to the parabolic constant based on oxide thickness k_t, (cm^2/s) through the following generic relationship

$$k_p = \frac{d^2 b^2 M_O^2}{M_{M_a O_b}^2} k_t \quad (5.6)$$

where d is density of the oxide, $M_{M_a O_b}$is the molecular weight of the oxide $M_a O_b$, and M_O is the atomic weight of oxygen. Thus, for an Al_2O_3 scale, $k_p = 3.54 k_t$ .Equating 5.3 and 5.5 gives

$$X_d = \frac{1}{(N_{Al}^{o} - N_{Al}^{\gamma})} \left(\frac{V_{all}}{V_{ox}}\right) (k_t t)^{1/2} \quad (5.7)$$

The Base and Base+3Si alloy has comparable parabolic rate constants ($4.9x10^{-13}$and $4.5x10^{-13}$ $g/cm^4 \cdot s$ for the Base and Base+3Si alloys, respectively), and therefore k_t does not factor into in the differences in the γ-Ni thickness. Using equation 5.7, X_d is predicted as shown in Table 5.3.

Table 5.3 Predicted and experimental values of γ-Ni thickness for the Base and Base+3Si alloys

Alloy	Predicted (μm)	Experimental (μm)
Base	13	7
Base+3Si	9	4

The values predicted are twice of the experimental values. The predicted values given here are a maximum as the simplified approach did not consider the Al supplied from the γ′ matrix as there is a shallow Al concentration gradient in the γ′ at the γ′/ γ boundary. Besides, it did not consider the alloy/scale interface moving inward during scale growth because θ-Al_2O_3 grows mainly through outward diffusion of Al [118-121]. Both of factors would contribute to decreasing the γ-layer thickness and hence an over prediction. In spite of the overall prediction, clearly, the predicted X_d of the Base+3Si alloy is smaller than that of the Base alloy, which is consistent with the experiments. The addition of Si deceases Al content in γ-Ni, and therefore causes X_d to decrease.

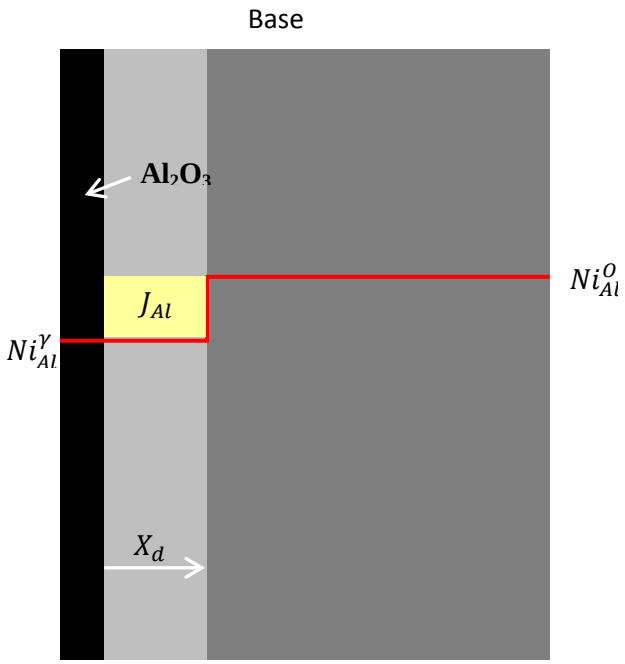

Figure 5.37 Schematic showing the flux of Al to the surface for oxidation through a flat Al diffusion profile

It was further noticed in Figure 5.9 that the depletion zone front (the γ-Ni /γ′-Ni_3Al boundary) formed on Base+3Pt is non-planar, while it is planar in the other alloys. A non-planar interface indicates that to maintain local equilibrium of that moving boundary, the volume fraction of γ′-Ni_3Al and γ-Ni must be changing. This morphology is formed through diffusion and can be explained according to the model of Rapp et al.[122]. The group investigated the kinetics of solid-state displacement reaction and predicted resulting interface morphologies from a knowledge of pertinent thermodynamic and diffusion data. Their prediction and model is shown in Figure 5.38. In a diffusion couple A/B_qX, if the diffusion of A through the product layer ApX is rate determining, the interface will be planar. If the diffusion X through the other product layer B is rate determining, the interface will be non-planar.

The model illustrated in Figure 5.38 is applicable to our current situation of alloy oxidation, as shown in Figure 5.39. Occasional protuberance of the γ-Ni /γ′-Ni_3Al interface can occur during oxidation. If Al diffusion through γ-Ni is rate determining, the interface will become planar, whereas if Al diffusion through γ′-Ni_3Al is rate determining, the interface will become even more non-planar. The non-planar γ-Ni /γ′-Ni_3Al interface observed in the Base+3Pt alloy was deduced to be the result of Pt hindering the diffusion of Al in γ′-Ni_3Al and/or Pt facilitating the diffusion of Al in γ-Ni. This deduction can be supported by Hayashi et al.'s investigation on interdiffusion in Pt-containing γ-Ni and γ′-Ni_3Al at 1150°C[125]. It was reported that in γ′-Ni_3Al the main-term interdiffusion coefficient of Al decreases with increasing Pt content, but it increases with increasing Pt content in γ-Ni [125]. The cross-stem interdiffusion coefficient of Al in both phases was reported to be independent of Pt content[125]. Thus, Pt can hinder the diffusion of Al in γ′-Ni_3Al and facilitate the diffusion of Al in γ-Ni, therefore causing a non-planar γ-Ni /γ′-Ni_3Al interface.

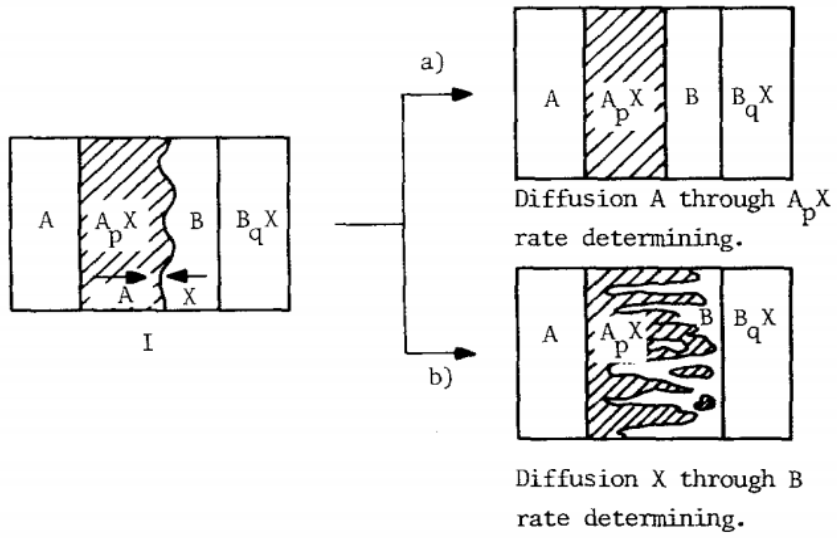

Figure 5.38 Schematic illustration of a displacement reaction $pA + B_qX \rightarrow qB + A_pX$ according to the model of Rapp et al. [122-124]

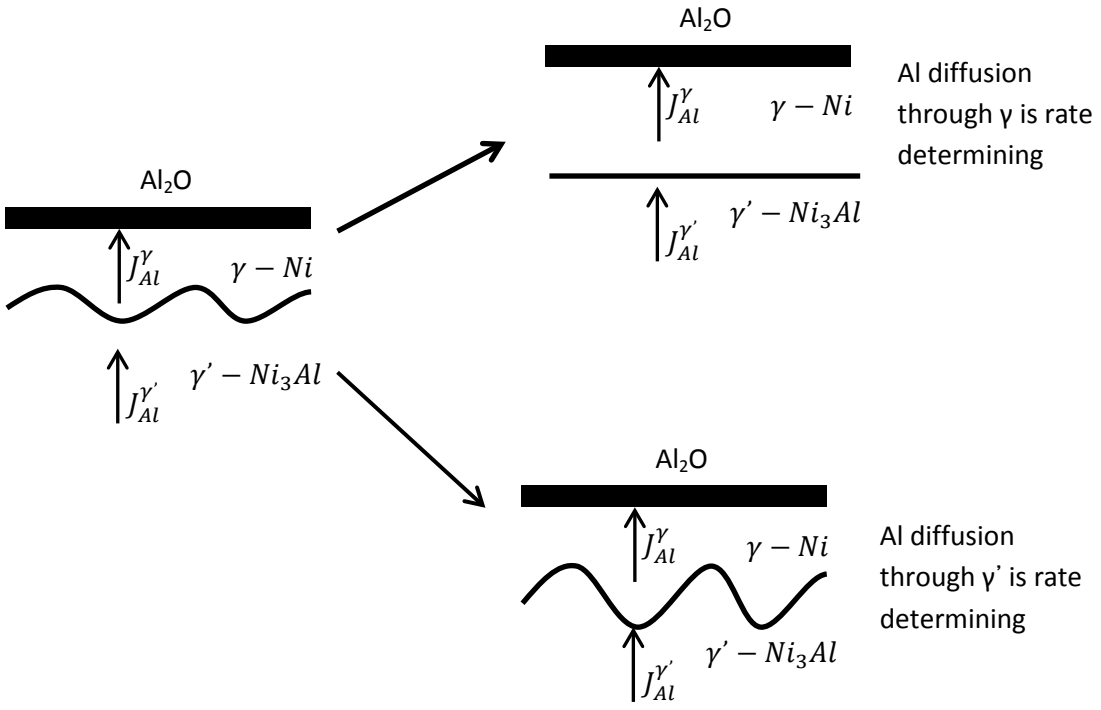

Figure 5.39 Schematic illustrations of a non-planar γ-Ni /γ′-Ni_3Al interface evolution during oxidation

5.1.3.3 Factors affecting the duration of the incubation stage in Type I hot corrosion

An important question to ask is, what are the key factors that affects the duration of the incubation stage for type I hot corrosion? As the experimental results in Figure 5.28 demonstrated, alumina crystal structure does not seem to affect the duration of incubation stage of type I hot corrosion. Results obtained from the various γ′-Ni_3Al model alloys at different stages of hot corrosion provide some guidance about what are affecting the incubation stage.

During the early stage of oxidation under a salt deposit (20 hours), the Base alloy formed a very thick layer of spinel without the inner layer, whereas the Base+3Si and Base+3Si+3Pt alloys formed a thick layer of spinel with a protective inner scale of Al_2O_3 or $(Al,Cr)_2O_3$. The Base+3Pt alloy formed a thin layer of α-Al_2O_3. Considering that the Base alloy exhibited breakaway right at the beginning of exposure, it is inferred that the formation of a continuous and tenacious oxide scale of Al_2O_3 or $(Al,Cr)_2O_3$ is necessary for hot-corrosion protection.

Investigation of the later stage revealed that alloys either formed a protective inner Al_2O_3 scale (as shown by Base+3Si and Base+3Si+3Pt in Figures 22 and 24, respectively) or were able to maintain a protective Al_2O_3 scale (shown by Base+3Pt alloys in Figure 23). Thus, the maintenance of a continuous Al_2O_3 scale is thought to be the key for the alloy to sustain the incubation stage. As mentioned in section 2.3.4.2, a protective oxide layer can be destroyed by salt-induced scale fluxing or stress-induced scale spallation. Therefore, re-healing a new protective oxide is requisite due to the fact that if the molten salt is able to make contact with a greatly depleted alloy, catastrophic attack will ensue. It is inferred that the maintenance of a protective alumina scale or sub-scale depends on scale adhesion and the re-healing capability of the alloy subsurface.

Investigation of alloys at the breakaway stage showed that, the protective alumina scale was lost at least in certain regions and that the alloy subsurface was depleted in Cr and Al to the point that the re-healing of the alumina scale was impossible (see Figure 5.26). This breakaway can start in local regions. Consistent with the inference from later stage investigation, the onset of breakaway is deduced to correspond to the inability of the alloy to maintain protective-alumina scale formation.

Thus, maintaining a protective Al_2O_3 scale is thought to be the key to extending the incubation stage. Similar research from our group [2] reported that, for β-NiAl systems, it is important for an alloy to rapidly form an Al_2O_3-rich surface scale at the beginning of exposure and to heal this oxide if it is breached during exposure to type I hot corrosion. Task [2] compared the re-healing capability of different alloys by artificially spall off the pre-formed oxide scale and re-exposing the alloy at 900°C in air. It was found that the alloy which demonstrated longer extension of the incubation stage showed better re-healing capability. However, these re-healing tests were done in air. In reality, re-healing must happen in the presence of salt or sulfur. It is, therefore, necessary to study the role of environmental sulfur and salt on oxidation and hot corrosion of an alumina scale forming alloy. This will be presented in section 5.2-5.4

5.1.3.4 The role of Si and Pt during hot corrosion in air

When oxidation takes place under a salt deposit, as shown in Figure 5.11, Base+Pt alloys formed α-Al_2O_3, while the rest of the alloys formed spinel. Thus, the Pt and Si greatly affect the nature of the oxide scale formed under salt.

During oxidation in air with an Na_2SO_4 deposit, Si and Pt are found to be beneficial for type I hot corrosion, with the role of Si being more obvious. As discussed in Section 5.1.3.2, Si

probably hinders the transient oxidation and facilitates the establishment of an exclusive alumina scale during oxidation in air. This may help to improve alloy resistance to Type I hot corrosion. Because the Base+3Si alloy intrinsically tends to grow less transient oxidation, compared to the Si-free Base alloy, therefore, it is more likely to rapidly establish a scale which provides an effective barrier between the salt and the underlying alloy. This inference is supported by the fact that a protective inner scale of Al_2O_3 was formed on the Base+3Si alloy, whereas base alloy without Si alloy was not able to form a continuous Al_2O_3 scale at the beginning of exposure to salt deposit. Another contributing factor of the beneficial effect of Si is thought to be that Si increases the re-healing ability of the alloys. As discussed in section 5.1.3.2, with similar amount of Al consumption, the depletion zone of a Si containing alloy was thinner than that of base alloy without Si addition. This is due to the fact that the addition of Si decreases Al content in γ-Ni in equilibrium with γ′-Ni_3Al. Thus, Si containing alloy may have larger potential to supply more Al for the scale re-healing. Similarly, the observed beneficial effect of Pt is thought to be that this element also increases the re-healing ability of alloys, as there was apparent Al_2O_3-scale spallation from the Pt-modified alloy during testing, and base alloy without Pt addition showed no re-healing capability.

5.1.3.5 The role of salt on alumina formation

As observed in section 5.1.2.3, Na_2SO_4 deposits were found to promote the α-Al_2O_3 establishment. There are a number of potential causes for this effect on alpha nucleation, e.g., the presence of S, the presence of Na, the presence of salt. The next step was to test alloys in sulfur-containing environments to identify whether the α-Al_2O_3 establishment was promoted by the presence of sulfur. This will be presented and discussed in-depth in section 5.2.

5.1.4 Summary and conclusions

Four γ′-Ni_3Al model alloys were oxidized in air at 900°C for 20 hours and 100 hours. All alloys formed primarily a θ-Al_2O_3 scale. The addition of Pt and Si only slightly affected the oxidation behavior in air based on similar growth kinetics and scale characterization. Si reduced the extent of the transient oxidation of Ni. Si also affected the aluminum diffusion within the substrate through deceasing Al content within γ-Ni, which was in equilibrium with γ′-Ni_3Al.

The same alloys were oxidized at 900°C in air under an Na_2SO_4 deposit. It was found that the addition of Pt and Si is beneficial for improving hot corrosion resistance. Pt and Si both increased the duration of the incubation stage of base alloy and with the addition of Si, the lifetime of the base alloy increased dramatically. The tracking of alloy performance during different stages of hot corrosion showed that: 1) the formation of a continuous and tenacious oxide scale of Al_2O_3 or $(Al,Cr)_2O_3$ is necessary for hot-corrosion protection; 2) The maintenance of a protective alumina scale or sub-scale depends on the scale adhesion and the re-healing capability of the alloy subsurface; and 3) Onset of breakaway corresponds to the alloy's inability to maintain protective-alumina scale formation. The beneficial effect of Si to hot corrosion at 900°C is considered to be that Si facilitates the establishment of a protective inner alumina scale and increases the alloy's ability to re-heal this scale. The beneficial effect of Pt to hot corrosion at 900°C is thought to be that Pt increases the re-healing ability of alloy.

With the presence of an Na_2SO_4 deposit, a continuous layer of α-Al_2O_3 formed on the Base+3Pt alloy. By contrast, a predominantly θ-Al_2O_3 scale formed when oxidation was done in air without an Na_2SO_4 deposit. Thus, the Na_2SO_4 deposit promotes the α-Al_2O_3 establishment.

The hot corrosion of pre-oxidized samples showed that the influence of initial alumina crystal structure seems not to affect the incubation stage of type I hot corrosion.

5.2 EFFECT OF ENVIRONMENTAL SULFUR ON THE STRUCTURE STABILITIES OF ALUMINA SCALE

5.2.1 Materials tested

In this chapter, the following γ′-Ni_3Al alloy compositions were tested. The nominal composition is shown in Table 5.4. The processing, thermal treatment and test-sample preparation were described in the section 4.1.1.

Table 5.4 Nominal composition of the alloy studies.

Alloy #	Element (at.%)						
	Ni	Al	Cr	Pt	Si	Hf	Y
Base	Bal.	20	5	-	-	0.1	0.05
Base+3Si	Bal.	20	5	-	3.0	0.1	0.05
Base+3Pt	Bal.	20	5	3.0	-	0.1	0.05
Base+3Si+3Pt	Bal.	20	5	3.0	3.0	0.1	0.05
5	Bal.	20	5			0.05	0.05

5.2.2 Results

5.2.2.1 γ′-Ni_3Al model alloys 900°C oxidation in O_2+1000ppm SO_2

One key finding in the last chapter is that Na_2SO_4 deposit can promote α-Al_2O_3 establishment. There are a number of potential causes for this effect, e.g., the presence of S, the

presence of Na, the presence of salt on alpha nucleation. The cause that is easiest to test is whether sulfur play a role in promoting the α-Al_2O_3 establishment. This was done by exposing γ'- Ni_3Al model alloys to an O_2+1000ppm SO_2 atmosphere at 900°C for 20 hours. The surface morphology and the GIXRD of the oxide scales are shown in Figure 5.40 and Figure 5.41, respectively. Figure 5.40 shows that a continuous and dense oxide scale formed on each alloy. The scales formed on the Base and Base+3Pt alloys are granular with a graded appearance and free of any needles. X-ray analysis identified the scale to be α-Al_2O_3, as indicated in Figure 5.41, which shows diffraction peaks from γ'-Ni_3Al (underlying substrate) and α-Al_2O_3 (scale). Considering that θ-Al_2O_3 growth predominated when oxidation took place in air (see section 5.1.2.2), the current results suggest that sulfur from the salt deposit or gas atmosphere promoted the α-Al_2O_3 establishment. This same phenomenon was previously found in β-NiAl-based alloys, reported in Task's Ph.D. thesis [2]. Specifically, Ni-46Al-5Pt (in at.%) alloy was oxidized in air and O_2+0.1%SO_2 at 900°C for 100 hours. It was found that an exclusive θ-Al_2O_3 scale formed in the air; while, α-Al_2O_3 predominated in O_2+0.1%SO_2. Therefore, Task concluded that sulfur promotes the θ-Al_2O_3 $\rightarrow$ α-Al_2O_3 transformation. The current results showed that this sulfur promoted $\theta \rightarrow \alpha$-$Al_2O_3$ transformation is not just limited to β-NiAl system but also observed on γ'-Ni_3Al system.

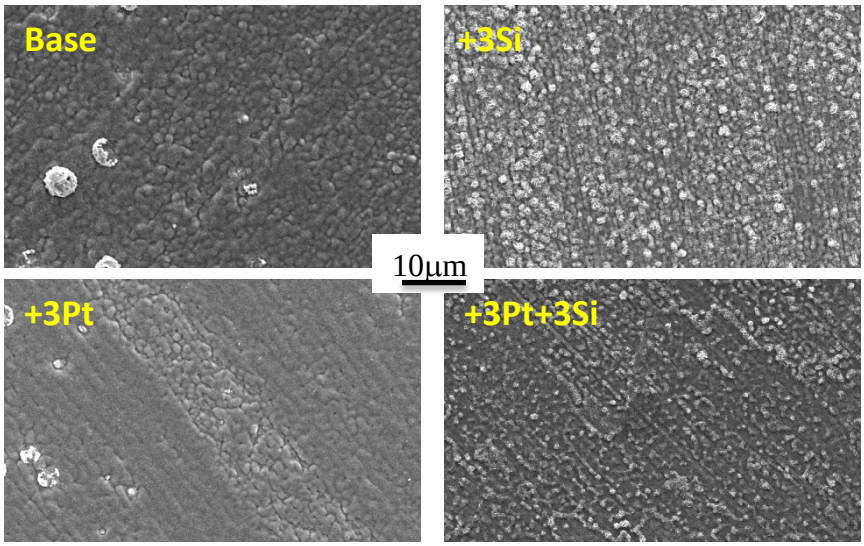

Figure 5.40 Surface morphology of

Ni-20Al-5Cr-(0,3)Pt-(0,3)Si-0.1Hf-0.05Y alloys after 20 hours of oxidation at 900^{o}C in flowing

O_2+0.1%SO_2

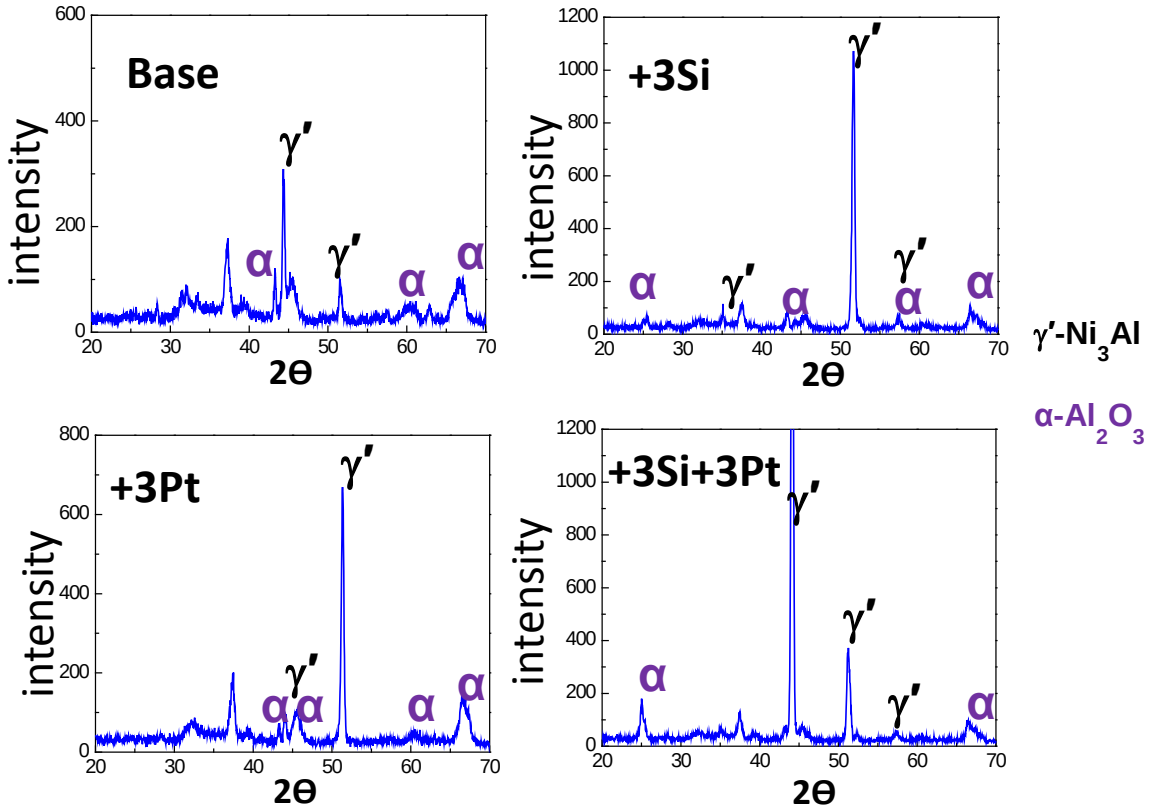

Figure 5.41 The GIXRD of

Ni-20Al-5Cr-(0,3)Pt-(0,3)Si-0.1Hf-0.05Y alloys after 20 hours of oxidation at 900°C in flowing

O_2+0.1%SO_2

To further understand how α-Al_2O_3 sale was promoted in the presence of sulfur, short-term oxidation tests in air and O_2+0.1%SO_2 at 900°C were conducted. Alloy 5 was exposed to O_2+0.1%SO_2 and air for 1, 2, 5, 10 and 20 hours. For each exposure, one sample was prepared. The oxide phase formed was identified by PSLS. Representative luminescence spectra are shown in Figure 5.42 for air oxidation and in Figure 5.43 for oxidation in O_2+0.1%SO_2.Overall, a luminescence spectrum for α-Al_2O_3 consisting of R1-R2 doublet was detected at the wavelengths of 693nm and 695nm, respectively. The relative position of R1 and R2 was a few nm different from standards [126], which may due to stress (strain) in the oxide scale[60]. The θ-

Al_2O_3 luminescence spectrum consisting of T1-T2 doublet was detected at 685nm and 687nm. T1 peaks were always detected while T2 peaks were only detected on part of these conditions probably when the oxide scale formed was thick enough to yield sufficient intensity of θ-Al_2O_3-specified luminescence. The relative positions of T1 and T2 are in reasonably agreement with what has been reported in the literature for θ-Al_2O_3 [110].

During oxidation in air at 900°C, after 1 hour of exposure, the R1-R2 doublet was observed, indicating the formation of α-Al_2O_3. Even though the doublet characteristic is not clear due to its low intensity, the two peaks of α-Al_2O_3 were clearly discernible. A broad θ-specific T1 peak was observed at the wavelength of 685nm, indicating θ-Al_2O_3 is also present. After 2 hours of exposure in air, the T1-T2 doublet of θ-Al_2O_3 was clearly discernible. The T1-T2 peak intensities and area are much larger than those of the R2 luminescence due to α-Al_2O_3. This clearly shows that θ-Al_2O_3 outgrows α-Al_2O_3 at this stage. After 5 hours of exposure in air, the intensities and peak area of both the θ-specified T1-T2 doublet and the α-specified R1-R2 doublet were greater than what were observed after 2 hours. The T1-T2 doublet was still larger than the R1-R2 doublet. After 10 and 20 hours of exposure, overall θ-Al_2O_3 outgrows α-Al_2O_3 based on the comparison of the associated doublets. In short, θ-Al_2O_3 growth quickly predominates during oxidation in air.

During oxidation in O_2+0.1%SO_2 at 900°C, after 1 hour of exposure, only the R1-R2 doublet was observed and there was no evidence of θ-specified T1-T2 doublet. These results indicate that α-Al_2O_3 growth predominated during the initial 1 hour of exposure. After 2 hours of exposure, the T1 peak became apparent with a very weak intensity, indicating the minor formation of θ-Al_2O_3. The R1-R2 doublet increased in intensity and had a larger peak area than the T1 peak. Thus, α-Al_2O_3 was still predominant. When the exposure increased to 5, 10 and 20

hours, the luminescence spectra from θ-Al_2O_3 and α-Al_2O_3 both increased in intensity, but the R1-R2 doublet remained dominant, which indicates that the scale was primarily α-Al_2O_3 during its entire early-stage growth period. In summary, during oxidation in O_2+0.1%SO_2, α-Al_2O_3 was the predominant oxide in the scale since the very early stages of oxidation. This is distinct from the oxidation in air.

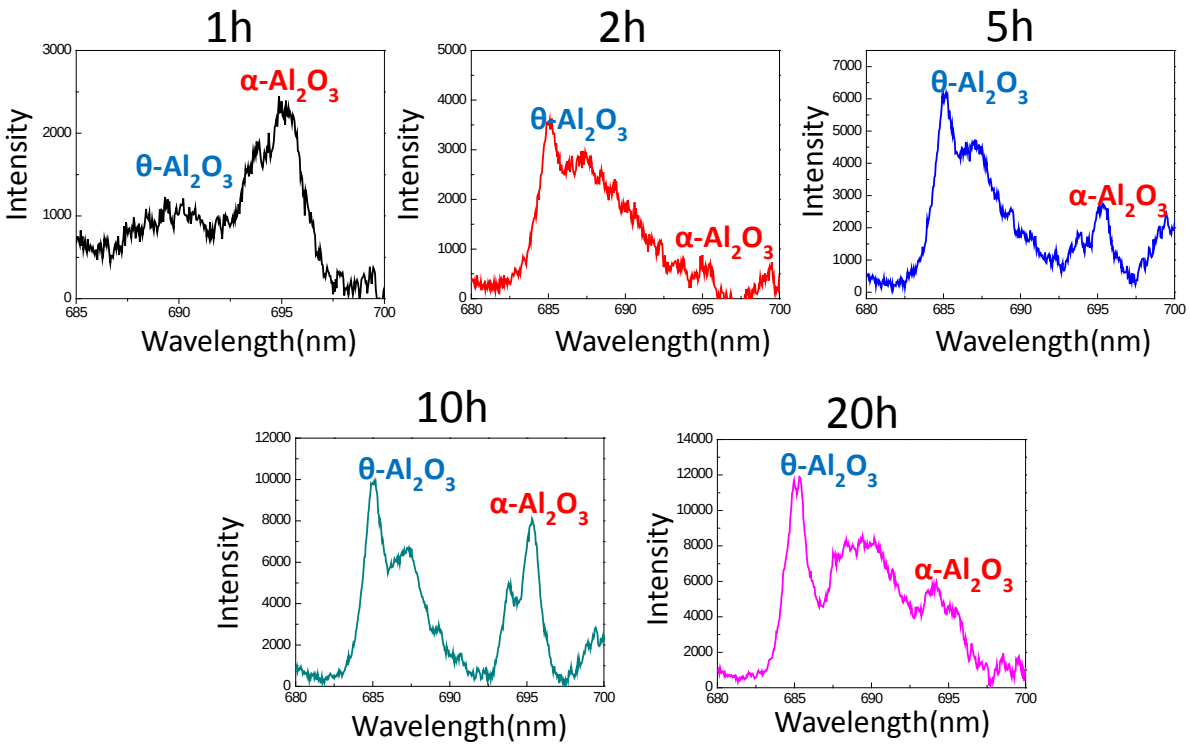

Figure 5.42 PSLS spectra from the scales formed on alloy 5 during isothermal oxidation in air at 900°C for various times.

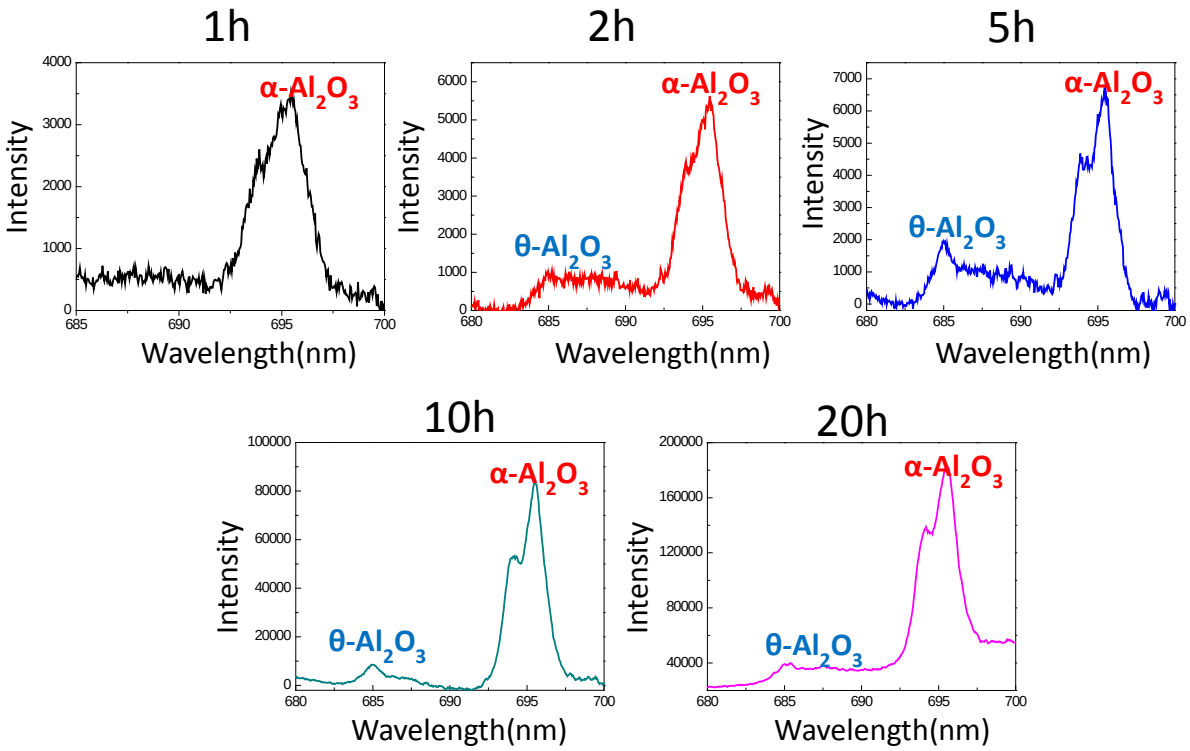

Figure 5.43 PSLS spectra from the scales formed on alloy 5 during isothermal oxidation in O_2+0.1%SO_2 at 900°C for various times.

Using the semi-quantitative method as described in section 4.3, the fraction of α-Al_2O_3 after 5, 10 and 20 hours was estimated using the following equation.

$$f_\alpha = \frac{A_{R1}+A_{R2}}{A_{R1}+A_{R2}+\phi(A_{T1}+A_{T2})} \qquad (5.8)$$

The constant ϕ is introduced to adjust for the relatively weaker luminescence from θ-Al_2O_3. In this research, ϕ is assumed to be a constant, realizing that, in reality, it is probably not a constant due to dynamic effects. Even so, this treatment will still allow one to gain insights on trends from the PSLS spectra. The value of ϕ was set as 12, since a previous study reported θ-Al_2O_3 luminescence can be 10-12 times weaker than α-Al_2O_3 luminescence [60]. Although the real α-Al_2O_3 fraction within the oxide scale may be different from the calculated value, still the

estimated trend in the variation in the α-Al_2O_3 fraction will be correctly represented, regardless of the ϕ value used. The result is plotted in Figure 5.44. Clearly, a larger percentage of α-Al_2O_3 was formed in the SO_2-containing atmosphere compared to what formed in air. The fraction of α-Al_2O_3 was very small during oxidation in air, thus clearly the alloy formed a predominant θ-Al_2O_3 scale. While the fraction of α-Al_2O_3 increased with exposure time when oxidation was done in O_2+1%SO_2 atmosphere; indicating that there was a promoted α-Al_2O_3 establishment during scale growth. These results are further evidence that sulfur promoted α-Al_2O_3 establishment.

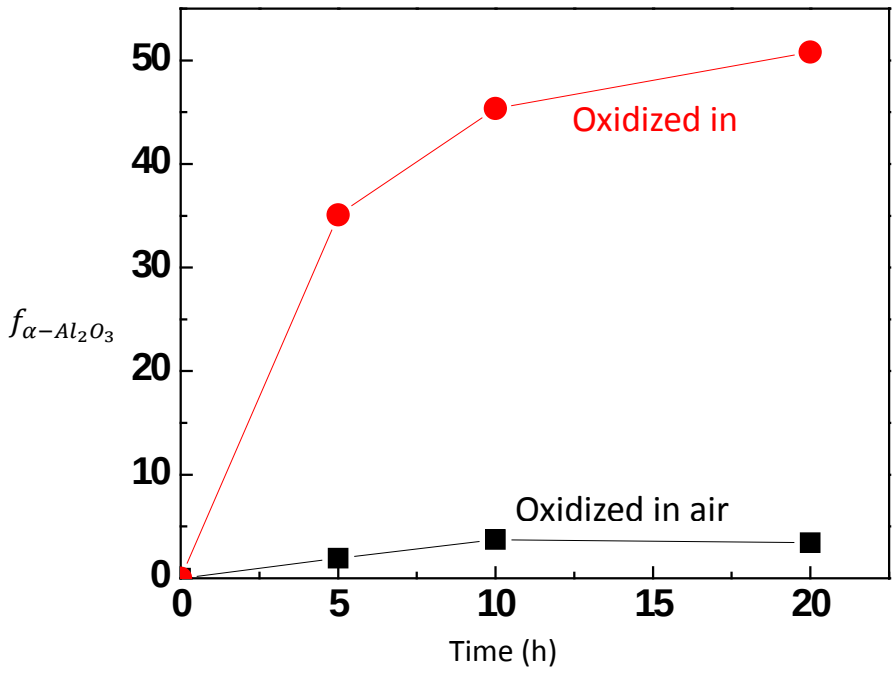

Figure 5.44 Estimated volume fraction of α-Al_2O_3 within the oxide scale formed on alloy 5 exposed to air and O_2+0.1%SO_2 at 900°C for 5, 10 and 20 hours.

5.2.2.2 Sample condition before exposure to an O_2+0.1%SO_2 atmosphere at 900°C

To understand the sulfur effect in promoting the α-Al_2O_3 establishment, the sample surface condition in O_2+0.1%SO_2 atmosphere before being exposed to high temperature was investigated. Based on the experimental procedure of exposing samples to O_2+0.1%SO_2, the samples sit outside the hot zone at around 150°C for at least 12 hours in an O_2+0.1%(SO_2+SO_3) environment prior to being inserted to the hot zone. To assess the nature of the surface prior to high temperature exposure, one sample exposed for 12 hours in the pre-test position was observed using SEM. A representative surface image is shown in Figure 5.45. EDS analysis of the scale showed a strong sulfur peak.

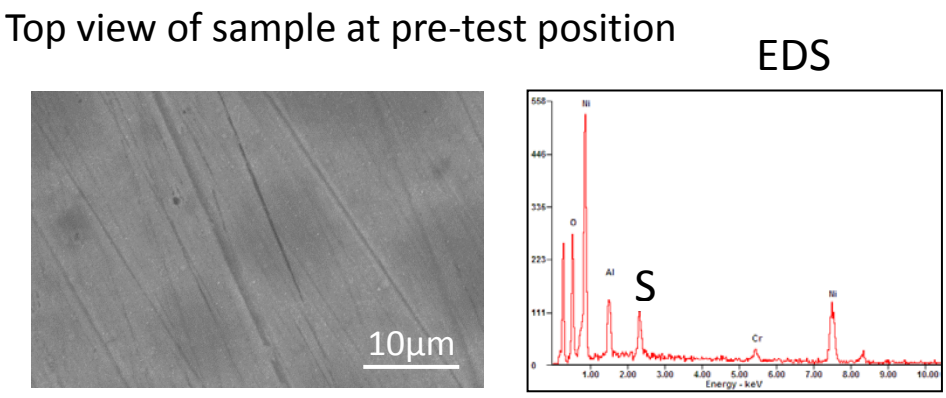

Figure 5.45 Surface image and associated EDS of alloy 5 after 12h exposure to O_2+0.1%SO_2 at ~150°C in the pre-test position.

5.2.2.3 The verification of the effect of surface-enriched sulfur

It is conjectured that the promoted α-Al_2O_3 establishment may be related to the measured surface enrichment of sulfur prior to high-temperature exposure. To test this hypothesis, samples of alloy 5 were given the pre-test exposure (O_2+0.1%SO_2 at 150°C) and then oxidized in air at 900°C for 10 and 20 hours. The specific testing procedure involved: (1) laying the sample in the

pre-heat zone of the furnace (maximum temperature~150ºC) and exposing to flowing Ar gas for 2 hours followed by O_2+0.1%SO_2 for 12 hours and then (2) removal of the sample from the pre-test position followed immediately by exposure to air at 900°C for 20 hours.

PSLS was performed on the exposed surfaces and the luminescence spectra are shown in Figure 5.46. The α-specific R1-R2 doublet was detected with very strong intensity and the θ-specific T1-T2 doublet was detected with low intensity. These results showed a predominant α-Al_2O_3 growth when sulfur is enriched on the sample surface, even though the high-temperature exposure was done in air. The same alloy without a pre-test exposures and, instead, exposed directly to air forms predominantly θ-Al_2O_3, as shown in Figure 5.42 and Figure 5.44. Thus a small amount of sulfur on the alloy surface can promote α-Al_2O_3 establishment.

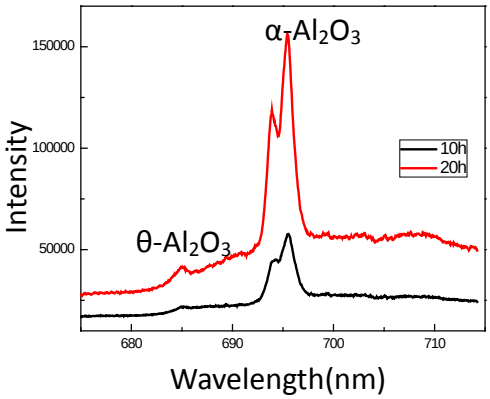

Figure 5.46 PSLS spectrum from the scales formed on alloy 5 during isothermal oxidation in air at 900°C after 150°C pre-exposure to O_2+0.1%(SO_2+SO_3)

5.2.2.4 The chemical state of sulfur at pre-tested condition

XPS was used to identify the chemical state of the sulfur enriched on the sample surface during the pre-test exposure. The resulting spectra in Figure 5.47 are from a sample exposed to O_2+0.1%SO_2 at the pre-test position (~150°C) for 12hours. From the broad region scan (Figure

5.47a), main spectra are from Ni, O and S, with very minor Cr spectrum. The Sp2 peak (Figure 5.47c) is located at 168.9 eV, which corresponds to sulfate state (S^{6+}) [127]. Deconvoluting the spectrum to separate S^{6+} from elemental S, it is found that 98% of sulfur exists in the sulfate state (S^{6+}). The main Ni $2p\,^{3}/_{2}$ peak (Figure 5.47b) is located at 857 eV, which corresponds to $NiSO_4$ [128-130]. As the sample contains >70at.% Ni and the majority of cation spectra are from elemental Ni, it is therefore deduced that the surface enriched sulfur exists primarily in the form $NiSO_4$. Johansson et al. [131] also reported SO_2 formed sulfate on the oxide surface of a 304L steel exposed to O_2+40%H_2O+ 100ppmSO_2 at 600°C.

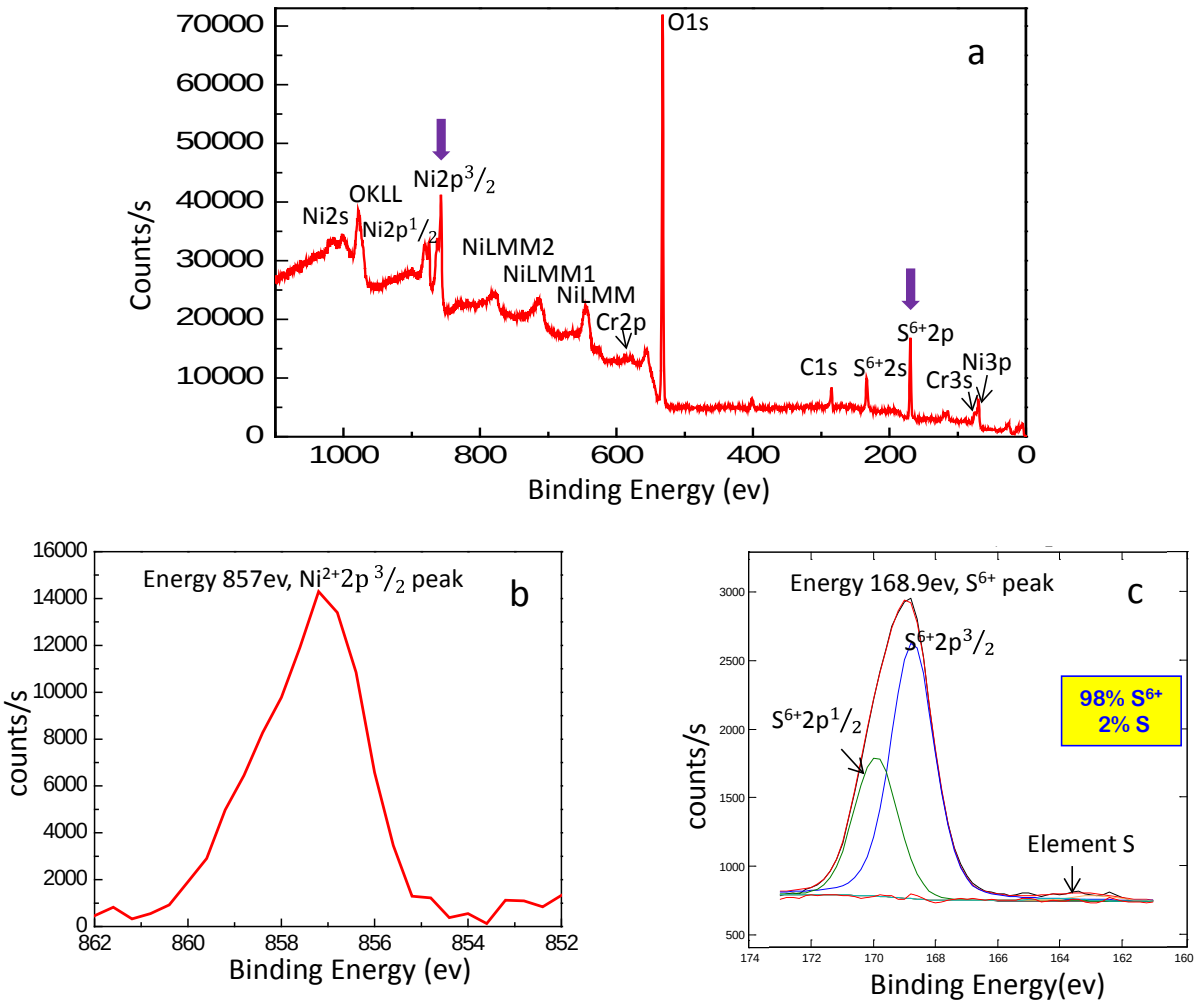

Figure 5.47 XPS binding-energy spectra on alloy 5 exposed to O_2+0.1%SO_2 at pre-test position (~150°C) for 12hours (a) broad region, (b) $Ni^{2+}2p\,^3/_2$ region, (c) $S^{6+}2p$ region

5.2.2.5 The distribution of sulfur at pre-tested condition

ChemiesSTEM was used to analyze the sulfur distribution on the sample surface during the pre-test exposure. The resulting images in Figure 5.48 are from alloy 5 exposed to O_2+0.1%SO_2 at pre-test position (~150°C) for 12 hours. It is seen that oxygen was enriched in a 90 nm band close to the surface, indicating a very thin oxide scale formed on the sample surface

when being exposed at ~150°C for 12 hours. Within the oxygen enrichment band, sulfur was observed to be enriched in a 20nm band nearest to the surface. These results confirm that there is indeed a surface enrichment of sulfur on the sample during the pre-test exposure to O_2+0.1%SO_2 atmosphere.

As a comparison, chemiesSTEM was also done on sample 5 exposed to air at ~150°C for 12 hours. Sulfur was not detected.

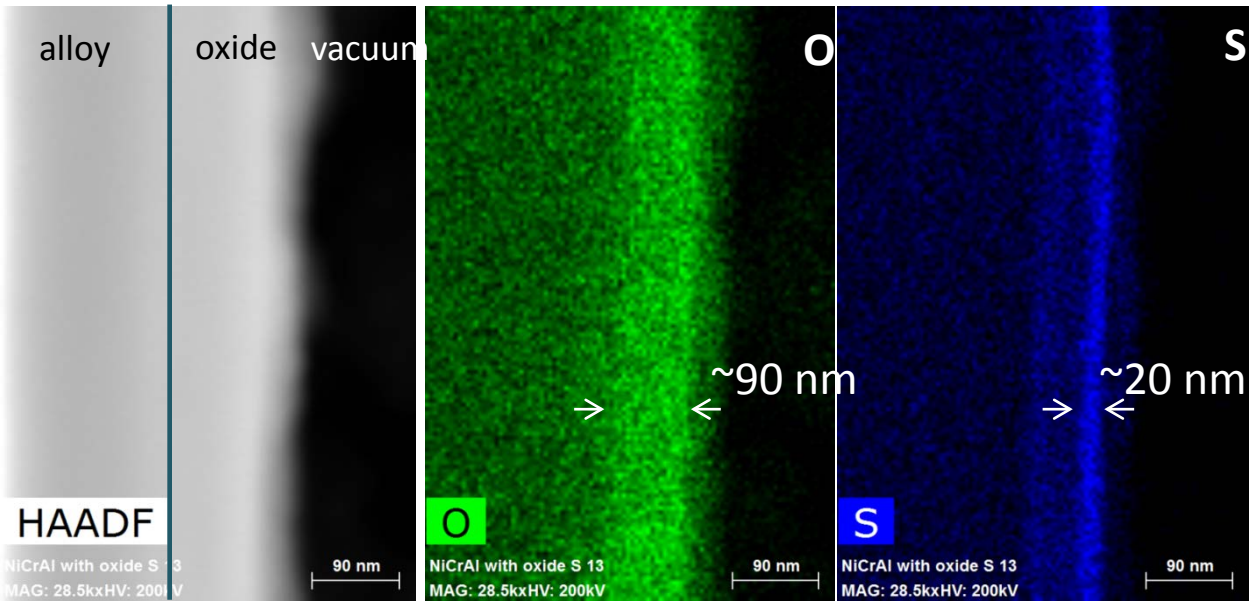

Figure 5.48 ChemieSTEM of alloy 5 exposed to O_2+0.1%SO_2 at pre-test position (~150°C) for 12 hours

5.2.3 Discussion

5.2.3.1 The kinetic competition of alpha and transient aluminas

The sulfur promoted α-Al_2O_3 establishment is within the research topic of θ→α-Al_2O_3 transformation in the oxide scale. The reason to investigate θ→α-Al_2O_3 transformation is that this phenomenon was commonly observed during alumina scale growth and has a significant

potential effect on the protectiveness of the alumina scale. The metastable-to-stable transformation causes a two orders of magnitude decrease [48] in the oxidation rate and around 8-10% volume reduction[59]. The volume reduction can cause cracking within the oxide scale. The growth rate of the scale determines the aluminum consumption rate within the alloy, which largely affects the lifetime of the alloy in corrosive environments.

The $\theta \rightarrow \alpha$-$Al_2O_3$ transformation has been the subject of much interest in the field of high temperature corrosion and a large amount of research has been dedicated to investigate the fundamental mechanism of this transformation, the influences of alloying element[48, 61, 64-73], surface condition, and environmental reasons[74-77]. A brief review of past studies on the $\theta \rightarrow \alpha$-$Al_2O_3$ is provided in section 2.2.3.4 of this thesis. A key finding in this study is that the presence of trace sulfur in the atmosphere can promote the establishment of α-Al_2O_3. Such a finding has only been recently reported[2, 132].

The nature of the $\theta \rightarrow \alpha$ transformation is diffusion controlled [63] and it generally involves the heterogeneous nucleation of α-Al_2O_3 followed by lateral growth and then conversion of the initially-grown θ to α. Nucleation is a thermally activated process [63], in which nuclei have to overcome a certain free energy barrier and elements will migrate to nuclei sites by diffusion. Once α-Al_2O_3 nucleates, it grows laterally more rapidly than it grows vertically [62, 111, 133, 134], with the α-Al_2O_3 nuclei eventually impinging and developing into a complete layer on the alloy. This layer significantly slows the outward flow of Al cations and thus stifles further θ-phase growth [135].

The α-Al_2O_3 nucleation rate and the relative growth rates of α-Al_2O_3 and θ-Al_2O_3 are important factors in determining the phase structure of the established oxide. The nucleation rate of α-Al_2O_3 is important because a larger density of nuclei will make it easier for the α-Al_2O_3 to

coalesce and form a continuous layer. The growth rates of aluminas are important because before α-Al_2O_3 eventually establishes a complete layer, there is a competitive growth of θ-Al_2O_3 and α-Al_2O_3 [62, 136]. This competitive growth stems from the different growth rate of θ-Al_2O_3 and α-Al_2O_3, during which α-Al_2O_3 and θ-Al_2O_3 compete with each other in obtaining Al and O for their growth. Usually at low temperature in air, the much faster growth of the θ-Al_2O_3 phase would be favored and be predominant, which in turn slows the speed for α-Al_2O_3 to coalesce at the alloy/oxide interface. Based on this, any effects that change the relative growth rate of α-Al_2O_3 and θ-Al_2O_3 can affect the phase structure of the alumina scale. More generally, any effect that facilitates α-Al_2O_3 nucleation and lateral growth would serve to promote the establishment of α-Al_2O_3.

The kinetic competition between θ-Al_2O_3 and α-Al_2O_3 was observed in this research. As shown in Figure 5.42, the ratio of the peak areas of the θ-specific T1-T2 doublet and the α-specific R1-R2 doublet changes after different oxidation times. In particular, there is a dramatic difference in this ratio when going from 1 hour to 2 hours of oxidation. This ratio reflects the relative amounts of θ- and α-Al_2O_3 formed within the oxide scale and this amount varies with oxidation time. The changes in this relative amount reveal that, during the scale growth, there is a kinetic competition of metastable alumina and stable alumina. Theta alumina wins the kinetic competition against α-Al_2O_3 and is therefore the predominant phase (Figure 5.42) during early-stage oxidation in air; whereas, α-Al_2O_3 is the predominant phase (Figure 5.43) during oxidation in O_2+1%SO_2. Thus, clearly sulfur has affected the kinetic competition between θ-Al_2O_3 and α-Al_2O_3 during scale establishment.

An interesting result related to the kinetic competition between θ-Al_2O_3 and α-Al_2O_3 is that the latter predominates in both atmospheres during the initial 1 hour of oxidation.

Eventually, though, this initial α-Al_2O_3 growth in air is later overtaken by θ-Al_2O_3. This phenomenon was unexpected, given the widely reported results that the first-formed scale is usually comprised of metastable aluminas [62, 133], with stable α-Al_2O_3 taking over at a later stage [62]. The underlying reason for this currently observed sequence is still not clear. However, a recent study by Chegroune et al.[136] on the Fe-based alloy "Aluchrom YHfAl" exposed for various times at 925 °C in Ar+15%O_2 also showed an initial growth of the α-Al_2O_3, followed by transient alumina growth and later transformation back to α-Al_2O_3. Their results are summarized in Figure 5.49. It shows the ratio of the θ and α-Al_2O_3 peak amplitudes as a function of time. At 30 minutes, only α- Al_2O_3 was detected. θ-Al_2O_3 was detected later and its percentage increased with time up to a maximum at 14 hours, after which α-Al_2O_3 again predominated.

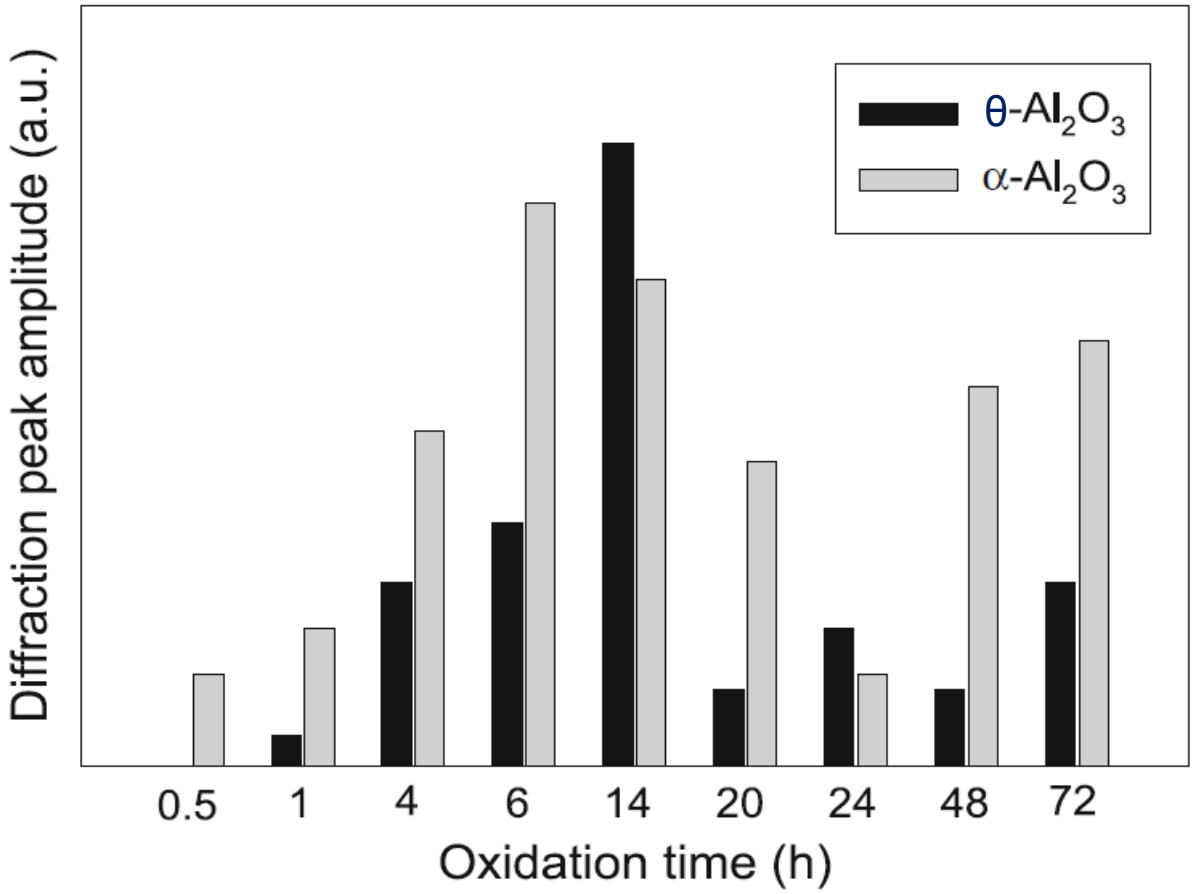

Figure 5.49 The recent reported observation of α-Al_2O_3 forming earlier than θ-Al_2O_3[136]

5.2.3.2 The surface blocking effect induced by the surface enrichment of sulfur

A key finding in this study is that a continuous 20μm-thick layer enriched with sulfur formed on the sample surface when exposed for 12 hours to O_2+0.1%SO_2 at the pre-test position (~150°C). Based on XPS analysis, the layer was deduced to $NiSO_4$ (i.e. S^{6+} state). Another key finding is that the sample with sulfur surface enrichment formed a primarily α-Al_2O_3 scale when subsequently exposed to air (Figure 5.48). Thus, the low-temperature surface enrichment of sulfur, which is in the form of $NiSO_4$, can promote α-Al_2O_3 establishment during subsequent thermal exposure. These findings are novel and a detailed mechanistic understanding of the α-Al_2O_3 establishment has not been presented in the open literature.

To seek a mechanistic understanding of the observed sulfur effect, the formation path of $NiSO_4$ at low temperature is analyzed. $NiSO_4$ can be formed by the following reaction[137]:

$$NiO(s) + SO_3(g) = NiSO_4(s) \quad (1)$$

Though $NiSO_4$ had formed at the surface, an analysis based on bulk materials thermodynamics can still provide guidance on stabilities. As can been in the NiO/$NiSO_4$ stability diagram (Figure 5.50), reaction (1) is only stable to proceed to the right at temperatures below about 675°C in an equilibrated O_2+0.1%SO_2 atmosphere. Thus, the $NiSO_4$ formed at low temperature (~150°C) in the pre-test position may dissociate during heating to 900°C.

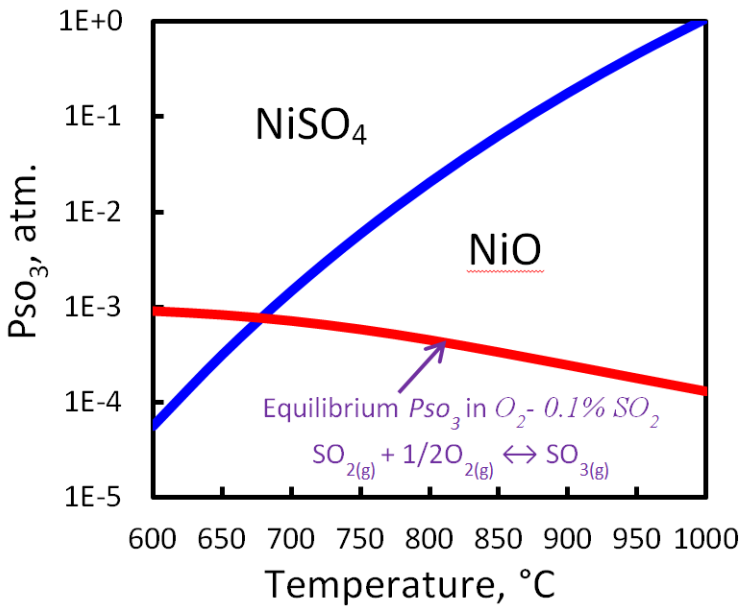

Figure 5.50 Stability diagrams of NiO and $NiSO_4$

An important question would be: How is the alumina phase transformation affected at high temperature if $NiSO_4$ dissociates? One possibility is that after $NiSO_4$ dissociation, sulfur is still preserved on the sample surface and has a poisoning effect on the oxidation reaction. It has been reported that sulfur can chemisorb on an alloy surface and block the surface sites required for the decomposition of the gas molecules responsible for corrosion[138, 139]. Further, recent study on 9-12%Cr steels by Quadakkers et al.[140] also showed that in terms of adsorbing strength, SO_2>O_2. Thus it is possible that once the available reactive adsorption sites are occupied by SO_2 or sulfur in general, O_2 adsorption, and hence reaction adsorption is impeded. Whether sulfur or a sulfur containing species inhibits the O_2 adsorption or the O_2 decomposition on sample surface, the oxygen supply for the scale growth will be hindered. Therefore, the following hypothesis is proposed to explain the sulfur promoting the α-Al_2O_3 establishment: the enrichment of sulfur blocks the surface sites for oxygen reaction, thus leading to a decreased oxygen supply for scale growth and affecting the kinetic competition between α-Al_2O_3 and θ-

Al_2O_3 in such a way that θ-Al_2O_3 growth is hindered more than α-Al_2O_3 growth to the extent that predominance of the latter becomes favored. It is assumed that such a process caused the experimental appearance of sulfur promoted θ→α-Al_2O_3 transformation. Regardless of the form of sulfur on the sample surface at high temperature, the sulfur-inhibited oxygen supply will be generally referred to in this thesis as a "the blocking effect by surface enriched sulfur".

5.2.3.3 Evaluation of the surface blocking effect hypothesis

The hypothesis outlined in the previous section assumes that the blocking by sulfur at the surface results in a decrease in the oxygen supply such that the growth rate of θ-Al_2O_3 and α-Al_2O_3 can be affected to different extents; that establishment of thermodynamically stable α-Al_2O_3 becomes kinetically facilitated. To evaluate this hypothesis, first the oxygen consumption need for θ-Al_2O_3 and α-Al_2O_3 growth will be calculated, and then the oxygen supply in air and in the O_2+0.1%SO_2 atmosphere will be estimated, respectively. Finally, the comparison and analysis will be made between these obtained values. These are presented in sequence in the following.

The instantaneous amount of oxygen needed to grow α- or θ-Al_2O_3 is dictated by the oxidation kinetics. From the Arrhenius plot for Al_2O_3 scale growth rate constants in Figure 5.51, it is seen that theta can grow three orders of magnitude faster than alpha. The oxygen supply needed for alpha or theta growth, J_o, can be calculated by equation 5.9.

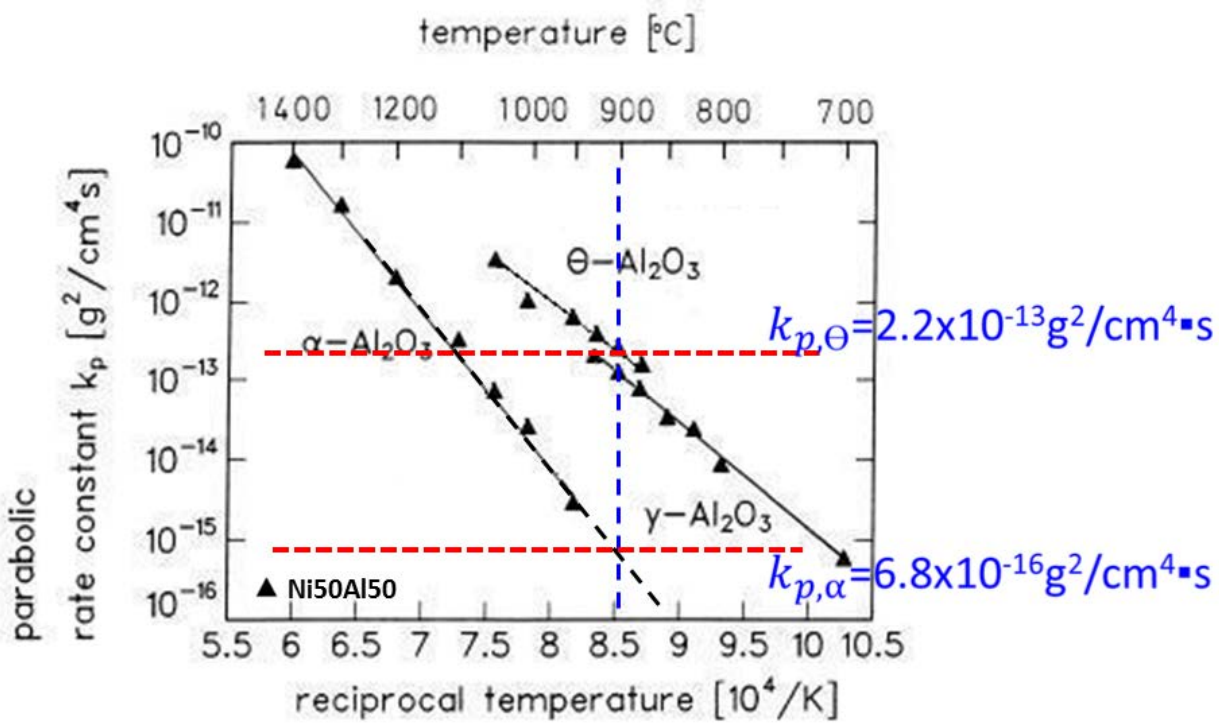

Figure 5.51 Temperature dependence of the growth rate constants for θ-Al_2O_3 and α-Al_2O_3scale growth[61]

$$J_O = \frac{d(\Delta m_O)}{dt} = \frac{1}{2}\sqrt{\frac{k_p}{t}} \quad (5.\ 9)$$

where k_p is the parabolic rate constant and t is time. The calculated J_o is plotted as a function of reaction time in Figure 5.52. The oxygen needed for θ growth is much more than that for α due to the three-orders of magnitude difference in the respective k_p values. As time increases, the instantaneous growth rate decreases, and so the oxygen supply needed correspondingly decreases.

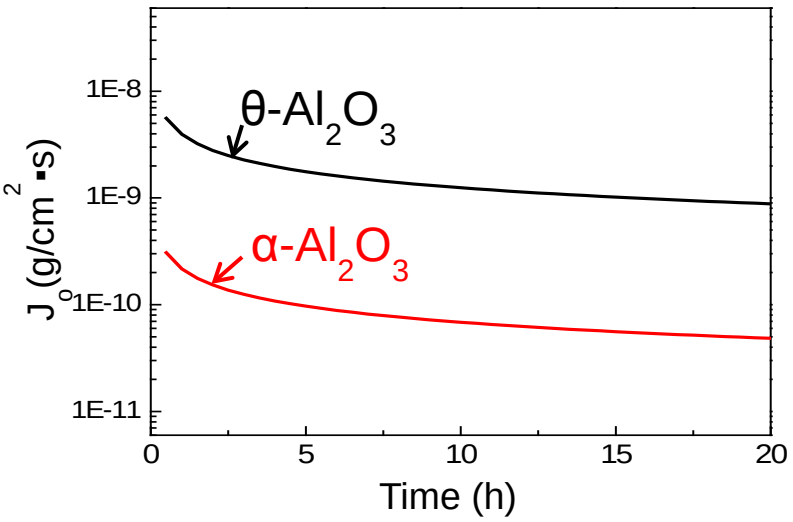

Figure 5.52 Comparison of J_o vs. t curves for α-Al_2O_3 and Θ-Al_2O_3 growth at 900°C.

Based on the treatment of gas mass transfer in the viscous flow regime [141], the oxygen supply in the air can be calculated. The calculation assumes that the flux of the reacting gases is flowing parallel to a flat surface and that air is 79% N_2 +21% O_2. Gas flow rate is fixed at 0.002cm/s which was done in the present experiments. The corresponding Reynolds number is calculated to be 2.64×10^{-4}, confirming that the gas flow is laminar. In laminar flow, the oxygen flux, J_{O_2}, flowing parallel to sample surface is given by

$$J_{O_2} = \frac{k_m}{RT}\left(pO_2^{(o)} - pO_2^{(i)}\right) \text{ (mole } O_2/\text{cm}^2\text{s)} \qquad (5.10)$$

where k_m is the mass-transfer coefficient (cm/s), T the absolute temperature (K), R the gas constant 82.057cm^3·atm/mole·K, $pO_2^{(o)}$ the bulk gas pressure (0.21 atm in the air), and $pO_2^{(i)}$ the gas pressure at the sample surface (assumed to be zero). k_m can be estimated using[142]:

$$k_m = 0.664\left(\frac{D_{AB}}{\nu_{AB}}^4\right)^{\frac{1}{6}}\left(\frac{\upsilon_x}{L}\right)^{1/2} \text{(cm/s)} \qquad (5.11)$$

where D_{AB} is the diffusion coefficient in an A-B binary gas (cm^2/s), with the subscripts A and B representing oxygen and nitrogen, respectively. v is the kinematic viscosity (cm^2/s), v_x the linear gas flow rate (0.002cm/s), and L the length of the sample surface parallel to the gas flow (1cm). The Chapman-Enskog expression for D_{AB} can be written as[142, 143] :

$$D_{AB} = \frac{1.858 \times 10^{-3} \sqrt{T^3\left(\frac{1}{M_A}+\frac{1}{M_B}\right)}}{P\sigma_{AB}^2 \Omega_{D,AB}} \ (cm^2/s) \qquad (5.12)$$

where

$$\sigma_{AB} = \frac{\sigma_A+\sigma_B}{2} \ (Å) \qquad (5.13)$$

and

$$\frac{\varepsilon_{AB}}{k} = \frac{\sqrt{\varepsilon_A \varepsilon_B}}{k} \ (K^{-1}) \qquad (5.14)$$

Here, σ_{AB} is the average collision diameter, $\Omega_{D,AB}$ a dimensionless function of the temperature that represents the interaction potential between an atom (or molecule) of A and an atom (or molecule) of B. ε_{AB} is the interaction energy (based on the *Lennard-Jones potential*), M is the molecular weight, k is the Boltzman constant and P the total system pressure (set to 1 atm during TGA analysis). The values of σ, ε/k and molar mass for O_2, N_2 and Ar are listed in Table 5.5 [142-144].

Table 5.5 Intermolecular force parameters [142-144]

Species	σ (Å)	ε/*k* (K)	*M* (g/mol)
O_2	3.467	106.7	32.00
N_2	3.798	71.4	28.013
Ar	3.542	93.3	39.948

Using the values of σ provided in Table 5.5, from equation (5.13)

$$\sigma_{O_2-N_2} = \frac{\sigma_{O_2}+\sigma_{N_2}}{2} = 3.6325\text{Å}$$

Using the values of ε/*k* provided in Table 5.5, from equation (5.14)

$$(\frac{\varepsilon}{k})_{O_2-N_2} = \sqrt{(\frac{\varepsilon}{k})_{O_2} \cdot (\frac{\varepsilon}{k})_{N_2}} = 87.3K$$

At 900°C (1173K),

$$(\frac{kT}{\varepsilon})_{O_2-N_2} = \frac{900+273}{87.3} = 13.4$$

Using the above calculated value of 13.4, and the relationship between kT/ε_{AB} and $\Omega_{D,AB}$ provided in Table 5.6, a linear interpolated value of $\Omega_{D,AB}$ is found to be 0.7157.

Table 5.6 The dependence of $\Omega_{D,AB}$ on kT/ε_{AB} [145]

kT/ε_{AB}	$\Omega_{D,AB}$
10	0.7424
20	0.6640

Substituting the various input parameters into equation (5.12), it is found that, at 900°C (1173K)

$$\mathrm{D}_{\mathrm{O_2-N_2}} = 2.045\mathrm{cm}^2/\mathrm{s}$$

Kinematic viscosity *v* is given by

$$\nu = \frac{\eta}{\rho}(\mathrm{cm}^2/\mathrm{s}) \qquad (5.15)$$

where reciprocal ρ is the density of the gas and η is the viscosity of the gas. If the gas is a mixture, then η_{mix} is given by

$$\eta_i = 2.6693 \times 10^{-5} \frac{\sqrt{M_i T}}{\sigma^2 \Omega}(\text{poise}) \qquad (5.16)$$

$$\eta_{mix} = \sum_{i=1}^{n} \frac{X_i \eta_i}{\sum_{j=1}^{n} X_j \Phi_{ij}} \text{ (poise)} \quad (5.17)$$

$$\phi_{ij} = \frac{1}{\sqrt{8}}\left(1 + \frac{M_i}{M_j}\right)^{-1/2}\left[1 + \left(\frac{\eta_i}{\eta_j}\right)^{1/2}\left(\frac{M_i}{M_j}\right)^{1/4}\right]^2 \quad (5.18)$$

where η_i is the viscosity of the pure species i, η_{mix} the viscosity of the mix of species, and Ω the viscosity collision integral.

For oxygen, using its ε/*k* value provided in Table 5.5, at 900°C,

$$\frac{kT}{\varepsilon} = \frac{1173}{106.7} = 10.99$$

Using the above calculated value of 10.99, and the relationship between kT/ε and Ω provided in Table 5.7, a linear interpolated value of Ω is found to be 0.81461.

Table 5.7 The dependence of Ω on kT/ ε[145]

kT/ε	Ω
10	0.8242
20	0.7432

Therefore, using equation (5.16)

$$\eta_{O_2} = 2.6693 \times 10^{-5} \frac{\sqrt{M_{O_2} T}}{\sigma^2 \Omega} = 5.270 \times 10^{-4} \text{(poise)}$$

For nitrogen, using its ε/*k* value provided in Table 5.5, at 900°C,

$$\frac{kT}{\varepsilon} = \frac{1173}{71.4} = 16.43$$

Using the above calculated value of 16.43, and corresponding values of kT/ε and Ω provided in Table 5.7, a linear interpolated value of Ω is found to be 0.7721. Therefore, from equation (5.16)

$$\eta_{N_2} = 2.6693 \times 10^{-5} \frac{\sqrt{M_{N_2} T}}{\sigma^2 \Omega} = 4.344 \times 10^{-4} \text{(poise)}$$

Using the above calculated values of η_{O_2} and η_{N_2} , from equation (5.18)

$$\Phi_{O_2-N_2} = 1.105$$

$$\Phi_{N_2-O_2} = 0.911$$

$$\Phi_{N_2-N_2} = \Phi_{O_2-O_2} = 1$$

Then, substituting the various input parameters into equation (5.17), it gives

$$\eta_{mix} = \frac{X_{O_2}\eta_{O_2}}{X_{O_2}\Phi_{O_2-O_2}+X_{N_2}\Phi_{O_2-N_2}} + \frac{X_{N_2}\eta_{N_2}}{X_{N_2}\Phi_{N_2-N_2}+X_{O_2}\Phi_{N_2-O_2}} = 4.519 \times 10^{-4}\text{(poise)}$$

Next, to calculate the kinetic viscosity of air at 900°C, one should first calculate the density of air at this temperature. A rough estimation can be calculated as follows:

$$\rho_{N_2} = \frac{PM}{RT} = 2.901 \times 10^2 g/m^3$$

$$\rho_{O_2} = \frac{PM}{RT} = 3.314 \times 10^2 g/m^3$$

$$\rho_{air} = X_{N_2}\rho_{N_2} + X_{O_2}\rho_{O_2} = 2.988 \times 10^2 g/m^3$$

$$\nu_{air} = \frac{\eta_{air}}{\rho_{air}} = 1.512 cm^2/s$$

Substituting the various input parameters into equation (5.11), it is found that,

$$k_m = 0.045 \text{ cm}/s$$

This gives from equation (5.10),

$$J_{O_2} = 9.817 \times 10^{-8} \text{ (mole/cm}^2\text{s)}$$

$$J_O = 3.132 \times 10^{-6} \text{ (g/cm}^2\text{s)}$$

This value of J_o is shown by the golden line in Figure 5.53. It is seen that the amount of oxygen supply in air is sufficient for both θ and α-Al_2O_3 to grow freely. Theta grows much faster in the kinetic competition with alpha, thus it is easy for theta to predominate in air. When sulfur is present, it is postulated that there is a surface blocking effect that essentially reduces oxygen

supply in O_2+0.1%SO_2. It is possible that the blocking is so much that it can dramatically decrease oxygen supply. If the oxygen supply is decreased to the level indicated by the blue arrow in Figure 5.53, there would not be enough oxygen for theta to grow at its maximum rate, but sufficient for the growth of α-Al_2O_3. In this case, $k_{p,\theta}$ would decrease to a much larger extent compared with $k_{p,\alpha}$. When theta formation is significantly hindered, the stable alpha can more easily establish itself as a complete scale. So, the hypothesis is that when oxygen supply is limited, Θ-Al_2O_3 formation is inhibited to the extent that the kinetic competition favors α.

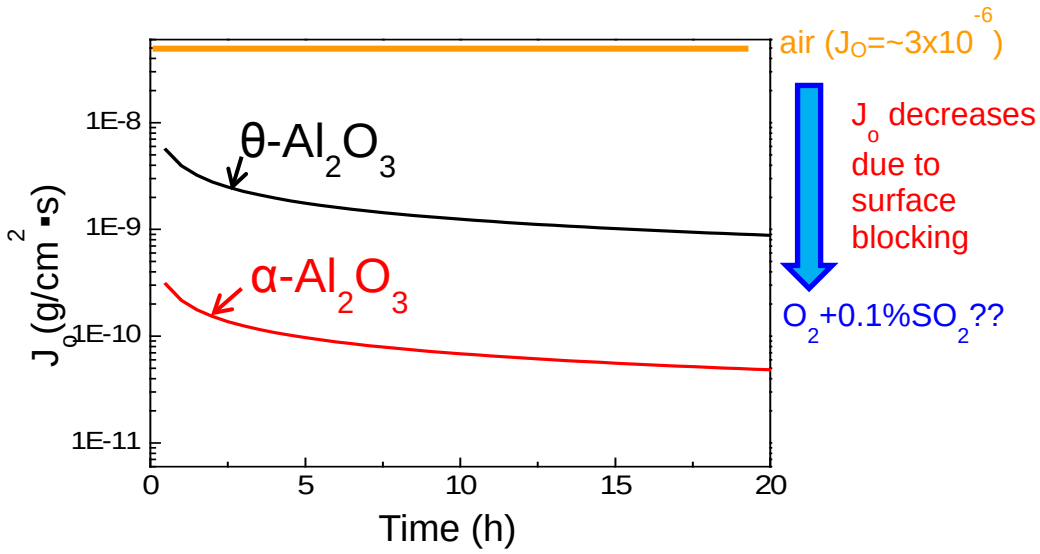

Figure 5.53 The oxygen supply available in the air at 900°C (represented by the golden line) and the proposed decreased oxygen supply in O_2+0.1%SO_2 atmosphere due to surface blocking effect (schematically shown by blue arrow)

To test this hypothesis, samples were oxidized in 99.999% high purity Ar (O_2<1.4ppm). Gas flow rate was fixed at 0.01cm/s, giving a Reynolds number of 72, so that the gas flow was laminar. Using the values of σ provided in Table 5.5, from equation (5.13)

$$\sigma_{Ar-O_2} = \frac{\sigma_{Ar} + \sigma_{O_2}}{2} = 3.5045$$

Using the values of ε/*k* provided in Table 5.5, from equation (5.14)

$$(\frac{\varepsilon}{k})_{Ar-O_2} = \sqrt{(\frac{\varepsilon}{k})_{O_2} \cdot (\frac{\varepsilon}{k})_{Ar}} = 99.8K$$

At 900°C (1173K),

$$(\frac{kT}{\varepsilon})_{Ar-O_2} = 11.75$$

Using this value of 11.75, it is found from Table 5.7 that

$$\Omega_{D,AB}=0.729$$

Thus using the above calculated values of σ_{Ar-O_2} and $\Omega_{D,AB,}$ from equation (5.12), it is found

$$\mathrm{D}_{\mathrm{O_2-Ar}} = 1.978\mathrm{cm}^2/\mathrm{s}$$

As 99.999% of the gas is Ar, for simplification, η_{Ar} was calculated instead of η_{Ar-O_2}.

As provided in Table 5.5, the value of ε/*k* for Ar equals to 93.3. at 900°C (1173K)

$$\frac{kT}{\varepsilon} = 12.572$$

Using this value of 12.572, it is found from Table 5.7 that $\Omega = 0.8034$

Therefore, from equation (5.16)

$$\eta_{Ar} = 2.6693 \times 10^{-5} \frac{\sqrt{M_{Ar}T}}{\sigma^2\Omega} = 5.7328 \times 10^{-4} \text{ (poise)}$$

The density of Ar at 900°C is

$$\rho_{Ar} = \frac{PM}{RT} = 4.137 \times 10^2 g/m^3$$

From equation (5.15),

$$\nu_{Ar} = \frac{\eta_{Ar}}{\rho_{Ar}} = 1.386 cm^2/s$$

The linear Ar flow rate is 0.010 cm/s, so that from equation (5.11)

$$k_m = 0.099\text{cm}/s$$

Thus from equation (5.10)

$$J_{O_2} = 1.440 \times 10^{-12} \ (\text{mole}/\text{cm}^2\text{s})$$

$$J_O = 4.608 \times 10^{-11} \ (\text{g}/\text{cm}^2\text{s})$$

The oxygen supply in Ar is indicated by the purple line in Figure 5.54. The value is below that for un-inhibited Θ growth, but close to the oxygen supply needed for α growth at its reported rate. Thus, if the hypothesis that limited oxygen supply favors α-Al_2O_3 formation is valid, then one should expect to see the promoted establishment of α-Al_2O_3 in Ar.

Before testing alloys in Ar, it is worthwhile analyzing whether the J_O values determined are valid to real experimental conditions. The mass transfer theory used in this analysis is based on gas flowing over a flat plate in an unconstrained space, thus J_o may possibly be underpredicted due to the effects of reactor tube walls on flow patterns. Næss et al. [146] recently reported that the real value can be 2 or 3 times higher than the predicted value based on computational fluid dynamic modeling of their system with their flow parameters. However, with the tube cross-section and sample position being similar, the gas flow rate in this experiment is two orders of magnitude smaller than that used by Næss et al. [146]. Gas flow will be less constrained by the reactor tube wall when the flow rate is much smaller. Thus, in this study, the real value should be close to the prediction.

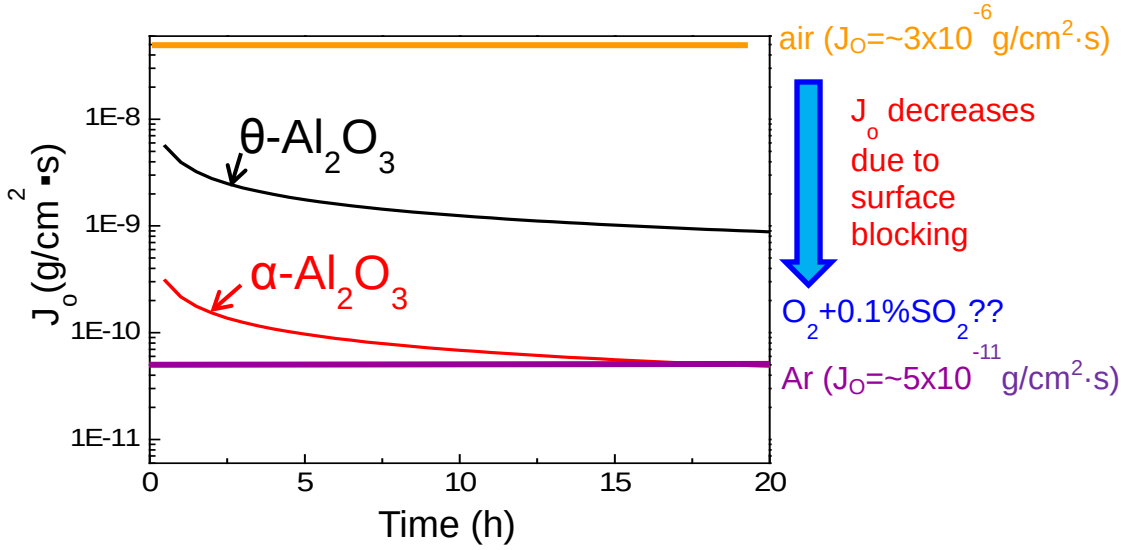

Figure 5.54 The oxygen supply available in 99.999% high purity Ar (represented by the purple line)

Figure 5.55 shows PSLS spectra from the scales formed on alloy 5 during isothermal oxidation in Ar at 900°C. Clearly, very strong alpha peaks are observed after 10 and 20 hours oxidation. The same alloy, when oxidized in air for 10 and 20 hours, formed primarily θ-Al_2O_3, as shown in Figure 5.42 and Figure 5.44. Thus the establishment of α-Al_2O_3 was favored when exposure was done in high-purity Ar. In other words, low P_{O_2} or, in turn, low J_o, favors α-Al_2O_3 establishment. A similar result was observed on an EBPVD NiCoCrAlY coating during oxidation at 1100°C [147, 148]. Specifically, it was found in those studies that after 1 hour oxidation in 0.1Pa oxygen atmosphere, an exclusive α-Al_2O_3 scale was formed; θ-Al_2O_3 scale formed when oxidized at 100Pa oxygen. Orozco[113] and Orozco et al.[121] recently conducted a kinetics study of the competitive growth between θ-Al_2O_3 and α-Al_2O_3 in low P_{O_2}. The analysis was based on 1) alumina is an ionic oxide with scale growth supported by transport via defects[37]; 2) θ-Al_2O_3 is mainly a p-type oxide[113] with Al vacancies (V_{Al}''') being the predominant ionic

defect, so that Al^{3+} cation diffusion predominates [118-120]. By contrast, α-Al_2O_3, is mainly n-type oxide [113] and the dominant defects are oxygen vacancies ($V_O^{\cdot\cdot}$), meaning a predominance of oxygen diffusion. Thus,

For θ-Al_2O_3, $\left[V_{Al}^{'''}\right] = \left(\frac{K_1}{81}\right)^{3/16} {p_{O_2}}^{3/16}$, $k'_{V_{Al}^{'''}} = C_1\left[\left(p''_{O_2}\right)^{3/16} - \left(p'_{O_2}\right)^{3/16}\right]$;

For α-Al_2O_3, $[V_{O}^{\cdot\cdot}] = \left[\frac{K_1}{16}\right]^{1/6} {p_{O_2}}^{-1/6}$, $k'_{V_O^{\cdot\cdot}} = C_3\left[\left(p''_{O_2}\right)^{-1/6} - \left(p'_{O_2}\right)^{-1/6}\right]$.

where p''_{O_2} and p'_{O_2} represent the oxygen partial pressure at the scale/gas and alloy/scale interfaces, respectively. Generally, p''_{O_2} is much greater than p'_{O_2}. Being a p-type oxide, the growth rate of θ-Al_2O_3 is more affected by p_{o_2} than is α-Al_2O_3. Thus, when oxygen supply is limited, the growth rate of θ-Al_2O_3 decreases more dramatically than that of α-Al_2O_3. During the lateral growth, the inhibition of θ-Al_2O_3 formation will allow α-Al_2O_3 to gain advantage in establishing a continuous layer underneath.

For a complete analysis of the α-Al_2O_3 establishment, the nucleation rate must also be considered. For heterogeneous nucleation, there is a substrate structure effect such that any orientation that provides compatibility with α-Al_2O_3 will facilitate its nucleation [149-151]. The same is true for θ-Al_2O_3. For example, due to an epitaxial orientation relationship between β-NiAl and θ-Al_2O_3, β-NiAl substrate prefers θ-Al_2O_3 nucleation [66, 152, 153]. For β-NiAl, low Po_2 might not necessarily promote α-Al_2O_3 scale establishment. However, in this study, the alloy substrate is γ′-Ni_3Al and there is no known preference for either θ-Al_2O_3 or α-Al_2O_3 nucleation. Thus, given this condition, low Po_2 which inhibits θ-Al_2O_3 growth to larger extent, can promote α-Al_2O_3 scale establishment on γ′-Ni_3Al.

The promoted α-Al_2O_3 establishment in low p_{o_2} atmosphere oxidation on the present alloy system is considered as strong support for the hypothesis of surface blocking. A predominance α-Al_2O_3 scale growth occurs when oxidations were in O_2+0.1%SO_2 and low p_{o_2} atmosphere, even though these two conditions are much different. During oxidation in O_2+0.1%SO_2, surface blocking by sulfur enrichment effectively decreases the oxygen supply, which is advantageous to the establishment and growth of α-Al_2O_3.

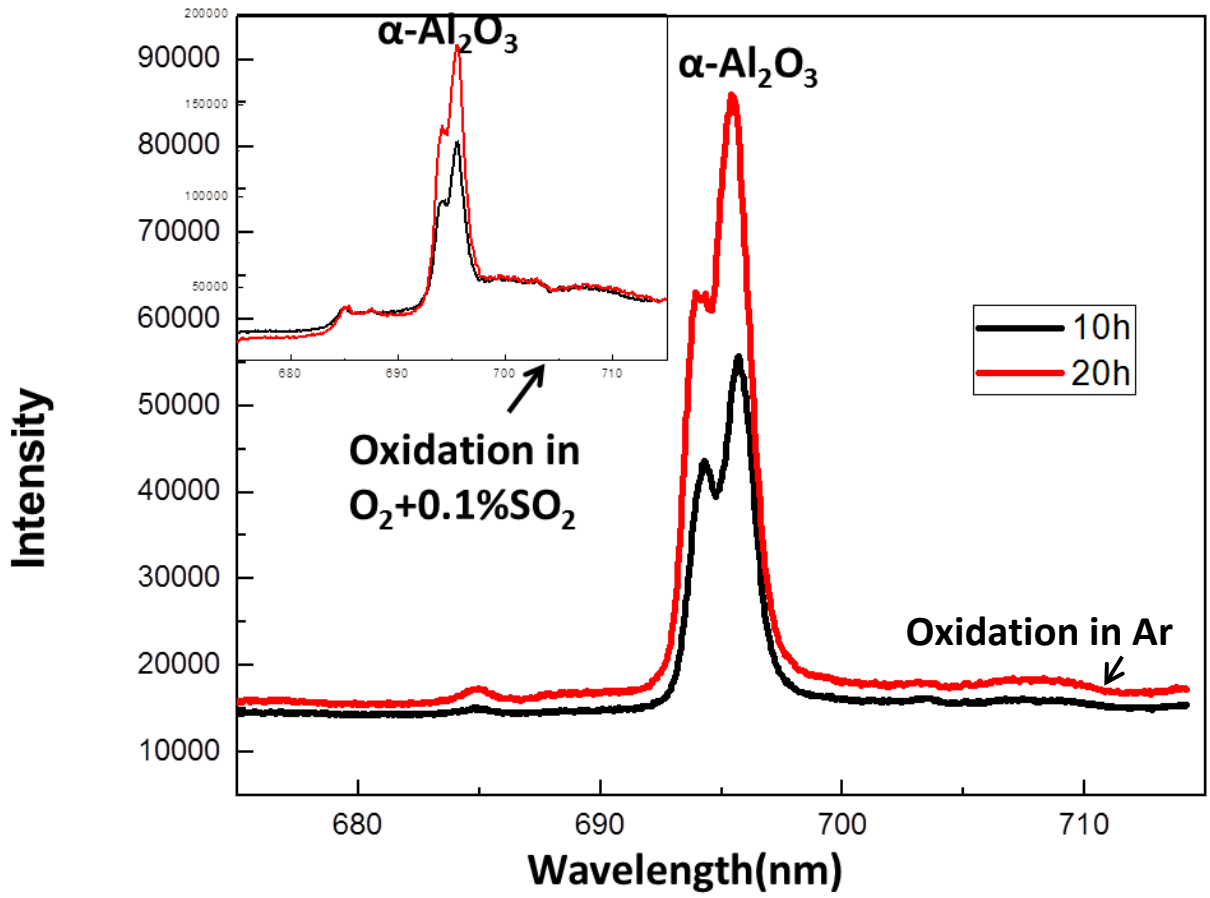

Figure 5.55 PSLS spectra from the scales formed on alloy 5 during isothermal oxidation in high purity Ar (O_2<1.4ppm) at 900°C. As a comparison, the PSLS spectra from the scales formed in O_2+0.1%SO_2 is plotted in the up left corner

5.2.4 Conclusions

Single-phase γ'-Ni_3Al model alloys were exposed at 900°C in an O_2+0.1%SO_2 atmosphere for 20 hours and, different from the air oxidation results which show a predominant Θ-Al_2O_3 growth on these alloys, α-Al_2O_3 scale growth predominated from the very early stage of oxidation in O_2+0.1%SO_2. Thus, sulfur from the gas atmosphere promoted the establishment of α-Al_2O_3.

One single-phase γ''-Ni_3Al alloy was oxidized in air and O_2+0.1%SO_2 for 1, 2, 5, 10 and 20 hours. A kinetic competition of θ-Al_2O_3 and α-Al_2O_3 was observed during the scale growth. θ-Al_2O_3 predominates during oxidation in air after a short time, while α-Al_2O_3 predominates during oxidation in O_2+0.1%SO_2 during that same time. Thus, the presence of sulfur can affect this kinetic competition of θ-Al_2O_3 and α-Al_2O_3.

This promoted α-Al_2O_3 establishment was due to sulfur enrichment on the alloy surface. This enrichment started when samples were exposed to O_2+1%SO_2 at the pre-tested position (~150°C) while setting up the gas equilibrium. It was found by XPS measurement, which has a ~10nm depth of penetration[154], that the sulfur was mainly in the form of $NiSO_4$ (i.e. S^{6+} state). However, whether the sulfur was exclusively as $NiSO_4$ is not certain. The chemieSTEM results showed a ~20nm band of sulfur enrichment at the surface of the sample exposed in the pre-test conditions. The surface enrichment of sulfur is inferred to block the surface sites for oxygen reaction and consequently effectively decrease oxygen supply for the scale growth. It is assumed that with limited oxygen supply, the faster growing θ-Al_2O_3 is less favored, thus allowing α-Al_2O_3 to have sufficient time to establish a continuous layer during the kinetic competition with θ-Al_2O_3. This hypothesis was supported by kinetic calculations and complementary tests in a low

p_{O_2} atmosphere. A promoted α-Al_2O_3 establishment was observed on a model alloy when oxidation took place in high purity Ar (O_2<1.4ppm) at 900°C. When oxygen supply is limited, the growth rate of θ-Al_2O_3 decreases more dramatically than that of α-Al_2O_3, during the lateral growth, the inhibition of θ-Al_2O_3 growth will allow α-Al_2O_3 to gain advantage in establishing a continuous layer underneath. Therefore, the sulfur-promoted α-Al_2O_3 establishment can be due to sulfur preferentially adsorbing and effectively limiting oxygen supply.

5.3 EFFECT OF ENVIRONMENTAL SULFUR ON THE ESTABLISHMENT OF AN ALUMINA SCALE

5.3.1 Materials tested

Four model alloys were prepared to study the oxide map in sulfur-containing conditions. The nominal compositions are shown in Table 5.8 and their positions on the oxide map [54] are shown in Figure 5.56. Alloy 2 is on the borderline between forming alumina internally and externally, alloys 1, 3 and 4 are in the NiO-forming region, while alloy 4 is closest to the kinetic boundary of forming alumina externally. All the model alloys are in the single phase γ-Ni (Cr,Al) phase region of the Ni-Cr-Al phase diagram at 1000°C [108]. PWA 1484 and PWA1487 were tested to study the effect of sulfur on commercial systems. Their nominal compositions are also given in Table 5.8.

Table 5.8 Nominal composition of the alloys studied

Alloy	Commercial alloys (wt.%)										
	Ni	Al	Cr	Co	Mo	W	Ta	Ti	Hf	Re	Y
Model #1	Bal.	2.4	4.6	-	-	-	-	-	-	-	-
Model #2	Bal.	3	5	-	-	-	-	-	-	-	-
Model #3	Bal.	3.1	3.2	-	-	-	-	-	-	-	-
Model #4	Bal.	3.9	3.3	-	-	-	-	-	-	-	-
PWA 1487	Bal.	5.6	5	10	2	6	8.7	-	0.1	3	0.01
PWA 1484	Bal.	5.6	5	10	2	6	8.7	-	0.1	3	-

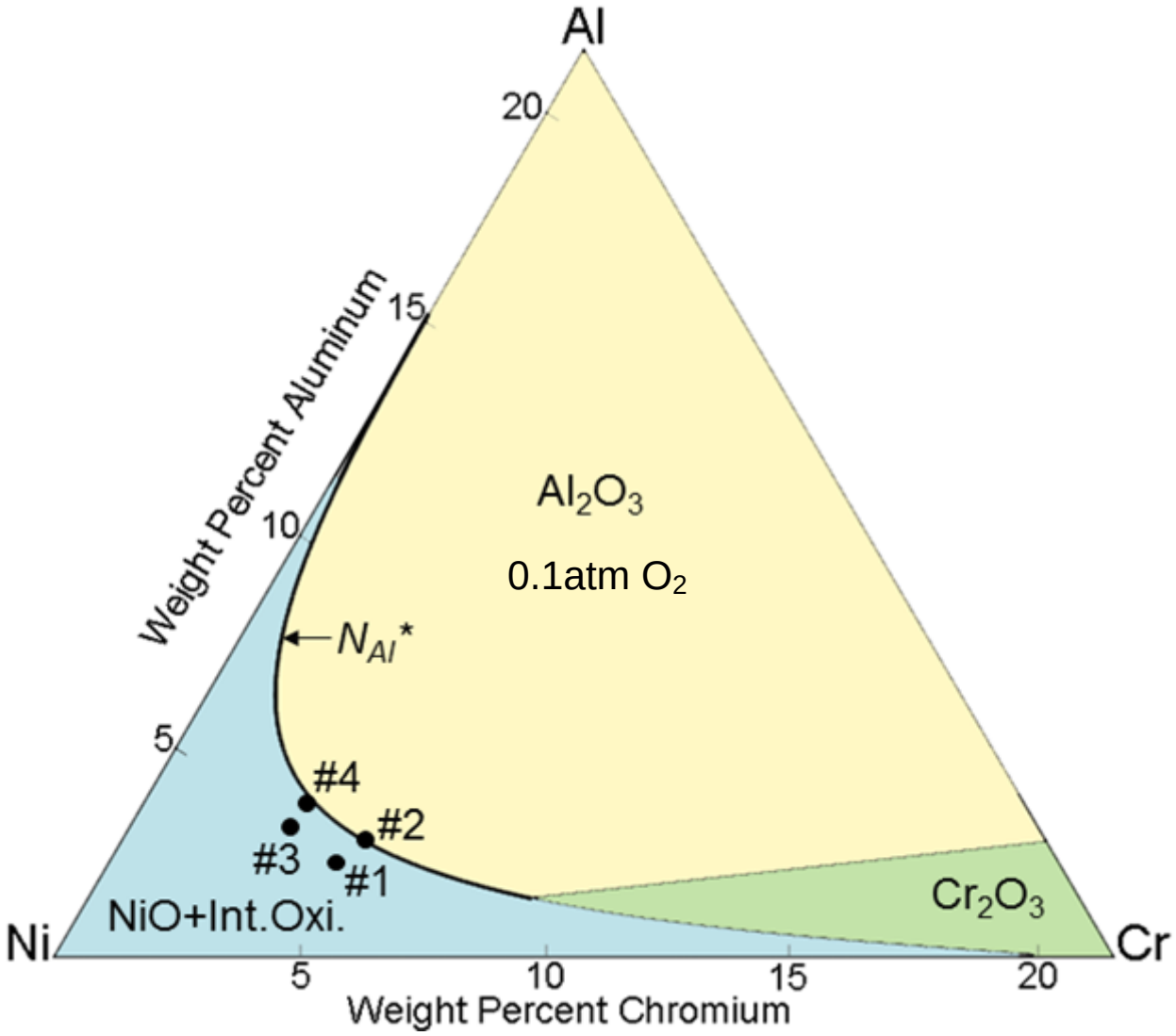

Figure 5.56 Oxide map for rolled Ni-Cr-Al alloy in 0.1atm O_2 at 1000°C (based on ref. [54])

5.3.2 Results

5.3.2.1 Oxide map for O_2+1%SO_2

Model alloys were oxidized in air and O_2+1%SO_2 at 1000°C for 20 hours. Resulting cross-sectional SEM images are shown in Figure 5.57. When exposed to air, alloys 1, 3, and 4

formed external NiO and internal Al_2O_3/spinel, as inferred from XRD and EDS compositional analyses. Alloy 2 oxidized in a mixed mode, with the majority of regions forming a non-protective product of internal Al_2O_3/spinel and external NiO. The remaining regions formed Al_2O_3 scale. These results are consistent with what is predicted by the oxide map [54] (Figure 5.56) . However, when oxidized in the O_2+1%SO_2 atmosphere, alloys 2 and 4 formed a continuous scale layer of Al_2O_3. Alloy 1 manifested localized oxidation in which some regions formed external Al_2O_3 scale and the rest of the alloy surface formed thick external NiO scale and internal Al_2O_3/$NiAl_2O_4$. This was similar to alloy 2 oxidation in air. A comparison of oxidation results in air and O_2+1%SO_2 shows that the alloys can form a protective Al_2O_3 scale with lower contents of Al and/or Cr (e.g. alloys 2 and 4) when oxidation takes place in the SO_2-containing atmosphere. Thus, a small amount of sulfur in the atmosphere can promote the transition from internal-to-external Al_2O_3 formation. Based on the performance of this group of alloys, a new critical aluminum content boundary in the oxide map can be estimated for environments that contain a small amount of SO_2. This new kinetic boundary passes through the border-line composition of alloy 1, which is shown by the solid line in Figure 5.58. The N_{Al}^{*} kinetic boundary for O_2+1%SO_2 shifts towards lower Al/Cr concentrations when compared with the original boundary (the dash line) for the SO_2 free environment, and the shift is significant.

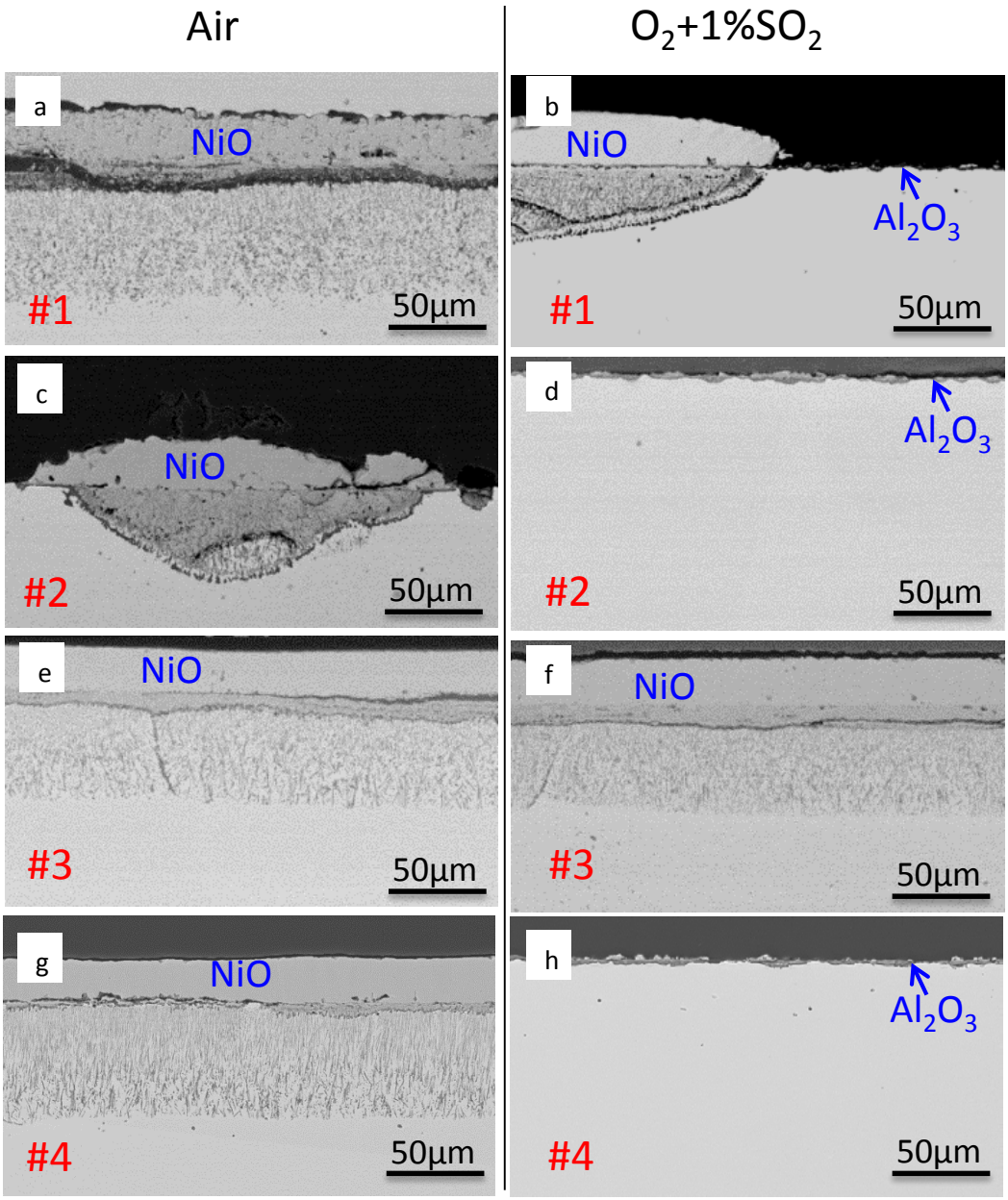

Figure 5.57 SEM cross section images of model alloy 1-4 oxidized in air (column left) and O_2+1%SO_2 (column right) for 20 hours

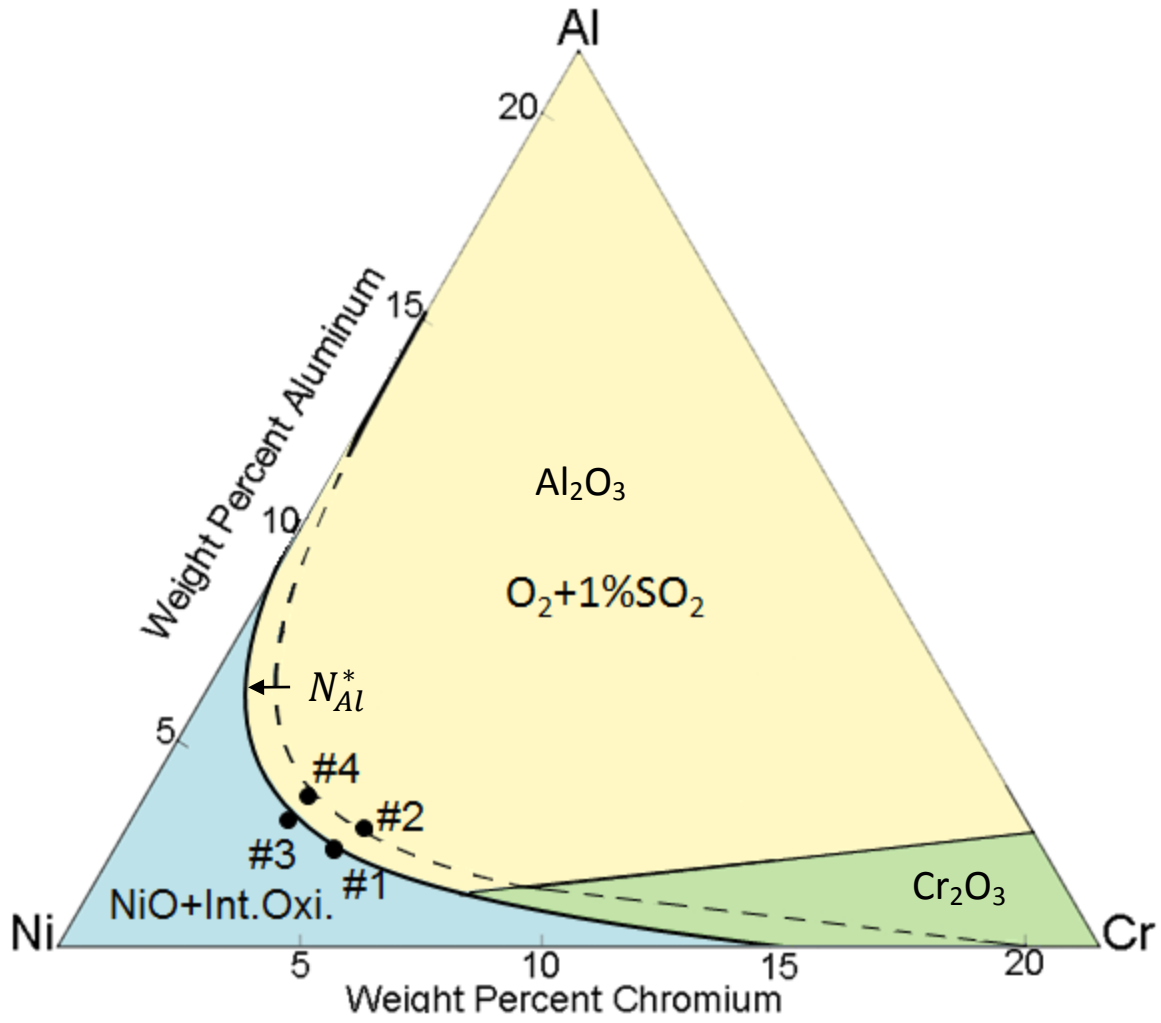

Figure 5.58 Oxide map for rolled Ni-Cr-Al alloy in O_2+1%SO_2 at 1000°C with the N^*_{Al} kinetic boundary represented by the solid line. For comparison, the N^*_{Al} kinetic boundary in air at 1000°C [54] is shown in this figure by the dashed line.

It was further found that this promotion of the internal-to-external transition in the presence of trace SO_2 does not necessarily need a continuous SO_2 supply from the gas atmosphere during reaction. This was demonstrated by pre-exposing specimens to O_2+1%SO_2 at low temperature and then oxidizing in air at 1000°C for 20 h. The test procedure consisted of two stages. First, the sample was laid in the pre-heat zone of the furnace (maximum temperature ~170ºC) with Ar gas

flowing for 2 hours, followed by O_2+1%SO_2 for 12 hours. Then the sample was removed from sulfur-containing gas exposure, followed immediately by exposure to air at 1000°C for 20 hours. The resulting cross-sectional images are shown in Figure 5.59. It is clear that both alloys formed an alumina scale. The appearance of the cross-sectional microstructures is almost the same as that of samples exposed to O_2+1%SO_2 (Figure 5.57d and 5.56h), even though the samples in Figure 5.59 was oxidized in air during the high-temperature exposure (1000°C). Sulfur was enriched on the sample surface after the pre-test exposure to the SO_2-containing atmosphere at ~170ºC, which is similar to what was reported in section 5.2.2.3. The surface enrichment of sulfur was confirmed to be $NiSO_4$ through XPS analysis, consistent with the findings in section 5.2.2.4. It is deduced that this surface-enriched sulfur promoted the internal-to-external alumina scale formation.

Concentration depth profiles in the samples after the pre-test exposure to the SO_2-containing atmosphere at ~170ºC were measured by XPS equipped with a sputtering gun. The results are shown in Figure 5.59. It was found that an oxide scale approximately 200nm thick had formed, with 4-5 at.% sulfur enrichment in the top half. The oxide scale was deduced to be a mixture of NiO and $NiSO_4$, with very little Cr or Al present. The $NiSO_4$ formed during the low temperature, pre-test exposure may dissociate during high-temperature exposure, as discussed in section 5.2.3.2. However, whether or not dissociation occurred, the surface-enriched sulfur clearly has an effect on the oxidation behavior. One possibility is that before being completely dissociated at high temperature, $NiSO_4$ may affect the oxidation behavior during the heating stage. Recent work appears to indicate that the product formed in the very early stages of oxidation can influence steady-state growth kinetics [155]. Another possibility is that, after $NiSO_4$ dissociation, sulfur is still preserved on the sample surface and has a poisoning effect on

the oxidation reaction (i.e. site blocking at preferred reaction sites). In either case, the surface-enriched sulfur could inhibit O_2 consumption at the reacting surface due to some form of blocking [156], which is discussed in greater detail in section 5.2.3.2. As will be discussed later in section 5.3.3.3, this may lead to the promotion of the internal-to-external alumina scale formation.

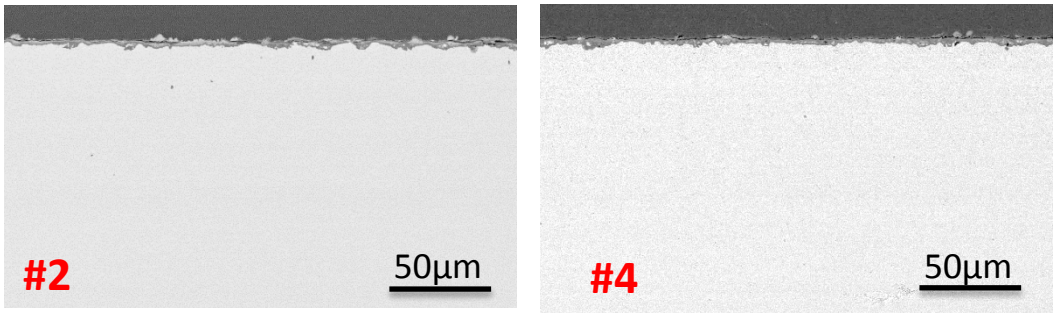

Figure 5.59 Cross-sectional images of model alloys 2 and 4 with chemisorbed sulfur after oxidation in air at 1000°C for 20 hours

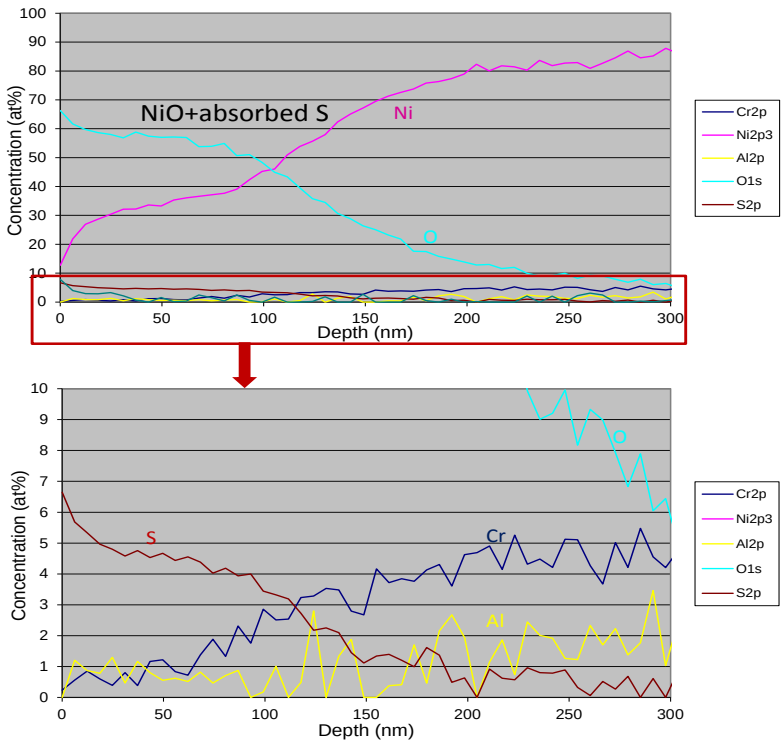

Figure 5.60 XPS depth profile of model alloy 5 exposed to O_2+0.1%SO_2 at pre-test position (~170°C) for 12hours

5.3.2.2 Effect of trace SO_2 on the oxidation behavior of commercial alloys

A similar beneficial effect of trace SO_2 was observed for the commercial alloys (~5wt.% Cr) assessed in this study, even at different temperatures. Figure 5.61 shows cross-sectional SEM images of PWA1487 after 100 hours of oxidation at 900°C. When oxidized in air, the Al oxidized internally; while oxidation in O_2+1%SO_2 led to the eventual establishment of a continuous Al_2O_3 scale. These results confirm that a small amount of sulfur in the atmosphere can promote the transition from internal to external Al_2O_3 formation. Figure 5.62 shows cross-sectional SEM images of the PWA1484 alloy after 20 hours of exposure at 900°C. When

oxidized in air, an internal Al_2O_3 layer with non-uniform NiO scale had formed; while when oxidized in uncatalyzed O_2+0.1%SO_2, a continuous thin Al_2O_3 scale formed.

Figure 5.63 shows cross-sectional SEM images of PWA1487 after 100 hours of oxidation at 1100°C. When oxidized in air and O_2+0.1%SO_2, the alloy formed an external scale comprised of an inner Al_2O_3 layer with an outer spinel scale. However, the spinel layer formed in O_2+1%SO_2 is thinner than that formed in air. This could be a result of an external Al_2O_3 layer established earlier in the sulfur-containing atmosphere. In other words, in the sulfur-containing environment, less transient oxidation occurred because a continuous alumina scale formed sooner which precluded the outward diffusion of Ni. These results are indirect evidence of sulfur's beneficial effect in promoting external Al_2O_3 formation.

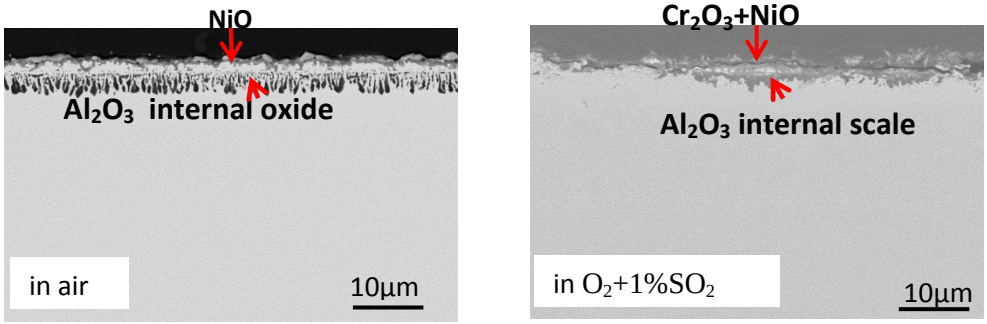

Figure 5.61 PWA1487 after 100 hours of oxidation at 900°C in air and O_2+1%SO_2

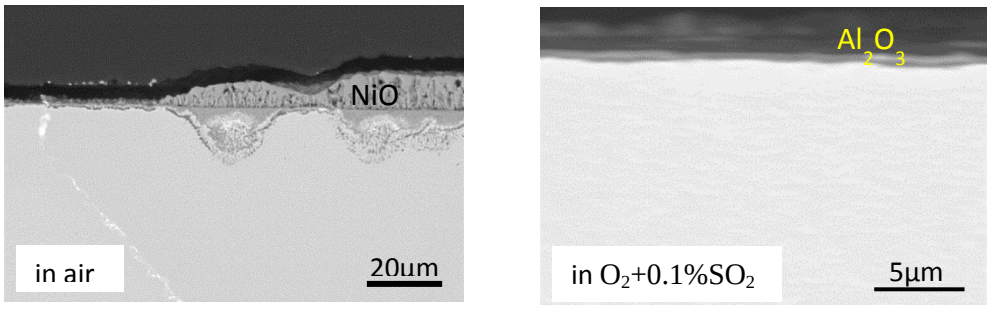

Figure 5.62 PWA1484 after 20 hours of oxidation at 900°C in air and uncatalyzed O_2+0.1%SO_2

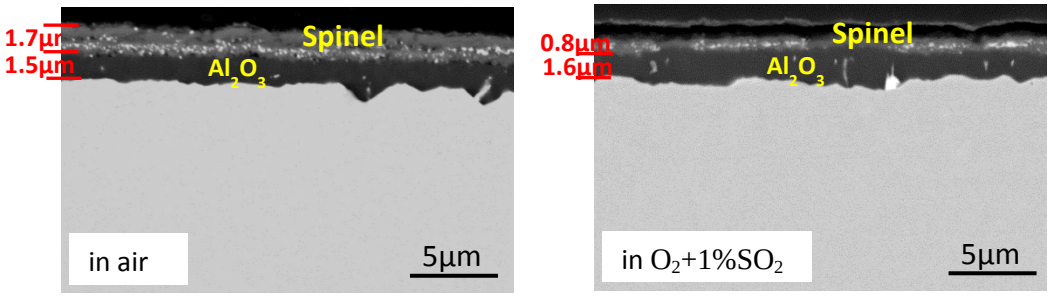

Figure 5.63 PWA1487 after 100 hours of oxidation at 1100°C in air and O_2+1%SO_2

It was found that the amount of SO_2 in the atmosphere affects the predominance of alumina in the scale. This was demonstrated by the oxidation of PWA1484 alloy in uncatalyzed O_2+(10-1000ppm)SO_2 for 20 hours. The resulting weight gains and surface morphologies are shown in Figure 5.64 and Figure 5.65, respectively. In all cases, external alumina scales formed. With an increase of SO_2 content in the atmosphere, the sample weight gain decreased and less amount of spinel was present in the scale. This more exclusive Al_2O_3 formation with increase in SO_2 content is inferred to be due to the preferential adsorption of sulfur that can block oxygen[138], thus affecting the initial oxidation of the alloy. Specifically, the blocking effect by the surface enrichment of sulfur is likely to effectively cause decreased oxygen supply (see section 5.2.3.2). Nickel oxide grows at least three orders of magnitude faster than alumina, requires more oxygen consumption compared to alumina, and is less likely to form when oxygen supply is limited. The sulfur surface coverage is expected to be directly dependent on the SO_2 content in the atmosphere when at low levels. Thus, a higher sulfur amount should lead to higher surface blocking of oxygen, thus favoring preferential Al_2O_3 formation.

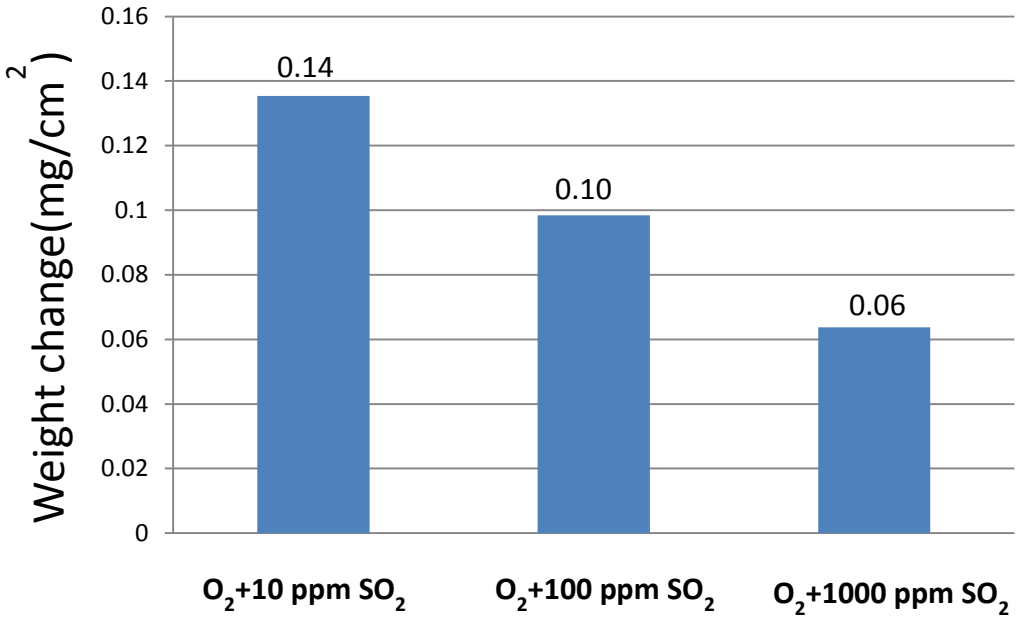

Figure 5.64 The weight gain of PWA 1484 after 20 hours of oxidation in uncatalyzed O_2-10-1000ppm SO_2 atmospheres

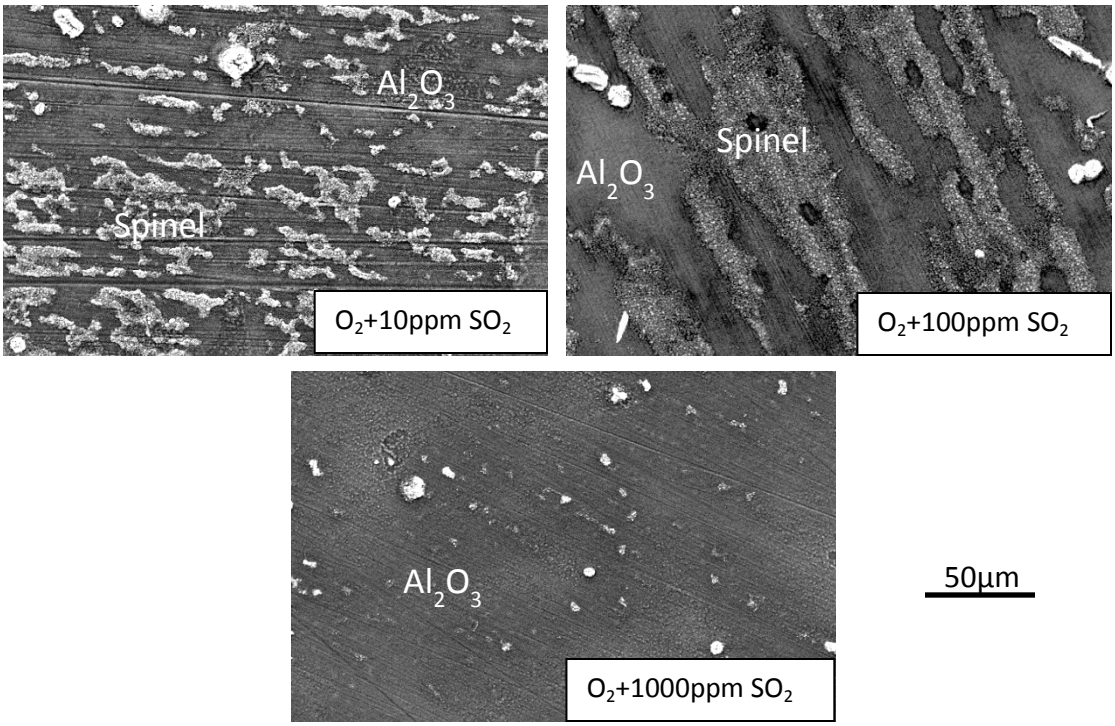

Figure 5.65 The surface morphologies of PWA 1484 after 20 hours of oxidation in uncatalyzed O_2-10-1000ppmSO_2 atmospheres

5.3.2.3 Effect of sulfur on the early stage of oxidation

To further understand the apparent sulfur effect, alloys 2 and 4 were oxidized in air and O_2+1%SO_2 at 1000°C for 1 minute. The resulting surface morphologies are shown in Figure 5.66. A difference in the oxidation behaviors of these alloys in the two environments is observed from the beginning. When alloys 2 and 4 were oxidized in O_2+1%SO_2, only Al_2O_3 formed at 1 minute. By contrast, when the same alloys were oxidized in air, NiO formed as discrete islands at 1 minute. To further elucidate if the differences in behavior started during the heating stage, alloys 2 and 4 were oxidized in air and O_2+1%SO_2 at an intermediate temperature of 500°C for 30s. No obvious oxidation was observed in either atmosphere, revealing that the differences started at temperatures above 500°C.

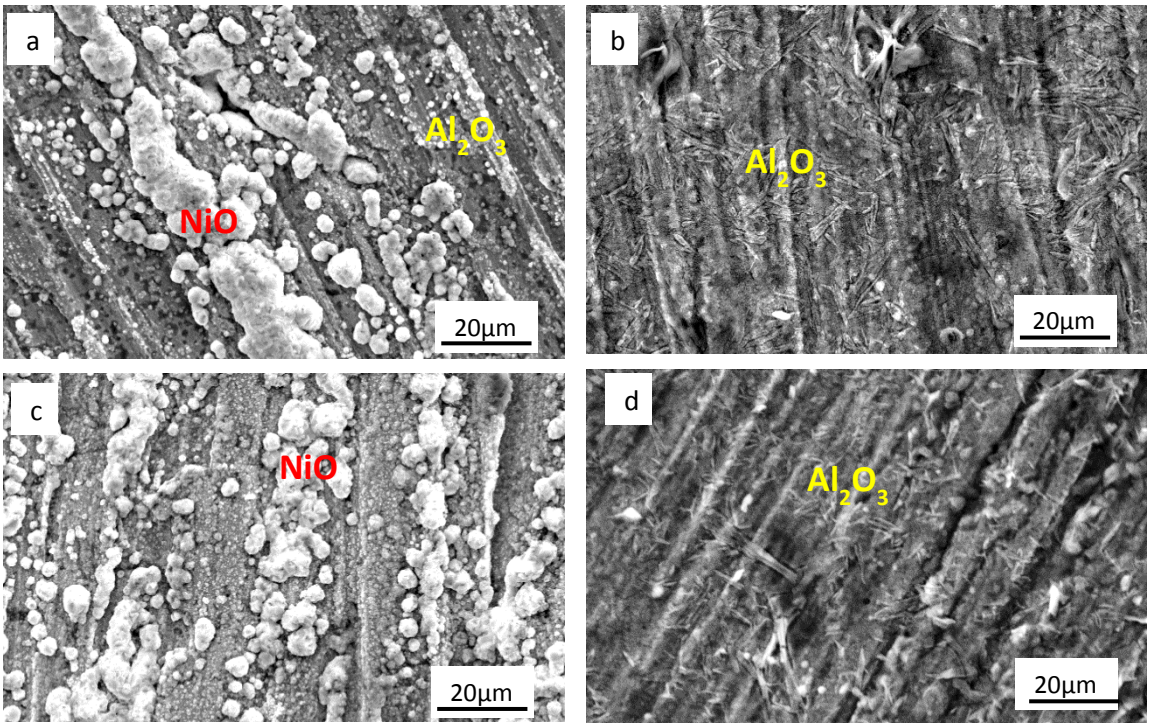

Figure 5.66 Surface morphologies of alloy 2 and 4 oxidized in air and O_2+1%SO_2 at 1000°C 1min (a) alloy 2 in air, (b) alloy 2 in O_2+1%SO_2, (c) alloy 4 in air, (d) alloy 4 in O_2+1%SO_2

5.3.3 Discussion

The key observations are as follows: 1) the presence of sulfur can promote the transition from internal to external alumina scale formation. In other words, the presence of sulfur can decrease the critical aluminum concentration for forming an Al_2O_3 scale; 2) sulfur was observed to be enriched on the sample surface in the form of $NiSO_4$ during low-temperature pre-exposure to an SO_2 containing atmosphere; and 3) the oxidation behaviors of alloys in air and in O_2+1%SO_2 are distinctly different from the beginning of reaction.

5.3.3.1 Comparison of oxygen permeability in air and O_2+1%SO_2

A plausible initial approach to rationalizing the observed results of sulfur decreasing N_{Al}^{*} is to consider Wagner's criterion for the transition from internal to external scale formation (see section 2.2.3.1). According to that criterion [38, 41]

$$N_{Al}^{*(1)} \propto \left(\frac{N_O^S D_O}{D_{Al}}\right)^{\frac{1}{2}} \tag{5. 19}$$

Where $N_{Al}^{*(1)}$ is the critical aluminum concentration for transition from internal to external oxidation, in other words, for establishing external alumina scale, N_O^S is the concentration of dissolved oxygen at the alloy surface, D_O is the diffusion coefficient of oxygen in the alloy, D_{Al} is the diffusion coefficient of aluminum in the alloy, and the product $N_O^S D_O$ is defined as the concentration-independent oxygen permeability into the alloy. During alloy oxidation, there is a counter-diffusion, with oxygen permeating in and aluminum permeating out. What this equation shows is that if oxygen permeates into the alloy very quickly, more Al is needed in the alloy to establish a complete and protective Al_2O_3 scale. Whereas, if the outward diffusion of Al is rapid, less Al is needed for the alloy to form an Al_2O_3 scale. Overall, the critical aluminum concentration is affected by both $N_O^S D_O$ and D_{Al}.

Based on this criterion (equation 5.19), the decreased critical aluminum concentration could be due to an increase of D_{Al} in the alloy or a decrease in oxygen permeability $N_O^S D_O$ owing to the presence of sulfur. These will be considered in turn.

Very little data are available on the effect of sulfur on aluminum diffusion D_{Al} in Ni alloy system. The known references [157, 158] are for Fe-based alloys. Smeltzer and Patnaik[157, 158] investigated the transition from internal sulfidation to external sulfide (Al_2S_3) scale growth on ferrite Fe-Al alloys at 900°C using both thermodynamic calculation and experiments. By

considering only the effect of sulfur on the aluminum diffusion within the alloy, a model was built which accounted for sulfur diffusion by a vacancy mechanism and the repulsive interaction between S and Al in the alloy. It was found that this repulsive interaction slightly increases the critical aluminum concentration needed for the external sulfide formation. This is in contrast to what was observed in this work, where the presence of sulfur actually decreased N_{Al}^{*}. Changing the system from BCC (iron) to FCC (nickel) is not likely to reverse the thermodynamic estimated trend of sulfur increasing N_{Al}^{*}. Therefore, the effect of sulfur on aluminum diffusion cannot explain the observed experimental result in this study. Thus, the effect of sulfur on the oxygen permeability, $N_O^S D_O$, needs to be considered.

The effect of sulfur on the oxygen permeability $N_O^S D_O$ can be explored by exposing a dilute alloy in environments with and without sulfur and comparing the depth of internal oxidation. If the morphologies of internal oxides formed in two environments are similar, the larger $N_O^S D_O$ will equate to deeper internal oxidation [159, 160].

Figure 5.67 shows cross-sectional images of the dilute alloy (Ni-3at.%Al) after 0.5 and 1 hour of oxidation in air and O_2+1%SO_2 at 1000°C. The morphologies of internal precipitates formed in two environments are similar; therefore the oxygen permeability should be directly reflected by the penetration depth of oxygen. The structures of the corrosion products are characterized by four interfaces. As marked in the left margin of Figure 5.67(d), the four interfaces are labeled I-IV. Interface I is the scale surface. Interface II is considered to be the original alloy surface. Internal oxidation precipitates which started from this interface serve as intrinsic markers. Interface III is between the external scale and the alloy, and interface IV is at the maximum depth of internal-oxide formation. The penetration depth of oxygen (ξ) is defined by the distance between interfaces II and IV. It is seen that ξ in O_2+1%SO_2 is smaller than that in

air. This was also true for longer exposures, as summarized in Figure 5.67. This comparison suggests that the oxygen permeability in the alloy decreases when a small amount of sulfur is present.

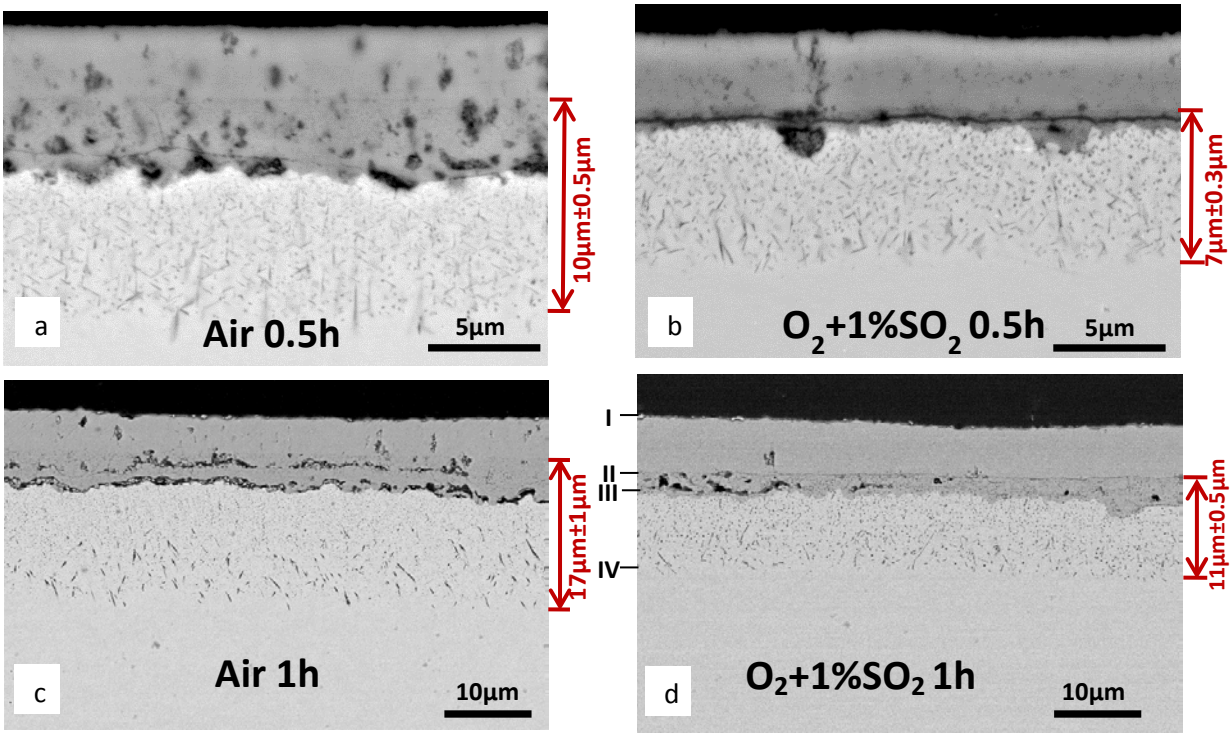

Figure 5.67 Cross-sectional images of Ni-3at.%Al after being oxidized in air and O_2+1%SO_2 at 1000°C for 0.5 and 1h

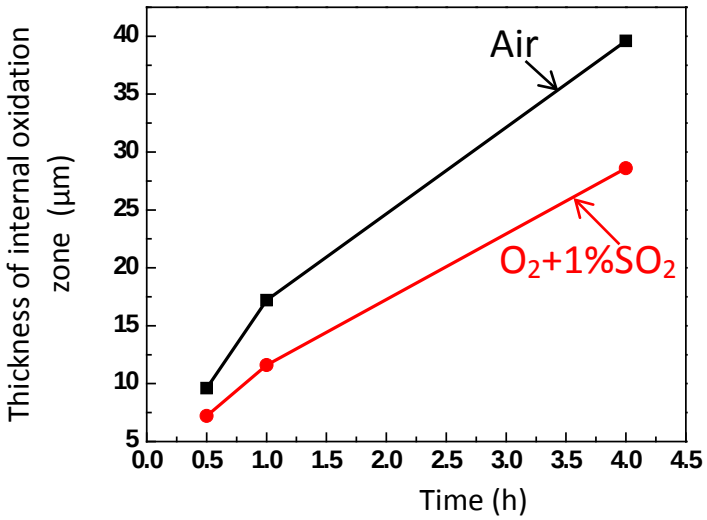

Figure 5.68 Comparison of IOZ thickness in air and O_2+1%SO_2 for Ni-3at.%Al oxidized at 1000°C

Quantitatively, based on Rapp's derivation for the case of negligible counter-diffusion in the absence of an external scale formation [41]

$$\xi \approx \left[\frac{2N_O^S D_O t}{\nu N_{Al}^o}\right]^{1/2} \quad (5.\ 20)$$

where N_{Al}^o is the Al concentration in the bulk alloy, ν is the stoichiometry factor of internal oxides, and t is time in seconds. Based on equation (5.20), ξ is directly proportional to the square root of oxygen permeability $N_O^S D_O$. Thus, a smaller ξ reflects a decreased oxygen permeability. Moreover, based on equation (5.19), decreased oxygen permeability can lead to the decrease of the critical Al concentration, and therefore helps to promote the internal-to-external transition.

A similar beneficial effect of the trace environmental sulfur has been reported by others [138, 139]. Those authors concluded that sulfur in the atmosphere chemisorbs on the alloy surface and blocks the sites required for decomposition of the oxygen molecules responsible for

oxidation. It is quite possible that the chemisorbed sulfur effectively decreases oxygen entry into the alloy, and thus reduces the permeability of oxygen. In particular, this is very likely for the concentrated alloys, alloy 2 and 4. These two alloys do not form NiO scale when oxidized in O_2+1%SO_2. The oxygen permeability, in these cases, is directly affected by the blocking effect of surface enrichment of sulfur. The promoted internal to external transition can be considered as another manifestation of the oxygen supply inhibition due to sulfur chemisorption, beyond the previous observed sulfur effect in promoting α-Al_2O_3 establishment [132] (refer to Section 5.2).

It is clear that the presence of sulfur decreases oxygen permeability, but it is not clear whether N_O^S or D_O or both are affected. In this study, the oxidation of dilute binary alloy which forms external NiO scale, N_O^S is the oxygen concentration in γ-Ni on interface II shown in Figure 5.67. A schematic of the corrosion product structure of Figure 5.67 is shown in Figure 5.69. It is seen that γ-Ni, NiO and $NiAl_2O_4$ are present at interface II. Thus, N_O^S is the oxygen solubility in γ-Ni corresponding to γ-Ni+NiO+$NiAl_2O_4$ equilibrium; assuming such local equilibrium exists. In the Ni-Al-O phase diagram (Figure 5.70), N_O^S is the oxygen concentration at the red point [161]. It is quite possible, however, that sulfur can modify the phase composition in the γ-Ni+NiO+$NiAl_2O_4$ equilibrium by acting as a fourth component. This could affect the positioning of the three-phase triangle, thus affecting the values of N_O^S. Sulfur might also introduce a cross-term for oxygen diffusion. For example, when sulfur is present the oxygen flux could be comprised of two parts: flux due to intrinsic oxygen diffusion, $D_{oo}\frac{\partial N_o}{\partial x}$; and flux due to extrinsic oxygen diffusion, $D_{os}\frac{\partial N_s}{\partial x}$, as shown by equation (5.21).

$$J_o = -D_{oo}\frac{\partial N_o}{\partial x} - D_{os}\frac{\partial N_s}{\partial x} \approx -D_o^{eff}\frac{\partial N_o}{\partial x} \qquad (5.21)$$

where D_{oo} is the main-term diffusion coefficient, D_{os} is the cross-term diffusion coefficient influenced by the presence of sulfur. As a result, the D_o^{eff} could be different from the D_o in the Ni-Al alloy. To determine which term plays a more important role, the penetration depth of sulfur in the subscale (region between III and IV in Figure 5.67) is needed. If sulfur exists within the regions between II and III, N_O^S can be affected. If sulfur exists in the internal precipitate region(regions between III and IV), D_O can be affected. Measurement of the sulfur penetration depth require detailed analyses using highly sensitive characterization methods that were beyond the scope of this study.

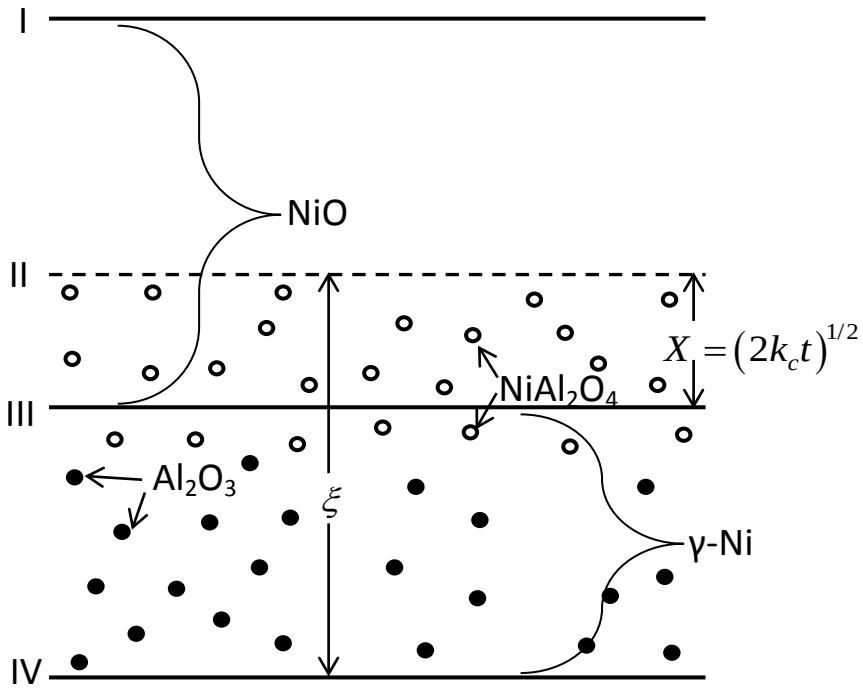

Figure 5.69 The schematic view of oxidized Ni-3at.%Al alloy (figure 7b): I) actual scale/gas interface; II) original alloy surface; III) scale/alloy interface; IV) Internal precipitation front[162].

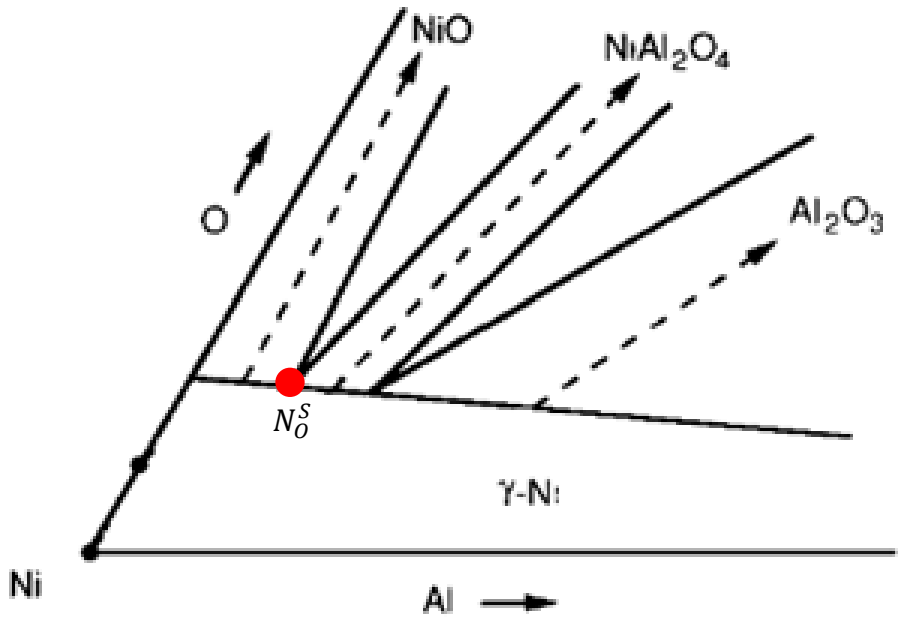

Figure 5.70 The Schematic of the Ni-Al-O phase diagram[161] at the Ni-rich corner

5.3.3.2 The sulfur promoting α-Al_2O_3 formation can help the maintenance of external alumina scale

As discussed in Section 5.2, the presence of sulfur in the atmosphere can promote the kinetic establishment of α-Al_2O_3. This promotion of α-Al_2O_3 formation requires less Al consumption compared to a metastable alumina and thus lessens the likelihood of the chemical breakdown of the external alumina scale due to subsurface Al depletion. Specifically, the maintenance of the external alumina scale requires that the Al supply from the substrate is at least equal to the Al consumption caused by the new oxide formation. A lower growth rate corresponds to a smaller aluminum consumption rate, which makes it possible for the scale to be maintained with a lower Al concentration in the alloy. As the growth rate of α-Al_2O_3 is orders of magnitude smaller than that of θ-Al_2O_3 [48] (refer to Figure 2.16 in section 2.2.3.4), when

sulfur promotes α-Al_2O_3 formation, it also reduces the possibility of chemical breakdown of this external scale.

Meier[46] did a semi-quantitative assessment of the effect of metastable-to-stable phase changes within alumina scale on Ni-Al binary systems using the supply criterion of Wagner's theory (see in section 2.2.3.2).

$$N_{Al}^{*(2)} \geq \frac{V_m}{32v}\left(\frac{\pi k_p}{D_{Al}}\right)^{1/2} \quad (5.\ 22)$$

where $N_{Al}^{*(2)}$ is the critical aluminum concentration for sustaining the growth of an external alumina scale. From the above equation, it is seen that at a fixed temperature, V_m and D_{Al} are fixed, and as k_p of α-Al_2O_3 is significantly smaller than k_p of θ-Al_2O_3, then $N_{Al}^{*(2)}$ for sustaining α-Al_2O_3 scale is smaller than $N_{Al}^{*(2)}$ for θ-Al_2O_3. The $N_{Al}^{*(2)}$ values for sustaining α-Al_2O_3 and θ-Al_2O_3 scales were estimated to be 0.03 and 0.3, respectively. When these values are plotted on the Ni-Al oxide map as shown in Figure 5.71, it is found that 0.03 is smaller than $N_{Al}^{*(1)}$ set by the transition criterion for establishing an external alumina scale[45], whereas 0.3 is larger than that. Based on this estimation, to establish and sustain a θ-Al_2O_3 scale, the alloy needs to contain at least 30% of aluminum. However, to establish and sustain an α-Al_2O_3 scale, the alloy only needs to contain approximately 15at.% of aluminum. Thus, the early promotion of α-Al_2O_3 scale formation makes it possible for alloy to establish and maintain an external scale at relatively lower aluminum concentration.

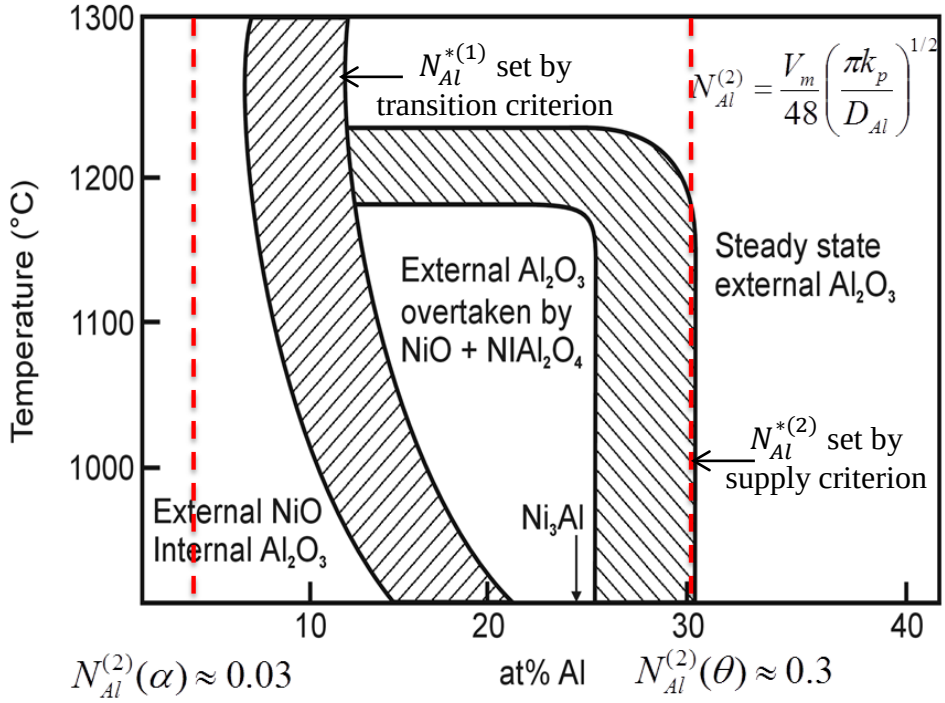

Figure 5.71 The critical aluminum concentration for α-Al_2O_3 growth and θ-Al_2O_3 growth on Ni-Al oxide map [45, 46]

For the Ni-Cr-Al ternary system, the situation becomes more complex. Chromium decreases $N_{Al}^{*(1)}$ for establishing an external alumina scale which is ascribed to the so-called gettering effect (see section 2.2.2.3). The value of $N_{Al}^{*(1)}$can drop to ~5 at.% based on Ni-Cr-Al oxidation maps at 1000°C-1200°C [54]. Sulfur may decrease $N_{Al}^{*(1)}$ for establishing external alumina scale as it decreases oxygen permeability. Sulfur can also decrease $N_{Al}^{*(2)}$ for sustaining alumina scale as it promotes early establishment of α-Al_2O_3. If α-Al_2O_3 scale is formed, the $N_{Al}^{*(2)}$ for sustaining alumina scale can be reduced to the level of 3at.% based on Meier' estimation [46], or 2at.% at 1200°C based on Young's calculation [163]. These values are much smaller than ~5at.% for establishing an external alumina scale in Ni-Cr-Al system. This means that, for the

oxidation of Ni-Cr-Al alloy in the presence of sulfur, the $N_{Al}^{*(1)}$ for establishing an external alumina scale is larger than $N_{Al}^{*(2)}$ for sustaining the scale growth. Therefore, in this case, it is the transition criterion that is more important in governing the external formation and continuous growth of the alumina scale. Further, the key role of sulfur in facilitating the transition criterion to be the most important.

In the last two sections, sulfur's beneficial effect on the establishment of alumina scale was justified from the perspective of transition criterion and sustaining criterion. The two criteria, although established based on binary system, have provided some useful guidance to understand the N_{Al}^{*} decrease in Ni-Cr-Al system with the presence of sulfur.

5.3.3.3 The sulfur blocking effect on the external alumina scale establishment

The presence of sulfur in favoring establishment of an alumina scale can also be rationalized from the perspective of kinetic competition of the oxides that may form. There exists a kinetic competition between NiO, Al_2O_3 or Cr_2O_3 during the scale establishment. Similar with the kinetic competition of θ-Al_2O_3 and α-Al_2O_3, as discussed in section 5.2.3.1, the fast nucleating and growing oxides are kinetically favored to establish a continuous layer. Nickel oxide grows fast than Cr_2O_3 than Al_2O_3, thus NiO is favored to establish a continuous layer in air at relatively low Cr and Al contents in the alloy. When a sample is oxidized in O_2+1%SO_2 atmosphere, oxygen supply is limited due to the sample surface enrichment of sulfur (as discussed in section 5.2.3.2). In this case, NiO, which requires more oxygen consumption than Al_2O_3, is hindered in its ability to establish a continuous layer.

The value of N_{Al}^{*} is predicted based on the assumption that the volume fraction of Al_2O_3 in the internal oxidation zone, g^{*}, increases with increasing Al concentration to the extent that

oxygen diffusion in the alloy becomes so restricted that external Al_2O_3 formation is favored[34, 38, 162]. If the oxygen supply is limited due to the surface enrichment of sulfur, less oxygen diffuses into the alloy; and therefore smaller N_{Al}^{*} results.

5.3.4 Conclusions

The effect of environmental sulfur on the establishment of alumina scale was investigated on both low Cr (<6wt.%) Ni-Cr-Al model alloys and Ni-based commercial alloys. It was found that a small amount of sulfur in the atmosphere can promote the transition from internal to external Al_2O_3-scale formation. This promoted transition is inferred to be due in part to sulfur decreasing the oxygen permeability into the alloy, thus making it easier for Al_2O_3 to establish externally. Other than this, the sulfur promoting α-Al_2O_3 establishment, which requires less Al consumption compared to a metastable alumina and thus lessens the likelihood of the chemical breakdown of the external alumina scale.

5.4 EFFECTS OF ENVIRONMENTAL SULFUR AND SALT ON THE TYPE I HOT CORROSION OF ALUMINA-SCALE FORMING ALLOYS

5.4.1 Materials tested

Single-crystal and polycrystalline PWA1484 alloys were tested. The nominal compositions (in wt. %) were listed in Table 5.8 in section 5.3.

5.4.2 Results

5.4.2.1 900°C Type I hot corrosion in catalyzed and uncatalyzed O_2+1000 ppmSO_2

Single-crystal PWA1484 alloys with ~2mg/cm^2 pre-deposited Na_2SO_4 were exposed at 900°C in air, and catalyzed and uncatalyzed O_2+1000ppm SO_2 atmospheres for up to 40 hours. The salt was re-deposited after every 20 hours. The resulting weight gain kinetics is shown in Figure 5.72. A representative cross-sectional image of each sample after 40 hours exposure in the three different atmospheres is also shown Figure 5.72. When exposed in air, the weight gain was small and thin corrosion products had formed. The structure of the corrosion products was typical for type I hot corrosion, with the oxides forming on top and a few internal sulfides forming underneath. When exposed to a catalyzed O_2+1000ppm SO_2 atmosphere, the weight gain was much larger and more corrosion products had formed. The internal corrosion products were a mixture of oxide and sulfide (Cr_xS_y and Ni_3S_2), as determined by EDS measurement. Comparing the results from these two exposures, clearly sulfur in the atmosphere activated more extensive internal attack of this second-generation superalloy during type I hot corrosion exposure. This result is at variance with some past studies reviewed in the Literature Survey of

this thesis (section 2.3.2.3). In those studies of type I hot corrosion of β-NiAl[92], Ni-20Cr-X[93] and pure Ni[94], it was deduced that the extent of attack caused by type I hot corrosion is usually considered as independent of Pso_2 or Pso_3. When exposed in an uncatalyzed O_2+1000ppm SO_2 atmosphere, larger weight gain and much more internal attack was observed. Based on the thermodynamic calculation shown in Table 4.1 in Chapter 4, around 25% of SO_2 should be converted to SO_3 if the gas atmosphere is catalyzed. Thus, a higher SO_2 partial pressure is expected in the uncatalyzed atmosphere. Given that the results in Figure 5.72 show more internal attack when exposed to the uncatalyzed atmosphere, it is deduced that SO_2 is the main reactant causing the extensive internal attack. If this deduction is correct, then one would expect to see a dependence of type I hot corrosion attack on SO_2 concentration. That set of measurements is presented in the following.

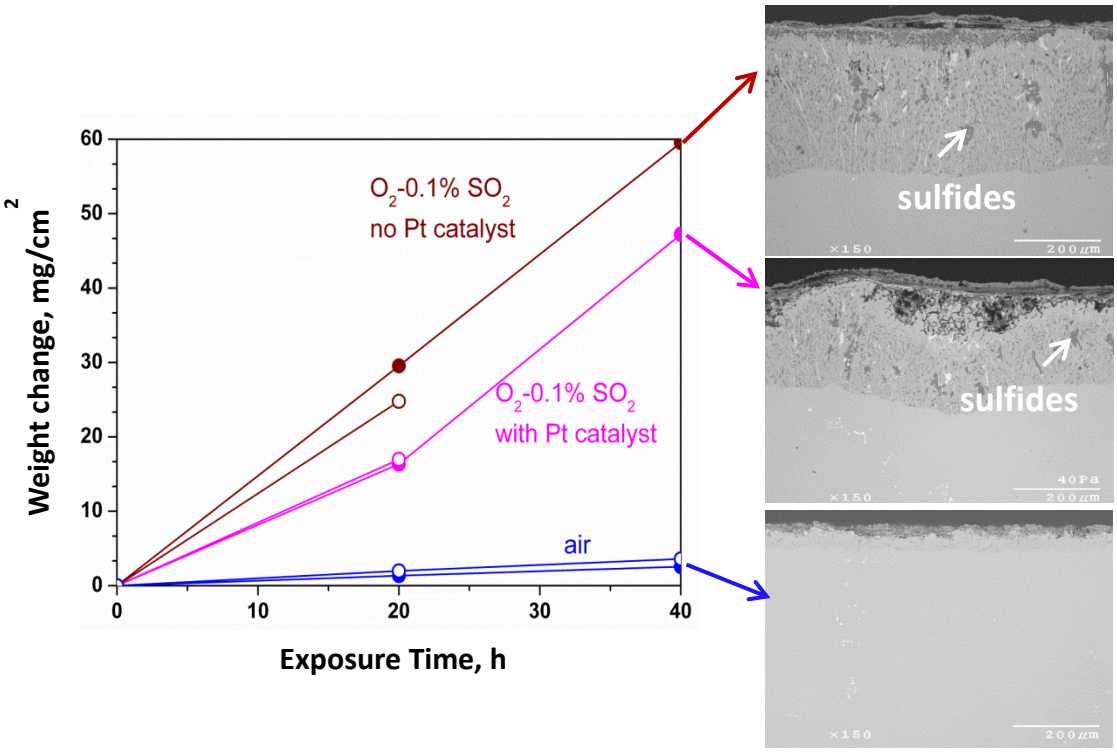

Figure 5.72 Na_2SO_4-induced hot corrosion at 900°C of PWA1484 alloy exposed in air, and catalyzed and uncatalyzed O_2+1000ppm SO_2 atmospheres: the weight gain as a function of time (left); the cross-section images after 40 hours exposure (right) [83]

5.4.2.2 900°C Type I hot corrosion in uncatalyzed O_2+(10~1000)ppmSO_2

To verify whether there is a dependence of SO_2 content in the atmosphere, the commercial alloy was exposed to type I hot corrosion in an uncatalyzed atmosphere with different SO_2 content. The resulting weight gains after 20 hours exposure in air and uncatalyzed O_2+(10-1000)ppm SO_2 atmosphere are shown in Figure 5.73 and the corresponding cross-sectional images are shown in Figure 5.74. Polycrystalline PWA 1484 alloys were tested. Figure 5.73 shows that with an increase in Pso_2, the sample weight gain increases. Consistent with the weight gain, the extent of attack also increased with an increase in Pso_2, as can be seen in Figure 5.74. When exposed to air, the alloy formed an outer oxide layer with internal Cr-rich sulfides.

This is a typical structure of salt-induced type I hot corrosion reported by many researchers [103]. When exposed to O_2+10ppm SO_2, the alloy formed similar corrosion products to what formed in air, but with the former having more oxide and internal Cr-rich sulfides penetrating to a larger depth. It is surprising that 10 ppm SO_2 can increase degradation to such an extent during type I hot corrosion. No known past studies have reported type I hot corrosion at such a low SO_2 concentration. When the oxidation was done in O_2+100ppm SO_2, the internal corrosion product penetrated even further. The overall product was comprised of non-protective oxide (NiO and/or CoO) on the scale surface, internal oxide precipitates in the middle, and (Cr, Ni)-rich internal sulfide precipitates deeper in. When the SO_2 concentration in the gas atmosphere increased from 100ppm to 1000ppm, the weight gain of the sample jumped dramatically from 7.1 to 41.1mg/cm^2 and the penetration of internal attack was almost an order of magnitude deeper, though with a similar appearance to the exposure in 100ppm SO_2. Ni_3S_2 was identified within in the internal sulfides and, at 900°C, it would have been liquid which penetrated preferentially down grain boundaries (shown in Figure 5.74e) and caused rapid inter-granular attack due to rapid diffusion through the liquid [164]. All these results show that there is a dependence of hot corrosion attack on SO_2 concentration for polycrystalline PWA 1484 alloys.

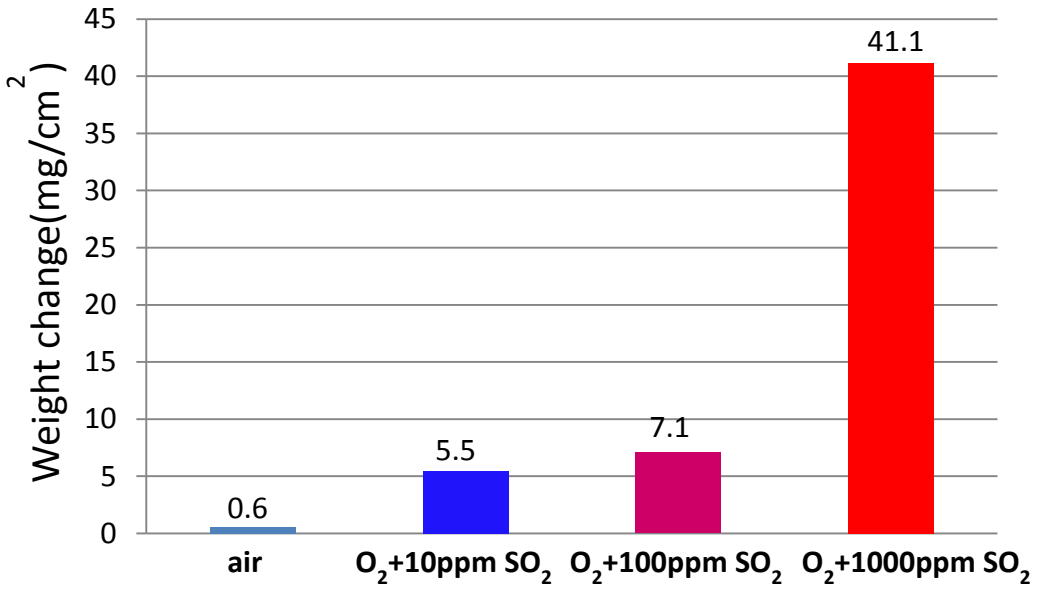

Figure 5.73 The weight gain as a function of time for Na_2SO_4-induced hot corrosion at 900°C of polycrystalline PWA1484 alloy exposed in air and uncatalyzed O_2+(10~1000ppm)SO_2 atmosphere for 20 hours.

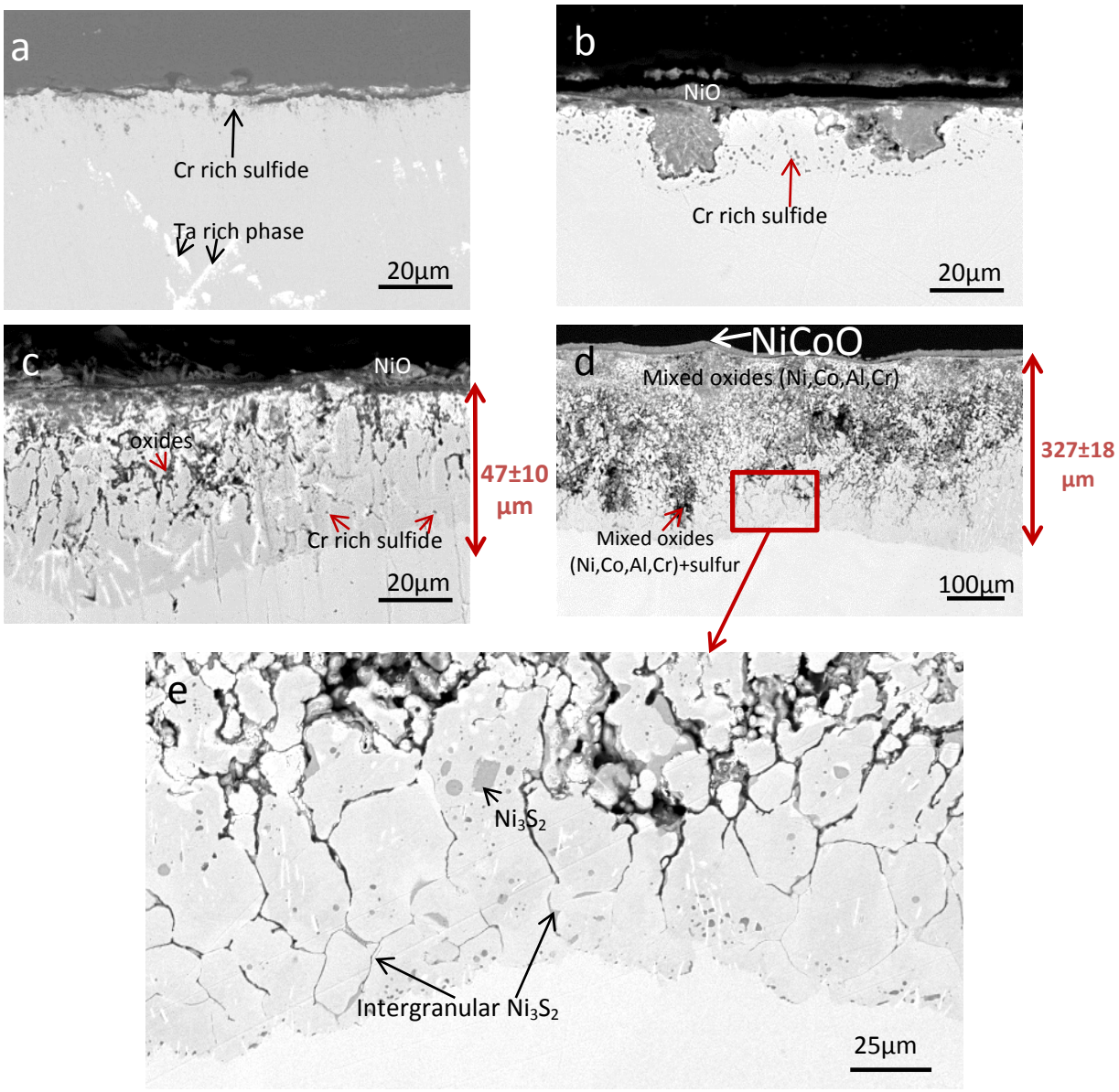

Figure 5.74 The cross-sectional images of polycrystalline PWA 1484 alloy after 20 hours of Na_2SO_4-induced hot corrosion at 900°C in (a) air and uncatalyzed O_2-SO_2 atmosphere: (b) O_2+10ppm SO_2, (c) O_2+100ppm SO_2 and (d,e) O_2+1000ppm SO_2

The same tests in an uncatalyzed atmosphere were done on the single-crystal PWA 1484 alloy and the resulting weight gains are shown in Figure 5.75. A similar dependence on SO_2 content was observed for the single-crystal alloy. A representative cross-sectional image of a sample exposed to the O_2+1000ppm SO_2 atmosphere is shown in Figure 5.76. An external scale of nickel and cobalt oxides had spalled in this region during cooling. Around 100-200 μm of internal oxide attack was observed. Underneath that internal oxide was a band of internal sulfides (Cr_xS_y or Ni_3S_2).

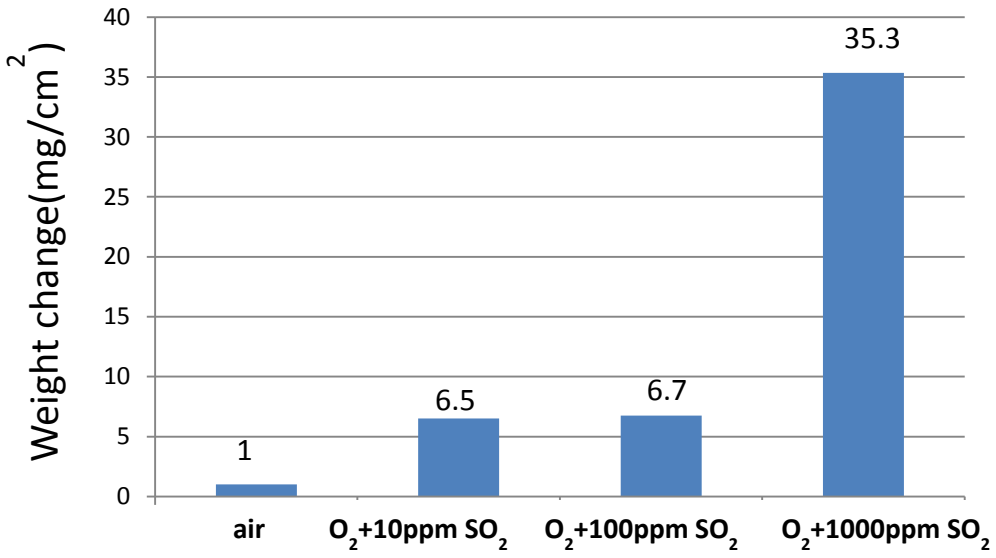

Figure 5.75 The weight gain for Na_2SO_4-induced hot corrosion at 900°C of a single crystal PWA1484 alloy exposed in air and uncatalyzed O_2+(10~1000ppm)SO_2 atmosphere for 20 hours.

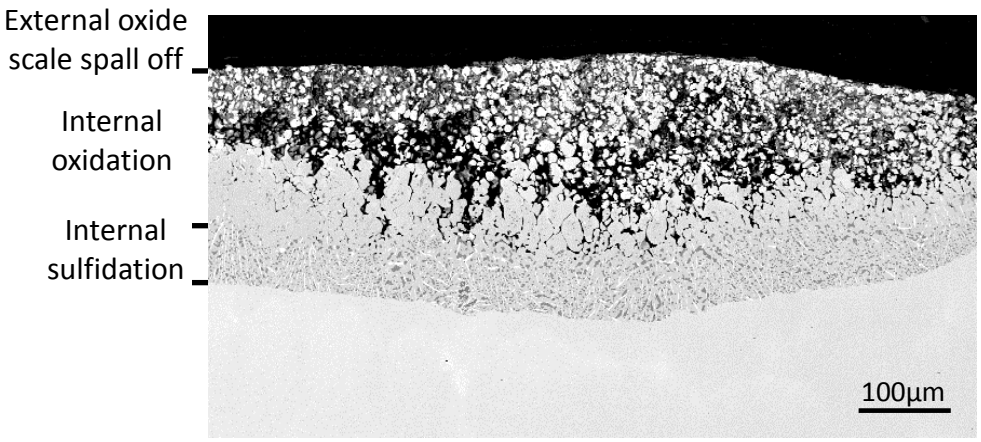

Figure 5.76 Cross-sectional image of single crystal PWA1484 alloy exposed for 20 hours Na_2SO_4-induced hot corrosion at 900°C in uncatalyzed O_2-1000ppm SO_2 atmosphere

The observed dependence of extent of attack on Pso_2 during type I hot corrosion confirmed that the presence and content of SO_2 have significant effects. Sulfur penetrated to form a large amount of internal sulfides. Based on the gas equilibrium in the uncatalyzed atmosphere, which is to be described in section 5.4.3.1, and the dependence of attack on SO_2 content, it is deduced that SO_2 is the main reactant which provides sulfur for the internal sulfide formation.

How does SO_2 penetrate the oxide scale into the alloy system and cause internal sulfidation? To address this question, it is necessary to know the nature of the oxide scale formed on PWA1484 alloy in SO_2 and salt-containing environments. Understanding the early-stage of oxidation behavior should provide some guidance about the very complex corrosion products that formed after long-term exposure, as shown in Figure 5.74. Indeed, during hot corrosion, SO_2 and the Na_2SO_4 deposit might play different roles. It would be meaningful to separate these two environmental factors to better understand the scale evolution at the very early stage. Therefore,

short-time exposures in SO_2-containing atmosphere with and without salt deposit were carried out.

5.4.2.3 900°C early stage oxidation in O_2+1000ppm SO_2

Single-crystal PWA1484 alloy was exposed to an uncatalyzed O_2+1000ppm SO_2 atmosphere with and without Na_2SO_4 deposit at 900°C for 40s. Thin oxide scales had formed and the resulting surface morphologies are shown in Figure 5.77. When the Na_2SO_4 deposit was not present, the alloy formed a uniform and very thin oxide scale in an O_2+1000ppm SO_2 atmosphere and the structure of the cast alloy could be seen beneath the thin scale. When the Na_2SO_4 deposit was present, the alloy formed a non-uniform oxide scale, as shown in Figure 5.77(c). EDS showed that the thick region is nickel rich, while the rest of regions was too thin to be identified by EDS.

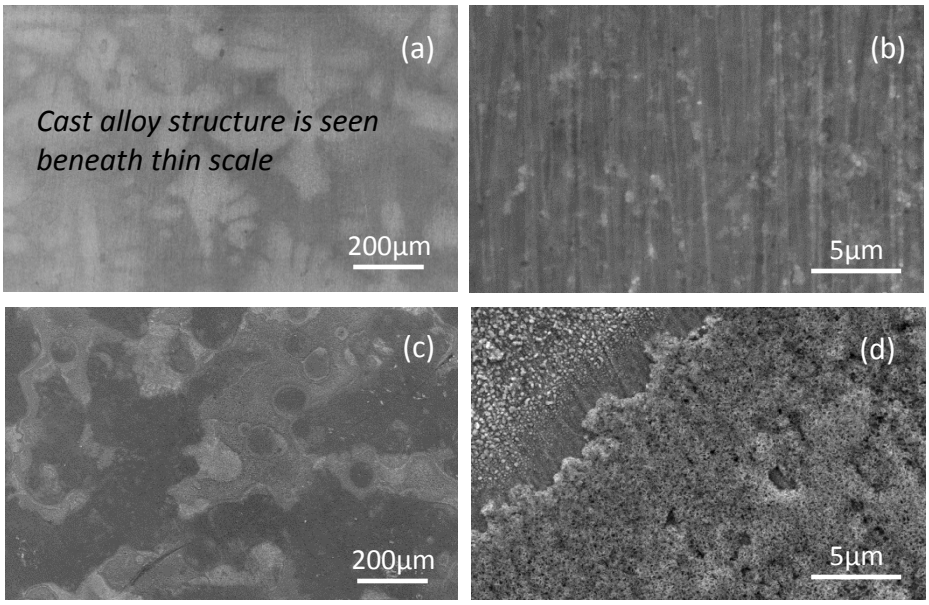

Figure 5.77 Surface morphology of single crystal PWA1484 exposed for 40 s at 900˚C in uncatalyzed O_2+1000ppm SO_2 atmosphere (a,b) and uncatalyzed O_2+1000ppm SO_2 atmosphere with Na_2SO_4 (c,d) deposit (Before observation,Na_2SO_4 was washed way in distilled water and no obvious scale spallation occurred during salt removal)

To further characterize the chemical composition and element distribution of these thin oxide scales, area analysis and element mapping were done using AES and representative results are shown in Figure 5.78 and Figure 5.79 (no deposit) and Figure 5.80 and Figure 5.81 (with deposit). For the element mapping images, brightness and contrast correlates with the atomic concentrations of the element. When the exposure was done in an SO_2-containing atmosphere without an Na_2SO_4 deposit, Ni, Al, O, S were identified within the oxide scale, as can be seen in Figure 5.78. The average composition measured was 14.9Ni-5.2Al-4.1S-75.8O in atomic percent, which does not correspond to a particular oxide or sulfide. However, as reported, the accuracy of AES quantitative composition analysis is generally very poor [165] due to errors induced by instrumental factors, and unverified data analytical algorithms [166]. Moreover, the data

collected were from very small regions near the surface with the spatial resolution in plane being only as good as 5nm [165] and the depth penetration was around 1-10nm. It may be that the surface composition is different from the composition of the bulk of the scale. As shown in section 5.3.2.2, the same alloy formed a continuous external Al_2O_3 scale after 20 hours of exposure to the O_2+0.1%SO_2 atmosphere. So, during a short-time exposure, sulfides probably do not form. Therefore, according to the measured composition, it is inferred that the product formed in a short-time exposure in an SO_2-containing environment is (Ni, Al)-rich oxide. Figure 5.79 indicates that these elements are uniformly distributed and there is no enrichment, which is consistent with the uniform surface morphology observed by SEM in Figure 5.77b. When the exposure was done in the SO_2-containing atmosphere with the presence of an Na_2SO_4 deposit, there resulted a non-uniform element distribution as shown in Figure 5.81. Nickel and aluminum were enriched at different regions; oxygen concentration was relatively high in the aluminum-enriched regions. An Auger spectrum from a nickel-rich region is shown in Figure 5.80. Analysis of this spectrum gave the atomic composition to be (in at.%) 19.3Ni-36.8O-1.2S-1.1Al. Even though this differs from NiO, it is inferred to be NiO-rich. This inference was confirmed by EDX element mapping of a TEM cross-section from the same region, which will be shown in Figure 5.84. Using the same method, the Al+O-enriched region gave a composition of 17Al-75.3O-4.0S-3.5Ni in atomic percent, which is inferred to be Al_2O_3-rich. Thus, the scale formed under salt deposit is inferred to be comprised of NiO and Al_2O_3.

A notable observation is the presence of sulfur at the interphase boundaries between the NiO-rich and Al_2O_3-rich oxides (Figure 5.81). These phase boundaries can possibly act as faster paths for sulfur transport. Once sulfur gets through the oxide scale, it may form sulfides underneath.

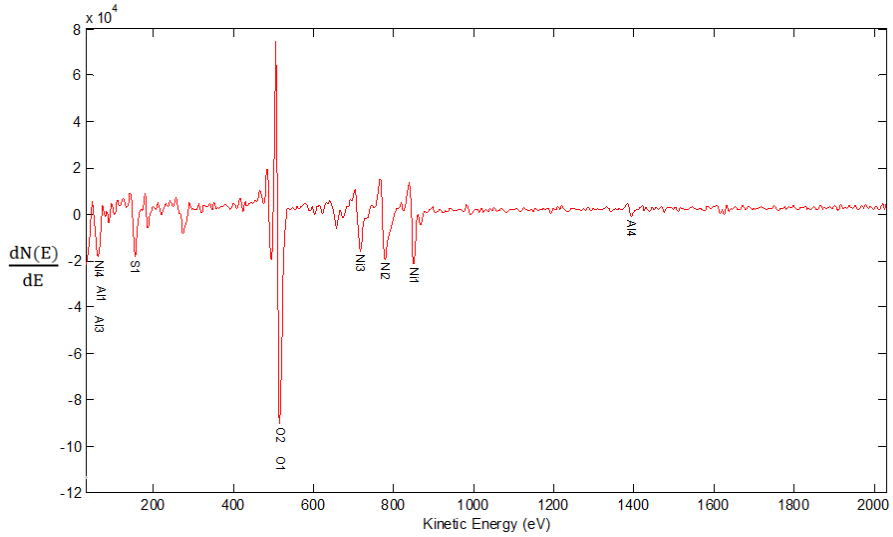

Figure 5.78 Area analyses of the oxide scale formed on PWA1484 after 40s of exposure at 900˚C in O_2+1000ppm SO_2

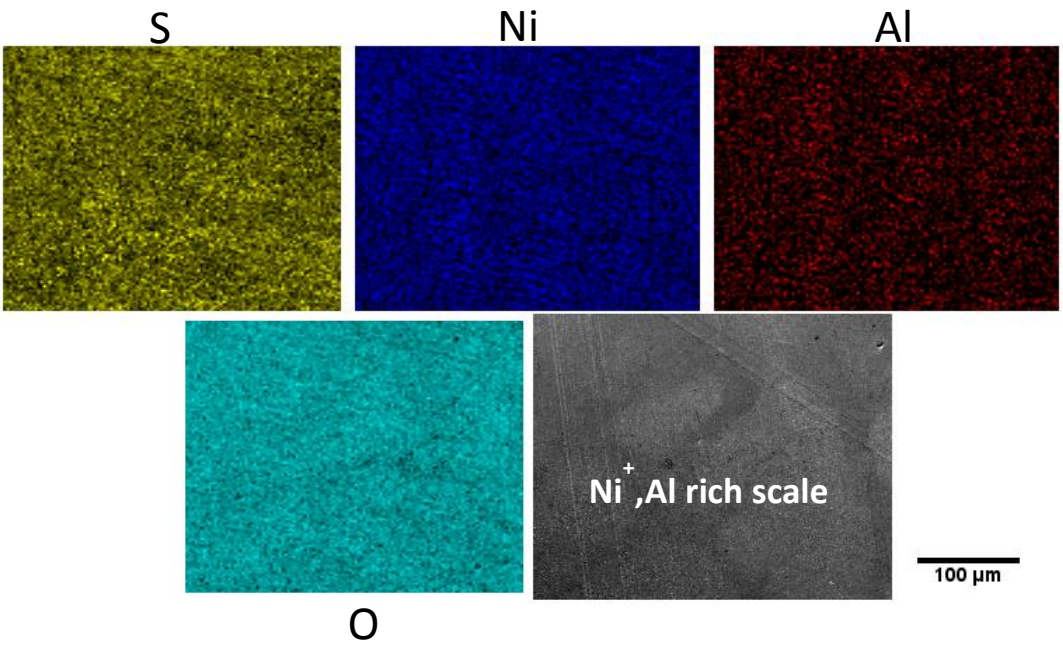

Figure 5.79 Auger element maps for the oxide scale formed on PWA1484 after 40s of exposure at 900˚C in O_2+1000ppm SO_2

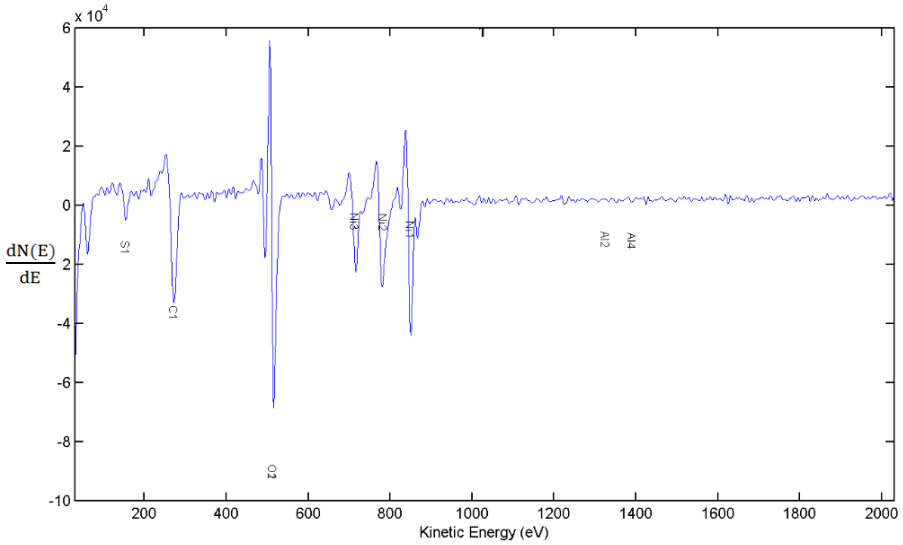

Figure 5.80 Area analyses of the thick region of the oxide scale formed on PWA1484 after 40s of exposure at 900˚C in O_2+1000ppm SO_2 with a Na_2SO_4 deposit

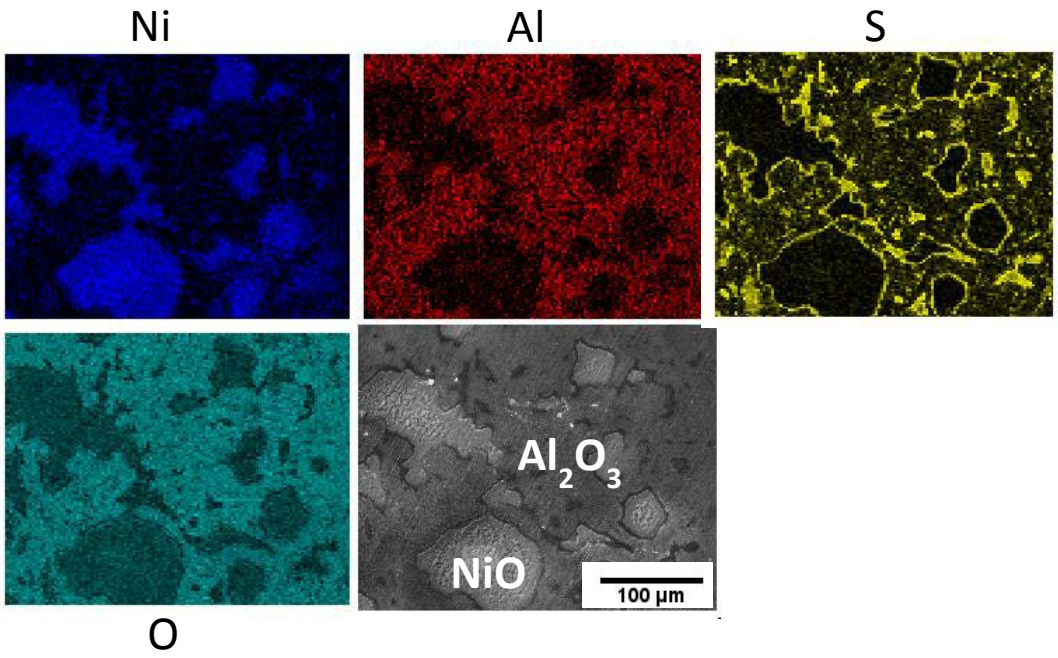

Figure 5.81 Auger elements mapping for the oxide scale formed on PWA1484 40s exposure at 900˚C in O_2+1000ppm SO_2 and a Na_2SO_4 deposit (Na_2SO_4 washed away before mapping)

In order to test whether sulfur indeed penetrates through NiO/Al_2O_3 phase boundaries and causes sulfide formation underneath, an attempt was made to construct a 3D element distribution within the oxide scale and its subscale. This was done using AES 2D mapping coupled with ion sputtering. Every interval for mapping, ~7nm of materials was removed. Unfortunately, very little useful information was obtained from the element distribution measurement apart from an indication of the thickness of the scale formed underneath Na_2SO_4 deposit: ~500nm in NiO rich region and ~100nm in Al_2O_3 rich region. After removing 1µm of surface material, subscale was exposed and the element mapping results are shown in Figure 5.82. Sulfur was observed to be locally enriched. The Auger spectrum detected on this sulfur-enriched region is shown in Figure 5.83. Sulfur, nickel, hafnium were clearly detected, but no oxygen was detected. These results confirmed that the sulfur-enriched region forms sulfide and this can be considered as the

evidence that sulfur had transported through the non-uniform oxide scale within 40s of exposure and caused internal sulfidation within the substrate.

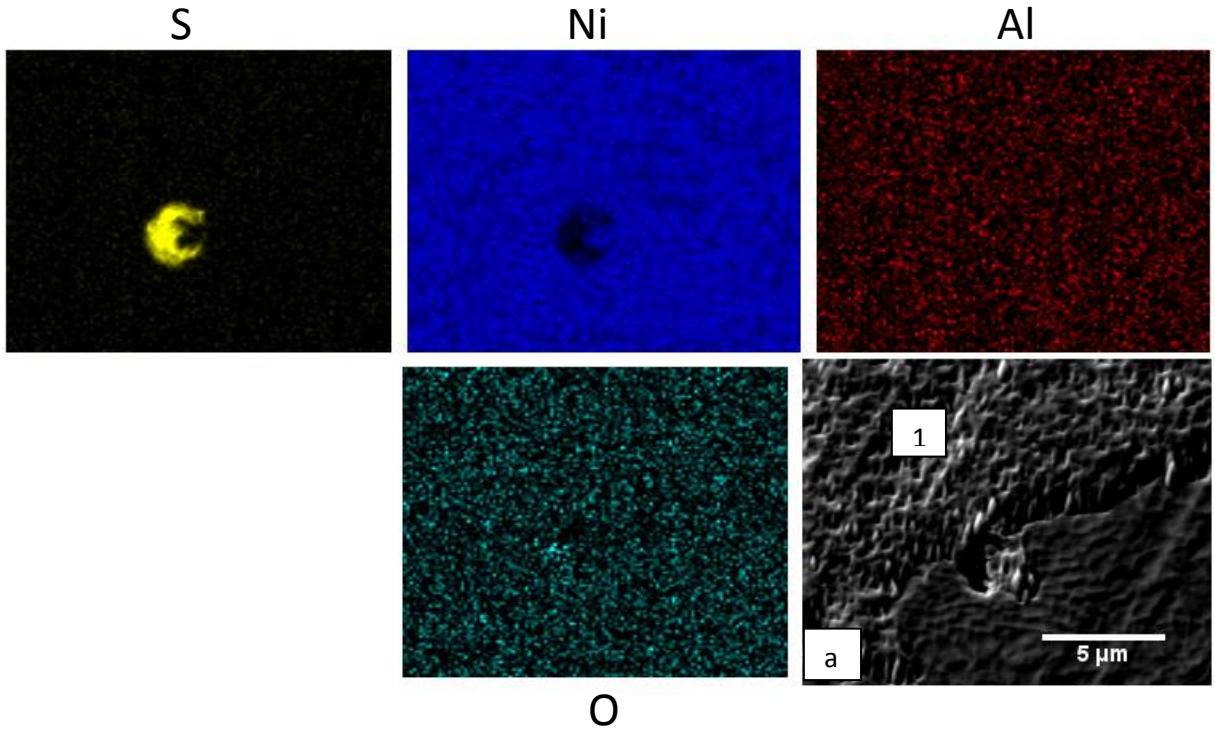

Figure 5.82 Auger element maps for PWA1484 exposed for 40s at 900˚C in O_2+1000ppm SO_2 and with a Na_2SO_4 deposit (Na_2SO_4 washed away before mapping)

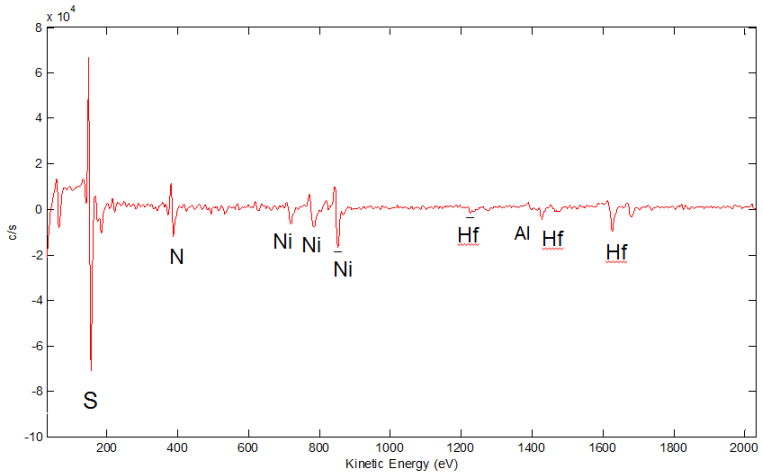

Figure 5.83 The Auger spectrum of the sulfur enriched phase.

A cross-section containing an NiO/Al_2O_3 phase boundary was prepared for TEM characterization using FIB. The FIBed region is indicated in Figure 5.84. The resulting cross-sectional image and the element distribution measured by EDS are shown in Figure 5.85. It can be seen from the cross-sectional image that NiO is much thicker than Al_2O_3. The NiO is porous in the image due to excessive removal during FIB thinning. The element maps show that sulfur is indeed enriched in the vicinity of the Al_2O_3/NiO phase boundary at the very early stage of exposure. Moreover, sulfur was not limited to the Al_2O_3/NiO phase boundary, but was also seen further along oxide/alloy interface underneath NiO, probably as a result of short-distance lateral diffusion after sulfur transport through the Al_2O_3/NiO phase boundary.

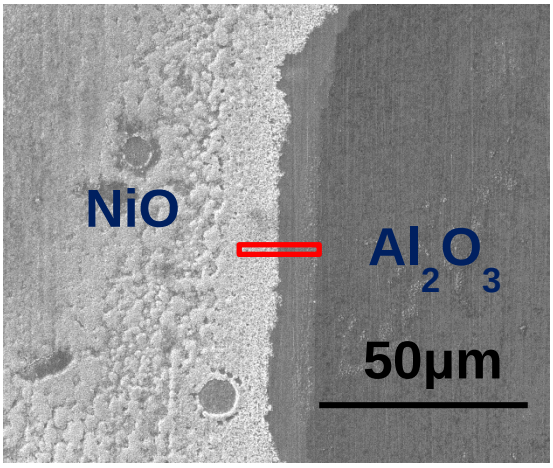

Figure 5.84 The FIBed region for TEM observation. PWA1484 exposed for 40s at 900˚C in O_2+1000ppm SO_2 and with a Na_2SO_4 deposit (Na_2SO_4 washed away before FIB cutting)

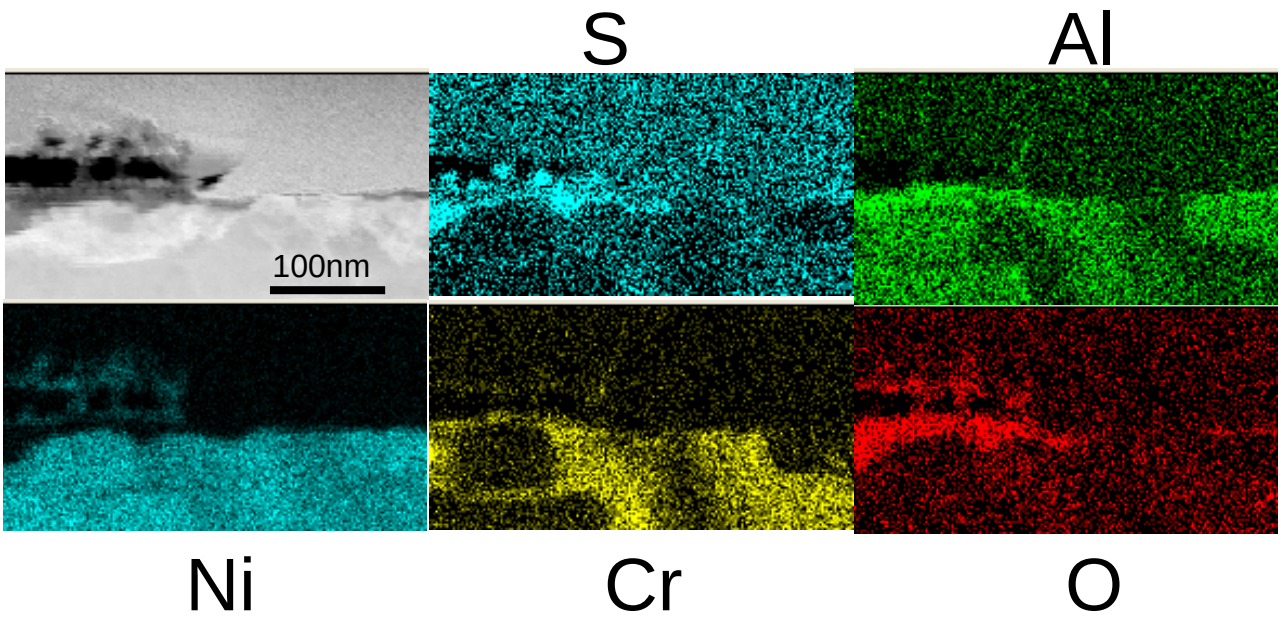

Figure 5.85 Cross-sectional image of the region indicated in Figure 5.84 observed by TEM and corresponding EDS element distribution maps at the NiO and Al_2O_3 phase boundary.

5.4.3 Discussion

5.4.3.1 The role of SO_2 on PWA1484 alloy type I hot corrosion and its major mode of degradation

To understand the Pso_2 dependence on the extent of attack, it is informative to conduct a quantitative rationalization of the results from the uncatalyzed O_2+1000ppm SO_2 and O_2+100ppm SO_2 exposures. The possible chemical reactions for the testing gases are listed below:

$$SO_3 \rightarrow \frac{1}{2}S_2 + \frac{3}{2}O_2 \quad (5.\ 23)$$

$$SO_2 + \frac{1}{2}O_2 \rightarrow SO_3 \quad (5.\ 24)$$

$$SO_2 \rightarrow O_2 + \frac{1}{2}S_2 \quad (5.\ 25)$$

Reaction (5.23) is not thermodynamically stable (i.e. ΔG=265.93kJ/mole at 900°C). This indicates that SO_3 is unlikely to be the source of sulfur S_2 for the internal sulfide formation. The reverse reaction of (5.23) is thermodynamically stable, however as the starting gas composition is O_2 and SO_2, the S_2 concentration in the testing gases will be small, as a result, the reverse reaction of (5.23) is not important. Reaction (5.24) is very sluggish without a catalyst [167]. Thus, the relevant equilibrium to consider is inferred to be reaction (5.25), and its equilibrium constant for this reaction is:

$$K_3 = \frac{P_{O_2} \cdot \sqrt{P_{S_2}}}{P_{SO_2}} \quad (5.\ 26)$$

Sulfur dissolves into the alloy and diffuses in to cause internal sulfidation. Based on Sieverts's law, sulfur surface concentration, C_s, is proportional to the square root of P_{S_2}.

$$C_s = \sqrt{K_s \cdot \mathrm{P}_{\mathrm{S}_2}} \tag{5. 27}$$

From (5.26) and (5.27)

$$C_s = K \cdot \frac{\mathrm{P}_{\mathrm{SO}_2}}{\mathrm{P}_{\mathrm{O}_2}} \tag{5. 28}$$

For the test condition used, $\mathrm{P}_{\mathrm{O}_2}$≈1atm, and thus C_s is directly proportional to $\mathrm{P}_{\mathrm{SO}_2}$. Assuming semi-infinite diffusion with fixed boundary conditions, the total amount of sulfur diffused into the alloy can be approximated as [168]:

$$M_s = 2A \cdot C_s \sqrt{\frac{D_s t}{\pi}} \tag{5. 29}$$

where M_s is the amount of sulfur uptake, D_s is the diffusion coefficient of sulfur in the alloy, t is time, and A is cross-sectional surface area. Given that D_s, t, and A are similar, the ratio of M_s is equal to the C_s ratio, when considering two P_{SO_2} exposures. Thus, this ratio can be approximated by comparing the measured weight gains at two known P_{SO_2} exposures. Experimentally, this formed ratio can be approximately determined by comparing the measured weight gains. The ratio is 6 from values in Figure 5.75 for $P_{SO_2} = 1000\mathrm{ppm}\,\mathrm{and}\,100\mathrm{ppm}$. Such a ratio is reasonably close to that predicted, which is 10. The weight gains include both oxygen and sulfur, but considering the product formed in the two conditions are similar, the ratio should reasonably reflect the differences due to S pick-up associated with internal sulfide formation.

Supported by the evidence of an increased extent of attack in the uncatalyzed atmosphere compared with that in the catalyzed atmosphere and air (Figure 5.72) and the dependence of attack on Pso_2 (Figure 5.73 and Figure 5.75) in an uncatalyzed atmosphere, SO_2 is deduced to be important in type I hot corrosion conditions if the scale exhibits some degree of permeability.

Thus, when SO_2 is present, an additional mode of attack via internal sulfidation is possible. This internal sulfidation is significantly beyond what is caused by the presence of salt deposit and can be quite significant even when 100ppm or 1000ppm SO_2 is present in the atmosphere

To understand the mechanism of SO_2-induced internal sulfidation, the following model of degradation is proposed to occur when an Na_2SO_4-deposited sample is exposed to an SO_2-containing atmosphere. This model is in accordance with the internal oxidation/sulfidation mechanism reported by Grabke et al.[116]. As shown in Figure 5.86(b), if the oxide layer formed micro-channels, gas molecules can transport through these micro-channels and reach the underlying alloy. If the transport of gas molecule within those micro-channels is selective to the extent that SO_2 gets through while O_2 does not, then P_{SO_2} will remain similar across the oxide scale while P_{O_2} will maintain a decreasing gradient within the scale and reach a very small value at the oxide/metal interface. This small value is fixed by the local equilibrium at the scale/metal interface. Based on the equilibrium constant shown in equation (5.26), the partial pressure of sulfur is inversely related to P_{O_2} when the temperature and P_{SO_2} are constant, as shown in Figure 5.86(a). As a result, the chemical potential of sulfur will have an increasing gradient (demonstrated in Figure 5.86 (b)) across the scale and, at a certain level, the potential will be high enough to stabilize sulfide formation.

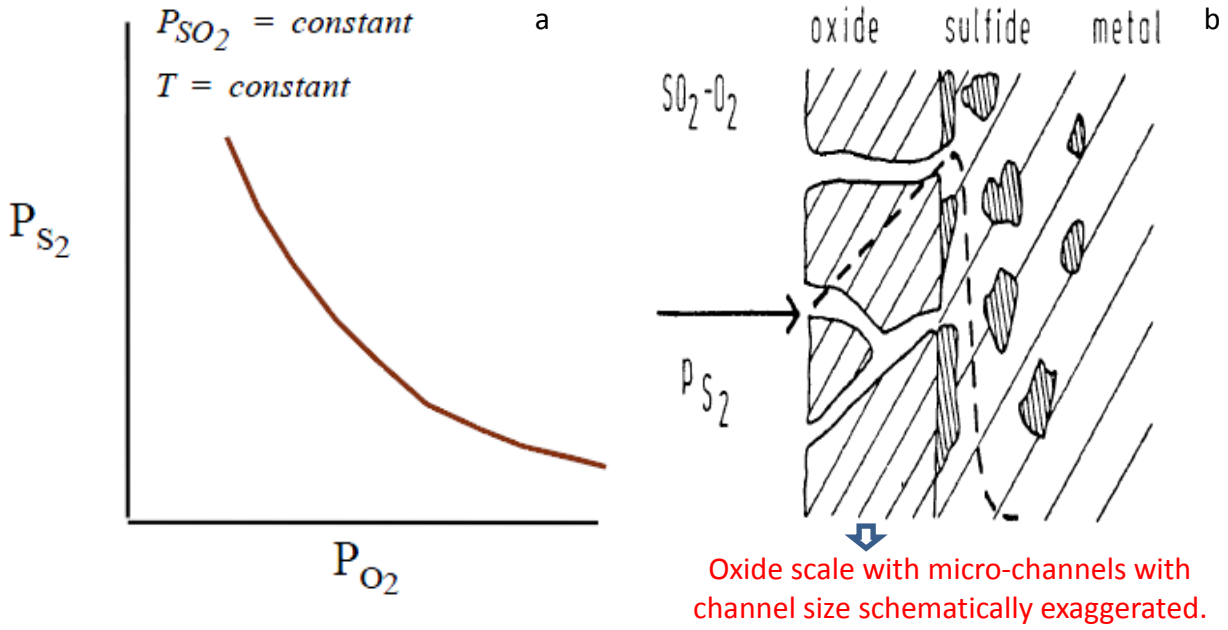

Figure 5.86 The mechanism of internal sulfidation in O_2-SO_2 atmosphere (a) the relationship of P_{S_2} and P_{O_2} (b) an oxide scale with micro-channels[116]

For the above degradation mechanism to apply, the formation of micro-channels within in the oxide scale is important. Studies on duplex NiO scales have proposed a model [169] to account for the micro-channel formation within a thermally grown oxide scale. The model first proposed by Gibbs and Hales[169] is schematically shown in Figure 5.87. During oxidation, the outward diffusion of cations creates an inward flux of vacancies and those vacancies can condense at scale/metal interface and form cavities in the metal at the scale/metal interface. The scale above an interfacial void is not stable and anisotropic dissociation along oxide grain boundaries can produce micro-channels which give gas direct access to the scale/metal interface [170-173]. The driving force is the oxygen partial pressure difference within the void and the external gas atmosphere[169]. It was surmised that the micro-channel has an equilibrium diameter of which the oxygen activity at any position in the micro-channel is equal to that in the

adjacent oxide, as indicated in Figure 5.87 (c). Micro-channels of smaller diameter will open by oxide dissociation and micro-channels of larger diameter will oxidize and fill [169, 174]. In this study, it is proposed that micro-channels formed in the oxide scale and allowed for molecular SO_2 ingress, but not O_2 ingress, so that sulfur developed an increasing gradient, thus causing internal sulfidation. As discussed in section 5.2, sulfur chemisorption can block the surface sites for oxygen [138, 175]. Once the O_2 permeation would be hindered, sites near the upper region of phase boundaries are occupied by SO_2. A larger segregation at the upper region can possibly give more driving force for SO_2 to transport across the scale. Figure 5.88 schematically shows phase boundaries providing access paths for SO_2 when oxide scale was formed in the presence of salt.

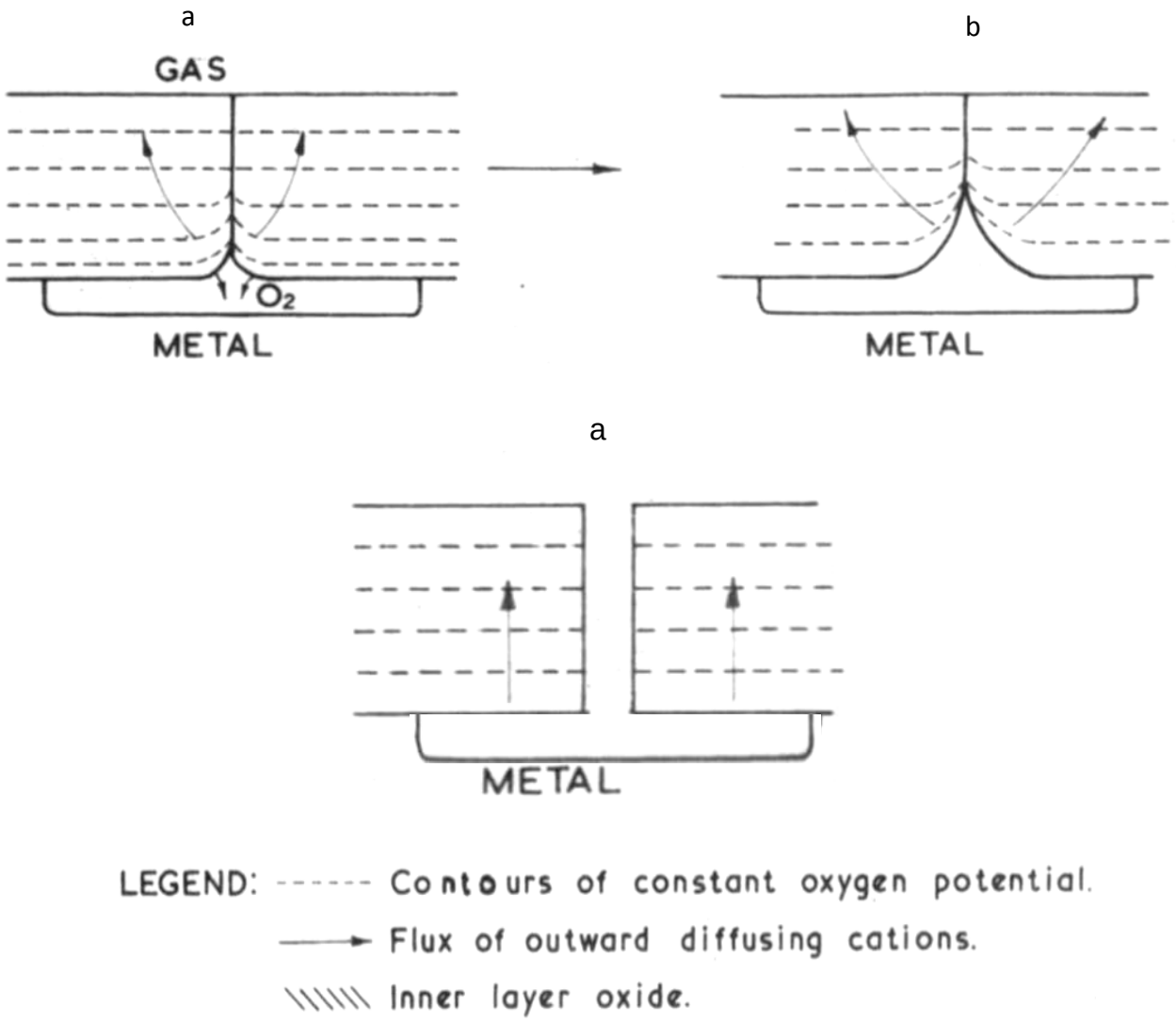

Figure 5.87 The development of micro-channel above interfacial voidage

Figure 5.76 shows that internal sulfides formed beneath a zone of internal oxides. The internal sulfides forming underneath the internal oxides zone are not due to sulfur diffusing faster than oxygen into the alloy. The opposite would be expected as sulfur diffuses by substitutional transport [176, 177], whereas oxygen is by interstitial transport [44]. Instead, the internal oxides forming in the upper region are because oxides are more stable than sulfides. The more stable phases have a lower equilibrium solubility product [4] and are more likely to precipitate.

Specifically, the solubility product of sulfides was not exceeded within the internal oxidation zone. Accordingly, sulfur has to diffuse through the internal oxidation zone and reach a deeper region where the activity of metal is high enough such that the solubility product of sulfides was exceeded.

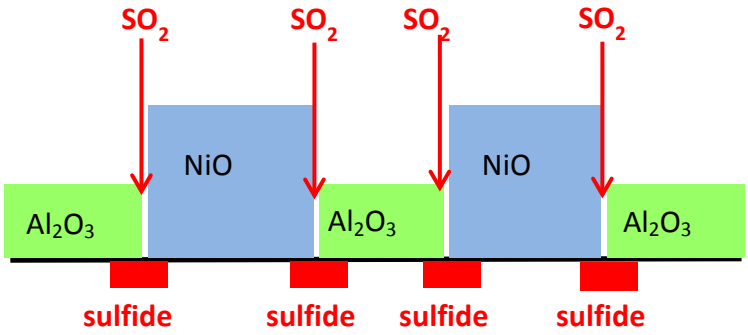

Figure 5.88 Phase boundaries provide a faster path for molecular SO_2 transport.

5.4.3.2 The role of salt in affecting the early stage oxidation

Another interesting phenomenon observed is the role of salt in affecting the early-stage oxidation. In Figure 5.78, a uniform oxide scale was formed when PWA1484 alloys were exposed in O_2+1000ppm SO_2 atmosphere only, without Na_2SO_4 deposit. As shown by Figure 5.62b and Figure 5.65 in section 5.3, 20 hours of oxidation of the PWA 1484 alloy in SO_2-containing atmosphere promoted exclusive external α-Al_2O_3 scale formation due to the presence of trace amounts of SO_2 inhibiting the fast growing NiO and θ-Al_2O_3. This was discussed in detail in section 5.2 and 5.3.

When salt is present in an O_2-1000ppmSO_2 atmosphere, it creates an inhomogeneous oxide-scale formation, as shown in Figure 5.81, thus disrupting the protective oxide-scale

formation at a very early stage. Phase boundaries in the disrupted oxide scale provide an access path for molecular SO_2 transport, causing internal sulfidation underneath.

In short, SO_2 and salt play an important role in affecting early-stage oxide scale establishment. As a summary, the scale evolution in SO_2 environments with and without salt is schematically shown in Figure 5.89. The top row shows when oxidation takes place in an atmosphere containing a trace amount of SO_2. Due to the preferential adsorption of sulfur, it helps to promote an external alumina scale formation. In this situation, the presence of SO_2 is clearly beneficial. The bottom row shows when oxidation takes place in an atmosphere containing both SO_2 and an Na_2SO_4 deposit. The oxide scale that forms underneath the salt deposit was not uniform. Certain regions formed NiO and certain regions formed Al_2O_3. This scale allows SO_2 permeation and causes internal sulfide formation underneath. In this situation, the presence of SO_2 is detrimental.

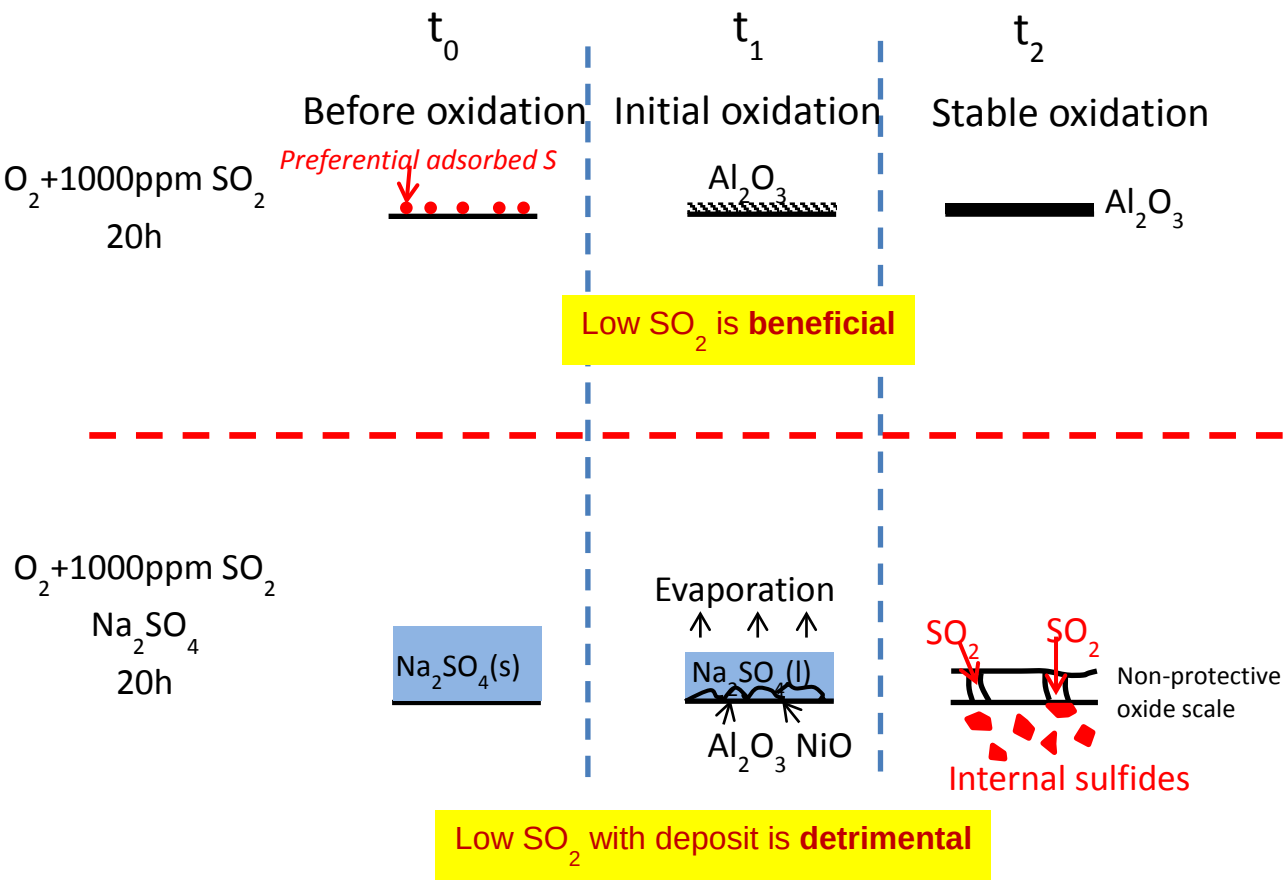

Figure 5.89 The scale evolution in SO_2 environments with and without salt

5.4.4 Conclusions

Oxidation tests of Na_2SO_4 –deposited PWA1484 were conducted at 900°C in gases with SO_2 concentration ranging from 0 to 1000ppm. With an increase in SO_2 content, the extent of attack increased, particularly the extent of internal sulfidation. Thus, with a deposit, SO_2 can be detrimental. This was due to SO_2 introducing internal sulfidation as a mode of degradation beyond that found with Type I hot corrosion. The former can be quite significant, depending on P_{SO2}. The experimental results showed a previously unreported bi-mode corrosive attack involving (1) hot corrosion and (2) extensive internal sulfidation.

SO_2 can access into the oxide scale mainly because salt affects the early-stage oxidation by disrupting the protective oxide scale. NiO/Al_2O_3 phase boundaries provide access paths for molecular SO_2 transport.

By contrast, without deposit, a small amount of SO_2 can be beneficial due to the preferential adsorbed sulfur favouring preferential Al_2O_3 formation.

6.0 MAIN CONCLUSIONS

6.1 INVESTIGATION OF THE KEY FACTORS OF OXIDE SCALE PROPERTIES AND ALLOY ABILITY FOR EXTENDING THE INCUBATION STAGE IN TYPES I HOT CORROSION

- Initial alumina crystal structure seems not to affect the incubation stage of type I hot corrosion
- the formation of a continuous and tenacious oxide scale of Al_2O_3 or $(Al,Cr)_2O_3$ is necessary for hot-corrosion protection;
- The maintenance of a protective alumina scale or sub-scale depends on the scale adhesion and the re-healing capability of the alloy subsurface;
- The onset of breakaway corresponds to the alloy's inability to maintain protective-alumina scale formation. The ability of alloy to maintain protective alumina scale can be affected by the addition of minor elements such as Si and Pt.
- The Na_2SO_4 deposit promotes the α-Al_2O_3 establishment

6.2 INVESTIGATION OF THE EFFECTS OF SO_2 AND NA_2SO_4 DEPOSIT ON THE OXIDATION AND CORROSION BEHAVIOR OF ALUMINA-SCALE

Without deposit, a small amount of SO_2 can be <u>beneficial</u>:

- Sulfur promotes the establishment of α-Al_2O_3. This promoted α-Al_2O_3 establishment was due to sulfur enrichment on the alloy surface. This enrichment started when samples were exposed to O_2+1%SO_2 at the pre-tested position (~150°C) while setting up the gas equilibrium. It was found by XPS measurement that the sulfur was mainly in the form of $NiSO_4$ (i.e. S^{6+} state). The chemieSTEM results showed a ~20nm band of sulfur enrichment at the surface of the sample exposed in the pre-test conditions. The surface enrichment of sulfur is inferred to block the surface sites for oxygen reaction and consequently effectively decrease oxygen supply for the scale growth. It is assumed that with limited oxygen supply, the faster growing θ-Al_2O_3 is less favored, thus allowing α-Al_2O_3 to have sufficient time to establish a continuous layer during the kinetic competition with θ-Al_2O_3. This hypothesis was supported by kinetic calculations and complementary tests in a low p_{O_2} atmosphere. A promoted α-Al_2O_3 establishment was observed on a model alloy when oxidation took place in Ar at 900°C. When oxygen supply is limited, the growth rate of θ-Al_2O_3 decreases more dramatically than that of α-Al_2O_3, during the lateral growth, the inhibition of θ-Al_2O_3 growth will allow α-Al_2O_3 to gain advantage in establishing a continuous layer underneath. Therefore, the sulfur-promoted α-Al_2O_3 establishment can be due to sulfur preferentially adsorbing and effectively limiting oxygen supply.

- Sulfur promotes the transition from internal to external Al_2O_3-scale formation. This promoted transition can be due in part to sulfur decreasing the oxygen permeability into the alloy, thus making it easier for Al_2O_3 to establish externally. Other than this, the sulfur promoting α-Al_2O_3 formation, which requires less Al consumption compared to a metastable alumina and thus lessens the likelihood of the chemical breakdown of the external alumina scale.

With deposit, SO_2 can be <u>detrimental</u>:

- Presence of SO_2 allows for internal sulfidation as a mode of degradation beyond that found with Type I hot corrosion. The former can be quite significant, depending on P_{SO2}.
- Salt affects the early-stage oxidation by disrupting the protective oxide scale.
- NiO/Al_2O_3 phase boundaries provide access paths for molecular SO_2 transport

7.0 FUTURE WORK

The following aspects are suggested for future investigation.

One direction could be to investigate the role of SO_2 and Na_2SO_4 on low temperature (Type II) hot corrosion of alumina-forming alloys. This subject was not touched upon in the current thesis.

Another area of research could be to better quantify the extent to which attack caused by salt-induced Type I hot corrosion is affected by the presence SO_2. It was shown in this thesis that the presence of SO_2 under Type I hot-corrosion conditions can lead to an amount of internal sulfidation, beyond that associated solely with hot-corrosion attack. However, it is not clear whether the presence of SO_2 affected the salt-induced Type I hot corrosion itself. This can be a research subject for future investigation.

A third research topic could be to investigate how the presence of a small amount of SO_2 in the atmosphere affects the oxygen permeability in nickel-based alloys. It was concluded in section 5.3.3.1 of this thesis that the presence of trace SO_2 can decrease oxygen permeability. $N_O^S D_O$. in dilute Ni-3at.%Al alloys and Ni-Cr-Al alloys. However it is not known whether N_O^S, D_O, or both were affected. Resolving this question requires the measurement of the sulfur penetration depth using highly sensitive characterization methods. It would be worth analyzing this aspect using glow discharge optical emission spectroscopy (GD-OES).

Regarding the breakaway from the incubation stage during hot corrosion, the failure due to chemical breakdown was investigated. However, the breakdown of protective behavior can be a dynamic process that depends on both mechanical failure and chemical composition change. Another research subject could be the importance of mechanical failure of the scale on hot corrosion. As for alloying elements, the role of minor additions, such as Y and Hf, on hot corrosion behavior was not clear. This subject can be explored to a greater extent in future research.

Finally, high resolution TEM observation of the selective transport of SO_2 through NiO/Al_2O_3 phase boundaries and investigations of the mechanism underlying this phenomenon are needed.

BIBLIOGRAPHY

[1] EPRI, Palo Alto, CA, Colorado School of Mines, Golden, Co. Office of Naval Research Center, Arlington. VA and Department of Energy, Oak Ridge 2003.

[2] M.N. Task,Ph.D. Thesis, The University of Pittsburgh, (2012).

[3] M.N. Task, B. Gleeson, F.S. Pettit, G.H. Meier, Surface and Coatings Technology, 206 1552-1557.

[4] B. Gleeson, High Temperature Corrosion of Metallic Alloys and Coatings, in: M. Schütze (Ed.) Corrosion and Environmental Degradation of Materials, Wiley-VCH, 2000, pp. 173.

[5] R.C. Reed, The Superalloys: Fundamentals and Applications, Cambridge University Press, Cambridge, 2008.

[6] C.T. Sims, N.S. Stoloff, W.C. Hagel, John Wiley&Sons, New York, 1987.

[7] C.T. Sims, W.C. Hagel, The Superalloys, Wiley, New York, 1972.

[8] M.J. Donachie, S.J. Donachie, Superalloys: A Technical Guide, 2nd Edition.

[9] S. Copley, B. Kear, AIME, TRANSACTIONS, 239 (1967) 984-992.

[10] F. Furillo, J. Davidson, J. Tien, L. Jackman, Materials Science and Engineering, 39 (1979) 267-273.

[11] P. Caron, T. Khan, Materials Science and Engineering, 61 (1983) 173-184.

[12] P. Caron, T. Khan, Aerospace Science and Technology, 3 (1999) 513-523.

[13] T.M. Pollock, S. Tin, Journal of Propulsion and Power, 22 (2006) 361-374.

[14] C.T. Sims, Superalloys, TMS_AIME, Warrendale, PA, 1984, pp. 399.

[15] http://www.grc.nasa.gov/WWW/StructuresMaterials/AdvMet/research/turbine_blades.html.

[16] R. Darolia, Wright-Patterson, APF, Dayton, OH, 2006.

[17] G. Goward, D. Boone, Oxidation of Metals, 3 (1971) 475-495.

[18] D.L.R. Olson, G.R. Edwards, O.R.N. Laboratory, U.S.O.o.N. Research, J. Colorado School of Mines. Center for Welding, C. Research, Workshop on Materials and Practices to Improve Resistance to Fuel Derived Environmental Damage in Land- and Sea-based Turbine, Center for Welding, Joining and Coatings Research, Colorado School of Mines, 2003.

[19] D.R.G. Achar, R. Munoz-Arroyo, L. Singheiser, W.J. Quadakkers, Surface and Coatings Technology, 187 (2004) 272-283.

[20] J.R. Nicholls, JOM, 52 (2000) 28-35.

[21] J.R. Nicholls, N.J. Simms, W.Y. Chan, H.E. Evans, Surface and Coatings Technology, 149 (2002) 236-244.

[22] Z.H. Tang, B. Gleeson,To be published results,(2013).

[23] D.J. Sordelet, S. Hayashi, B. Gleeson, W. Wang, Materials Science Forum, Trans Tech Publications, 2004, pp. 213-222.

[24] S. Hayashi, W. Wang, D.J. Sordelet, B. Gleeson, Metallurgical and Materials Transactions A, 36 (2005) 1769-1775.

[25] V.P.Deodeshmukh,Ph.D. Thesis, Iowa State University, (2007).

[26] J. Tien, F. Pettit, Metallurgical Transactions, 3 (1972) 1587-1599.

[27] A.S. Radcliff, Materials Science and Technology, 3 (1987) 554.

[28] S. Jansen, E.A. Gulbransen, 4th International Congress on Metallic Corrosion, Amsterdam 1969.

[29] E. Opila, N. Jacobson, D. Myers, E. Copland, JOM, 58 (2006) 22-28.

[30] G.R. Wallwork, A.Z. Hed, Oxidation of Metals, 3 (1971) 171-184.

[31] M.S. Smith Jr, M.S. Hilboldt, T.A. Bhat, Google Patents, 1983.

[32] E.J. Opila, Journal of the American Ceramic Society, 86 (2003) 1238-1248.

[33] T.A. Kircher, E.L. Courtright, Materials Science and Engineering: A, 155 (1992) 67-74.

[34] M.P. Brady, I.G. Wright, B. Gleeson, JOM, 52 (2000) 16-21.

[35] F.A. Elrefaie, W.W. Smeltzer, Journal of the Electrochemical Society, 128 (1981) 2237-2242.

[36] G.H. Meier,Private communication

[37] N.Birks, G.H.Meier, F.S.Pettit, Introduction to High Temperature Oxidation of Metals, Arnold, London, 2006, pp. 207.

[38] C. Wagner, Zeitschrift für Elektrochemie, Berichte der Bunsengesellschaft für physikalische Chemie, 63 (1959) 772-782.

[39] G. Böhm, M. Kahlweit, Acta Metallurgica, 12 (1964) 641-648.

[40] F. Maak, Z. Metallkde., 52 (1961) 545.

[41] R.A. Rapp, Acta Metallurgica, 9 (1961) 730-741.

[42] W. Gust, M.B. Hintz, A. Loddwg, H. Odelius, B. Predel, Physica Status Solidi (a), 64 (1981) 187-194.

[43] W. Zhao, B. Gleeson, Oxidation of Metals, 79 (2013) 613-625.

[44] J.-W. Park, C. Altstetter, MTA, 18 (1987) 43-50.

[45] F.S.Pettit, Transactions of the Metallurgical Society of AIME, 239 (1967) 1296-1305.

[46] G.H. Meier,Private communication,(2013).

[47] C. Wagner, Journal of the Electrochemical Society, 103 (1956) 571-581.

[48] G.C. Rybicki, J.L. Smialek, Oxidation of Metals, 31 (1989) 275-304.

[49] F.S. Pettit, Transactions of the Metallurgical Society of AIME, 239 (1967) 1296-1305.

[50] C. Wagner, Corrosion Science, 5 (1965) 751-764.

[51] B.H. Kear, F.S. Pettit, D.E. Fornwalt, L.P. Lemaire, Oxidation of Metals, 3 (1971) 557-569.

[52] Y. Niu, X.J. Zhang, Y. Wu, F. Gesmundo, Corrosion Science, 48 (2006) 4020-4036.

[53] H.W. Pickering, Journal of The Electrochemical Society, 119 (1972) 641-649.

[54] C.S. Giggins, F.S. Pettit, Journal of the Electrochemical Society, 118 (1971) 1782-1790.

[55] G.C. Wood, I.G. Wright, T. Hodgkiess, D.P. Whittle, Werkst. Korros. , 21 (1970) 900.

[56] J.R. Nicholls, P. Hancock, L.H. Al-Yasiri, Materials Science and Technology, 5 (1989) 780-798.

[57] W. Zhao,Ph.D. Thesis, The University of Pittsburgh, (2012).

[58] K. Wefers, C. Misra, Alcoa Laboratories, Pittsburgh, PA, (1987).

[59] D. Lipkin, D. Clarke, M. Hollatz, M. Bobeth, W. Pompe, Corrosion Science, 39 (1997) 231-242.

[60] V.K.Tolpygo, D.R. Clarke, Microscopy of Oxidation: Proceedings of the fourth international conference on the microscopy of oxidation, Science Reviews, Cambridge, 2000, pp. 59-70.

[61] M. Brumm, H. Grabke, Corrosion Science, 33 (1992) 1677-1690.

[62] B. W. Veal, A. P. Paulikas, R.C. Birtcher, Applied Physics Letters, 89 (2006) 161916.

[63] R.B. Bagwell, G.L. Messing, P.R. Howell, Journal of Materials Science, 36 (2001) 1833-1841.

[64] B. Pint, M. Treska, L. Hobbs, Oxidation of Metals, 47 (1997) 1-20.

[65] X.F. Zhang, K. Thaidigsmann, J. Ager, P.Y. Hou, Journal of Materials Research, 21 (2006) 1409-1419.

[66] J. Doychak, M. Rühle, Oxidation of Metals, 31 (1989) 431-452.

[67] B. Gleeson, Z.H.Tang, MS&T conference, Pittsburgh, 2009.

[68] Y. Cadoret, M.P. Bacos, P. Josso, V. Maurice, P. Marcus, S. Zanna, Materials Science Forum, 247 (2004) 461-464.

[69] Y. Cadoret, D. Monceau, M.P. Bacos, P. Josso, V. Maurice, P. Marcus, Oxidation of Metals, 64 (2005) 185-205.

[70] K.M.N. Prasanna, A.S. Khanna, R. Chandra, W.J. Quadakkers, Oxidation of Metals, 46 (1996) 465-480.

[71] H.J. Grabke, Materials Science Forum, (1997) 251-254.

[72] J. Jedliński, S. Mrowec, Materials Science and Engineering, 87 (1987) 281-287.

[73] B. Pint, J. Martin, L. Hobbs, Solid State Ionics, 78 (1995) 99-107.

[74] Z.H. Zhou, H.B. Guo, M. Abbas, S.K. Gong, Corrosion Science, 53 (2011) 2943-2947.

[75] S. Chevalier, P. Juzon, K. Przybylski, J.P. Larpin, Science and Technology of Advanced Materials, 10 (2009) 045006.

[76] F. Liu, H. Liu, H. Josefsson, J.E. Svensson, L.G. Johansson, M. Halvarsson, Materials at High Temperatures, 3 (2005) 521-526.

[77] H. Götlind, F. Liu, J.E. Svensson, M. Halvarsson, L.G. Johansson, Oxidation of Metals, 67 (2007) 251-266.

[78] X. Liu, B. Gleeson, Oxidation of Metals, 80 (2013) 517-527.

[79] P. Kofstad, High Temperature Corrosion, Elsevier Applied Science Publishers Ltd, Essex, England, 1988.

[80] J.G. Tschinkel, Corrosion, 28 (1972) 161-169.

[81] M.A. DeCrescente, N.S. Bornstein, 24 (1968) 127-133.

[82] R. Sokhi, World Atlas of Atmospheric Pollution, Anthem Press, Anthem Press, New York, 2008.

[83] Z.H. Tang, B. Gleeson,To be published results,(2012).

[84] J. Stringer, in: R.A. Rapp (Ed.) NACE, Houston, TX, 1983, pp. 389.

[85] L.F. Aprigliano, in: D.W. Taylor (Ed.), Naval Ship Research and Development Center, 1977.

[86] K.L. Luthra, D.A. Shores, Journal of the Electrochemical Society: Solid-State Science and Technology, 127 (1980) 2202.

[87] K.A. Bol'shakov, P.I. Fedorov, Zh. Obshch. Khim, 26 (1956) 348.

[88] K.L. Luthra, MTA, 13 (1982) 1647-1654.

[89] F. Pettit, Oxidation of Metals, 76 (2011) 1-21.

[90] R.L. Jones, in: R.A. Rapp (Ed.) Proceeding of International Conference on High Temperature Corrosio, San Diego March, 1981, pp. 513-518.

[91] R.L. Jones, S.T. Gadomski, Journal of the Electrochemical Society, 129 (1982) 1613-1618.

[92] F. Pettit, Oxidation of Metals, 76 (2011) 1-21.

[93] P.S. Sidky, M.G. Hocking, Corrosion Science, 27 (1987) 183-203.

[94] N. Otsuka, R.A. Rapp, Journal of the Electrochemical Society, 137 (1990) 46-52.

[95] A.K. Misra, Journal of the Electrochemical Society, 133 (1986) 1038-1042.

[96] K. Lillerud, P. Kofstad, Oxidation of Metals, 21 (1984) 233-270.

[97] P. Kofstad, G. Åkesson, Oxidation of Metals, 14 (1980) 301-323.

[98] R.A. Rapp, N. Otsuka, The Electrochemical Society, 2008.

[99] R.A. Rapp, K.S. Goto, The Second International Symposium on Molten Salts, 1981.

[100] R.A. Rapp, K.S. Goto, Hot Corrosion of Metals by Molten Salts, Electrochemical Society, 1981.

[101] T.E. Strangman, Thin Solid Films, 127 (1985) 93-106.

[102] R.A. Rapp, Materials Science and Engineering, 87 (1987) 319-327.

[103] J. Goebel, F. Pettit, Metallurgical and Materials Transactions B, 1 (1970) 1943-1954.

[104] M.N. Task, B. Gleeson, F.S. Pettit, G.H. Meier, Oxidation of Metals, 80 (2013) 125-146.

[105] R.A. Rapp, N. Otsuka, ECS Transactions, 16 (2009) 271-282.

[106] M.N. Task, B. Gleeson, F.S. Pettit, G.H. Meier, 8th INTERNATIONAL SYMPOSIUM ON HIGH-TEMPERATURE CORROSIONAND PROTECTION OF MATERIALS, Les Embiez, 2012.

[107] Materials Preparation Center, Ames Laboratory of US DOE, Ames, IA, USA, http://www.mpc.ameslab.gov.

[108] Y. Kitajima, S. Hayashi, T. Narita, Materials Science Forum, 522 (2006) 103.

[109] D.B. Hovis, A.H. Heuer, Journal of Microscopy, 240 (2010) 173-180.

[110] Q.Z. Wen, D.M. Lipkin, D.R.Clarke, Journal of the American Ceramic Society, 81 (1998) 3345-3348.

[111] V.K. Tolpygo, D.R. Clarke, Materials at High Temperatures, 17 (2000) 59-70.

[112] Q. Z. Wen, D. M. Lipkin, D.R. Clarke, Journal of the American Ceramic Society, 81 (1998) 3345-3348.

[113] J.M.A. Orozco,Ph.D. Thesis, Cinvestav, (2013).

[114] W. Zhao, Z. Li, B. Gleeson, Oxidation of Metals, 79 (2013) 361-381.

[115] B. Gleeson, Materials Research, 7 (2004) 61-69.

[116] H.J. Grabke, R. Lobnig, P. Papaiacovou, Selected Topics in High Temperature Chemistry: Defect Chemistry of Solids, Elsevier, New York, 1989.

[117] B. Ahmad, P. Fox, Oxidation of Metals, 52 (1999) 113-138.

[118] J. Jedliński, G. Borchardt, S. Mrowec, Solid State Ionics, 50 (1992) 67-74.

[119] B.A. Pint, J.R. Martin, L.W. Hobbs, Solid State Ionics, 78 (1995) 99-107.

[120] J.L.S. J. Doychak, and T. E. Mitchell, Metallurgical and Materials Transactions A: Physical Metallurgy and Materials Science 20A (1989) 499.

[121] J.M. Alvarado-Orozco, R. Morales-Estrella, M.S. Boldrick, J.L. Ortiz-Merino, D.G. Konitzer, G. Trápaga-Martínez, J. Muñoz-Saldaña, Oxidation of Metals, 78 (2012) 269-284.

[122] R. Rapp, A. Ezis, G. Yurek, Metallurgical Transactions, 4 (1973) 1283-1292.

[123] J.A. Beek, P.M.T. Kok, F.J.J. Loo, Oxidation of Metals, 22 (1984) 147-160.

[124] F.J.J. Loo, J.A. Beek, G.F. Bastin, R. Metselaar, Oxidation of Metals, 22 (1984) 161-180.

[125] S. Hayashi, D. J. Sordelet, L.R. Walker, B. Gleeson, Materials Transactions, 49 (2008) 1550-1557.

[126] J. He, D.R. Clarke, Journal of the American Ceramic Society, 78 (1995) 1347-1353.

[127] B. Lindberg, K. Hamrin, G. Johansson, U. Gelius, A. Fahlman, C. Nordling, K. Siegbahn, Physica Scripta, 1 (1970) 286.

[128] F. Jin, H. Long, W. Song, G. Xiong, X. Guo, X. Wang, Energy & Fuels, (2013).

[129] R.B. Shalvoy, P.J. Reucroft, Journal of Vacuum Science and Technology, 16 (1979) 567-569.

[130] D.L. Legrand, H.W. Nesbitt, G.M. Bancroft, American Mineralogist, 83 (1998) 1256-1265.

[131] A. Järdnäs, J.-E. Svensson, L.-G. Johansson, Oxidation of Metals, 69 (2008) 249-263.

[132] X. Liu, B. Gleeson, Oxidation of Metals, 80 (2013) 517-527.

[133] P.Y. Hou, Annual Review of Materials Research, 38 (2008) 275-298.

[134] P.Y. Hou, A. Paulikas, B. Veal, Materials Science Forum, Trans Tech Publ, 2004, pp. 671-680.

[135] E. Schumann, Oxidation of Metals, 43 (1995) 157-172.

[136] R. Chegroune, E. Salhi, A. Crisci, Y. Wouters, A. Galerie, Oxidation of Metals, 70 (2008) 331-337.

[137] K.P. Lillerud, B. Haflan, P. Kofstad, Oxidation of Metals, 21 (1984) 119-134.

[138] G. Luckman, R.S. Polizzotti, Metallurgical and Materials Transactions A, 16 (1985) 133-136.

[139] H.J. Grabke, R. Möller, A. Schnaas, Werkst. Korros., 30 (1979) 794-799.

[140] W.J. Quadakkers,Private communication,(2013).

[141] R.B. Bird, W.E. Stewart, E.N. Lightfoot, Transport phenomena, Wiley, 2006.

[142] D.R. Poirier, G.H. Geiger, Transport phenomena in materials processing, Minerals, Metals & Materials Society, 1994.

[143] D.R. Gaskell, An introduction to transport phenomena in materials engineering, Prentice Hall, 1992.

[144] R.C. Reid, J.M. Prausnitz, B.E. Poling, The properties of gases and liquids, 1987.

[145] J.O. Hischfelder, R.B. Bird, E.L. Spotz, Chemical Reviews, 44 (1949) 205.

[146] M. Næss, D. Young, J. Zhang, J. Olsen, G. Tranell, Oxidation of Metals, 78 (2012) 363-376.

[147] T.J. Nijdam, G.H. Marijnissen, E. Vergeldt, A.B. Kloosterman, W.G. Sloof, Oxidation of Metals, 66 (2006) 269-294.

[148] T.J. Nijdam, L.P.H. Jeurgens, W.G. Sloof, Acta Materialia, 53 (2005) 1643-1653.

[149] J. Wynnyckyj, C. Morris, Metallurgical and Materials Transactions B, 16 (1985) 345-353.

[150] Z. Nishiyama, M.E. Fine, M. Meshii, C.M. Wayman, Martensitic transformation, Academic Press, 1978.

[151] M. Kumagai, G.L. Messing, Journal of the American Ceramic Society, 68 (1985) 500-505.

[152] J. Doychak, J.L. Smialek, T.E. Mitchell, MTA, 20 (1989) 499-518.

[153] H.J.Grabke, Intermetallics, 7 (1999) 1153-1158.

[154] J.M. Wagner, X-Ray Photoelectron Spectroscopy: Chemical Engineering Methods and Technology, Nova Science Publishers, Inc., 2013.

[155] B.Gleeson, J.C. Yang,Private communication,(2013).

[156] A. Agüero, M. Gutiérrez, L. Korcakova, T.T.M. Nguyen, B. Hinnemann, S. Saadi, Oxidation of Metals, 76 (2011) 23-42.

[157] W.W. Smeltzer, P.C. Patnaik, Journal of the Electrochemical Society, 132 (1985) 1233-1236.

[158] P.C. Patnaik, W.W. Smeltzer, Journal of the Electrochemical Society, 132 (1985) 1226-1232.

[159] A.R. Setiawan, M. Hanafi Bin Ani, M. Ueda, K. Kawamura, T. Maruyama, ISIJ International, 50 (2010) 259-263.

[160] F.H. Stott, G.C. Wood, Materials Science and Technology, 4 (1988) 1072-1078.

[161] F.A. Elrefaie, W.W. Smeltzer, Journal of the Electrochemical Society, 128 (1981) 2237-2242.

[162] F. Gesmundo, F. Viani, Oxidation of Metals, 25 (1986) 269-282.

[163] J. Young, Chapter 6 Oxidation of Alloys II: Internal Oxidation, in: Y. David John (Ed.) Corrosion Series, Elsevier Science, 2008, pp. 247-314.

[164] P. Hancock, First International Conference on Metallic Corrosion, Butterworth, London, 1962, pp. 193-198.

[165] C.J. Powell, M.P. Seah, Journal of Vacuum Science & Technology A: Vacuum, Surfaces, and Films, 8 (1990) 735-763.

[166] J.T. Grant, P. Williams, J. Fine, C.J. Powell, Surface and Interface Analysis, 13 (1988) 46-50.

[167] G. Kreysa, M. Schütze, Wiley-VCH, 2008.

[168] M.E. Glicksman, Diffusion in solids: field theory, solid-state principles, and applications, Wiley, 2000.

[169] G.B. Gibbs, R. Hales, Corrosion Science, 17 (1977) 487-507.

[170] A. Brückman, J. Romanski, Corrosion Science, 5 (1965) 185-191.

[171] S. Mrowec, T. Werber, Corrosion Science, 5 (1965) 717-727.

[172] S. Mrowec, Corrosion Science, 7 (1967) 563-578.

[173] A. Brückman, R. Emmerich, S. Mrowec, Oxidation of Metals, 5 (1972) 137-147.

[174] J. Robertson, M.I. Manning, Materials Science and Technology, 4 (1988) 1064-1071.

[175] J. Liu, J.P. Lu, P.W. Chu, J.M. Blakely, American Vacuum Society, 10 (1992) 2355-2360.

[176] C.I. Smithels, Metals Reference Book Butterworths, 1967.

[177] J.P. Pfeiffer, Z. Metallk, 46 (1965) 516.